Interaction of Single Metallo-Porphyrins with Titania Surfaces

-Advanced Atomic Force Microscopy Studies-

Inauguraldissertation

zur

Erlangung der Würde eines Doktors der Philosophie

vorgelegt der

Philosophisch-Naturwissenschaftlichen Fakultät

der Universität Basel

von

Res Jöhr
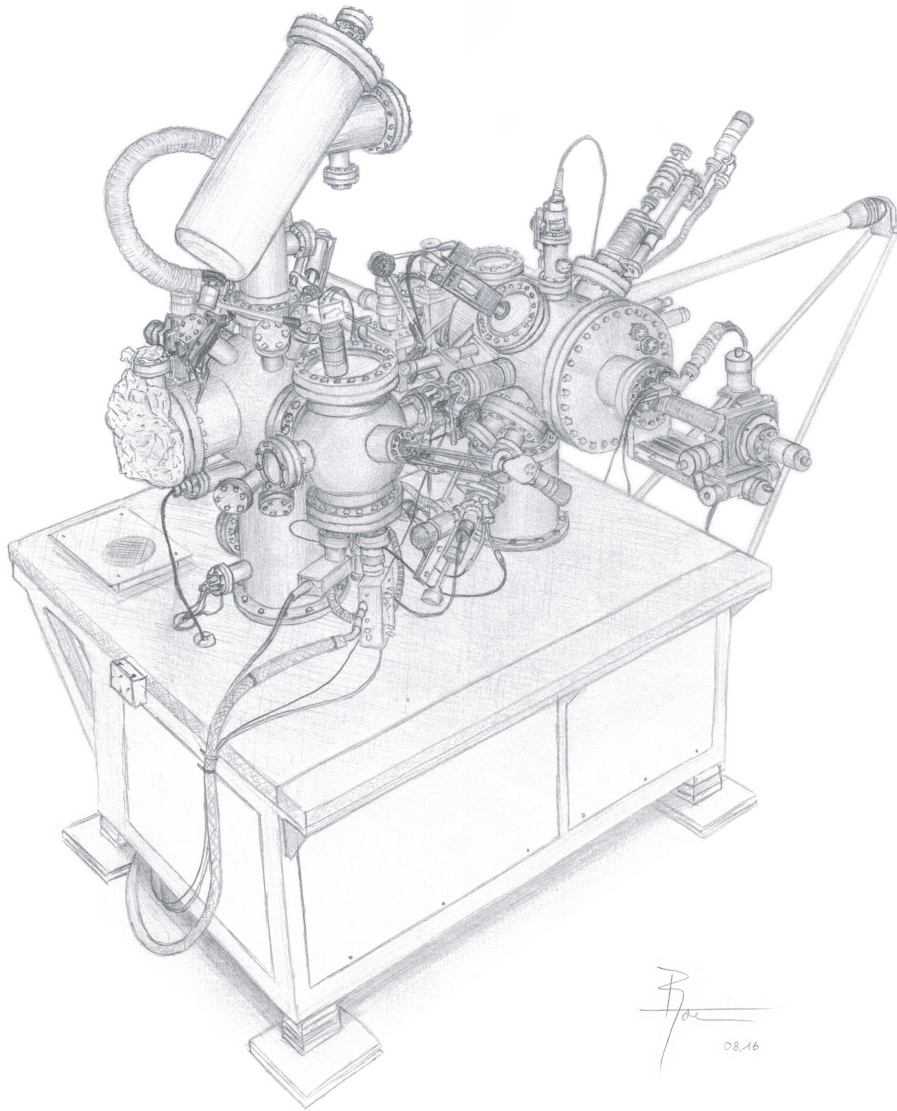
aus Buchholterberg (BE)

Basel, 2017

Genehmigt von der Philosophisch-Naturwissenschaftlichen Fakultät
auf Antrag von

Prof. Dr. Ernst Meyer
Prof. Dr. Christian Loppacher

Basel, den 21.06.2016

Prof. Dr. Jörg Schibler
Dekan

Science is art!

Abstract

In recent years, nanotechnology emerged as a new research field that has the goal to get control over matter at the nanoscale. Hence, basic research aims to understand and tailor the properties of the nanoscale building blocks such as single molecules or nanoparticles. The potential applications of such nanosystems comprise surface science, microfabrication, medicine and many more. The present thesis examines this aspect for individual molecules that are adsorbed on surfaces. Thereby the surface gets functionalized with the molecular properties. The porphyrin-titania interfaces, which were studied in particular, become able to absorb light in the visible region. They are therefore suitable for application in organic-inorganic photovoltaics or photocatalysis. In order to enhance the performance of these interfaces it is important to investigate the molecular adsorption on the nanoscale. In this thesis, this task was first accomplished using a combined experimental approach with scanning probe microscopy (SPM) and photoelectron spectroscopy (PES) as well as density functional theory (DFT) calculations. The capability of atomic force microscopy (AFM) was further expanded during the thesis by the use of a recently developed measurement scheme. Applying this new method, it was demonstrated that the adsorption configurations of a single molecule at room temperature can be characterized by AFM alone. Hence, this thesis successfully pursued two main goals: the improvement of a well-known experimental technique and its use for high-resolution investigation of single molecules in application relevant organic-inorganic interfaces.

Contents

Contents

Introduction

The human dream to design materials with predefined properties is a main goal in today's materials research. For a long time, most of the used materials were characterized by their bulk properties. With the emergence of nanotechnology, materials research was promoted to the next level. It offers the possibility to assemble complex structures out of smaller building blocks like with Lego. These prospects were already considered in the famous talk entitled "There is plenty of room at the bottom" by R. Feynman, who was one of the fathers of nanotechnology.[1] He already considered the manipulation of individual atoms as a new synthetic way to build up nanostructures. However, it took time until his vision was realized by the invention of scanning probe microscopy techniques in the 1980s.[2,3] These experimental methods use extremely sharp tips that are scanned over the surface in order to sense the sample topography. This allows imaging clean or adsorbate covered surfaces on the nanoscale and manipulating single atoms or molecules with the tip into predefined structures.[4–7] Besides controlled manipulation, it became apparent that large and well-defined molecular structures can also be built up by self-assembly. As a simple example, it was found that molecules can arrange in ordered 2D architectures at interfaces or surfaces.[8–14] More complicated three-dimensional self-assemblies are also possible.[8,15] In the ideal case, different building blocks are assembled into larger superstructures with new functionality such as the nanomachines in biological cells.[16,17] Somehow, it is generally an intricate task to assemble 3D nanoarchitectures. It is thus the aim of nanosciences to understand the interaction between the different components and to tune them systematically in order to allow the assembly of larger superstructures. To achieve this goal, nanosciences have become a highly interdisciplinary field of research. Molecular building blocks are often inspired by the structure of biomolecules. Synthesis or customization is done by chemistry. Computational simulations and methods from experimental physics, such as scanning probe methods, are applied to study the peculiarities of an assembled system.

The miniaturization offers the possibilities to design or tune materials in order to yield customized functionality. A widely applied approach is called surface functionalization, where the surface is covered with a molecule layer. In the simplest case, the molecular properties are transferred to the substrate as e.g. for hydrophobic coatings. In more complex systems, the molecule interacts with the substrate and forms a functional interface that exhibits new functionality. Examples for
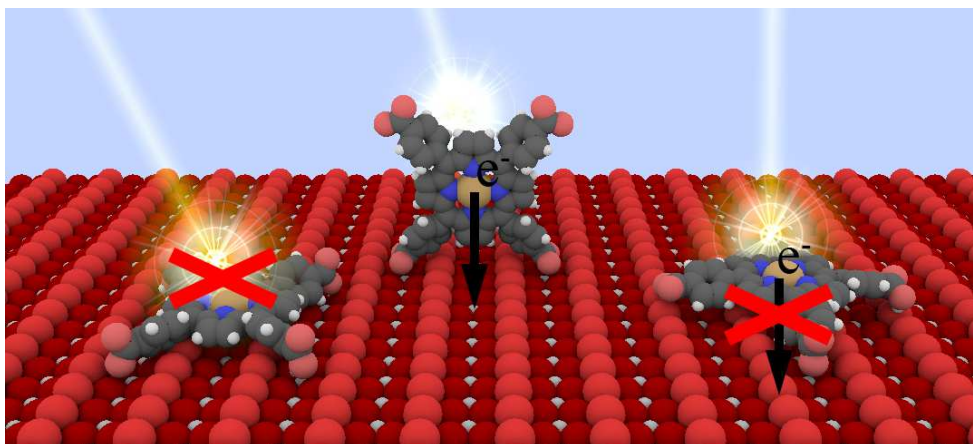
Figure 1.: Influences of the molecular adsorption mode on the performance of a surface that is functionalized with a light absorbing molecule: (left) no light absorption due to undesired interaction of molecular orbitals with the surface, (middle) functional dye that absorbs light and is able to inject an electron (e^-) into the substrate and (right) configuration with good light absorption properties but low electron injection efficiency.

applications are hybrid organic-inorganic interfaces for photovoltaics, catalysis, sensors, molecular switches and molecular electronics in general.[18–25] This also emphasizes the importance of nanotechnology for sustainable, environmental or renewable energy applications.

This work studies porphyrin sensitized titanium dioxide, that find application in dye-sensitized solar cells.[26] The key working principle of these devices is as follows. The adsorbed molecules, also known as the sensitizers, absorb the incoming photons. Thereby electrons are excited to higher energy levels and are injected into the conduction band of the TiO_2 substrate. The injected electrons can then be collected in form of an electron current. The efficiency of such an interface is found to rely on the adsorption configuration of the molecule on the surface. Some illustrative cases are shown in Fig. 1. This issue has been studied to a great extent for different sensitizers.[26–30] However, many investigations were mainly done by fabrication of devices with different dyes followed by rationalizing their photon to current conversion efficiency using potential models of the adsorption mode. It has to be stressed that this approach does not directly give information about the individual molecule nor does it allows studying the working mechanism in situ. Therefore, an atomic probe is needed. Scanning tunneling microscopy (STM), has thus been used to a wide extend to study the adsorption of individual molecules on metals.[13,31–33] Unfortunately, it is limited to conductive samples and cannot be used on poorly conducting substrates such as insulators. As an alternative, atomic force microscopy (AFM) was used for nonconducting samples and high-resolution of planar molecules was obtained at low temperatures that even revealed the molecular structure.[34–38] Despite these spectacular results, there were only few investigations on larger adsorbates or at room temperature, where the molecules generally wiggle around and might even diffuse on the sample surface.[39,40] Therefore, this work aimed to resolve and characterize

the adsorption mode of single molecules at room temperature using non-contact (nc) atomic force microscopy. Knowing the properties of individual adsorbates is supposed to further elucidate interface processes that might hinder device performance such as electronic coupling of molecular orbitals with the surface or recombination of charge carriers. In summary the aim of this thesis was two-fold: first to enhance the capability of nc-AFM at the submolecular length scale and second to use it for the study of an application relevant system. The disposition of the thesis is separated in two parts that are theory and experimental methods as well as results and discussion.

The first chapter reviews the theory of molecules on surfaces. It explains the different types of molecule-surface and intermolecular interactions that determine the adsorption behavior of a molecule. Thereby the role of functional groups that are used to immobilize molecules on the surface, e.g. by means of covalent bonds, is emphasized. Furthermore, the influence of the substrate on the molecular properties, which could potentially affect the performance of a hybrid interface, is discussed.

The second chapter covers the theory of the applied experimental techniques. The main focus is on high-resolution non-contact atomic force microscopy in ultra-high vacuum. Possible methods to overcome the resolution of standard nc-AFM such as bimodal or multipass AFM are explained in detail. Besides this, Kelvin probe force microscopy (KPFM), which is an extension of nc-AFM, and scanning tunneling microscopy are introduced. Photoelectron spectroscopy (PES), which was used for chemical analysis of the samples, will be explained briefly at the end of the chapter.

The third chapter is about materials and methods. It starts with an introduction to titanium dioxide and its different polymorphs, which is followed by a detailed discussion of the rutile TiO_2 (110) and anatase TiO_2 (101) surfaces. The idea behind surface functionalization of titania and the details about metallo-carboxyphenylporphyrins (MCPP) as sensitizers are further outlined. This is then followed by an explanation of the ultra-high vacuum (UHV) room temperature nc-AFM setup, comprising the preparation of the measuring tip and the functionalized titania surfaces. The chapter ends with specifications on the measurement control for nc-AFM and information about complementary methods such as density functional theory (DFT) calculations and the photoelectron spectroscopy setup at the Paul Scherrer Institute.

The fourth chapter covers the experimental results on the rutile TiO_2 (110) surface. It starts with the study of the bare surface and its defects. This is followed by a combined study of copper-tetracarboxyphenylporphyrin (CuTCPP) on rutile TiO_2 with nc-AFM and KPFM. In this study, nc-AFM on the second resonance was used to reveal the adsorption configurations of individual molecules. The experimental results were further assessed and corroborated by DFT calculations. The study suggested that MCPPs might get anchored covalently by annealing after deposition. This anchoring process was investigated and observed for trans zinc-di(carboxy-phenyl)-diphenylporphyrin (tr-ZnDCPP) using scanning tunneling microscopy and photoelectron spectroscopy at the Paul Scherrer Institute. The chapter further shows results from other zinc-

carboxyphenylporphyrins (ZnCPPs) that highlight the importance of the carboxylic anchor for molecular immobilization on rutile TiO$_2$ (110). It closes with submolecular imaging using bimodal and dual-pass nc-AFM at room temperature.

The fifth chapter treats the results from nc-AFM investigation on anatase TiO$_2$ (101). This substrate is much less known in literature. First, the bare substrate is studied and possible topography contrasts are explained by the tip termination. The adsorption behavior of ZnCPPs with a different number of carboxylic anchors on anatase, which is significantly different to rutile TiO$_2$ (110), is discussed afterwards. The last part covers detection of adsorption configurations by high-resolution dual-pass bimodal nc-AFM. It is shown that submolecular resolution on single molecules comprising detailed structural information of the substrate is possible using nc-AFM at room temperature. Furthermore, it gave evidence that nc-AFM is potentially able to detect the functional anchor groups.

The last chapter gives a conclusive summary of the whole dissertation that covers the key findings of this work and gives an outlook to future research topics in the field.

Part I.

Theory and Methods

1.
Molecules on Surfaces

The aim of this chapter is to introduce the reader to the theoretical background of molecule-surface interactions and to apply it to relatively large molecules. Substantially, this contains the review of basic concepts from chemistry, such as different interaction forces and interface processes. Large molecules consist of different building blocks and functional groups. Hence their adhesion to the surface as well as their mutual interaction are rather complex. Furthermore, the behavior of the molecules is strongly influenced by the temperature and the surrounding medium, e.g. by solvents. Thus a lot of interesting chemistry takes place at the interface and it is challenging to make a concise summary. Because the main part of this thesis considers samples where the molecules have been deposited by evaporation in ultra-high vacuum (UHV), it is convenient to describe the molecule-surface interface from this point of view. In order to keep the introduction as clear and instructive as possible the treatment will be limited to low coverage, i.e. below one mono-layer. In such cases the molecule-substrate interaction is dominant over the intermolecular forces.

The review will firstly focus on the interplay between a single molecule and the surface. The various types of interaction and their relevance on different substrates like metals, semiconductors and insulators will be discussed. Afterwards our attention is turned to weakly bound molecules, i.e. mobile species, where diffusion and interaction with defects or step edges become important. The influence of the surface structure on the diffusion, which is responsible for anisotropic diffusion, will be highlighted. Diffusion also allows the molecules to interact with each other, which can lead to the formation of self-assemblies, which is the last topic of this review. For brevity, the chapter will be limited to small self-assemblies and their growth processes with emphasis on the specific intermolecular interactions that are usually applied for tuning the growth and shape of the self-assemblies.

1.1. Interaction of Isolated Molecules with Surfaces

In order to understand the interaction of single molecules it is instructive to consider the adsorption process in more detail. Molecules that are evaporated to the surface have been thermally excited. Their kinetic energy is rather low. Hence it is observed that they survive the arrival without damage. After landing, the molecule will dissipate its excess thermal energy to the sur-
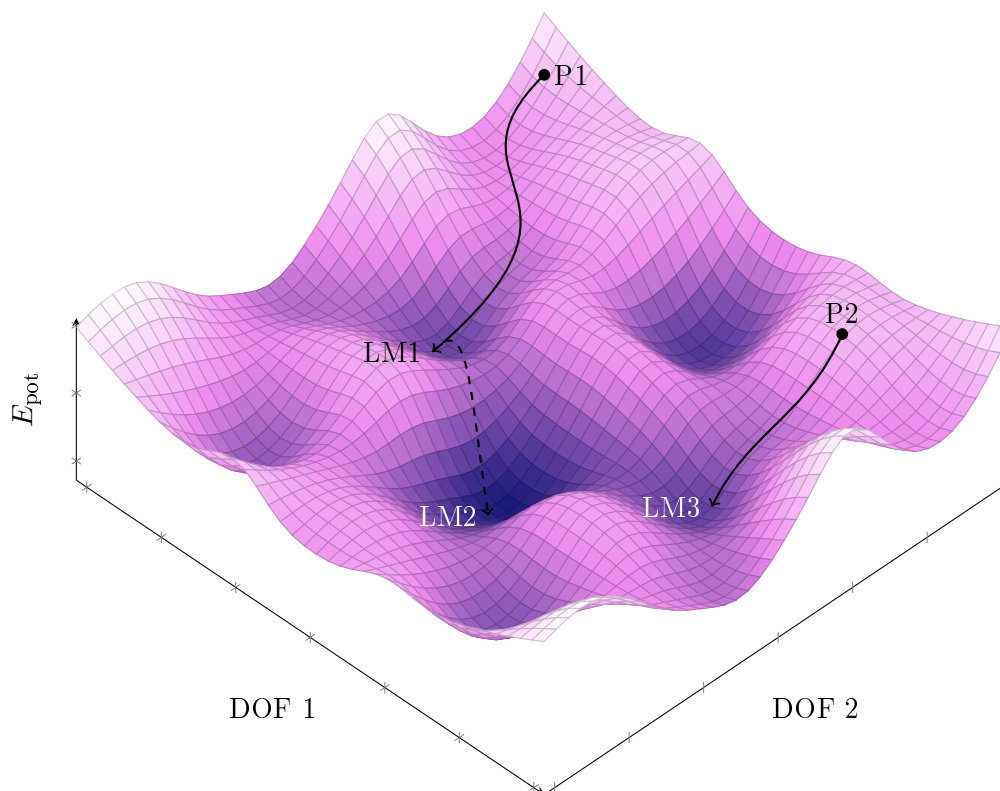
Figure 1.1.: Example of a potential energy surface with two degrees of freedom (DOF). The molecule lands at position P1 and has an initial configuration that relaxes first to a local minimum LM1. Excitation of the molecule, by e.g. heating allows to overcome potential barriers and to discover other minima with lower energy, like e.g. LM2. Landing at a different position or in another configuration, e.g. P2, might cause the molecule to end up in another local minimum LM3.

face, a process also known as thermalization and the new constraints imposed by the geometry and composition of the surface will force the molecule to adapt its configuration. This process is rather complex, because larger molecules cover a certain surface area and constitute of individual chemical building blocks, which generally interact in a characteristic manner. Due to the inherent degrees of freedom, the molecule will explore the most suitable adsorption configuration. This adaptation process can be described as the search for the absolute minimum on a multi-dimensional potential energy surface that has various local minima (see Fig. 1.1). Even though, the strength of the different interactions will determine the way to the final adsorption configuration, it is clear that the molecule might not end up in the most stable adsorption mode. The starting point, i.e. the initial configuration of the molecule and the location on the surface, might influence the final configuration. This quest for the ideal adsorption configuration is temperature dependent. The more energy a molecule has the more potential barriers it might overcome, enabling it to find deeper minima and allowing for more stable configurations. In summary, the

Table 1.1.: Basic characteristics of the relevant forces for molecule-molecule and molecule-surface interaction as well as adsorption and diffusion. Based on values from reference [13].

Interaction	Strength [eV]	Distance* [pm]	Peculiarity
Covalent bonding	1-8	100-200	selective, directional
Metal-ligand (coordination)	0.5-2	150-250	selective directional
Hybridization	≈ 1	100-200	selective
Hydrogen bonding	0.05-1.7	150-350	selective, directional
Ion-ion	0.1-2.5	200-400	nonselective
Ion-dipole & dipole-dipole	0.05-0.5	200-300	nonselective
Dispersion (van der Waals)	0.01-0.1	300-500	nonselective

* Values represent typical equilibrium distances. The actual range can be much longer.

adsorption process is minimizing the energy of the total system and leads to an energy gain, the so-called adsorption energy E_{ad}. It is calculated by subtracting the sum of the energies representing the free molecule $E_{mol,free}$ and substrate E_{sub} from the final energy of the combined system $E_{mol@sub}$.

$$E_{ad} = E_{mol@sub} - (E_{mol,free} + E_{sub}) \tag{1.1}$$

For stable configurations at room temperature, meaning low desorption rates, $|E_{ad}|$ should be bigger than $1\,\mathrm{eV}$.[13] The substrate will also try to adapt to the molecule albeit it is less flexible. The displacements of the surface atoms are thus often relatively small. However, for some substrates it has been observed that adsorbates can change the position of surface atoms and might even induce or lift surface reconstructions.[41–44]

In order to make an educated guess of the expected adsorption configurations it is helpful to consider the diverse interaction types and their corresponding strength. Generally, all these interactions are either chemical, i.e. quantum mechanical origin, or electrostatic in nature. For practical and also historical reasons they are further subdivided. Covalent bonds and hybridization effects are considered as chemical interactions. Ion-dipole and dipole-dipole interactions as well as van der Waals forces have an electrostatic origin. Other type of interactions, such as hydrogen bonds and charge transfer phenomena exist as well but it is hard to assign them to one of the two classes. Nevertheless, the dominant type of interaction is often used to classify them as chemisorbed or physisorbed. As these two terms are somewhat ill-defined they will be avoided in this work. Many of these interactions, especially the strong ones, are surface site dependent and are commonly used for specific anchoring of molecules. These functional anchor groups often represent the molecular parts that bind the strongest and thus steer the molecular orientation and configuration on the surface. The following review of the interaction types is thus arranged in order of decreasing strength. An overview of the interaction types with their characteristic strengths and bond lengths is given in Tab. 1.1.

1.1.1. Covalent Bonds

Covalent bonds are the strongest interaction between single atoms. The binding is often termed as chemical. As implied by the word covalent these bonds develop if atomic orbitals of two atoms overlap and share their valence electrons in order to achieve a state of filled electron shell. The attraction of the atoms is caused by the exchange interaction which is a pure quantum mechanical effect and arises from the indistinguishability of the electrons in the bond. The state of filled valence electron shell is very stable and thus generally desired. Certain elements are able to share more than one electron resulting in multiple bonds. The strength of covalent bonds is in the range of 1–8 eV.

The atoms in molecules or surfaces are often already in the state of filled electron shells. Hence, the formation of new chemical bonds involves the breaking of existing bonds before new ones can be formed. The reactivity is thereby highly increased for atoms exhibiting electron lone pairs or atoms that take part in polarized bonds, i.e. bonds where the electrons are not shared equivalently between the two partners. Many functional groups as well as substrates fulfill this prerequisite. Substrates that meet this condition are often covalent crystals such as metal oxides. Their covalent bonds are highly polarized and undercoordinated surface oxygen atoms present their electron lone pairs. Other substrates like elemental semiconductors such as silicon or germanium are also highly reactive due to the polarization of the topmost atoms induced by surface reconstruction.[45] In addition some valence orbitals of the surface atoms might not be saturated (dangling bonds). As a result the surface is accessible by a wealth of chemical reactions known from organic chemistry, which facilitates the immobilization of molecules via the formation of covalent bonds.[45, 46]

Many anchor groups have been developed, depending on the specific composition and structure of the surface. A huge amount of work has been done on anchors for application relevant metal oxides like TiO_2. Common functional groups that have been employed are e.g. carboxylates, phosphonates or silanes.[47, 48] Other anchors, have been selected and successfully tested on silicon and gallium arsenide.[49, 50] For metals, especially gold, thiol groups have been the anchor of choice.[51] In this case it has been observed that the formation of the covalent bond, i.e. the dissociation of the S−H and formation of the S−Au bond, might need some time.[52] This seems to be characteristic for other substrates too. An anchor group that is made for covalent bonding does not have to bind covalently, because the formation of a chemical bond is often a thermally activated process. In some cases the bonding even needs another reactant. This approach is sometimes used on metals for the formation of M−C bonds.[53]

To further complicate the matter, certain anchoring groups can adopt various adsorption modes. This is exemplified in Fig. 1.2 for the commonly used carboxylic acid, which also plays an important role in the present work. Even though the binding strength varies between the modes, implying a preferable configuration for the anchor, the prevailing mode is influenced by the geometry of the rest of the molecule. Another consequence is that binding to the same surface site with different anchors might not result in the same configuration.
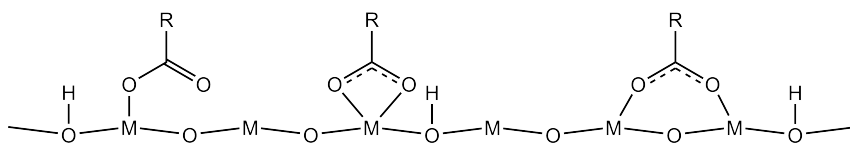
Figure 1.2.: Possible covalent binding modes of carboxylic acids on a metal oxide.[54] The carboxyl proton is transferred to a surface oxygen to enable the bond formation.

Especially under ultra-high vacuum conditions, covalent bonds are nearly irreversible, because the required reaction partner is missing. This fact gives them their outstanding importance for the immobilization of adsorbed molecules. The chemical binding is the only interaction where the binding energy of a single bond is already enough to bond an adsorbate on the surface at room temperature. Despite the usefulness of reactive substrates for molecule immobilization one also has to keep in mind that the chemical interaction might lead to unwanted chemical side reactions that cause modification or decomposition of the adsorbate. This is especially important for catalytic substrates like titanium dioxide.[45,46]

Apart from the classic covalent bonds, where each atom gives electrons, there also exist so-called dative or coordination bonds where the bond electrons originate only from one of the atoms. This interaction is of outstanding importance in the field of coordination chemistry. The electron donors are typically atoms with lone pairs such as oxygen or nitrogen, but can also be delocalized π-systems such as benzenes.[53,55,56] The acceptors are often Lewis acidic metal atoms such as gold. Apart from the importance for binding organic molecules on metals, coordination bonds might also occur on covalent crystals if the adsorbate is metallo-organic like e.g. phthalocyanines or porphyrins.

1.1.2. Ion-Ion Interaction

In order to achieve a filled valence electron shell, atoms form chemical bonds with other atoms and these bonds can be polarized because these electrons are not equally shared. In the extreme case, atoms even give off or take up electrons and get ionized. Atoms with a low electronegativity χ, i.e. atoms from the group I and II of the periodic system, become positively charged, whereas atoms with high χ, from the VI and VII group, get negatively charged. If such a bond is split the charge will remain on the atoms. An ionic bond with another ion can be readily made and does not need the splitting of bonds. The attraction in an ionic bond is mainly electrostatic and has strength of about 0.1–2.5 eV. Its typical length is about 200–400 pm. However, the real interaction distance is long-range and decreases as r^{-1}. In contrast to chemical bonds, the electrostatic interaction can be repulsive, i.e. in the case of similarly charged ions.

Ionic interactions are common in inorganic salts but are not limited to ionized atoms. Since molecules or functional groups, e.g. acidic groups, can get ionized as well, they play a role in organic chemistry too. By definition ionic bonds between molecules and substrate are only possible

if the substrate is an ionic crystal. Due to the technological relevance of insulators in molecular electronics these bonds are becoming more and more important. Since ionic substrates are inert and thus prevent the formation of covalent bonds, they often require that the ionic counterpart is formed before the adsorption, which is challenging under UHV conditions. Hence, so far, there exist only few publications that consider ionic anchoring groups.[57,58] Interestingly, it was found that carboxylate groups are suitable anchors for salts as well.[57,58] This finding is explained by the high acidity of the carboxylic proton, which enables the deprotonation at relatively low temperatures. Because most of the potential binding groups are acidic it is suitable to use salt substrates that are proton acceptors, like e.g. calcite.[57]

1.1.3. Hydrogen Bonds

Covalent bonds can be strongly polar resulting in partial charging of the atoms. Because the hydrogen atom has a low electronegativity χ it often carries a positive partial charge. Consequently, it likes to interact with electron lone pairs from molecules or the surface (see Fig. 1.3). The interaction is particularly strong for hydrogen atoms that are bound to oxygen or nitrogen atoms. This coupling is generally termed as hydrogen bond (H-bond). The H-bond is highly specific with respect to the interaction site and shows a strong directionality due to the orientation of the participating electron lone pair. H-bonds have typical interaction strength of about 0.05–1.70 eV. Strong interactions are observed for binding partners with high χ. Most common bonds are H$\cdots$O, H$\cdots$N and H$\cdots$F. Bonding of less polarized hydrogen atoms or with lone pairs of other elements, e.g. sulfur, are possible but generally weaker. Hence these interactions are less suitable for anchoring groups. Single functional groups, like hydroxyl or carboxyl groups, often act as acceptor and donor for lone pairs and can build more than one H-bond. The formation of H-bonds to surfaces is limited to substrates that offer the desired binding partners like metal oxides or nitrides (see Fig. 1.3b). Considering molecular anchoring, one has to bear in mind

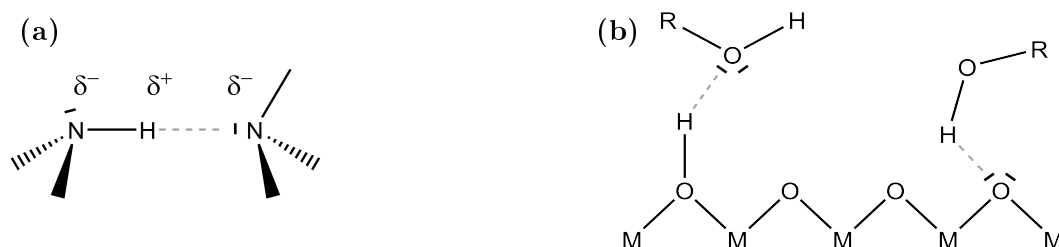**Figure 1.3.:** Hydrogen bonds and their binding modes. **(a)** Example of a hydrogen bond between a partially charged hydrogen and a negatively polarized nitrogen atom. The H-bond is indicated with a gray dashed line. **(b)** Examples of H-bonds between a hydroxy group and a metal oxide. Their surfaces are often covered with hydrogen adatoms and can thus accept and donate electron lone pairs.

that a single H-bond to the surface is, in most cases, not sufficient for immobilization at room temperature. Since H-bonds cannot be used for anchoring to metals or salts, they are useful to tune the intermolecular coupling on these substrates.[13]

1.1.4. Electrostatic Interactions Involving Dipoles

Like ionic bonds, interactions of polarized groups with other dipoles or ions are described by basic electrostatics. The coupling strength between an ion and a dipole is in the range of few hundred meV. The interaction can also become repulsive if the dipole is misaligned. The dipole-ion interaction is especially important for the anchoring of adsorbates on salts. Hence, molecules have been substituted with strongly polarized groups, comprising e.g. cyano groups or halides, in order to immobilize them on the surface.[44,59–64]

In contrast, pure dipole-dipole interactions are relatively weak and are therefore less important for the molecular geometry of single adsorbates. Nevertheless, they can have a great impact on the formation of self-assemblies. Besides their use as anchors, which is based on site specific interactions, dipoles are known to influence the electronic structure of the surface by shifting the work function (see Fig. 1.4).[65–68] In this case the overall dipole of the molecule is relevant. For a covered surfaces the shift of the work function $\Delta\Phi_s$ can be calculated as

$$\Delta\Phi_s = q\frac{\sigma P_{\mathrm{mol},\perp}}{\varepsilon_0\varepsilon_r},$$

where σ is the surface density of molecules, $P_{\mathrm{mol},\perp}$ is their dipole moment perpendicular to the surface and $\varepsilon_0\varepsilon_r$ is the permittivity.[66,69,70] The $\Delta\Phi_s$ is especially important for applications like dye-sensitized solar cells, where it has direct influence on the maximum open circuit voltage.[27] Another not site specific effect is the formation of interface dipoles due to adsorbate induced mirror charges on metals, which results in attractive binding too.[71]
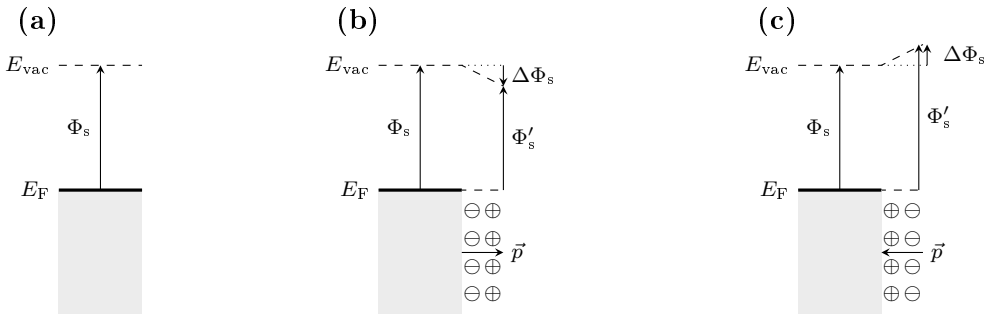

Figure 1.4.: Influence of surface dipoles on the work function. **(a)** Bare substrate and **(b,c)** after adsorption of molecules with a dipole moment pointing away and towards the surface, respectively. Φ_s and Φ_s' are the corresponding work functions and $\Delta\Phi_s$ is the potential change at the surface induced by the molecules.
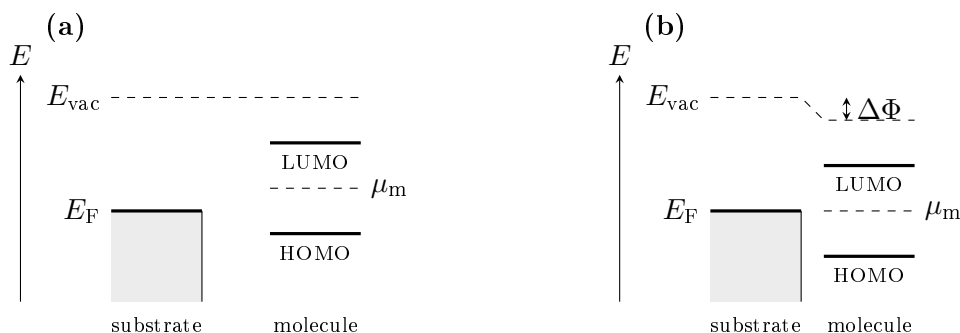
Figure 1.5.: Simplified picture of interfacial charge transfer for an electron donating molecule (weak interaction). **(a)** Before contact, the Fermi energy E_F of the substrate and the chemical potential μ_m of the molecule are different (i.e. $\mu_m > E_F$). **(b)** After contact, the energy levels are equal ($\mu_m = E_F$). The leveling is achieved by charge transfer from the molecule to the substrate. The resulting surface dipole causes a shift of the work function $\Delta\Phi$.

1.1.5. Charge Transfer and Hybridization

So far, classical interaction types that have direct influence on the atomic configuration of the molecule and the surface were discussed. The mutual interplay between the surface and the molecule does however affect the electronic structure as well. In order to get a first idea one often considers the band structure of the substrate as well as the highest occupied and lowest unoccupied molecular orbitals (HOMOs and LUMOs) of the adsorbate. These properties are well defined for isolated or free compounds and the corresponding Fermi level E_F and chemical potential μ_m, both representing the energies up to which electronic states are filled, can be assigned. As a first approximation, one can assume that the μ_m of an adsorbate is in the middle of the HOMO-LUMO gap. E_F and μ_m are normally not aligned. During contact formation these levels will equalize, whereby charge is transferred between the molecule and the surface (see Fig. 1.5). The molecular orbitals will be shifted in energy. The direction of the transfer depends on the position of μ_m with respect to the Fermi level. Thus if $\mu_m > E_F$ before contact, one expects electron transfer from the molecule to the surface and vice versa for $\mu_m < E_F$. One can therefore separate molecules into electron donors and acceptors. The charge transfer causes an interface dipole, which alters the work function (see Fig. 1.5b). This simple model allows one to make a first estimate of the amount and direction of the expected charge transfer. However, the description implies that the electronic structures of the molecule and the substrate remain unchanged and is thus only valid for weakly interacting systems like e.g. halogenated copper-phthalocyanines on gold[72] or graphite[73] or copper-octaethylporphyrin on noble metals.[74]

For many systems the molecular orbitals are altered when the molecule is brought to the surface. Under these circumstances one can no longer talk of a weak interaction and the made approximation fails to determine the direction of the charge transfer. A more rigorous description that

includes the direct interaction of molecular orbitals with the substrate is needed. Especially from studies on metals, it is known that molecular orbitals may hybridize with surface states.[23,55,75–79] In this interaction empty states on one side are mixed with filled states on the other side to form a so-called interface state. Evidently, the hybridization is therefore also associated with an interfacial charge transfer. The energy of this new state is below the energy levels of the unmixed states.

The hybridization is especially important for metals because they have delocalized electrons and often a Fermi level close to the molecular orbitals. Coupling of LUMOs with electronic states from metals has thus been reported several times.[23,25,77,78] As a simple rule of thumb one can expect that conjugated molecules exhibit stronger hybridization than saturated molecules.[49] Furthermore, unfilled or virtual molecular orbitals show a stronger tendency for hybridization than filled ones, because they are more diffuse and protrude farther from the adsorbate.[80] Since the hybridization depends also on the overlap of the orbitals it is distance dependent. For example anthradithiophene on Cu (111) could be switched by STM from a hybridized state to a hardly interacting state, which was accompanied by change of adsorption height.[25] Molecules were further reported to be decoupled if a thin insulating layer was in between the substrate and the adsorbate.[76] Despite all these examples, hybridization is not limited to metals. The only prerequisite is the presence of suitable states on both sides of the interface. Interesting examples are catechol on anatase TiO_2 or aromatic adsorbates on silicon.[49,81] In the latter, hybridization involves the HOMO of the adsorbate.

In summary, there are two main charge transfer phenomena. One includes hybridization of molecular orbitals and the other does not. Because the hybrid states are at the interface they are likely to influence charge transfer processes across it.[81] For large molecules both channels might be present as for example suggested for metallo-phthalocyanines on Au (111).[79] The total charge transfer is then balanced between the two channels. The hybridization also has a strong influence on the electronic properties of the adsorbate and the interface, most importantly on the optical absorption due to the alteration of the HOMO-LUMO gap. It has to be highlighted that hybridization needs empty orbitals in either molecule or substrate. The interaction of filled orbitals would lead to repulsion. For instance, on metals it has been observed that non-reactive adsorbates, such as noble gases, are able to push back the electron gas into the substrate due to Pauli repulsion.[55,82] This effect also causes an interfacial dipole but should not be confused with the surface dipole originating from interfacial charge transfer.

1.1.6. Van der Waals Forces

The only interactions present for all molecule substrate systems are London-dispersion interactions, often called van der Waals (vdW) forces. They are hardly specific and are caused by fluctuations in the electron density of atoms which represent spontaneous dipoles. These temporary dipoles induce other dipoles in nearby atoms, resulting in an attractive dipole-dipole interaction.

Typical interaction energies are 0.01–0.1 eV. Their strength is influenced by the polarizability of the atoms and the individual electron densities. If one considers different types of substrates, i.e. metals, insulators and semiconductors it is found that they are strongest on metals but only weak on insulators.[59] For insulators it is expected that the strength of van der Waals forces decreases with increasing band gap, because of decreasing polarizability.

For strongly interacting systems vdW forces are not that relevant for the molecular binding configuration. Nevertheless, they can contribute significantly to the total adsorption energy. Especially for large molecules, vdW forces are already strong enough to prevent re-evaporation. However, the potential energy surface is rather flat if only vdW forces are present, which results in low diffusion barriers and thus migration of the molecules at sufficiently high temperatures.[83] Under these conditions, it is observed that molecules are only immobilized at steps or in pits.[83–86]

1.2. Surface Diffusion

This section investigates the behavior of weakly bound molecules. They are suggested to have adsorption energies lower than 1–1.5 eV. These values constitute barriers that can be overcome at room temperature.[13,59] However, the stability of a molecule on the surface is usually not determined by the energy barrier for desorption as described by E_{ad}. The diffusion barrier, which is the barrier that an adsorbate has to overcome in order to move to the next adsorption site, is more important. For immobilized molecules this barrier has to be higher than 1–1.5 eV as well. It is important to keep in mind that the barrier height is significantly influenced by the type of molecule-surface interaction. For example molecules adsorbed only by van der Waals interactions typically show lower diffusion barriers than covalently anchored adsorbates.

Typically, one defines weak binding by a diffusion barrier lower than 1 eV. It is crucial to note that the molecules themselves do not possess enough energy to diffuse around. They still have preferred states and adsorption sites, which can be represented as local minima on a potential energy surface. But the molecules may have enough energy to wiggle around or maybe even to rotate at their adsorption site.[87] The hopping between neighboring adsorption sites is however driven by the surface, which provides thermal energy through vibrations of surface atoms, thereby acting as a heat bath. For simple cases, the jump rate Γ can be written in Arrhenius form

$$\Gamma = \Gamma_0 \exp\left(\frac{-E_A}{k_B T}\right),$$

where E_A is the activation energy for the transition.[13,88] In summary, weakly bound molecules are normally in a local potential minimum until they eventually get enough energy from the substrate to be excited to a state where they can actually overcome the diffusion barrier.

For flat and elementary surfaces, as e.g. most metals, the hopping is often isotropic. The hoping rate to the next neighbor sites does not depend on the direction. An example of a potential energy surface for this case is depicted in Fig. 1.6a. For covalent crystals the surface is often
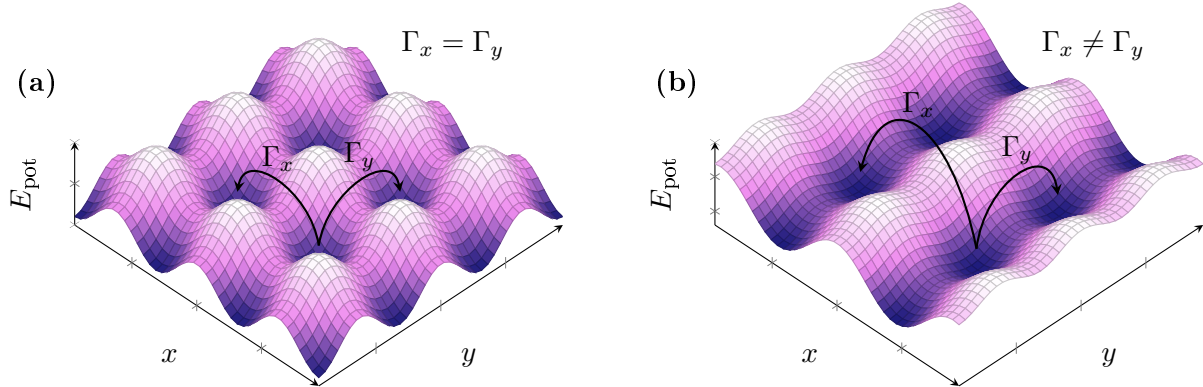
Figure 1.6.: Sketches of potential energy surfaces for surface diffusion of a small adsorbate. **(a)** Isotropic diffusion for the example of a (100) surface of a body centered cubic metal and **(b)** anisotropic diffusion as observed for the case of rutile TiO_2 (110).

more complicated due to reconstructions or surface structure. Hopping to next neighbor sites thus becomes anisotropic. In such a case the potential energy surface could look like depicted in Fig. 1.6b. Anisotropic diffusion behavior has e.g. been observed for rutile TiO_2 (110), where the surface forms a row pattern of alternating oxygen and titanium rows along which molecular diffusion takes place.[89,90]

Diffusing molecules will eventually meet defect states or step edges. Literally spoken defects are everything that does not belong to the perfect crystal structure of the substrate. Examples are small adsorbates, surface atom vacancies or even subsurface defects. For these defects the considerations about the different molecule-surface interactions made in Sec. 1.1 are still valid, the defect only offers additional interaction possibilities. Especially vacancies are often highly reactive and can promote anchoring. Interaction with subsurface sites could be imagined as a new type of interaction that might facilitate binding as well.[59] The fact that defects or adsorbates constitute additional binding possibilities has also been used on purpose e.g. by evaporation of metal adatoms on insulators where they permit the formation of coordination bonds.[91]

If the molecule does not find a defect it will eventually move to a step edge. For flat and homogeneous substrates, as e.g. metals, these steps are often described by the concept of the Ehrlich-Schwöbel barrier.[92,93] Within the theoretical description it is assumed that small adsorbates, like single atoms, have less binding partners at a descending step and are reflected back to the terrace. If however, they reach a rising step they have more binding possibilities and are thus more likely to stick. The potential energy of a step is shown in Fig. 1.7. For inhomogeneous surfaces or large adsorbates this is no longer true.[94] The step edge might present some undercoordinated and reactive atoms that increase the number of binding sites no matter from which side the adsorbate is approaching. Furthermore, for covalent crystals there are various step edges that expose different microfacets. Each of these facets shows a different chemistry and it is therefore
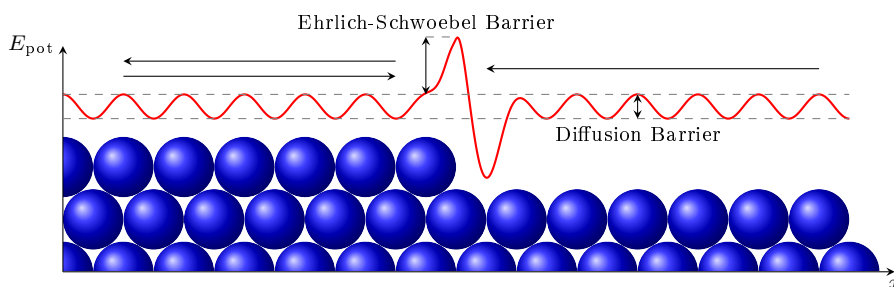
Figure 1.7.: Schematic illustration of the Ehrlich-Schwöbel barrier at a step edge. Adsorbates that approach a descending edge are typically reflected, whereas adsorbates that encounter an ascending step are likely to be trapped.

difficult to predict their influence on molecule diffusion and binding. New effects like diffusion along the step edges might emerge as well.[61] Because step edges are probably the last possibility of the molecule to get bound it is not astonishing that step edges or pits have also been created on purpose for the immobilization of molecules.[83–86]

1.3. Intermolecular Interactions

For higher coverage it is probable that diffusing molecules meet and interact. The arrangement of the molecules is then determined by the interplay between molecule-surface and intermolecular interactions. Some of the latter were already mentioned in Sec. 1.1. Important are H-bonds and electrostatic forces. However, thanks to the wealth of functional groups and molecular binding blocks, additional interactions become possible. They are relatively weak, but this does not lower their importance. One of them is similar to hydrogen bonds. Namely, it is found that halogen atoms themselves have regions with different polarization, which allow directed interaction with other polarized species. Halogen-halogen bonding, where an electrophilic cap on a halogen atom attracts a nucleophilic site of another halogen atom on an adjacent molecule, has also been reported and shown to be relevant for self-assemblies.[37] Another electrostatic interaction arises from the quadrupole moments of phenyl rings.[95] For benzene the ring is positively charged due to the delocalized π- electron systems above and below the molecular plane. This charge distribution causes attraction between adjacent phenyl groups and governs their relative orientation. Preferential arrangements are sandwich, T-shape and parallel displaced configurations.[96] For halogenated phenyl groups the charging is inverted. Thus the molecular organization can be tuned by changing the quadrupole moment of the building block with suitable substituents.[95] These examples are only two representative for the complexity of the molecule-molecule interaction.

When molecules bind to each other, this is coupled to an increase in the diffusion barrier, because they would like to diffuse together. Hence the cooperative effect of molecule-surface and intermolecular interaction can cause immobilization and has been used to assemble well defined
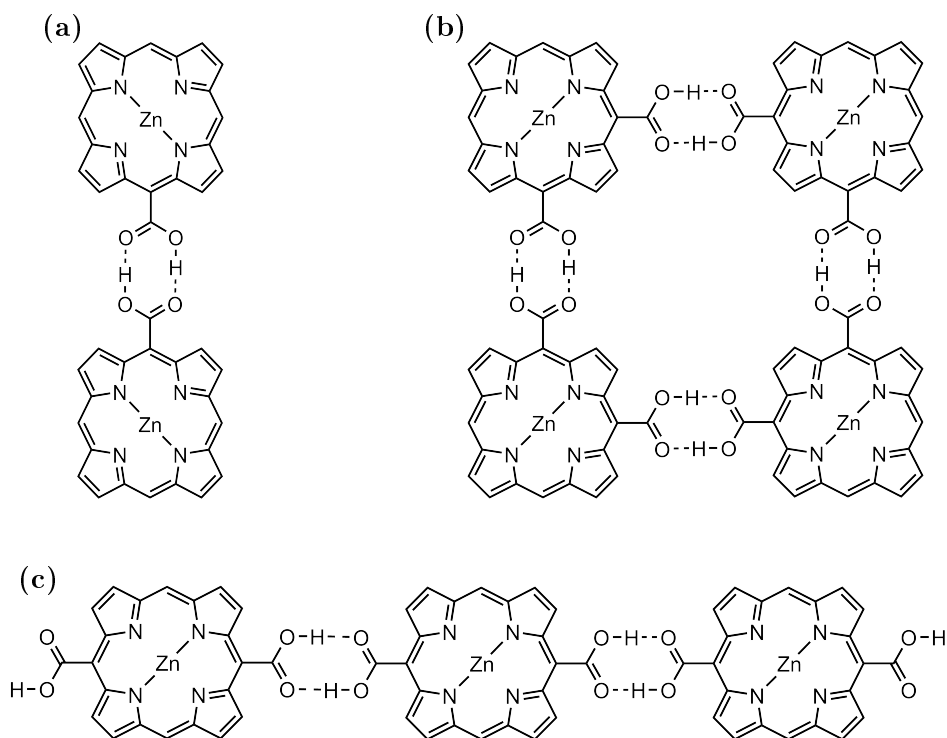
Figure 1.8.: Examples of porphyrin self-assemblies whose structure is governed by the interaction and position of carboxyl groups. **(a)** Dimer formed by porphyrins with one functional group, **(b)** tetramer of porphyrins with two COOH in cis-configuration and **(c)** molecular chain consisting of porphyrins with two COOH in trans-position.

oligomers.[13] Depending on the arrangement of the functional groups these oligomers have been used as starting point for the growth of molecular wires or complex 2D structures (Fig. 1.8). In some case these oligomers might diffuse around as well before they become too big or get trapped. The growth of larger assemblies therefore often starts at a defect or at step edges. If the molecule-surface binding is significantly weaker than the intermolecular attraction one observes the so-called dewetting of the surface meaning that the molecules start to interact in 3D and form multilayered islands or clusters. Small clusters might even diffuse or can be displaced via manipulation with a SPM tip.[97]

1.4. Summary

This chapter reviewed the basic interactions between molecules and surfaces. Besides the well-known interactions from chemistry other effects, such as formation of interface states due to hybridization, as well as charge transfer were considered. The sum of all present molecule-surface interactions determines how the molecule will adapt and bind to the surface. Therefore, careful

analysis of the molecule and surface structure allows making an educated guess for the adsorption mode and energy (see Tab. 1.1). Chemical bonds are strong and of crucial importance since they allow stable immobilization of the molecule, which is often required for the applications of these interfaces. Even though the chemistry of covalent linking seems to be well-known, one should keep in mind that these anchors might be able to interact in different ways (prime example COOH) and that chemical bonds often need activation energy. Furthermore, one has to consider that the molecules are generally confined to the surface, even before formation of the bonds. Hence, additional structural limitations may apply that prevent chemical reaction with the surface. Chemical anchoring is suitable for covalent crystals and metals but hardly achievable on insulators. On salts it is generally hard to anchor molecules to the surface. Other interactions like hydrogen bonds or electrostatic interactions might work on these substrates. Because they are often not strong enough to immobilize a molecule by themselves one should consider using more than one anchoring group. This increases the binding strength and allows one to steer the orientation of the molecule on the surface.[59] The generally weak interaction with the salt surfaces is however also a benefit. Coupling of molecular orbitals to surface states is not present and the electronic properties of the free molecule are mainly preserved. This is often not the case for metals or semiconductors. For tightly bound adsorbates the intermolecular interactions can be neglected for low coverage ($\ll$ 1 monolayer). With decreasing adsorption energy the molecules start to diffuse and the balance between molecule-surface and intermolecular interaction determines the adsorption behavior. For example, the contribution of the substrate might induce anisotropic diffusion, which might play a role for a single molecule but no longer for a dimer because it is immobilized. For weak molecule-surface coupling, the wealth of intermolecular interactions enables the assembly of well-defined nanostructures. For very faint interaction with the substrate the molecules tend to aggregate and form clusters.

2.

Theory of Experimental Techniques

This chapter describes the experimental methods from a theoretical perspective. After a short introduction to scanning probe methods in general, scanning tunneling microscopy (STM) and its application to molecule covered surfaces will be described. The main experimental work presented in this thesis was done with non-contact atomic force microscopy (nc-AFM), which will be presented in the following. The different measurement modes and their limitations will be explained with emphasis on high resolution imaging at room temperature and in ultra-high vacuum. Further Kelvin probe force microscopy (KPFM), which is an expansion of nc-AFM and was used for probing the work function of adsorbate covered samples, is introduced. Complementary to scanning probe techniques, there was the opportunity to use the photoelectron spectroscopy (PES) setup at the PEARL beamline of the Swiss Light Source at the Paul Scherrer Institute. The theory of PES will thus be reviewed briefly at the end of this chapter.

2.1. Scanning Probe Microscopy

Ever since, humans believe in the things they can see. Imaging techniques, especially microscopy, have thus been of paramount importance in science. For long, the resolution in microscopy was limited by the wavelength λ of the probing light. This optical limitation is called Abbe limit and states that two points can only be resolved if they are separated by a distance $d \geq \lambda/2$. Meaning the resolution is maximum a few hundred nanometers for visual light. With the development of scanning electron microscopy, this boundary was further pushed by using short wavelength electrons. But even with this technique atomic structures can hardly be resolved. This limitation was overcome by the concept of scanning probe microscopy. In 1982 Binnig and Rohrer invented the scanning tunneling microscope.[2,98] Few years later, in 1986, the atomic force microscope was developed by Binnig, Quate and Gerber.[3] In both methods the surface topography is sensed using sharp tips that are scanned over the surface. In STM the tip and sample build a tunnel junction and the tunneling current serves as a measure of the tip-sample distance. In AFM the force F_{ts} between tip and sample is used. For this the tip is mounted to a micro-fabricated cantilever spring. In both cases, the tips probe a distance dependent measurement signal. In

order to acquire the sample topography this signal is kept constant, which is done by adjusting the vertical position of either tip or sample using a feedback loop. The recorded positions represent the sample topography.

Besides topography measurements, scanning probe methods are used for investigation of electronic properties of the sample. One of these methods is KPFM and was invented in 1991.[99, 100] It is an extension of AFM, that allows measuring the work function of the sample. All three techniques, STM, AFM and KPFM, can reach atomic resolution.[101–105] They give complementary information and are ideally suited to study the adsorption behavior of individual molecules. All three methods were used in this thesis and are introduced in more detail in the following sections. Emphasis will be made on the presentation of the nc-AFM working mode, since it was the main technique used in this work.

2.2. Scanning Tunneling Microscopy

A scanning tunneling microscope uses the tunneling current between tip and sample as measurement signal. This current is due to the quantum mechanical tunnel effect, which arises from the wave nature of electrons. Due to the extension of the electron wave-function they are delocalized and the probability of the electron to be found in a classical forbidden area is no longer zero. For example the electron wave at a metal surface is reaching into the vacuum. Hence the conduction

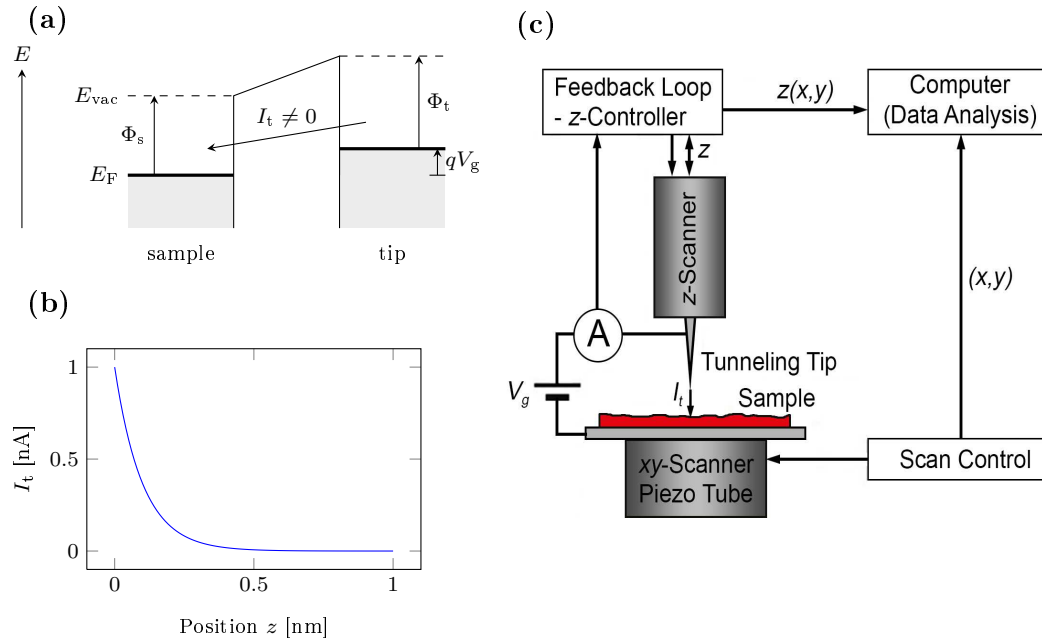**Figure 2.1.:** Operation of the STM. **(a)** Energy diagram of the tunneling contact between tip and sample under positive sample bias. **(b)** Example of tunneling current as function of the tip-sample distance. **(c)** Schematics of a STM setup.
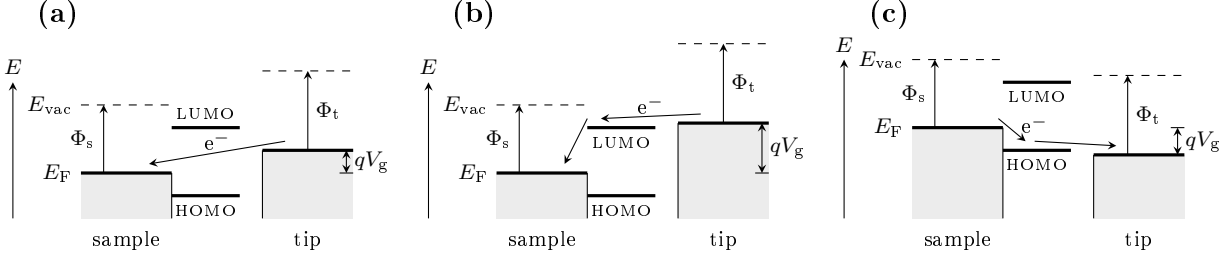
Figure 2.2.: Illustration of bias dependent tunneling paths for STM on an adsorbate covered metal surface. **(a)** Energy diagram for direct tunneling from tip to substrate states. **(b,c)** Indirect tunneling through the LUMO or the HOMO of the adsorbate.

through a small vacuum gap between two conductors gets possible. There will be a net current if a bias V_g is applied in between (see Fig. 2.1), which has the following approximate form[2]

$$I(z) = I_0(V_g) \exp\left\{-\frac{4\pi}{h}\sqrt{2m\Phi^*}z\right\}, \tag{2.1}$$

where $I_0(V_g)$ is the bias dependent current in the limit of contact, m is the electron mass and $\Phi^* = (\Phi_s + \Phi_t)/2$ is the average work function of the two conductors (see Fig. 2.1a). The tunneling current is strongly distance dependent as depicted in Fig. 2.1b. Just to illustrate this, the tunneling current is expected to change over 3 orders of magnitude if the tip position is changed by some hundred picometers, which corresponds to typical heights of atomic steps.[2] Hence the tunneling current is ideally suited as feedback signal to control the distance between the measuring tip and the sample. A schematic representation of the STM setup is shown in Fig. 2.1c. The steep monotonic behavior of $I_t(z)$ is the basis for stable scan conditions. High or even atomic resolution can be obtained readily because only the topmost atoms of the apex contribute significantly to the current.

As already implied by Eq. (2.1) the tunneling current depends on the sample material. Because the current arises from the overlap of the electron wave functions of the tip and the surface it reflects the local density of states of the sample. The states involved in tunneling change depending on the applied voltage V_g, rendering the image bias dependent. Consequently, the measured z-position corresponds to an electronic topography that gives information about the electronic structure of the surface. This fact is useful for the investigation of molecular orbitals that are close to the Fermi level. Carefully adjusting the gap voltage to the energies of the molecular orbitals allows one to map the HOMO and LUMO.[76] In this case the tunneling is mediated by the molecular orbitals as depicted in Fig. 2.2. If the gap voltage is in between these molecular orbitals, the molecule is hardly visible, because its orbitals are not involved in the tunneling process.

2.3. Atomic Force Microscopy

Besides the fact that STM measures an electronic topography, its operation is limited to conducting samples. A solution to overcome these problems is AFM.[106–108] The measurement signal does not need a conductive substrate because it is deduced from the forces that act between the tip and the sample. Before going to the experimental implementation of AFM, it is essential to understand these forces and their peculiarities such as their distance dependence. Thus a summary of all the relevant forces will be given first. Then the basic physical principles of the force detection using micro-fabricated cantilevers are discussed, which is followed by a description of different AFM modes as well as their limitations.

2.3.1. Tip-Sample Forces

The total force F_{ts} acting between the tip and the sample is the sum of different force components such as electrostatic, van der Waals and chemical forces. It has to be noted that this list is not exhaustive, but it covers all the forces relevant for the present work. Fig. 2.3 shows exemplary potential versus distance curves of the mentioned interactions. From there it is evident that these

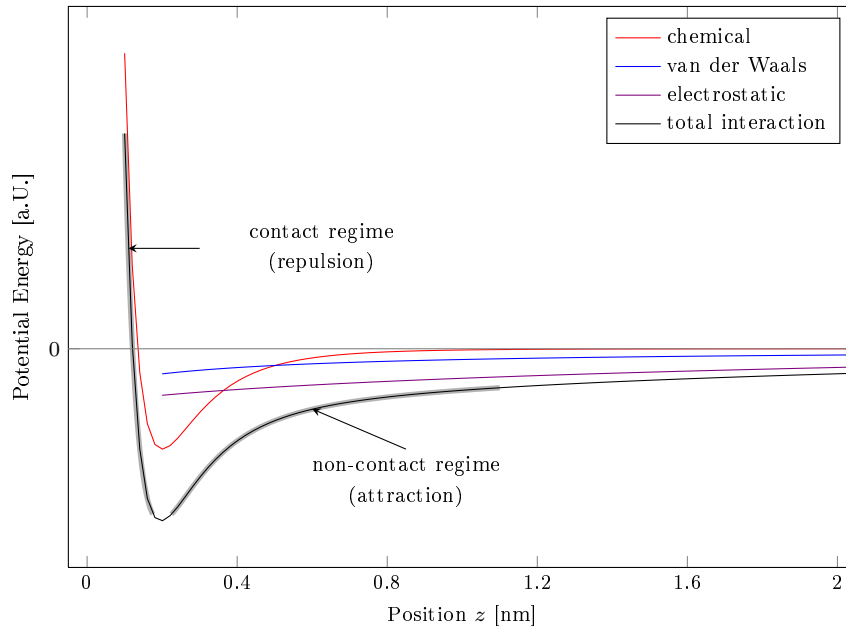**Figure 2.3.:** Composition of tip-sample interactions. The graphs show potential energy vs. distance curves for the most common forces present under UHV conditions. For close tip-sample distances one observes a negative slope. This is where the tip is repelled from the sample (also called contact regime). The slope of the potential energy gets positive for large distances. In this case, the tip is attracted to the surface.

forces differ in their distance dependence and strength. Some of the forces can be reduced during measurement, whereas others are given by tip-sample geometry and cannot be changed. The knowledge of these peculiarities is important because they directly affect the imaging process.

When focusing on single molecules adsorbed on surfaces, one has to get information at the atomic scale. Forces that give atomic contrast have a short-range nature. A prominent example is chemical forces. They are especially important for reactive surfaces and tips as for the case of silicon. They are called chemical because the top most atoms of the tip interact with the surface leading to the temporary formation of covalent bonds (see Sec. 1.1.1).[109,110] The potential energy of this interaction can be described by a Morse potential.

$$U_{\text{Morse}} = -E_{\text{bond}} \left(2\text{e}^{-\kappa(z-\sigma)} - 2\text{e}^{-2\kappa(z-\sigma)} \right) \tag{2.2}$$

Even though, the description reproduces the correct interaction strength and distance dependence, for proper choice of the equilibrium distance σ and the decay length κ, it does not include the orbital and thus directional dependence. Thus the Morse potential is strictly speaking only valid along the direction of the bond. Short-range electrostatic forces can also yield atomic contrast as observed on salt substrates, where the typical long-range behavior is screened by the alternating polarity of the ions on the surface.[111,112] Other short-range electrostatic forces e.g. arising from dipoles on the tip or due to the polarizability of atoms are also beneficial for high resolution.

Long-range forces are less desired for high resolution but contribute to a background interaction that enables stable measurement control. In UHV, long-range forces are composed of two distinct forces namely van der Waals and electrostatic ones (see also Fig. 2.3). Interestingly, macroscopic vdW forces originate from the short-range London dispersion interaction between single atoms. The interaction potential is often described by the empiric Lennard-Jones potential where the vdW forces are included with the short-range z^{-6} term. The z^{-12} describes the Pauli repulsion, which dominates in close contact.

$$U_{\text{LJ}} = -E_{\text{bond}} \left(2\frac{\sigma^6}{z^6} - \frac{\sigma^{12}}{z^{12}} \right) \tag{2.3}$$

Summing up vdW forces over macroscopic bodies results in a long-range behavior as shown by Hamaker.[113] For the interaction of a spherical tip with an infinite plane surface the potential is given by[114]

$$U_{\text{vdW}} = -\frac{A_{\text{H}}R}{6z}, \tag{2.4}$$

where A_{H} is the Hamaker constant, R is the radius of the tip apex and z is the distance between the plane and the center of the closest tip atom. From this formula it is evident that vdW forces are determined by the tip-sample geometry. Reduction of this force component can only be achieved by using sharp cantilever, i.e. small tip radius R.

Other long-range forces, which also origin from the macroscopic dimension of the tip-sample system, are electrostatic in origin. The force can be calculated by considering that the sample and tip form a capacitor.[115, 116]

$$F_{\mathrm{el}} = \frac{1}{2}\frac{\partial C}{\partial z}(V - V_{\mathrm{CPD}})^2$$

Here V_{CPD} is the contact potential difference (CPD). The electrostatic force depends on the square of the potential difference V between tip and sample. For the geometry of a spherical tip interacting with a plane surface the electrostatic force is given by[117]

$$F_{\mathrm{el}} = -\frac{\pi\varepsilon_0 R}{z(z + R)}(V - V_{\mathrm{CPD}})^2. \tag{2.5}$$

As is evident from this equation, the electrostatic long-range forces can be minimized by applying a suitable DC voltage. This will be explained in more detail in Sec. 2.4.

The different forces constitute the total interaction (see Fig. 2.3). It is interesting to note that these components can be extracted again from experimental force-distance curves as measured by AFM.[118] The force-distance curve is a function of the position on the sample, which is in essence due to the mentioned short-range forces. As will be explained later, this has severe implications for the evaluation of high resolution AFM topography images.

2.3.2. Cantilevers as Force Sensor

As known from classical mechanics forces can be measured using springs. For the measurement of normal forces the stiffness of the spring should be soft in the normal direction and rigid in the lateral ones. This requirement is fulfilled for micro-fabricated cantilevers.[119] Their spring constant is determined by the geometry of the lever. For a rectangular cantilever it is given by[120]

$$k = \frac{Ywt^3}{4L^3}, \tag{2.6}$$

where Y is the Young's modulus of the material, w the width of the beam, t its thickness and L the length (see Fig. 2.4a). In order to sense microscopic forces the cantilevers are equipped with sharp tips as shown in Figs. 2.4a,b. The tip-sample force can then be calculated from the deflection of the beam. The bending is e.g. measured with a laser that is deflected on the back of the cantilever as depicted in Fig. 2.4c. However, the force does not have to be known for the measurement itself. The information from the deflection signal is sufficient to control an AFM scan. In the simplest case, the static or so-called contact AFM, the deflection is directly used as the imaging signal. Even though, this mode is capable of giving atomic resolution, it is only applicable in limited cases.[119, 121, 122] Therefore, non-contact measurement schemes have been
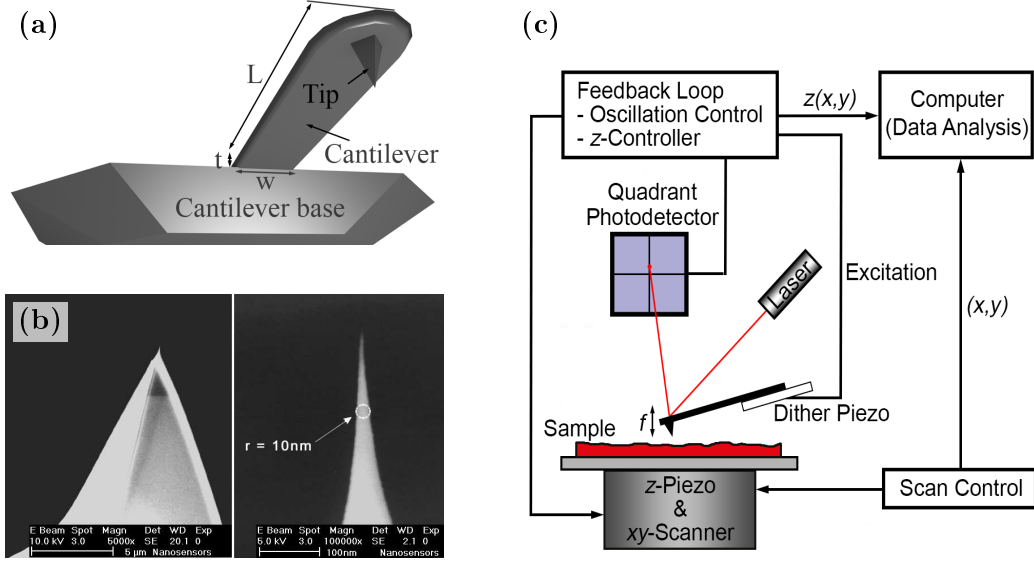
Figure 2.4.: Components of an AFM setup. **(a)** Schematic representation of the cantilever beam with integrated tip. **(b)** Scanning electron microscopy images of a microfabricated silicon tip (SuperSharpSilicon probe, Image modified with permission from Nanosensors). **(c)** Schematics of an AFM setup.

developed where the cantilever is oscillated at its fundamental resonance frequency f_1, which can also be expressed by the material parameters and dimensions of the cantilever.[120]

$$f_1 = 0.162 \frac{t}{L^2} \sqrt{\frac{Y}{\rho}}. \tag{2.7}$$

Here ρ is the density of the cantilever material. The AFM modes that use oscillating cantilevers are often called dynamic AFM modes. The application of oscillating cantilevers improves the sensitivity significantly.[123, 124] The control of the tip-sample distance is made by using the fact that the tip-sample forces F_{ts} alters the resonance frequency of the cantilever. In order to justify this measurement principle one considers the oscillation of a driven, damped oscillator as described by its differential equation

$$m\ddot{z} + \frac{m\omega_1}{Q_1}\dot{z} + k_1 z = F(t), \tag{2.8}$$

where $\omega_1 = 2\pi f_1$ is the angular resonance frequency, Q_1 is the Q-factor that describes the damping of the oscillation, $k_1 = m\omega_1^2$ is the spring constant and $F(t)$ the driving force. For a periodic excitation $F(t) = F_1 \cos(\omega_{\text{d}} t)$ with a driving frequency ω_{d}, the static solution of Eq. (2.8) is given by

$$z(t) = A_1 \cos(\omega_{\text{d}} t + \theta_1) \qquad A_1(\omega_{\text{d}}) = \frac{F_1}{m} \frac{1}{\sqrt{\left(\omega_1^2 - \omega_{\text{d}}^2\right)^2 + \left(\frac{\omega_1 \omega_{\text{d}}}{Q_1}\right)^2}}, \tag{2.9}$$
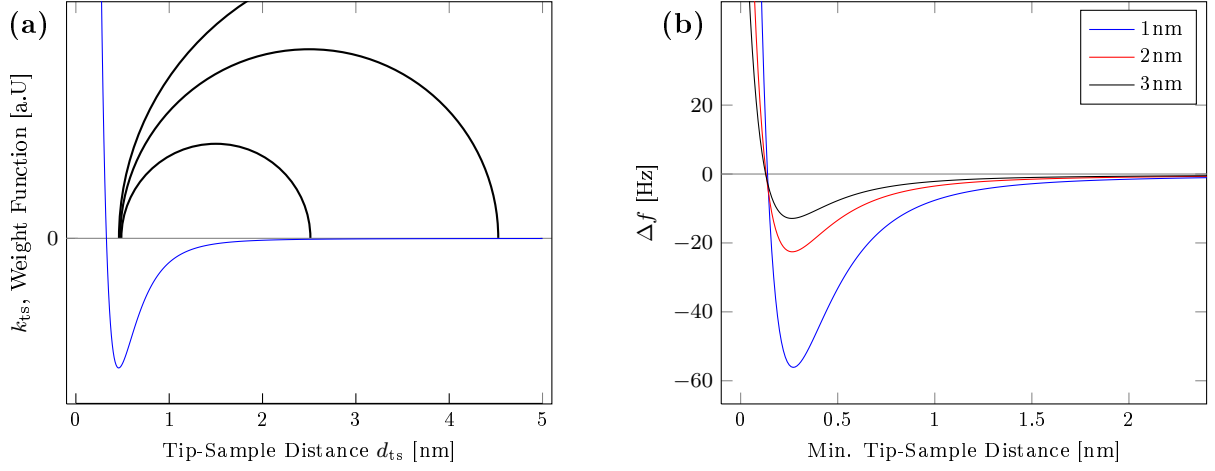
Figure 2.5.: Frequency shift of an oscillating cantilever. **(a)** Interpretation of the frequency shift as the convolution of a semispherical weight function with the tip-sample force gradient k_{ts}.[119] The radius of the weight function corresponds to the cantilever oscillation amplitude. **(b)** Corresponding frequency shift curves for different cantilever oscillation amplitudes. The x-axis corresponds to the tip-sample distance at the lower turning point.

where A_1 is the amplitude of the oscillation. The phase lag θ_1 of the oscillation is given by

$$\theta_1(\omega_d) = \arctan\left(\frac{\omega_1 \omega_d}{Q_1(\omega_1^2 - \omega_d^2)}\right). \tag{2.10}$$

The resonance frequency is determined by the cantilever properties and given by $f_1 = \frac{\omega_1}{2\pi} = \frac{1}{2\pi}\sqrt{k_1/m}$. The amplitude of the oscillation is maximum if the cantilever is oscillated at its resonance frequency. Since the excitation is compensating the damping of the cantilever one can calculate the phase lag to be $\theta_1 = -\pi/2$. The differential equation is then simplified to $m\ddot{z} + k_1 z = 0$. If the tip is approached to the surface it senses an additional force. For didactic reasons one often considers the case of small amplitudes that allow making a linear approximation of this force $F_{ts} = \alpha z$. The differential equation is then modified to

$$m\ddot{z} + k_1 z = \alpha z \tag{2.11}$$

and the static solution can be expressed with an effective spring constant $k_{eff} = k_1 - \frac{dF_{ts}}{dz} = k_1 + k_{ts}$. The resonance frequency is changed accordingly. For small force gradients it is given by

$$f_1' \cong \frac{1}{2\pi}\sqrt{\frac{k_1}{m}}\left(1 - \frac{1}{2k_1}\frac{dF_{ts}}{dz}\right) = f_1 + \Delta f_1. \tag{2.12}$$

The force gradient is positive in the attractive region and thus the Δf_1 becomes negative. In summary, the tip-sample interaction slows down the cantilever oscillation. This is also the case
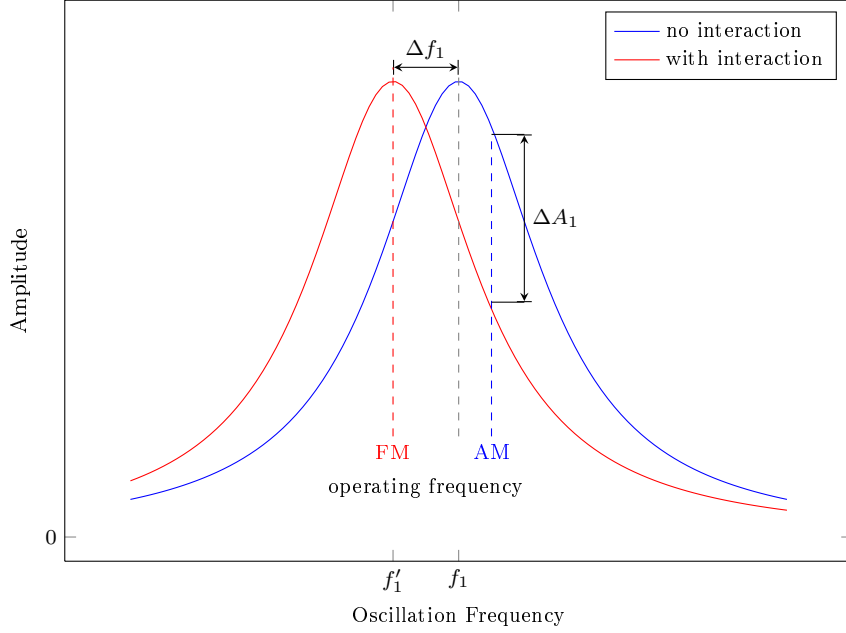
Figure 2.6.: Spectra of the oscillation amplitude for the case without and with tip-sample interaction. The shift of the spectrum is used to control the tip-sample distance by either tracking the changes in amplitude $A(z)$ (AM-mode) at a constant excitation frequency or by monitoring the shift of the cantilever resonance frequency $\Delta f(z)$ (FM-mode).

for larger amplitudes, where the effective spring constant is distance dependent. In this case the frequency shift can be calculated using canonical perturbation theory.[125]

$$\Delta f_1 = -\frac{f_1^2}{kA_1^2} \int\limits_0^{1/f_1} F_{\text{ts}}(d + A_1 + A_1\cos(2\pi f_1 t))A_1\cos(2\pi f_1 t)dt = -\frac{f_1}{kA^2}\langle F_{\text{ts}}A_1\cos(2\pi f_1 t)\rangle \quad (2.13)$$

As shown by Giessibl, this can be interpreted as a convolution of the tip-sample force gradient k_{ts} with a semi-circle weight function (see Fig. 2.5).[126]

There are two common possibilities how this resonance shift can be used for AFM measurements. The first one is the so-called amplitude modulation (AM) mode, where the cantilever is oscillated at its free resonance frequency with constant excitation.[123] The amplitude decreases if the tip is approached to the sample, because the resonance shifts to lower frequencies as illustrated in Fig. 2.6. The amplitude $A_\omega(z)$ of the cantilever thus represents the distance dependence of the tip-sample interaction, which is used to feed the z-control loop. To ensure that the $A_\omega(z)$ is a monotonic signal the cantilever is generally excited slightly above its resonance. In the AM mode one measures thus at a constant amplitude. In the frequency modulation (FM) mode the frequency shift itself is used as the feedback signal. For this the excitation frequency is continuously adjusted to the actual cantilever resonance. This is typically implemented using a phase-looked loop (PLL) that tracks the resonance frequency by adjusting the excitation frequency so that the phase lag

is $\theta_1 = -\pi/2$. Topography measurements are then done at a certain frequency shift setpoint. Comparing the two measurement modes one sees from Eq. (2.9) that the AM mode measures topography where the force is constant. For the FM mode the surface with a constant force gradient is measured as is indicated by Eq. (2.12). Because the adaption of the amplitude in the AM mode occurs with a delay time $\tau_{AM} \cong 2Q_1/f_1$, it is not suited for measurements in UHV, where the Q-factors typically reach several $10\,\mathrm{k}$.[124] The delay time of the frequency adaption in the FM mode is $\tau_{FM} \cong 1/f_1$ and thus much faster, making it the ideal choice for measurements in UHV.[124] Thanks to this benefit, FM-AFM has been used throughout this work and will now be discussed in more detail.

Compared to STM and AM-AFM, FM-AFM has a few drawbacks that complicate the control of the measurement.[119] The Δf is a non-monotonic function of the tip-sample distance (see Fig. 2.5b). This limits the minimum tip-sample distance and with it the maximum achievable resolution. Further it can cause scanning artifacts if the tip accidentally gets too close. In order to obtain high resolution one has to probe short-range interactions that origin from the individual atoms itself. They become more important for small amplitudes and tip-sample distances because the weight of the short-range forces is increased then (see also Fig. 2.5). Unfortunately, less energy is stored in the cantilever oscillation in this case, making it prone to crash into the surface. Therefore, the amplitude should fulfill the criterion $kA > F_{ts}^{max}$.[119]

2.3.3. Sample Topography and Tip Effects

The FM-AFM topography represents surfaces of constant Δf. It has to be stressed that this surface will only correspond to the sample topography if the $\Delta f(z)$ curve does not depend on the sample position, which is a case that might only be given for low resolution or large scale scans on homogeneous surfaces. In these cases it is sufficient to scan the tip quite far from the surface where it senses mainly long-range forces. Only electrostatic forces might give rise to a position dependent F_{ts} then. Since they can be compensated, as will be explained latter, the real sample topography can be measured.[127] For high-resolution measurements the tip has to be scanned closer to the surface in order to sense the short-range forces. Under these conditions the $\Delta f(z)$-curve is position dependent and the measured topography does not agree with the expected topography. To elucidate this issue it is helpful to define the atomic topography of FM-AFM using the minimum of the frequency shift curve. The value Δf_{min} of the minimum depends on the tip-sample interactions and on the position on the sample. Because FM-AFM measurements are not made at the minimum frequency but at a certain setpoint $\Delta f_{set} > \Delta f_{min}$ it becomes evident that the experimental topography will not agree with our defined one. This is illustrated in the following three examples, which are depicted in Fig. 2.7. In the first one, the two sample sites have the same height but differ in interaction strength as possibly expected for an ionic crystal with positive and negative ions (see Fig. 2.7a). The total interaction as well as the experimental topography is modulated, causing the overestimation of the height of the site
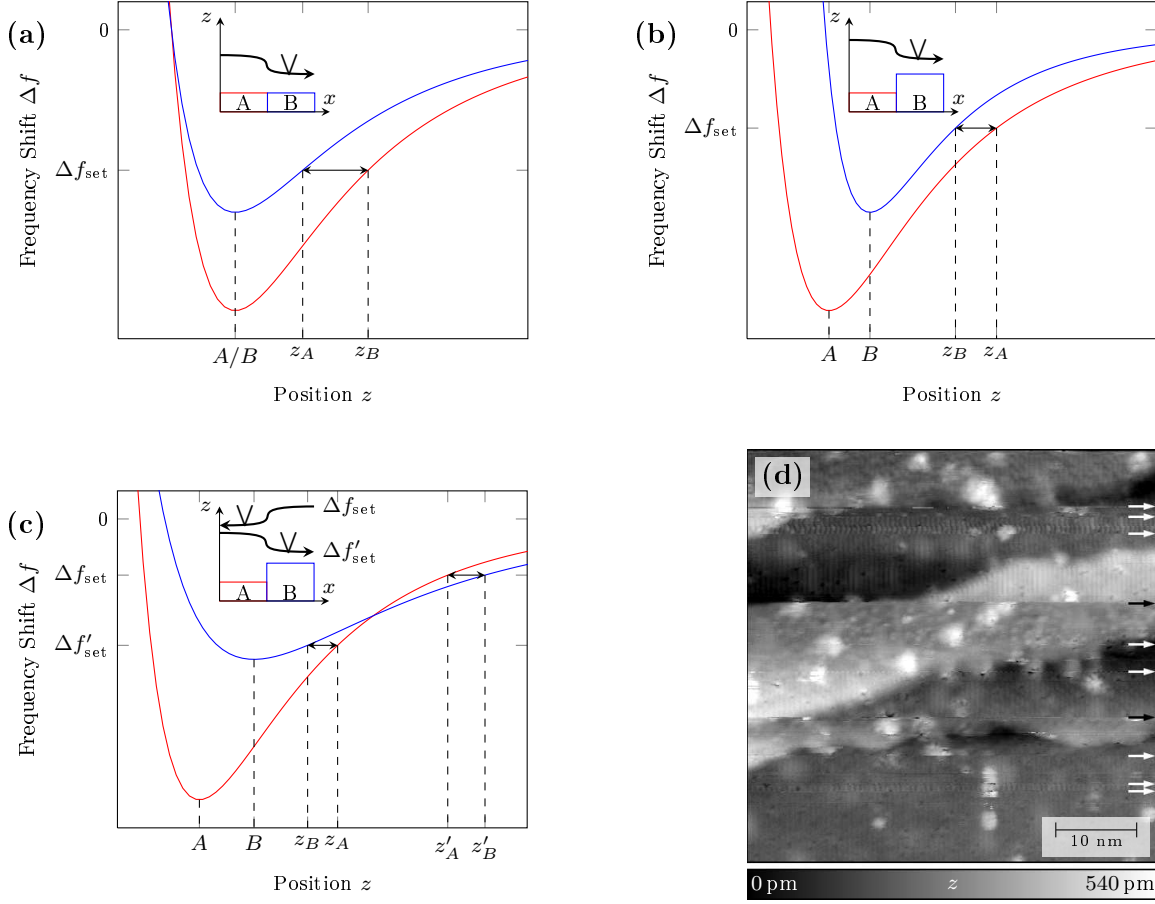
Figure 2.7.: Influence of site specific interactions and the corresponding Δf-curves on the experimental topography. The expected topography as defined in the text is given by the position of A and B and is also illustrated in the insets. The experimental topography is represented by z_A and z_B and visualized by tip traces in the inset. **(a)** Height overestimation of one species as well as **(b)** contrast inversion, both caused by varying interaction strength. **(c)** Case where the qualitative contrast depends on the tip-sample distance (frequency shift setpoint Δf_{set}). **(d)** Changing contrasts on a rutile TiO_2 (110) surface due to an unstable tip apex. Scan lines with tip changes are indicated with arrows.

with stronger interaction. For a sample with corrugation as shown in example two, one might observe an inverted topography (Fig. 2.7b). In the third example, the qualitative topography contrast even depends on the Δf_{set}, since the frequency shift curves of two sites are crossing in the attractive region (see Fig. 2.7c).[128]

These observations have strong implications for the interpretation of FM-AFM images. It is generally not possible to assign atomic species based on the expected topography alone. The experimental interaction potential depends strongly on the tip termination. However, its composition and exact atomic configuration are not known in room temperature measurements. Therefore,

interpretations need a model of the tip or at least its polarization.[129,130] Another intriguing fact is that the tip apex might be changed during the scan. Especially for reactive samples like TiO$_2$ different contrasts are sometimes observed in one single scan (see Fig. 2.7d). One one side this complicates high resolution imaging. But on the other side this wealth of information can be helpful to elucidate the topography maps. Besides this, the nature of known defects as well as spectroscopy measurements with different tip terminations can help in the determination of atomic species.[109,129,130]

2.3.4. Higher Resonances and Multimodal AFM

So far the focus was on the first resonance of the cantilever. It is a benefit of the cantilever geometry that further modes as well as their higher orders are available. Besides the normal modes there exist torsional or shear modes too (see Fig. 2.8). The second normal resonance of the cantilever is of crucial importance for this work because it can be used to increase the resolution and the scan stability.[131,132] Its resonance frequency is given by $f_2 \approx 6.28 \cdot f_1$ and the corresponding stiffness is $k_2 = k_1(f_2/f_1)^2 \approx 39.44 \cdot k_1$. This allows stable small amplitude operation, which enables sensing short-range forces at larger tip-sample distances, therefore avoiding the snap to contact problem.[133] The laser deflection is also magnified, due to the stronger bending of the cantilever in the second mode, thereby increasing the signal to noise ratio.

Thanks to the superposition principle multiple resonance modes can be excited at the same time offering the possibility to perform multimodal measurements.[131,132,134–136] This versatility offers an advanced approach to overcome some of the above mentioned problems of standard nc-AFM. Especially it enables measuring and separating different interaction forces simultaneously like F_{vdW} and F_{el} or long and short-range forces.[131,132,137,138] In multimodal scans a normal
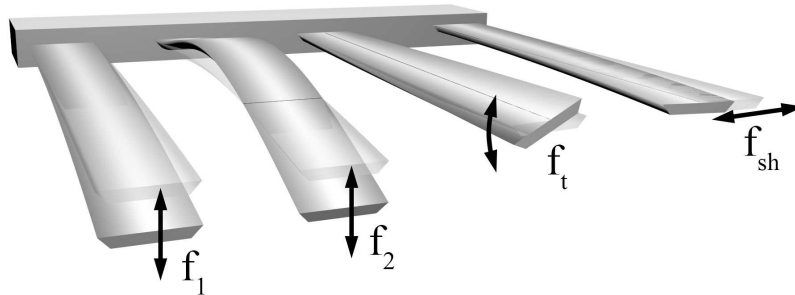

Figure 2.8.: Different types of cantilever modes that can be used in multimodal AFM. From left to right: 1st normal, 2nd normal, 1st torsional and 1st shear resonance.
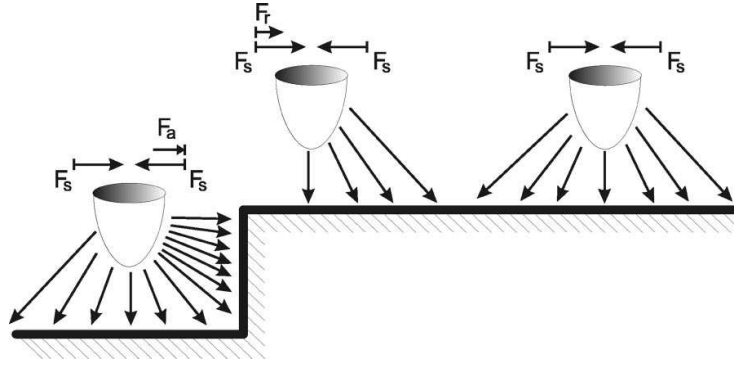
Figure 2.9.: Lateral forces at a step edge and their influence on the torsional resonance. Figure reproduced with permission from reference [135], APS.

resonance is used for the topography measurement, whereas the oscillations of other resonances are used for the evaluation of specific force components. Especially the use of the first torsional resonance has been of primary interest for the measurement of lateral forces, which play a huge role in the microscopic understanding of friction.[135, 139, 140] The measurement principle is the same as for the vertical modes. Attractive and repulsive forces give negative and positive frequency shifts, respectively.[135] For example, this can be observed on step edges as shown in Fig. 2.9. If the tip approaches from the lower terrace it senses an additional lateral force component that attracts the tip to the step and lowers the resonance frequency. After moving over the step the tip is pushed away from it, due to the step induced asymmetry of lateral forces on the upper terrace (see Fig. 2.9). The torsional resonance is further suitable for high resolution imaging since the amplitude is typically in the range of some tens of picometers making the oscillation highly sensitive to short-range forces.[140] This allows one to get atomic contrast on samples where this is hardly possible using standard FM-AFM.[132]

2.3.5. Multipass AFM

In the previous sections it was illustrated that the minimum tip-sample distance is limited by the nature of the non-monotonic $\Delta f(z)$ curve and that the FM-AFM topography does not correspond to the real topography for small tip-sample distances. The resolution of the topography map is therefore restricted. For the sake of higher resolution it would be worth to sacrifice the topographic information. A way to achieve this is to bring the tip closer to the surface but without feedback loop. The sample is then scanned at a constant height and the frequency shift is recorded as imaging signal. With this procedure the tip can reach into the repulsive region, which e.g. facilitates the imaging of the bonds inside a molecule thanks to Pauli repulsion.[34, 40] These measurements need high stability against thermal drift and are generally limited to small scan areas and low temperature setups. Furthermore, they have a fundamental drawback. Scans are limited to flat samples. Hence, in order to image a molecule one has to slightly retract the tip
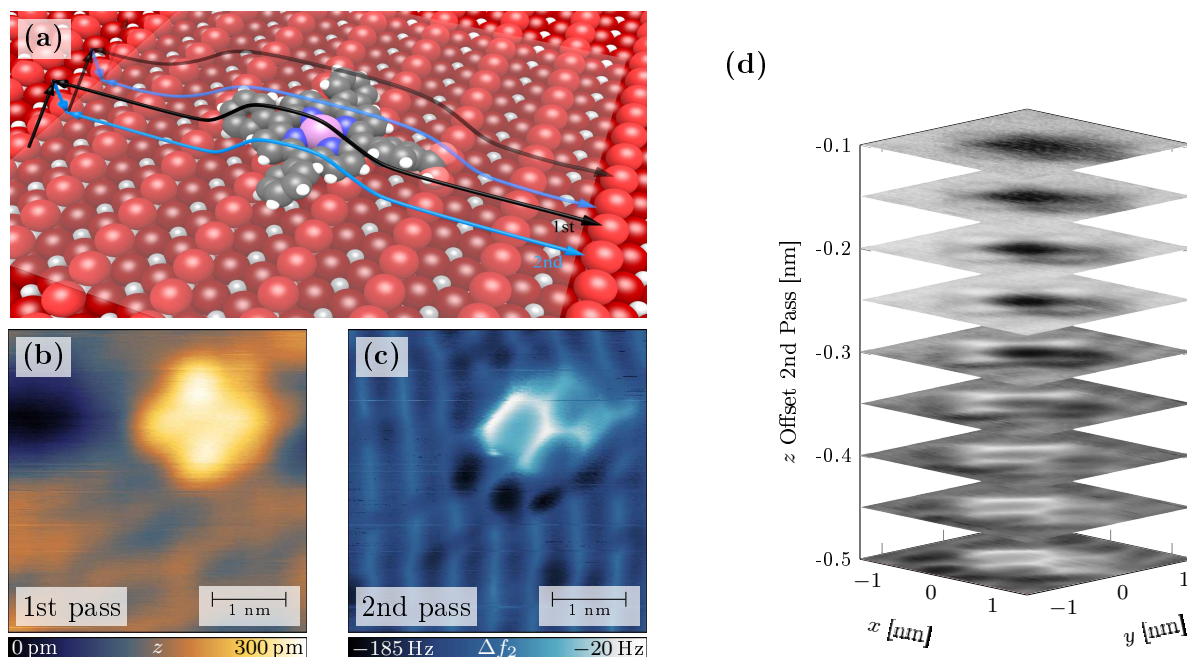
Figure 2.10.: Illustration of the multipass measurement method for ZnMCPP on rutile TiO$_2$ (110). **(a)** Schematic representation of the measurement. The topography of the 1st pass is recorded and replayed with an offset during the 2nd pass. **(b)** Topography image of the 1st pass obtained relatively far from the sample. **(c)** Frequency shift measured during the second pass. **(d)** Frequency shift images taken at various z-offsets.

from the substrate, which prevents the simultaneous study of the molecule and the substrate. To overcome these limitations, the group of Custance implemented a multipass measurement protocol, which combines the benefits from standard nc-AFM, i.e. the high tolerance against thermal drift and its 3D capability, with the high resolution from constant height scans (see Fig. 2.10a).[39] In the first pass a normal scan line with topography feedback is recorded (see Fig. 2.10b). This is typically done quite far from the surface, so that the positional dependence of the $\Delta f(z)$-curve is minimized. The topography is then replayed in the second pass and a z-offset of several hundred picometers is applied to bring the tip closer to the surface. During the second pass the frequency shift is measured as in constant height measurements (see Fig. 2.10c). This protocol is repeated for every scan line to obtain a full image. Hence, thermal drift can be minimized and high resolution detuning images of 3D objects such as large molecules or scans over step edges are possible. The protocol can further be expanded to investigate the distance dependence by applying different z-offsets in a row. This is illustrated in Fig. 2.10d. The method allows one to either choose the 1st or the 2nd resonance for the topography measurement. Multiple resonances might be used simultaneously as in the original publication by Moreno.[39]
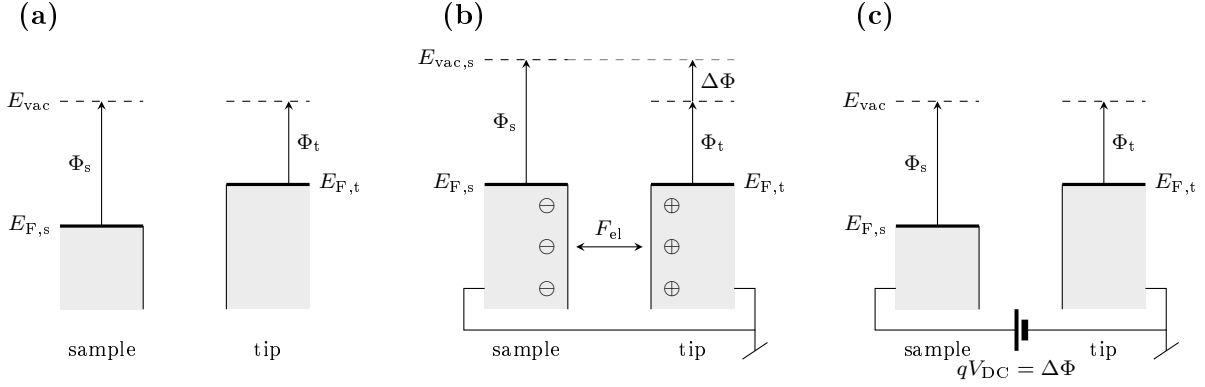
Figure 2.11.: Working principle of electrostatic force compensation in KPFM (illustrated for the example of a metallic tip and sample). **(a)** Energy diagrams of tip and sample without electrical contact. **(b)** Aligned Fermi levels of the wired system give rise to electrostatic forces. **(c)** Compensation of F_{el} by application of a voltage $qV_{DC} = \Delta\Phi$ to the sample.

2.4. Kelvin Probe Force Microscopy

Long-range electrostatic forces, which originate from the tip-sample geometry forming a capacitor, impede with high resolution imaging. As found by Lord Kelvin they arise because the work function of the tip and sample are not the same.[141] The difference is called the contact potential difference

$$V_{CPD} = \frac{1}{q}\left(\Phi_s - \Phi_t\right). \tag{2.14}$$

In other words, V_{CPD} depends directly on the work function of the sample Φ_s. The total capacitive force between tip and sample is now given by

$$F_{el} = \frac{1}{2}\frac{\partial C}{\partial z}(V_{DC} - V_{CPD})^2, \tag{2.15}$$

where V is an additional voltage that is applied to the sample. This implies that F_{el} can be compensated by applying a bias of $V = V_{CPD}$ to the sample, if the tip and sample are sufficiently conductive. The working principle is illustrated in Fig. 2.11. If the two parts of the capacitor are electrically separated their Fermi levels are not aligned due to the different work functions. If they are connected, the Fermi levels will equalize leading to charging on both sides (Fig. 2.11b). The two parts will now attract each other. Application of a voltage V_{DC} that corresponds to the difference of the work functions of both sides compensates the charge flow and thus the electrostatic force. The work function can even be determined on an absolute scale if the work function of the tip is known, which can be obtained by scanning a reference sample.

The easiest way to determine V_{CPD} is by means of a bias sweep, while oscillating the cantilever over the surface. The recorded frequency shift follows the parabolic dependence as is indicated by Eq. (2.15) and the position of the maximum corresponds to V_{CPD}. In AFM, this procedure is
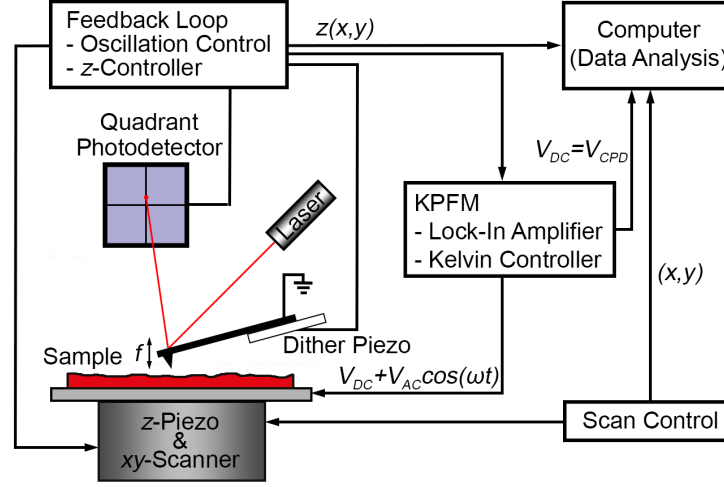
Figure 2.12.: Schematic representation of the KPFM setup. The standard nc-AFM setup is expanded with a lock-in amplifier that measures the amplitude of the electrostatically excited oscillation (AM-KPFM) or the modulated frequency shift (FM-KPFM). This signal is used by the Kelvin controller to adjust V_{DC} to V_{CPD}.

generally applied to measure the CPD at one point of the sample and this bias is then applied during the scan in order to reduce the electrostatic forces. A better way to minimize the electrostatic forces is to compensate them at every point of the scan. In KPFM this is implemented by using the fact that non-compensated electrical forces can be used to excite a cantilever motion by application of an AC voltage V_{AC} with angular frequency ω. The F_{el} then becomes

$$F_{\mathrm{el}} = \frac{1}{2}\frac{\partial C}{\partial z}\big[(V_{\mathrm{DC}} - V_{\mathrm{CPD}}) + V_{\mathrm{AC}}\cos(\omega t)\big]^{2}. \tag{2.16}$$

Expansion of the term in brackets gives the spectral composition of the resulting force.

$$F_{\mathrm{el}} = \frac{\partial C}{\partial z}\left(\frac{1}{2}(V_{\mathrm{DC}} - V_{\mathrm{CPD}})^{2} + \frac{V_{\mathrm{AC}}^{2}}{4}\right) \tag{2.17}$$

$$+ \frac{\partial C}{\partial z}\left(V_{\mathrm{DC}} - V_{\mathrm{CPD}}\right)V_{\mathrm{AC}}\cos(\omega t) \tag{2.18}$$

$$+ \frac{\partial C}{\partial z}\frac{V_{\mathrm{AC}}^{2}}{4}\cos(2\omega t) \tag{2.19}$$

The additional AC voltage V_{AC} excites oscillations at ω and 2ω. The amplitude at ω is proportional to $V_{\mathrm{DC}} - V_{\mathrm{CPD}}$. In AM-KPFM the amplitude of this signal is directly measured using a lock-in amplifier and nullified by a feedback loop that adjusts V_{DC} to match V_{CPD} (see Fig. 2.12).[99] The map of V_{DC} has the same contrast as the work function of the sample if the bias is applied to the sample. Even though, an oscillation can be forced at any frequency, the response of the cantilever and thus the sensitivity are increased if a resonance frequency is chosen.[115] Therefore,

one generally uses the second resonance for AM-KPFM.[137, 138, 142] Similarly to the AFM operations modes, a FM mode measurement can be applied as well, which uses the force gradient instead of the force for compensation.[104, 143, 144] In this case the additional AC bias is rather low (around $1\,\mathrm{kHz}$) causing the frequency shift of the first resonance to oscillate. In a standard FM-KPFM setup as shown in Fig. 2.12, the modulation of the oscillation signal is tracked with a PLL and then fed to a lock-in amplifier. A Kelvin controller uses the measured amplitude of this modulation as feedback signal for the compensation.

KPFM measures the work function of a surface and is thus also applicable for the investigation of surface dipole moments (see Sec. 1.1.4). Especially the lateral resolution of FM-KPFM, which lies in the sub-nanometer range allows the investigation of single isolated molecules. One often speaks of a local contact potential difference (LCPD) then. Even though the detailed analysis of LCPD maps requires model calculations, e.g. due to averaging effects,[105, 116] they already give valuable qualitative information. For example the measured LCPD indicates the direction of interface dipoles and can be used to deduce the orientation of adsorbed polar molecules or the direction of charge transfer across an adsorbate covered surface.

2.5. Photoelectron Spectroscopy

Despite the high spatial resolution of scanning probe techniques, they are not suited for identification of the chemical composition of the sample. The method of choice for this analysis is photoelectron spectroscopy (PES). The spectrum is obtained by irradiating the sample with X-rays while measuring the amount and kinetic energy of the photoelectrons that are emitted from the sample. Thanks to the uniqueness of the electron shell of an element they carry information about the sample composition. In this section the principle of PES will be explained and it will be shown how the binding configuration of atoms can be assessed.

2.5.1. X-ray Photoelectron Spectroscopy

X-ray photoelectron spectroscopy (XPS) is based on the photoelectric effect. The process is often described with 3 steps.[145, 146] First, the X-ray photon is absorbed by an atom, which leads to the excitation of a core level electron beyond the Fermi level. In the second step the electron moves to the surface, where it is ejected and travels to the detector, which is the third step. The excitation process is illustrated in Fig. 2.13a. The knocked-out electron has a kinetic energy E_{kin} that is determined by energy conservation and given by

$$E_{\mathrm{kin}} = h\nu - E_{\mathrm{b}}, \tag{2.20}$$

where E_{b} is the binding energy of a state, which is characteristic for a specific element. The knock-out of electrons by irradiation with X-rays causes charging of the sample. Electrons escaping from the sample are thus retarded by the developing electrostatic field between sample
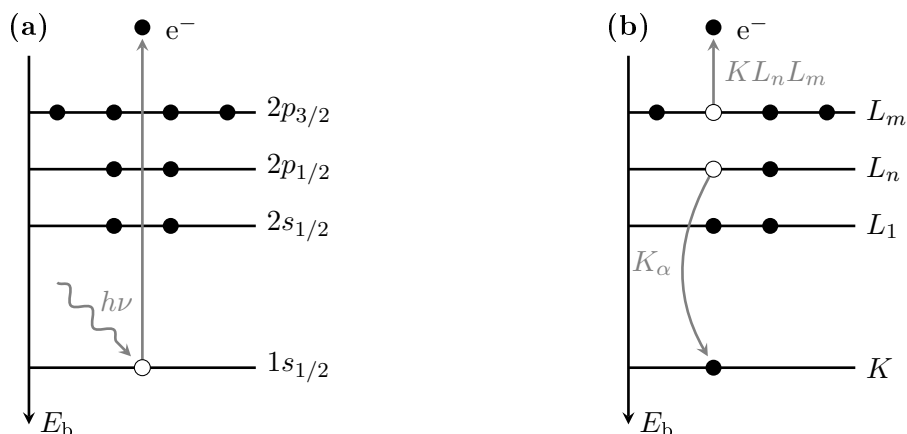
Figure 2.13.: X-ray induced transitions in atoms. **(a)** Ionization of a core level by knock out of an electron. The energy of the released electron is $h\nu - E_{\text{b}}$. **(b)** Relaxation of an outer shell electron to the ionized core. The energy of this transition can be transferred to another electron (Auger electron), which is then emitted.

and spectrometer. This leads to a significant shift of the kinetic energies, which complicates the analysis. For conductive samples the loss of electrons is compensated by connecting the sample to the detector.[147] In this case the Fermi levels of the sample and detector are aligned. As explained in the section on KPFM, the electrostatic field is given by the work function difference $\Delta\Phi$. The actual kinetic energy measured by the detector thus becomes

$$E_{\text{kin}} = h\nu - E_{\text{b}} + \Delta\Phi. \tag{2.21}$$

Since the kinetic energy alone cannot be used for data interpretation one normally uses this equation to calculate the binding energy. The binding energy of core electrons is rather high necessitating X-rays with photon energies around 1–2 keV, like e.g. produced by a synchrotron. The knocked out electron leaves back an ionized atom. This hole is filled by relaxing electrons from outer shells. The energy emitted in this process can be transferred to another electron in the shell, which is then emitted. This process is referred to as Auger effect and the ejected electron is called an Auger electron (see Fig. 2.13b). The Auger peaks appear as an artifact in XPS. In contrast to XPS, their kinetic energy does not depend on the photon energy. Thus their binding energies do not always appear at the same position.

The penetration depth of X-rays is in the range of some micrometers. However, electrons originating from these depths are prone to inelastic scattering and loose energy before they reach the surface. These electrons give rise to a background. Only electrons that origin from regions near the surface, i.e. the depth of some nanometers, are hardly scattered. Thus XPS has an intrinsic surface sensitivity, which can be further enhanced by decreasing the angle of incidence.[148] The same physical principle as used in XPS can also be applied to electronic states with low binding energies such as the ones in the valence band region. Typically X-ray irradiation with energies

below 100 keV or ultraviolet light is used to increase the interaction diameter of these states. The measurement is then either called valence band spectroscopy (VBS) or ultraviolet photoelectron spectroscopy (UPS).

2.5.2. PES and Chemical Analysis

Electron spectroscopy for chemical analysis (ESCA) as XPS was named originally by its inventor Kai Siegbahn indicates its capability beyond the detection of atomic species alone.[149,150] It is found that the core levels of an atom are not fixed in energy but depend on the chemical environment. Therefore, the measured binding energy gives information about the chemical state of an atom. The deviation from the reference binding energy can be understood by considering that an atom likes to retain its electrons. The binding energy of the electrons will therefore increase if some electrons are shared with other atoms or are even given away. Vice versa, the binding energy will decrease if an atom gets additional electrons due to high electronegativity or negative charging. This explanation gives a first qualitative understanding of the XPS spectra. For chemical analysis one generally needs the comparison with data of reference compounds. The analysis of single core energy levels might however be quite delicate if the investigated compound contains this atom in different states. These peaks have to be fitted carefully, which even enables quantitative analysis. However, the intricacies of this procedure are beyond the scope of this work.

2.5.3. PES for Molecular Adsorbates

XPS and VBS are commonly used to study adsorption configurations of molecules. In principle, they give information on the change of molecular states upon adsorption and might be used to monitor surface chemical reactions such as covalent anchoring. However, there are some prerequisites. XPS is a space averaging technique. The beam diameter is in the micrometer range, and the collected information is averaged over the beam area. Reliable conclusions on individual adsorption geometries can thus only be made if the surface can be prepared with only one particular adsorption configuration. Otherwise, additional information from e.g. SPM experiments is needed. Another prerequisite is the surface coverage. It is possible that an element is present in the substrate and the molecule. In this case the coverage has to be high enough to enable the discrimination between the contribution from the molecule and the substrate. One also has to consider that the X-ray beam could lead to decomposition or desorption of the adsorbate.

2.6. Summary

This chapter reviewed the theoretical background of the experimental techniques that were used in this work. First STM, which uses the quantum mechanical tunneling current to obtain sample topography, was introduced. The good lateral resolution that arises from the exponential distance dependence of the tunneling current is suitable to investigate the adsorption configurations of single molecules. The images are bias dependent and correlate to the density of states of the sample, which allows mapping of molecular orbitals such as the HOMO and LUMO. The main part of the chapter was devoted to the introduction of nc-AFM and its application to high resolution imaging under UHV conditions. The imaging uses the distance dependent tip-sample force to map the sample. The high resolution topography is affected by the nature and strength of the tip-sample interaction, which also depends on the tip termination. Therefore, the AFM topography does not necessarily correspond to the expected atomic topography of the sample. The corrugation might be overestimated, inverted or even dependent on the tip-sample distance. Different approaches to extend the versatility of standard FM-AFM such as the application of higher cantilever resonances for stable high resolution imaging or multimode nc-AFM and KFPM, which are able to measure different force components simultaneously, were reviewed.

Photoelectron spectroscopy was introduced as a complementary technique to SPM. It does not have the lateral resolution for the investigation of single molecules but it gives valuable information on the energy scale. PES spectra give the binding energies of core levels and allow the deduction of the oxidation state of an atom, which is helpful for chemical analysis. Applied to adsorbate covered surfaces, PES gives information on the change of molecular states upon adsorption and can be used to study surface based chemical reactions such as covalent anchoring. It is further useful to check the purity of substrates.

3.

Materials and Methods

The first part of this chapter gives an introduction to the hybrid organic-inorganic systems that are investigated in this work. It starts with a short discussion of the basic characteristics of titania and its different polymorphs. Thereby emphasis will be made on the technologically relevant rutile TiO_2 (110) and anatase TiO_2 (101) surfaces. The focus will then be turned to their functionalization with molecules. As for the scope of this work, this will be exemplified by a short review of metallo-carboxyporphyrins and their application in dye-sensitized solar cells. After having introduced all the materials, the second part of the chapter will cover the experimental methods. First, the ultra-high vacuum (UHV) system and the microscope head will be explained. The sputtering-annealing method that was used to prepare clean and atomically flat surfaces and the deposition of the molecules by evaporation will be outlined in the following. Then the preparation of the cantilevers and tips as well as the measurement control for nc-AFM and KPFM experiments are detailed. The chapter will close with a short explanation of the complementary techniques such as the density functional theory calculations and the STM and XPS setups at the Pearl beamline at the Paul Scherrer Institute.
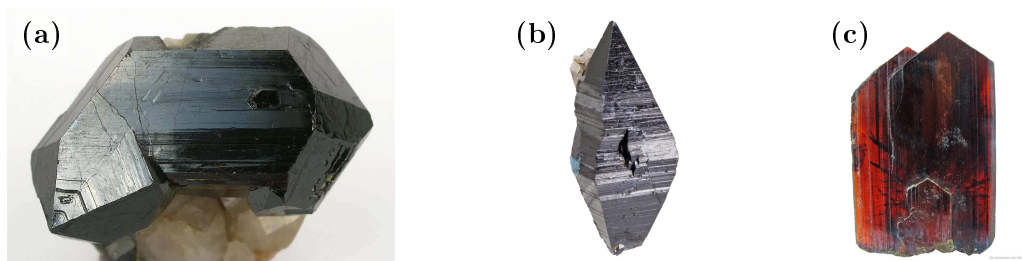

Figure 3.1.: Natural samples of the three TiO_2 polymorphs: **(a)** rutile, **(b)** anatase and **(c)** brookite. The color of natural crystals is determined by impurities or defects. High purity crystals are nearly colorless. Figures reproduced with permission from: The Arkenstone, www.irocks.com.

3.1. The TiO$_2$ Substrate

TiO$_2$ is the natural oxide of titanium. It has a band gap of 3–3.2 eV and belongs to the class of wide band gap semiconductors. Due to its stability, non-toxicity and abundance, it plays an important role as pigment or additive in a wide range of products. In recent years it has gained further importance for sensors, catalysis and photovoltaics.[20] These new applications are enabled by the surface chemistry of titania and are based on nanoparticles or mesoporous layers. To get a deeper understanding of their surface one has to study their different crystallographic planes. For this it is important to know that TiO$_2$ is a covalent crystal that occurs naturally in three modifications that are rutile, anatase and brookite (see Fig. 3.1). The anatase and brookite polymorphs are known to be metastable and can be converted to rutile under annealing.[151–153] Interestingly this metastability disappears for small anatase crystals.[152] Anatase nanoparticles below a size of 14 nm were even found to be thermodynamically more stable than rutile ones.[154, 155] Due to the similar stability of the nanoparticles it is possible to synthesize small crystals of either configuration. Rutile and anatase are thus the two most relevant titania polymorphs for the applications.[156] Considering the surface area of a particle it is found that certain crystallographic planes are dominant. The reason for this is given by their low surface energy. One can expect that these particular planes determine the surface properties of the crystal. Thus it makes sense to start the investigation on them. For rutile and anatase these are the (110) and (101) surface, respectively. They will be described in detail in the following sections.
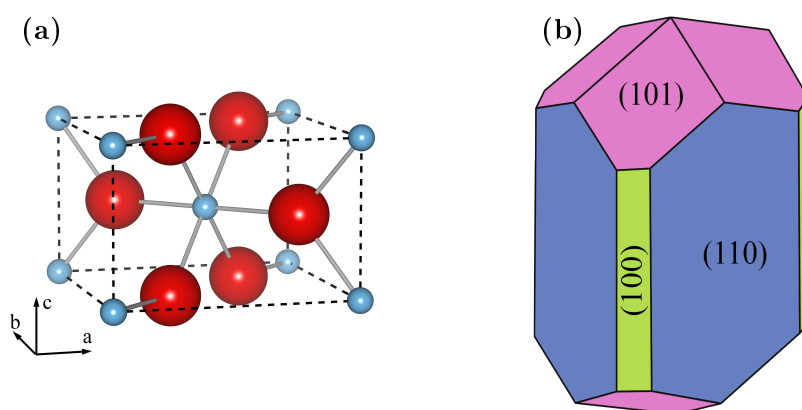
(a)

(b)

Figure 3.2.: Crystal structure of rutile TiO$_2$. **(a)** Unit cell of the rutile polymorph (oxygen=red, titanium=light blue). The lattice constants are a=459.4 pm and b=c=295.9 pm.[157] **(b)** Wulff construction of rutile after Ramamoorthy.[158] The area of a facet represents its relative stability. Equivalent faces are marked with the same color.
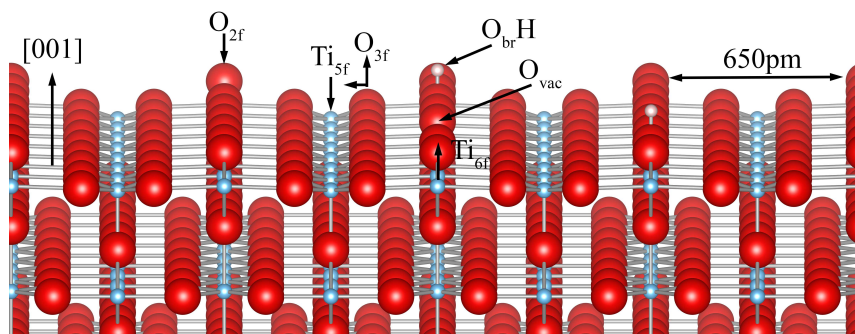
Figure 3.3.: Atomic model of the rutile TiO$_2$ (110) surface. Bridging oxygen atoms protrude from the surface and build a row structure along the [001] direction. Surface atoms and their relaxations as well as defects are indicated with arrows.

3.1.1. The Rutile TiO$_2$ (110) Surface

The availability of relatively large high purity rutile TiO$_2$ single crystals, fabricated by e.g. floating zone growth, promoted the research on titania surfaces. Due to its technological relevance, rutile TiO$_2$ has even become a model system for the investigation of metal oxides and their application for photovoltaics, photocatalysis, sensors and more.[20] A lot of experimental and theoretical studies comprising investigations of the bare substrate, adsorbate covered surfaces and surface reactions made that rutile is now one of the most studied substrates.[46, 159]

Rutile TiO$_2$ has a tetragonal structure with space group $P4_2$. The unit cell is depicted in Fig. 3.2a. Each bulk titanium atom is six-fold coordinated by oxygen atoms, which form an octahedron. The oxygen anions are threefold coordinated. Both atoms are charged, due to the strong ionic character of the Ti-O bond. Natural rutile crystals exhibit (110), (101) and (100) surfaces. The expected shape of a crystal in thermal equilibrium, which is calculated from the formation energies of the surfaces, is given by the Wulff construction displayed in Fig. 3.2b. From there it is evident that the (110) surface is the most stable one.[158, 159] It is normally bulk truncated and its structure is shown in Fig. 3.3. A stripe pattern along the [001] direction with a periodicity of 650 pm is characteristic for the (110) surface. The stripes origin from two-fold oxygen atoms (O$_{2f}$) that are vertically protruding from the surface plane. They are often referred to as bridging oxygen atoms (O$_{br}$). In the valleys are five-fold titanium (Ti$_{5f}$) and three-fold oxygen (O$_{3f}$) atoms. The surface atoms are slightly relaxed with respect to the bulk positions as measured by surface X-ray diffraction.[160] O$_{br}$ and Ti$_{5f}$ are pulled towards the bulk by -27 pm and -16 pm, respectively, whereas the Ti$_{6f}$ and O$_{3f}$ are pushed out of the surface by 12 pm and 5 pm. The O$_{3f}$ is also laterally displaced by 16 pm towards the next Ti$_{5f}$ row. The surface is autocompensated,[159] which means that charges arising from undercoordinated Ti$_{5f}$ are compensated by charges on the O$_{br}$. There are two dominant directions for step edges. They are along the $\langle 001 \rangle$ and $\langle 1\bar{1}1 \rangle$ direction. The height of a single terrace is 320 pm.[159]

The surface exhibits two well-known defects that are bridging oxygen vacancies O_{vac} and hydrogen adatoms $O_{br}H$. The oxygen vacancies originate from the sample preparation by sputtering and annealing.[159, 161, 162] It is observed that the color of the crystal changes from white to blue with increasing reduction.[161] The vacancies are quite stable on the surface and in the bulk.[163] The hydrogen adatoms are formed by adsorption of residual water to surface O_{vac} and the dissociated H adatoms are able to move along the bridging oxygen rows.[164] Oxygen vacancies in the bulk give rise to Ti^{3+} states, which are about $0.85\,eV$ below the Fermi level.[165, 166] The Ti^{3+} state acts as electron donor. Therefore, reduced rutile crystals are n-doped and show a relatively high conductivity, despite their relatively large direct band gap of $3.03\,eV$.[167, 168] The under-coordinated surface atoms as well as the defects are ideal candidates for the anchoring of adsorbates via covalent or H-bonds.

3.1.2. The Anatase TiO$_2$ (101) Surface

Even though rutile has been studied intensively as a model system,[46, 159] anatase is more relevant for the applications. It has been reported that it shows higher performance for photovoltaics or photocatalysis.[18, 156, 168, 170, 171] The major reason that much less research has been done on anatase is the availability of high purity samples. Only relatively small synthetic crystals can be grown.[156, 172, 173] For larger samples one has to use naturally grown crystals, which can be cleaved along in the (101) plane but possess contaminants in the order of some percent.[173, 174] This complicates the preparation of high purity surfaces in UHV and thus only few studies on atomic scale are available.[39, 173, 175–178] The tetragonal unit cell of anatase TiO$_2$ is depicted in Fig. 3.4a.
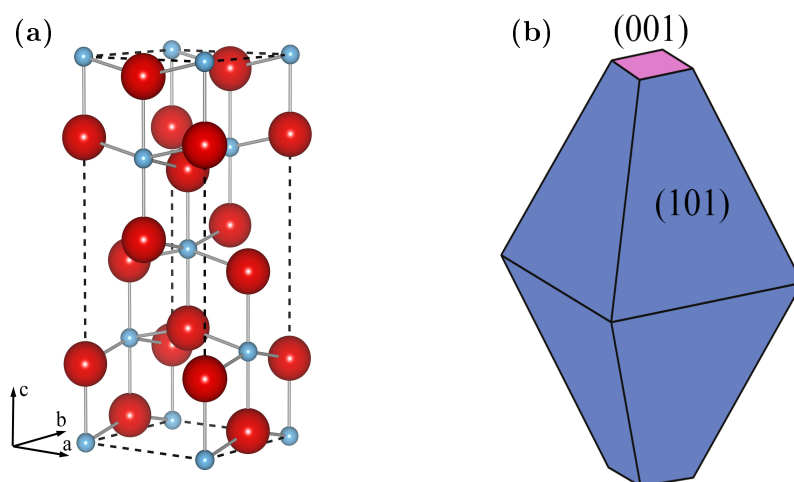

Figure 3.4.: Crystal structure of anatase TiO$_2$. **(a)** Unit cell of the anatase polymorph (oxygen=red, titanium=light blue). The lattice constants are $a=b=378.5\,pm$ and $c=951.4\,pm$.[157] **(b)** Wulff construction of anatase after Lazzeri.[169] The area of a facet represents its relative stability. Equivalent faces are marked with the same color.
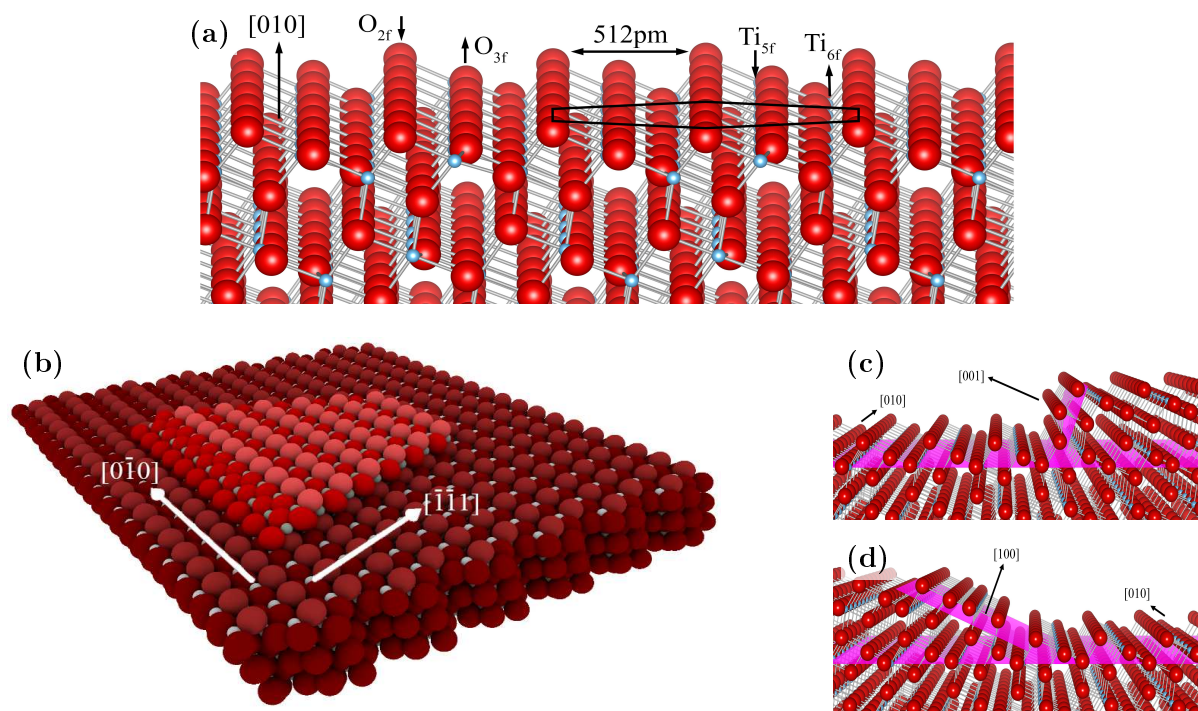
Figure 3.5.: Structure of the anatase TiO$_2$ (101) surface. **(a)** Atomic model of the pristine surface. The surface shows a saw-tooth pattern along the [010] direction due to protruding two-fold oxygen atoms. The types of surface atoms and their relaxations are indicated with arrows. **(b)** Model of a triangular island. **(c,d)** Atomic models of the two steps along the (010) direction that expose (001) and (100) microfacets, respectively.

It belongs to the space group $I4_1$. As for rutile the main structure are octahedrons formed by Ti atoms that are surrounded by 6 oxygen atoms. In the case of anatase they are slightly distorted. The same coordination numbers as well as the charging of the atoms mentioned for rutile apply for anatase too. As follows from the Wulff construction in Fig. 3.4b, the (101) surface is the most stable termination in naturally occurring crystals. Its surface structure is shown in Fig. 3.5a. It exhibits a saw-tooth pattern, where the top-most atoms are again two-fold oxygen atoms (O$_{2f}$). These atoms form a hexagonal structure as indicated in Fig. 3.5a. The periodicity of the saw-tooth pattern is 512 pm. Calculations have indicated that the surface atoms do also relax and thereby lower the surface corrugation.[179] O$_{2f}$ and Ti$_{5f}$ atoms are pulled towards the surface by 6 pm and 17 pm, respectively. O$_{3f}$ and Ti$_{6f}$ are relaxing outwards by 12 pm and 11 pm. The terraces are terminated with step edges along the $\langle 010 \rangle$ and $\langle \bar{1}11 \rangle$ direction and a height of 350 pm.[159, 175, 180] Islands on these terraces are common and have a triangular shape as depicted in Fig. 3.5b. Because the surface has a reduced symmetry, there are two different step edges along the [010] direction as shown in Figs. 3.5c,d.[180] The one that is on the steep side of a tooth exposes a (001) microfacet whereas the step on the other side shows a (100) termination.[180] Natural anatase crystals are often heavily reduced and have oxygen vacancies. It is found that they primarily reside in the bulk, so

that the surface has a much lower defect density than rutile.[176] The associated Ti^{3+} defect state does act as an electron donor with energy of about 0.8 eV below the Fermi level.[176, 181] Therefore, anatase becomes a n-type semiconductor too if highly reduced. The effective electron mass is smaller than for rutile and thus the conductivity is higher in anatase.[168] The band gap of anatase is 3.2 eV and indirect.

3.2. Metallo-Carboxyphenylporphyrins as Molecular Sensitizers

Due to its band gap of ca. 3 eV, titania does mainly absorb in the UV range. The thereby generated electron-hole pairs have been found to react with adsorbates leading to their decomposition. Thus titania has potential application in photovoltaics and photocatalysis.[20] However, due to the size of the gap, the efficiency of such systems is rather low. The performance can be enhanced by surface functionalization with suitable dye molecules. The light is then absorbed by the dyes and the excited electrons are injected into the conduction band of the TiO_2. These electrons can then be collected as a photo-current or be used for reactions on the surface. The performance of such an interface relies on its electronic structure, like e.g. position and location of energy levels, and depends on the adsorption configuration of the dye. Thus molecular sensitizers have to be designed carefully to give optimum performance. A particularly interesting group of molecules for sensitization of titania are metallo-porphyrins. Their macrocycles can be modified at different positions. This allows tuning their electrical and optical properties, but also facilitates the addition of anchoring groups so that they adsorb in a desired way. The metal core is another site that can be easily modified. Exploiting this tunability, it was possible to tailor highly efficient sensitizers for dye-sensitized solar cells (DSCs).[26] Other porphyrins have been improved for photocatalysis and sensing applications.[21, 182, 183] Insights on how the molecular adsorption mode is affecting the performance of the interface have mainly been gained by studying the average characteristics of large ensembles. Thereby it has been found that the distance of the metal core from the substrate and the tilt angle of the molecule with respect to the surface play an important role.[30, 184] The number of anchoring groups have been shown to affect the stability of the interface and their relative position has been found to influence the binding configuration.[28, 29] However, these measurements do not have direct access to the molecular adsorption mode and the conclusions might be oversimplified. Only few publications report on the investigation of individual porphyrins by e.g. SPM.[185] This methods allow a deeper understanding of the molecule-surface interaction and gives new insight for device optimization.

The set of metallo-carboxyphenylporphyrins (MCPPs) shown in Fig. 3.6 was chosen for this thesis in order to elucidate the above findings and questions by SPM. These porphyrins have different number and arrangement of the carboxylic acids. For further reference, the porphyrins are named with their abbreviation as defined in Fig. 3.6. The first part of the abbreviation indicates the configuration of the carboxylic anchors. Trans (tr) means that the COOH are on opposite phenyl legs
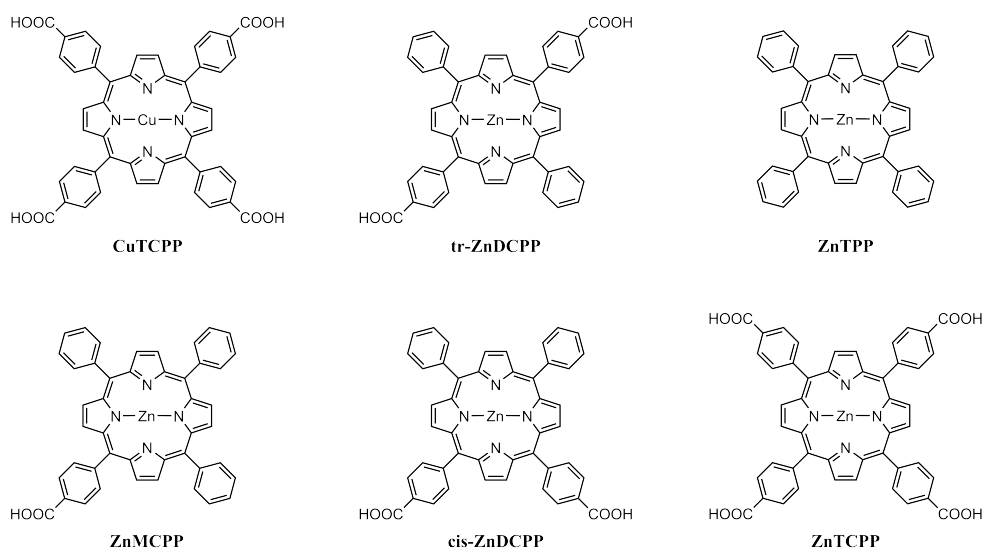
Figure 3.6.: Molecular structures of the investigated metallo-porphyrins with their abbreviations.

and cis stands for neighboring COOH. The second part of the abbreviation indicates the metal core (Zn=zinc, Cu=copper, M=non-specified metal core) and is followed by the number (M=1, D=2, T=4) and type of the functional group (PP=phenylporphyrin, CPP=carboxyphenylporphyrin). The number of anchors is sometimes omitted, as e.g. in ZnCPPs, which stands for all zinc-carboxyphenylporphyrins used in a particular experiment. It is supposed that the individual MCPPs adsorb in specific geometries that differ in binding strength, electronic coupling to the surface as well as intermolecular interaction. The investigation of individual molecules by nc-AFM and KPFM will allow the direct determination of the adsorption mode and electronic properties of a distinct molecule. Furthermore, one might deduce if a molecule is covalently anchored or not.

3.3. Non-Contact Atomic Force Microscopy in UHV

This section starts with the description of the experimental setup for nc-AFM in ultra-high vacuum. The second part covers the preparation of the bare and molecule covered TiO_2 samples as well as the cantilevers. Detailed information about bimodal AFM and KPFM measurements is given at the end of the section.

3.3.1. The Microscope

TiO_2 has highly reactive surfaces and is readily contaminated if exposed to air. Thus surface investigations have to be performed under ultra-high vacuum conditions. The UHV system for the room temperature nc-AFM in Basel is shown schematically in Fig. 3.7.
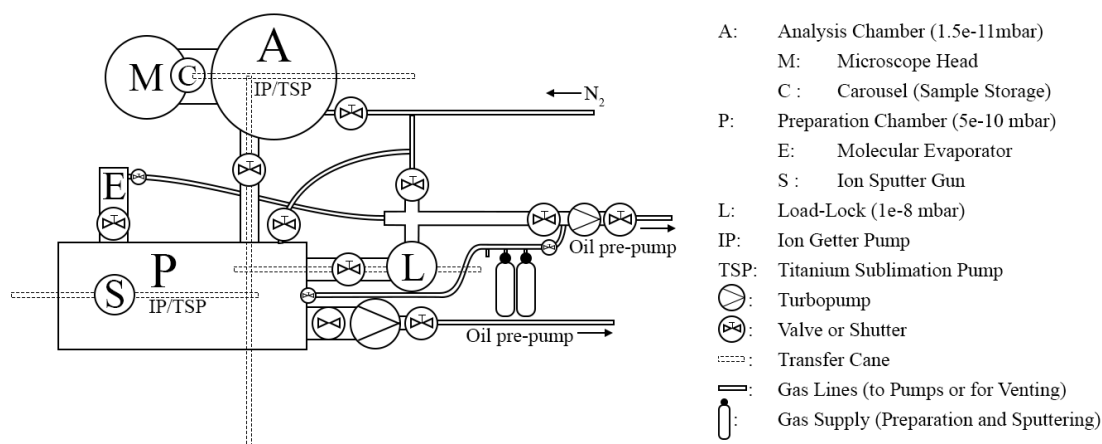
Figure 3.7.: Schematic drawing of the UHV system. The setup consists of three separated chambers: the analysis chamber with the microscope head, the preparation chamber for tip and sample preparation and the load-lock. The equipment of the chambers is listed in the description. The base pressures of the individual chambers are indicated as well.

The system is separated in three chambers. Samples and cantilevers are introduced through the load-lock. The lock is connected to a turbo and an oil pre-pump and has a base pressure of 10^{-8} mbar. After sample loading and pumping of the load-lock, the samples are transferred to the preparation chamber. This chamber is equipped with a heatable manipulator, a molecular evaporator and a sputter gun. All kind of preparation steps are made in this chamber to avoid contamination of the analysis chamber. The preparation chamber is pumped with a large turbopump as well as an ion getter and a titanium sublimation pump. Its base pressure is about 5×10^{-10} mbar. Prepared samples are transferred to the analysis chamber, where they can be investigated in the microscope or also be stored in a carousel. The base pressure in the analysis chamber is in the low 10^{-11} mbar range and is maintained by an ion getter and a titanium sublimation pump.

The microscope used in this work was developed and build at the University of Basel.[186] The microscope head is depicted in Fig. 3.8. The tip and sample are fixed on specific plates that are inserted in the corresponding holders. The tip holder is fixed on the microscope platform and connected to a dither piezo for excitation of the cantilever oscillation. The sample is held on top of a piezo tube. The tube is composed of different piezos that allow to displace the sample microscopically in all 3 dimensions. During the measurements the tube scans or moves the sample below the tip. The sample holder and the piezo tube are mounted on a slider, which is used for the macroscopic approach of the sample to the tip. The cantilever oscillation is measured by a laser beam. The light is introduced from outside the chamber with the help of an optical fiber. A first mirror is used to adjust the laser spot on the back of the cantilever. From there the laser
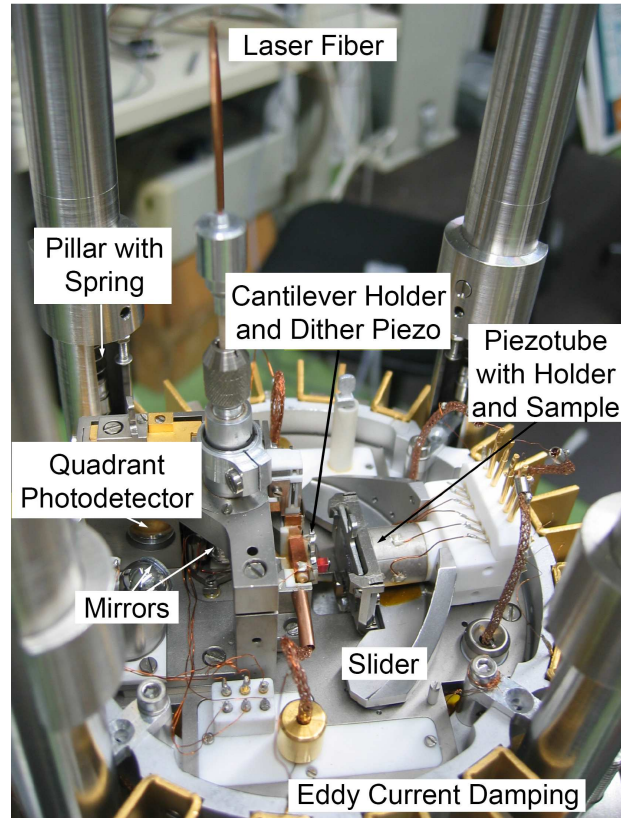
Figure 3.8.: Head of the AFM in Basel. The cantilever with the measuring tip is on the center of the microscope platform. It is hold on the dither piezo, which excites the cantilever oscillation. On the right are the slider with the piezo scanner and the sample holder. The optical components for the laser beam deflection are on the left. The microscope platform is decoupled from environmental vibrations by suspension with springs and by Eddy current damping elements.

is reflected to the second mirror, which deflects it to the quadrant photo-detector. This detector allows to measure the transverse and torsional oscillations of the cantilever. For further details of the system, the reader is referred to various PhD theses.[187–190]

3.3.2. Preparation of TiO$_2$ Single Crystals

High purity rutile TiO$_2$ (110) single crystals used in this work were grown synthetically and purchased from MaTeck GmbH (Jülich, Germany) or MTI corporation (Richmond CA, USA). Anatase (101) natural crystals were bought from SurfaceNet GmbH (Rheine, Germany). The crystals had dimensions of 5–10 mm×5 mm×0.5 mm and were polished to have a surface roughness in the range of the lattice constant. After sonicating in acetone and ethanol they were put on silicon wafer stripes and mounted on direct current sample holders as depicted in Fig. 3.9. The samples were introduced to the UHV chamber and outgassed at 600 °C overnight in order to remove adsorbates, such as water or solvents, from the holder. The sample temperature was
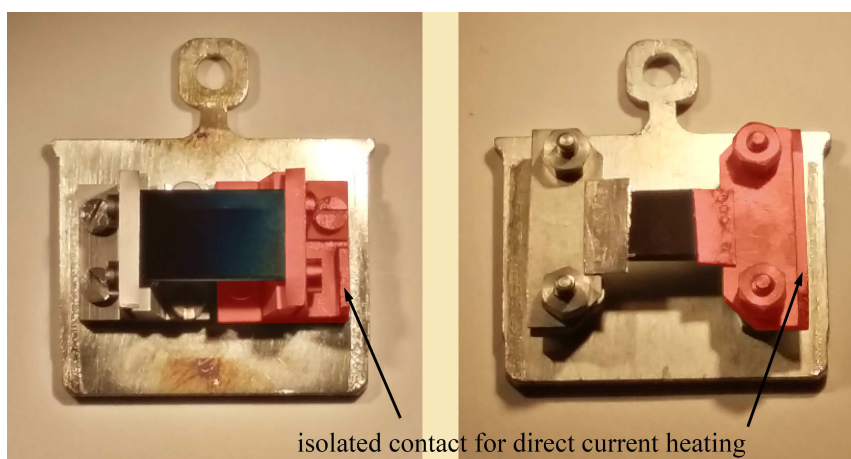
isolated contact for direct current heating

Figure 3.9.: Sample holders with mounted titania single crystals. The samples are heated by direct current flowing from the isolated contact through the piece of silicon wafer below the sample to the base plate. The sample holder on the left was designed for the experiments at the Paul Scherrer Institute and was only used for samples with the dimensions of $10\,mm \times 5\,mm \times 0.5\,mm$. The holder on the right is a standard one from Scienta Omicron GmbH (Taunusstein, Germany), which was modified with tantalum clamps for measurements on smaller samples.

monitored using an infrared pyrometer (Impac IGA 140, LumaSense Technologies) measuring the temperature of the resistively heated silicon upon which the sample was mounted. Emissivity was set to 64 % and 88.6 % for rutile and anatase samples, respectively. Preparation of the surface was done by Ar^+ sputtering (700–1000 eV, angle=30°, 10 min) and subsequent annealing to 800 °C for 15 min for rutile and 60 min at 600 °C for anatase. The annealing temperature was lower in case of anatase to prevent the phase transformation to rutile.[153] Sputtering removes surface atoms and contaminants due to collisions of the gas ions with the surface. It is not limited to the contaminants and disorders the crystal surface. Instead of being removed, impurities might also be pushed further into the substrate. Therefore, the sputtering is followed by annealing, which brings back these adsorbates to the surface, where they can be removed by renewed sputtering. In order to get a clean sample, the surface is prepared by repeated sputtering-annealing cycles. The annealing also restores the surface structure. The heating-up and cooling-down for the final annealing was done slowly, i.e. 10 min for the heating-up and 30 min for the cooling-down. Especially on rutile it was observed that the slow heating-up and cooling-down were beneficial for large terraces and the nice step edges, respectively. The annealing procedure was automatized using a LabVIEW program, that kept the sample temperature within an error of 5 °C of the programmed value.

New synthetic rutile (110) crystals, as shown in Fig. 3.10a, were normally treated with five cycles at 1 keV before first scanning by AFM or STM and typically exhibited a well-defined (1×1) bulk reconstructed surface with the corresponding step edges. Significantly more sputtering-annealing
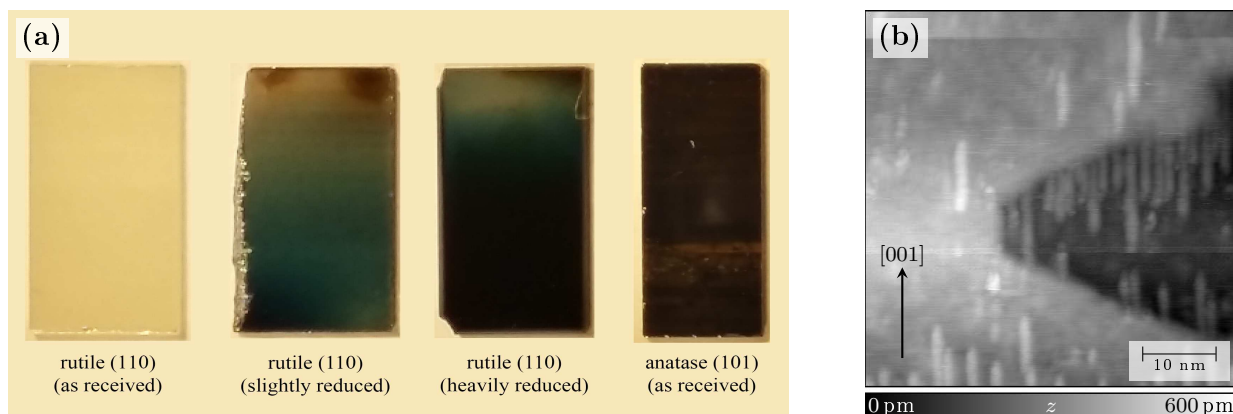
Figure 3.10.: Reduction state of TiO$_2$ crystals. **(a)** Appearance of fresh and sputter-annealed titania crystals. The received anatase crystals were already heavily reduced (dark) but also showed some brighter regions. **(b)** AFM topography image of a highly reduced rutile TiO$_2$ (110) crystal with starting (1 × 2) reconstruction.

cycles were necessary for the naturally grown anatase (101) crystal, which is attributed to natural contaminants.[173] Because water or hydrogen from the chamber likes to stick to TiO$_2$ the samples had to be reprepared regularly.[191–193] Samples that were stored in UHV or covered with molecules were typically cleaned with 3 cycles before they were reused. The repeated preparation of the crystals promotes removal of oxygen atoms. The reduction manifests itself by a color change. Fresh, oxidized rutile crystals exhibit a white color and are partly transparent. Under annealing the crystals become blueish, whereby the temperature and not only the time is relevant for the reduction state.[162] Highly reduced samples are dark blue to black (see Fig. 3.10a). This color was typically observed for samples that endured more than 50 cycles. If the reduction state was too advanced, the surface of the rutile crystal showed large stripe patterns indicating a starting (1 × 2) surface reconstruction (see Fig. 3.10b).[194] These samples were normally replaced by new ones. As received natural anatase crystals were already highly reduced and had brown to black color (Fig. 3.10a). The (1 × 1) surface was however preserved under preparation.[173] From time to time these crystals were reoxidized by annealing to 400 °C under 3.5×10^{-6} mbar oxygen atmosphere for 30 min and final heating to 600 °C for 1 h. Reoxidation was also done on the rutile crystals, but was less successful and not performed on regular basis, because the results depend on the oxidation state of the sample and on the applied temperature during O$_2$ dosing.[162,195] If not done correctly the sample is covered with an oxygen layer and had to be reprepared with several sputtering-annealing cycles.

3.3.3. Deposition of Molecules by Evaporation

All molecules were evaporated from a water cooled molecular evaporator. The CuTCPP was purchased from Rare Chemicals GmbH (Kiel, Germany) and the zinc porphyrins were received from the group of Prof. S. Decurtins from the University of Bern. A little quantity was filled in a small quartz crucible and placed in a slot of the evaporator. The evaporator was then baked overnight at $120\,^{\circ}\mathrm{C}$. The molecules were outgassed by stepwise increasing the temperature while monitoring the pressure in the chamber as well as measuring the evaporation rate using a quartz microbalance. The temperature was lowered by $10\,^{\circ}\mathrm{C}$, after a constant rate of about $100\,\mathrm{pm\,min^{-1}}$ was reached, and then kept for several hours till the pressure in the preparation chamber went back to the base pressure ($< 10^{-9}\,\mathrm{mbar}$). Evaporation was done to the freshly prepared surfaces. The coverage was tuned by the evaporation time. It has to be noted that the deposition rate decreased with time. Therefore, no rate is given in the results section. For the investigation of single molecules the evaporation time was kept as short as possible. If the desired coverage was not reached, the sample preparation was repeated. Depending on the experiment the sample was heated or cooled during the evaporation. For deposition at $300\,^{\circ}\mathrm{C}$ the sample was heated using the direct current method and the temperature was checked with a pyrometer. For room temperature deposition the sample was transferred to the analysis chamber directly after the final sputter-annealing cycle to prevent contamination from the preparation chamber. The evaporation was done after 1–2 h in order to allow the cooling-down to room temperature. After evaporation the sample was transferred immediately to the analysis chamber.

3.3.4. Preparation of Cantilevers

Standard non-contact cantilevers from NanoWorld SA were glued to holders from Scienta Omicron GmbH (Taunusstein, Germany) with conductive two-component epoxy glue (EPO-TEK H20S, Epoxy Technology Inc., Billerica MA, USA). The glue was only applied at four points on the side of the cantilever chip (see Fig. 3.11), since this has been proven to yield high Q-factors and thus high sensitivity on the first and second resonance of the cantilever.[189] Q-factors on the first resonance were ranging from about 20 k for PPP-NCL platinum coated to 39 k for high frequency PPP-NCH levers. For the second resonance Q-factors over 15 k could be obtained. The glued cantilevers were annealed in air to $140\,^{\circ}\mathrm{C}$ for 1 h. After introduction to the UHV they were outgassed for about 1.5 h at $130\,^{\circ}\mathrm{C}$ to get rid of remaining solvents and contaminants. The tips were then sputtered for 90 s ($680\,\mathrm{eV}$, $3 \times 10^{-6}\,\mathrm{mbar}$ Ar) to remove the native silicon oxide layer. Because a silicon tip termination is too reactive and thus not stable enough for high resolution imaging, further preparation was done in-situ.[130,196] The easiest way to modify the apex is to pick up sample material. For rutile (110) surfaces this was achieved by slowly approaching the tip to the surface while scanning over a step edge. New tips normally changed within few images. If the tip had to be reprepared afterwards, it is helpful to increase the tip speed and to scan a larger area

Figure 3.11.: Holder with cantilever, which was glued with the four point technique to ensure high Q-factor on the first and second resonance. The spots of the epoxy glue are marked in red.

with more steps (scan speed $>150\,\mathrm{nm\,s^{-1}}$), otherwise the recovery could be too time consuming. Dipping the tip into the surface by some hundred picometers was also observed to improve the tip but generally many attempts were needed. Thus it was only done if the previous method did not work. Once a tip crash occurred it was often faster to replace the tip than repreparing it on the surface. For anatase (101), scanning over the step edges was not a reliable method for tip preparation. However, the tip could be prepared by repeated dipping into the surface. Another successful approach for in situ tip preparation on anatase was the application of a bias pulse. However, the highest resolution, i.e. atomic contrast on the terraces, was only achieved if small adsorbates were picked-up while scanning. It has to be noted that all these preparation steps were more effective if the first resonance was used. Once a good tip was prepared, care was taken that no tip crash occurred. Meaning, the tip-sample distance was only changed slowly and the scan speed was reduced.

3.3.5. Measurement Control

The setup used for standard and bimodal nc-AFM is shown schematically in Fig. 3.12. The measurement setup is controlled with Nanonis electronics and software (SPECS Zurich GmbH, Switzerland). The oscillation of the cantilever is driven via positive feedback with a phase-locked loop (PLL). For standard nc-AFM the signal of the vertical deflection measured by the quadrant detector is fed to the PLL. The detected frequency shift goes to the z-controller and is used to control the tip-sample distance during automatic approach of the tip to the sample as well as during the topography scans. For single-mode nc-AFM either the first or second flexural resonance are used. For bimodal nc-AFM, the second oscillation is excited by an additional control loop. The frequency shift detected by this loop is only used for sensing but not for measurement control. Depending on the type of resonance, either the vertical or lateral signal of the photodetector is used. The oscillation of the cantilever was calibrated using the constant γ procedure after the
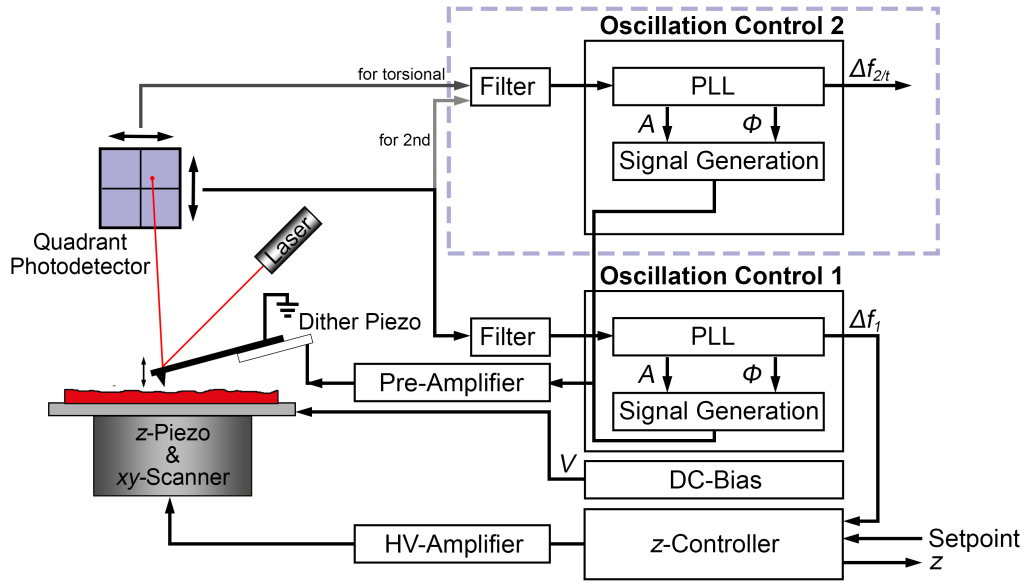
Figure 3.12.: Scheme of the measurement setup for nc-AFM. The first signal control unit is used to excite the cantilever oscillation for the topography measurement. The second signal control unit is only required for bimodal nc-AFM.
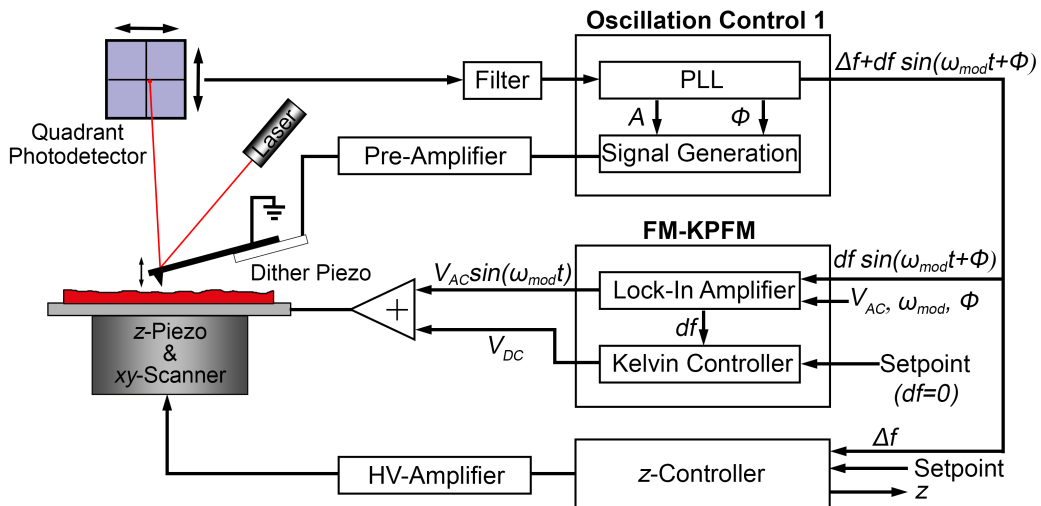

Figure 3.13.: Scheme of the measurement setup for FM-KPFM. The oscillating Δf signal is demodulated by a lock-in amplifier and minimized by the Kelvin controller, which applies a DC voltage to the sample.

tip had been approached to the surface.[119,197] Before the start of a measurement, the contact potential difference was determined by placing the tip at a fixed height over the surface and sweeping the sample bias. The position of the maximum of the recorded $\Delta f(V)$ corresponds to the V_{CPD} and was applied to the sample in order to minimize long-range electrostatic forces (see Sec. 2.4).

The setup used for the control of FM-KPFM experiments is illustrated in Fig. 3.13. In addition to the oscillation by the PLL, the cantilever is excited electrostatically by applying an AC Voltage V_{AC} to the sample. Typical parameters were V_{AC}=700 mV and a modulation frequency of 200 Hz. This causes an oscillation of the measured frequency shift. This signal is used as input for the lock-in amplifier, which measures its amplitude. The modulation of the Δf is minimized by the Kelvin controller, which adjust the DC bias component of the sample bias. The image contrast of the applied bias has the same contrast as the work function.[115]

3.4. Density Functional Theory Calculations

Complementary to the experimental methods, density functional theory calculations were done by the group of Prof. S. Goedecker. The main interest was on the adsorption configuration and the electronic interaction between molecule and substrate. Generally one has to say that high accuracy simulations are computationally expensive for large systems. Hence high level calculations such as the full configuration interaction or coupled-cluster methods, are reserved for small systems.[55,198,199] To treat large systems one has to make assumptions or approximations. This is also the case in density functional theory (DFT). Here the multi-electron problem is reduced to a system, where the electrons are non-interacting and move in an effective potential. Some of the physics, like van der Waals interactions, are thus no longer treated correctly.[55,200,201] There are different approaches to correct this drawback but they all increase the computational cost.[200] Hence, considering the adsorption of large molecules on TiO_2, most of the calculations in literature have been done using molecular mechanics or molecular dynamics simulations.[64,202,203]

DFT calculations presented in this work were carried out within the generalized gradient approximation using the BigDFT code[204] with homemade norm-conserving pseudopotentials.[205–207] Dispersion effects, like van der Waals forces, were included via the empirical pair potential of Grimme.[208] The model slab consisted of four TiO_2 trilayers each being a 4×9 cell. Periodic boundary conditions were applied along the two lateral directions but not along the third one, i.e. normal to the substrate surface.[209] The two layers at the bottom were kept frozen at their ideal crystal positions during geometry relaxations. Due to computational cost, the calculations were only made at the Γ point. Spin polarization was only included during test calculations using a model slab with two trilayers. The adsorption geometries were hardly influenced by the spin polarization and the binding energies were in the same range. Interfacial charge transfer was assessed by calculating the charge of every atom using Bader charge analysis.[210,211]

3.5. The PEARL Beamline

Additional STM and PES measurements were carried out on selected samples. These measurements were performed at the Photoemission and Atomic Resolution Laboratory (PEARL) at the Paul Scherrer Institute (PSI) in Villigen, Switzerland. The setup of the beamline is shown in Fig. 3.14. The sample was prepared in the preparation chamber, which is highlighted in red, using similar preparation methods as described for the nc-AFM setup in Basel. The main difference was that the manipulator in the preparation chamber was cooled to 77 K. Therefore, the manipulator acted as a cooling trap and minimized contamination from the chamber. STM measurements were made on a low temperature STM from Scienta Omicron GmbH (marked in blue) and were conducted directly after the sample preparation. Images were taken using the constant current mode with the bias voltage applied to the tungsten tip.

Photoelectron spectroscopy measurements were made at room temperature using the synchrotron radiation from the Swiss Light Source (SLS). PES spectra were acquired by measuring the kinetic energy of the electrons from the sample with a hemispherical Scienta EW4000 spectrometer with diameter of 0.4 m (Scienta Omicron GmbH, Taunusstein, Germany), while illuminating the sample with a constant photon energy. The beam energy was set using a monochromator.
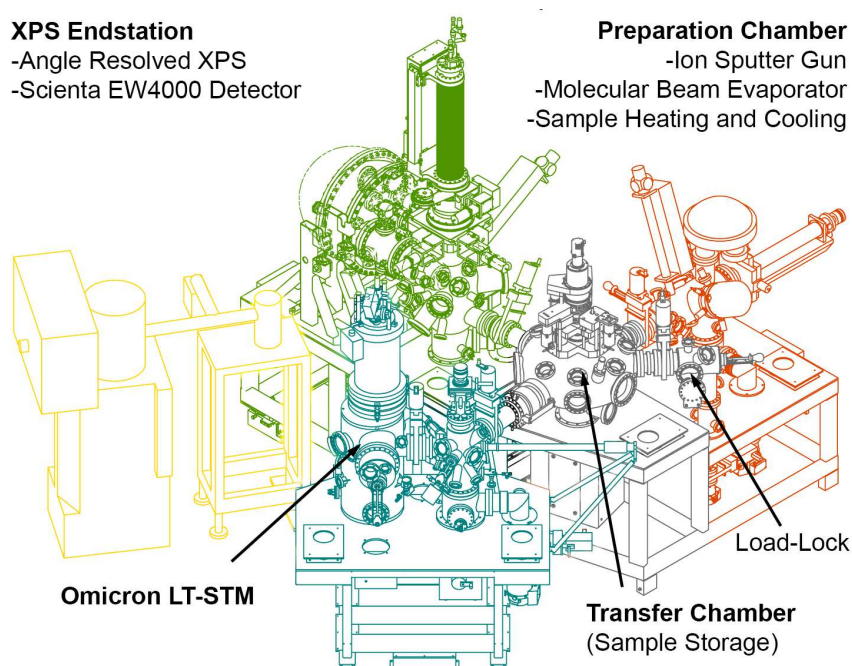
Figure 3.14.: Conceptual rendering of the PEARL beamline at the Paul Scherrer Institute. The PES endstation (green) is connected to a sample preparation chamber (red) and a LT-STM (blue) through a transfer chamber (grey). This facilitates to prepare and check the sample before exposure to the beam. Figure modified with permission from PSI, www.psi.ch.

3.6. Summary

This chapter described the basic properties of the rutile TiO_2 (110) and anatase TiO_2 (101) surfaces as well as their cleaning and preparation by standard sputtering-annealing cycles. Thereby emphasis was made on the creation and role of defects. The experimental setups for nc-AFM and the measurement control were discussed. Different in-situ tip preparation techniques on anatase TiO_2 (101) and rutile TiO_2 (110) were highlighted, which were of paramount importance for obtaining high resolution nc-AFM images.

Part II.

Results and Discussion

4.

CuTCPP and ZnCPPs on Rutile TiO$_2$ (110)

Rutile TiO$_2$ (110) is one of the most investigated surfaces in surface science.[159] It has been investigated as a model system in order to understand the surface chemistry for applications like catalysis or hybrid photovoltaics. It is thus an ideal reference system and was chosen to investigate the adsorption of metallo-carboxyphenylporphyrins on the single molecule level.

The beginning of this chapter covers preparatory examinations of the bare rutile TiO$_2$ (110) surface with nc-AFM. Emphasis will be made on the identification of defects and the influence of the tip polarity on the nc-AFM topography. Afterwards, the adsorption behavior of metallo-carboxyporphyrins on rutile TiO$_2$ (110) is investigated. A first study characterizes individual adsorption geometries of CuTCPP using a combined approach of high resolution nc-AFM on the second resonance frequency together with KPFM and DFT calculations. The second investigation studies the formation of covalent bonds to the surface for molecule immobilization. For this, the adsorption configurations of tr-ZnDCPP and ZnTPP as well as their binding stability were investigated by AFM and low temperature STM. Complementary chemical information was collected with PES. These two detailed studies are followed by experiments done on ZnCPPs with different number of carboxylic anchors. The last section gives an outlook on high resolution nc-AFM imaging on these porphyrins at room temperature using bimodal AFM and dual-pass methods.

4.1. The Rutile TiO$_2$ (110) Surface

In order to understand the adsorption of molecules it is necessary to know the properties of the substrate. Somehow, they are not solely determined by the structure of the surface but also by defects. Hence this section goes beyond the standard surface characterization with AFM and introduces bimodal nc-AFM as a potential tool for the identification of surface defects.
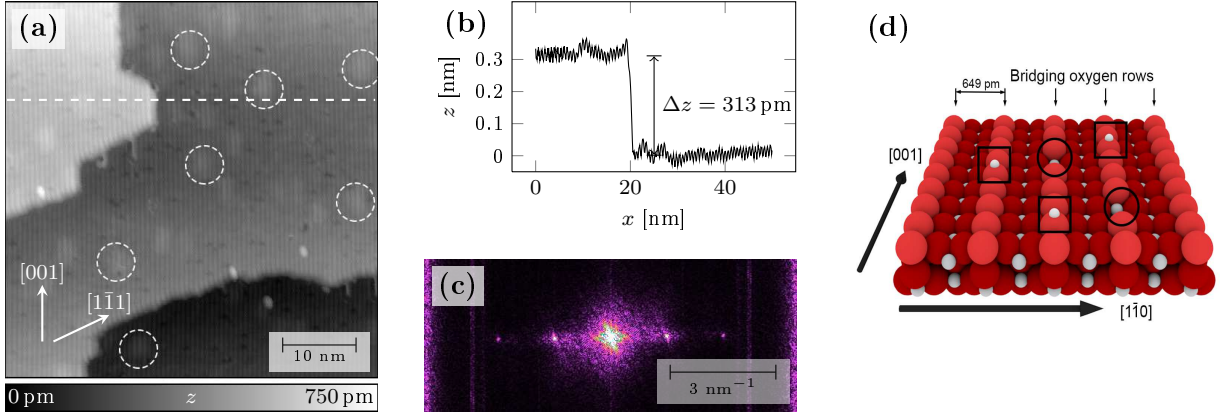
Figure 4.1.: Structure of the (1×1) reconstructed rutile TiO$_2$ (110) surface. **(a)** Nc-AFM topography showing oxygen rows along the [001] direction and step edges along the $\langle 001 \rangle$ and $\langle 1\bar{1}1 \rangle$ directions. The dashed circles indicate some of the subsurface defects (f_2=1.974 MHz, A_2=400 pm, Δf_2=-71 Hz, Q_2=8.8 k). **(b)** Height profile of a step edge along the [1$\bar{1}$0] direction as indicated with the dashed line in (a). **(c)** FFT spectrum of the surface shown in (a). **(d)** Model of the rutile TiO$_2$ (110) surface with defects. The size of the atoms is drawn corresponding to their ionic radii, which highlights the rows along the [001] direction. Oxygen vacancies and hydrogen adatoms are marked with circles and squares, respectively.

Fig. 4.1a shows a nc-AFM topography image of the freshly prepared rutile TiO$_2$ (110) surface. It reveals flat terraces with an average width of about 50 nm. Step edges were along the $\langle 001 \rangle$ and $\langle 1\bar{1}1 \rangle$ directions. The height of the step edge of 313 ± 10 pm was determined from profiles across the step edges as e.g. shown in Fig. 4.1b. The terraces exhibited a stripe pattern along the [001] direction that is attributed to bridging oxygen rows.[159] The spacing between single bridging oxygen rows was deduced from a FFT spectrum to be about 650 pm (see Fig. 4.1c). These experimental results are in good accordance with reported data on rutile TiO$_2$ (110) with a (1×1) reconstruction.[159] The terraces exhibited small circular elevations as is indicated in Fig. 4.1a. They were attributed to charged subsurface defects as possibly induced by the argon sputtering, which was used during the sample preparation.[212] The repeated sputtering-annealing cycles further reduced the crystals, which was evident from their blue color. Hence defects such as oxygen vacancies (O$_{vac}$) and hydrogen adatoms (O$_{br}$H) were present as is indicated in Fig. 4.2. A model of the defective surface is shown in Fig. 4.1d. Interestingly, these defects were not detected on the elevated spots above the charged subsurface defects (Fig. 4.1a). It is assumed that hydrogen adatoms and also oxygen vacancies are repelled from these sites.[212]

Considering that the known defects occur only on the bridging oxygen rows it is straightforward to identify the oxygen and titanium rows of the surface.[213] However, the determination of the defects is more complicated. Several imaging contrasts have been observed on TiO$_2$ (110) and were explained by the apex termination and tip polarity.[129, 130, 196, 214] As is evident from Fig. 4.2,
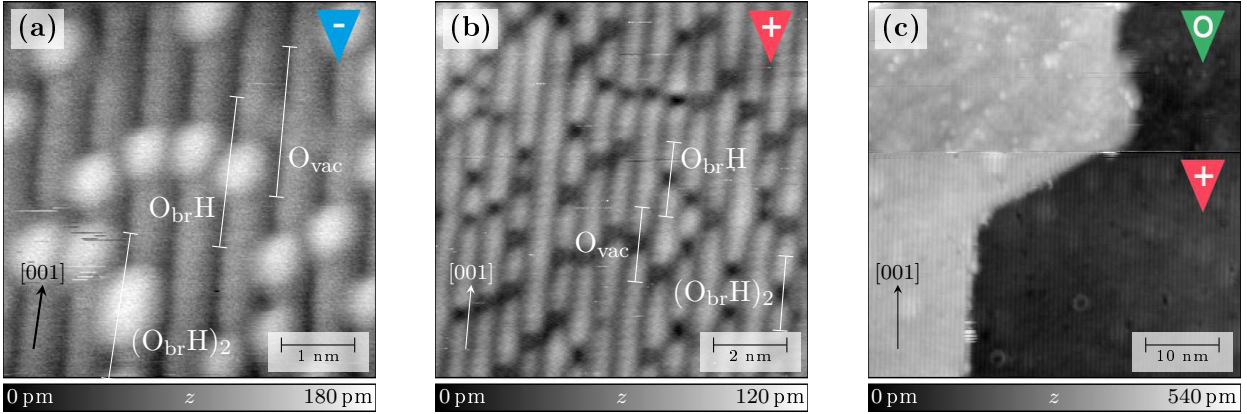
Figure 4.2.: High resolution nc-AFM contrasts and defect determination on rutile TiO$_2$ (110). **(a)** Imaging contrast arising from a negative tip termination. Bridging oxygen rows appear dark. Oxygen vacancies (O$_{vac}$) and hydrogen adatoms (O$_{br}$H) can be assigned. Indicated profiles are shown in Fig. 4.3b (PPP-NCL, f_1=154.9 kHz, A_1=5 nm, Δf_1=−40 Hz, Q_1=26.9 k). **(b)** Topography image acquired with a positively polarized tip. Defects are on the bright oxygen rows and cannot be distinguished. Indicated profiles are depicted in Fig. 4.3d (PPP-NCL, f_2=1.001 MHz, A_2=400 pm, Δf_2=−230 Hz, Q_2=13.3 k). **(c)** Change of tip termination from neutral to positive (PPP-NCH, f_1=318.4 kHz, A_1=10 nm, Δf_1=−7 Hz, Q_1=38.9 k).

not all contrasts allow the direct differentiation between the defect types because the topography of the rows or defects can be inverted. The expected topography, i.e. where the adatoms and vacancies appear as hills and dips on elevated bridging oxygen rows, respectively, is only imaged in the case of a neutral tip apex. On pictures with negative tip termination, as shown in Fig. 4.2a, both defects appear as bright protrusions on the dark oxygen rows. This is due to the attractive forces between the positively charged defects and the negative tip, which lowers the minimum Δf and thus causes retraction of the tip (see also Fig. 2.7b). Since hydrogen adatoms are real protrusions they are imaged brighter than the oxygen vacancies. In case of a positively polarized tip the interaction is repulsive and causes both defects to be imaged as dips on the now bright oxygen rows (Fig. 4.2b), making it difficult to distinguish the defect types.

In conclusion it has been found that defect types can only be assigned from the topography images if the tip is neutral or negatively terminated.[129,130] Investigation of the defects by high resolution imaging with neutral tips was however hardly possible because of apparent tip instability (see Fig. 4.2c). Furthermore, the positive tip termination appeared to be the most stable and thus the predominant one. Since the controlled manipulation of the tip termination has not been achieved at room temperature so far, it remains an intricate task to identify defects by nc-AFM. A possible solution to this problem is bimodal AFM. Using the 1st torsional resonance as an additional channel increases the sensitivity for short-range interactions and could thus reveal more information about the nature of a defect. It was therefore evaluated for defect identification. The lateral tip oscillation was along the [001] direction, meaning along the bridging
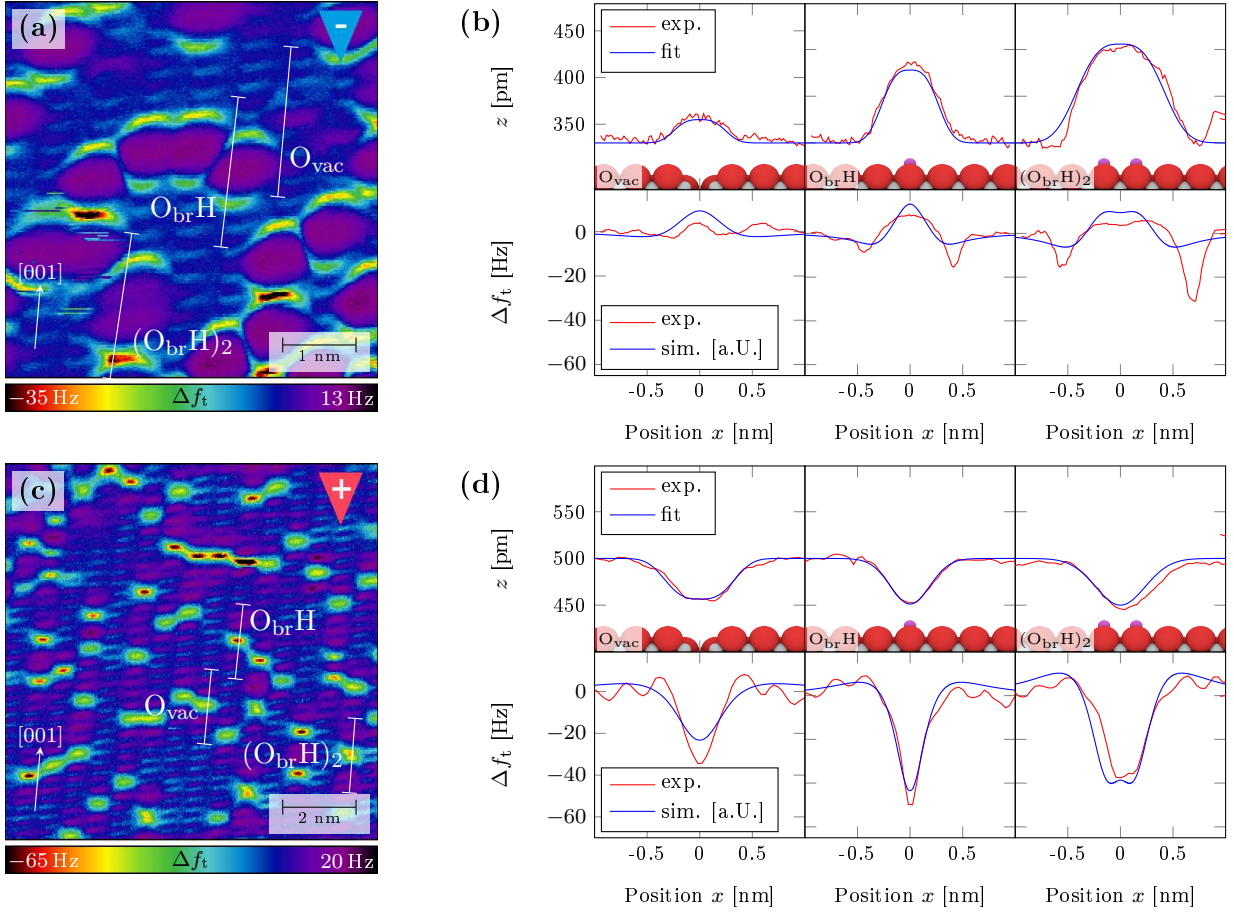
Figure 4.3.: Identification of defects by bimodal nc-AFM. **(a,c)** Images of the torsional resonance frequency shift corresponding to Fig. 4.2a (PPP-NCL, f_t=1.478 MHz, A_t=30 pm, Q_t=59.1 k) and Fig. 4.2b (PPP-NCL, f_t=1.561 MHz, A_t=30 pm, Q_t=52.8 k). The lateral tip oscillation was along the [001] direction. **(b,d)** Profiles and corresponding simulated torsional frequency shifts over the defects as indicated in (a) and (c) as well as in Fig. 4.2. (b) and (d) show the results for negative and positive tip termination, respectively. The atomic models of the defects are displayed in the center. (Hydrogen adatoms are marked in violet for better visibility).

oxygen rows. Fig. 4.3 shows the frequency shift signal of the torsional resonance that corresponds to the topography images shown in Figs. 4.2a,b. Both scans revealed three different features that were attributed to single and double hydrogen adatoms as well as bridging oxygen vacancies. The justification of these assignments was done by calculating the expected torsional frequency shift profiles for a simple model system and comparing them with the experimental profiles. The model consisted of a positively charged point defect and a charged measuring tip. The potential of the defect was modeled using a Coulomb potential. The torsional frequency shift is given as the lateral derivative of the force field and was evaluated on fits to the experimental topography profiles shown in the upper panels of Figs. 4.3b,d. The obtained frequency shift curves were convoluted with a

semicircular weighting function with the radius corresponding to a torsional amplitude of 30 pm, in order to consider for the averaging by the lateral oscillation.[126] The simulated torsional frequency shifts for negative and positive tip terminations are depicted in the lower panels of Figs. 4.3b,d. They reveal the same contrasts as the experimental curves. The shape of the curve is explained as follows. Far from the defect, the tip senses the increasing long-range electrostatic forces, causing either a positive or negative frequency shift for repulsive and attractive interactions, respectively. However, this force decreases in the vicinity of the defect and becomes zero over it since the lateral forces cancel out. Thus the frequency shift changes its sign when approaching the defect. The same behavior is observed again when the tip leaves the defect, which leads to symmetric profiles. The change of the lateral force component is strongly distance dependent, meaning close tip-sample distances cause large shifts in the torsional resonance. This facilitates the determination of the defects. Especially for the positively terminated tip, the minimum distance between tip and defect differs considerably between oxygen vacancies and hydrogen adatoms. This is due to the fact that the experimental topography is only inverted on one of the defects. Among the three defects, hydrogen adatoms show thus the strongest signal in the torsional image followed by double hydrogen atoms. Oxygen vacancies appear as faint dips only. In summary, bimodal AFM using the torsional resonance together with simple model calculations facilitated the identification of different defects on rutile TiO$_2$ (110). This makes this method a potential tool for the basic characterization and identification of defects on other surfaces as well.

4.2. CuTCPP on Rutile TiO$_2$ (110)

In order to get a deeper understanding of functionalized surfaces one has to investigate the adsorption behavior of molecules. This section shows that the characterization of individual molecules, comprising the determination of the adsorption configuration and the electrostatic interaction with the surface, can be achieved experimentally by nc-AFM and KPFM at room temperature. This is demonstrated by identifying two different adsorption configurations of isolated CuTCPP on rutile TiO$_2$ (110) in ultra-high vacuum. FM-KPFM was used to measure the local contact potential difference from which interfacial dipole moments as well as the amount of electron transfer from the CuTCPP to the TiO$_2$ was estimated. The experimental results were verified by state-of-the-art density functionl theory calculations.

4.2.1. Adsorption Geometries of CuTCPP

Evaporation of CuTCPP was done while the sample was still cooling down from the last sample preparation cycle. Thus the sample was still at a temperature of ca. T_s=130 °C during the deposition. The nc-AFM topography image obtained afterwards show isolated molecules as can be seen in Fig. 4.4a. The majority of the molecules were adsorbed on terraces, implying that the diffusion was suppressed due to strong interaction with the substrate. The molecules appeared as
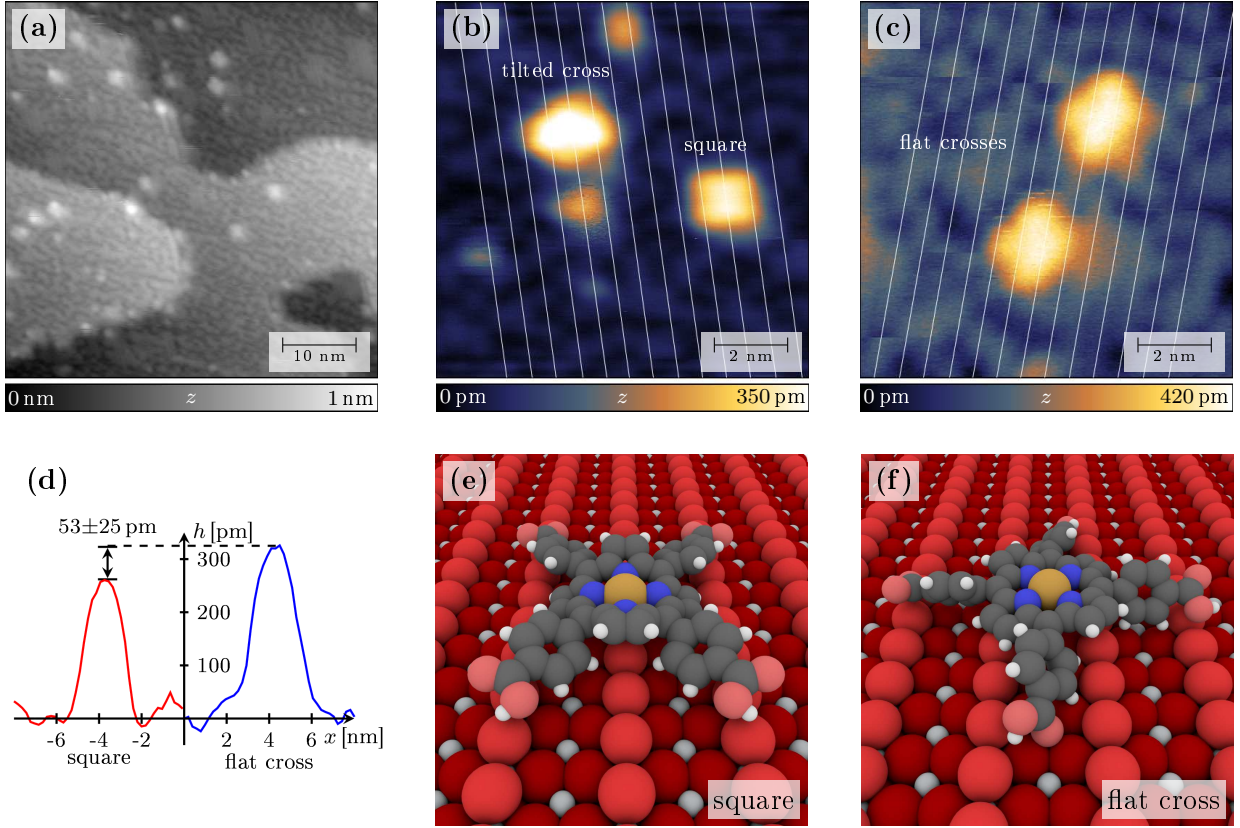
Figure 4.4.: Binding geometries of CuTCPP on rutile TiO$_2$ (110). **(a)** Large scale nc-AFM topography image (f_2=1.001 MHz, A_2=400 pm, Δf_2=−10 Hz, Q_2=7.5 k). **(b,c)** High resolution images of different adsorption geometries ((b): f_2=957.9 kHz, A_2=400 pm, Δf_2=−13 Hz, Q_2=10.4 k; (c): same as in (a)). Bridging oxygen rows are indicated with white lines. **(d)** Typical height profiles for the flat square and cross adsorption mode. **(e,f)** Proposed models for the symmetric square and cross orientations.

bright protrusions with a diameter of about 2 nm and a height of around 300 pm, indicating that the molecules lay flat on the surface. High resolution nc-AFM measurements of CuTCPP using the second resonance are depicted in Figs. 4.4b,c. They reveal submolecular contrast that includes contrast on the substrate as well. The molecules aligned themselves with respect to the rows, resulting in two main orientations. One part of them had their Cu-cores on a bridging oxygen row and their carboxyphenyl substituents were in a 45° angle with respect to this row. Depending on the obtained contrast they were sometimes only visible as squares. Therefore, this geometry will be referred as the square ($\square$) configuration (see Fig. 4.4b). The other molecules were rotated in plane by 45° with respect to the squares, having their axes along and perpendicular to the oxygen rows with their central copper atom positioned on a titanium row. They appeared as crosses and will thus be denoted as the cross ($\diamond$) configuration (see Fig. 4.4c). Apparent height profiles for the two configurations are shown in Fig. 4.4d. The corresponding heights were calculated from the profiles of 13 molecules per configuration. The averaged heights were $h_\diamond$=302 ± 13 pm and

$h_\square$=250 ± 21 pm for the cross and square orientation, respectively. Therefore, it was possible to distinguish the two adsorption configurations even on large scale images. Most of the molecules were found in these two symmetric geometries depicted in Figs. 4.4e,f. Asymmetric binding modes like the tilted cross shown in Fig. 4.4b were observed scarcely.

4.2.2. Stability of Geometries

So far it was observed that evaporation of CuTCPP to the still hot substrate resulted in two distinct adsorption geometries. Interestingly, some nc-AFM images revealed several noise lines or marks as shown in Fig. 4.5a. The number of these marks increased with decreasing tip-sample distance and can be attributed to tip induced displacements of porphyrins.[62, 215] Hence these features can give information about the individual stability of the two configurations. In fact, the comparison of two consecutive images showed that molecules in the square configuration moved along the oxygen rows (see Fig. 4.5b). Only in rare cases, molecules were displaced across the rows, even though this was the fast scan direction. Hence the preferential displacement was along the bridging oxygen rows. Movement of the cross configuration was not observed. They remained stable until the tip was too close so that the molecules were picked up. This results give a first hint that the two configurations differ in stability.

The ratio of the two configurations was changed in favor of the square adsorption mode if CuTCPP was evaporated to the cold substrate. This effect was already visible if the sample was at room temperature during deposition. However, because of the higher mobility of the square the scan
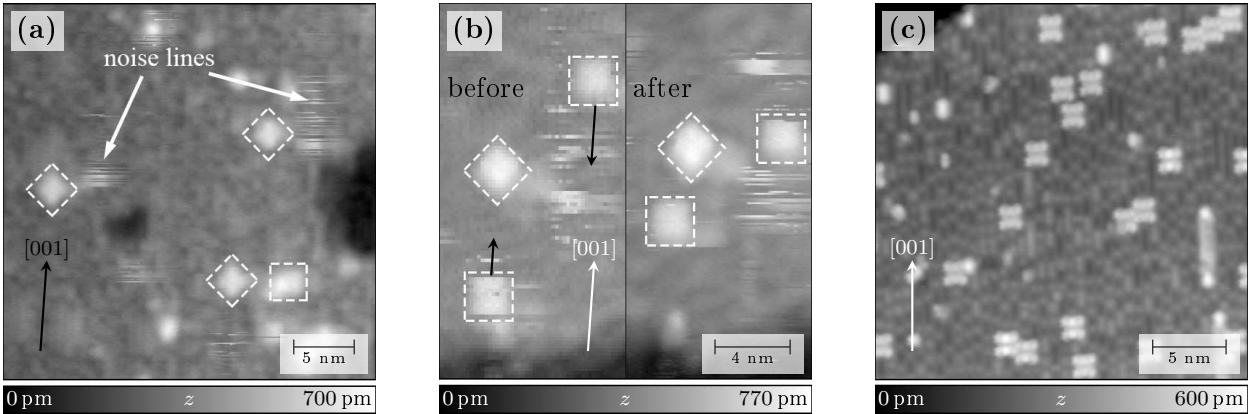
Figure 4.5.: Stability of CuTCPP on rutile TiO$_2$ (110). **(a)** AFM topography image with noise lines. **(b)** Two consecutive nc-AFM pictures showing the displacement of molecules in the square configuration. The black arrows indicate the direction of the tip induced molecule movement. Both figures were recorded using a PPP-NCL cantilever on the second resonance (f_2=1.001 MHz, A_2=400 pm, Q_2=7.9 k, Δf_2=−9 Hz for (a) and Δf_2=−10 Hz for (b)). **(c)** Low temperature (77 K) STM topography image of an ensemble of CuTCPPs in the square geometry after deposition to the cold substrate (I_t=10 pA, V_s=1.8 V).

conditions for AFM were deteriorated. Clear evidence that the CuTCPP was in the square mode was given by STM measurements at 77 K where the CuTCPP has been deposited to the cold sample just after taking it out from the microscope ($T_s < 25°$) (Fig. 4.5c). Heating of these CuTCPP to about 100 °C already resulted in an irreversible change from the square to the cross mode for some of the molecules. This behavior might be due to the thermally activated formation of covalent bonds between the carboxylic anchors of the CuTCPP and surface titanium atoms.

4.2.3. KPFM Measurements

The investigated geometries do all lie flat on the surface. Their delocalized orbitals or the metal core might thus electronically interact with the surface. KPFM measurements have been made in order to evaluate this coupling. The local contact potential difference (LCPD) between the sample and the tip was measured using frequency modulation Kelvin probe force microscopy (FM-KPFM), while the bias was applied to the sample (Sec. 2.4).[104] Fig. 4.6a and 4.6b show the topography and the corresponding slope corrected LCPD map, respectively. The correction of the background slope was justified by the presence of polarized step edges.[216] Single CuTCPP molecules were clearly visible as dark features in the LCPD map, indicating that the local contact potential difference on them was lowered by about 25 mV. There was no major difference between the two configurations. The lower LCPD on the CuTCPP can be attributed to an interface dipole caused by electron transfer from the CuTCPP to the substrate.[217,218]
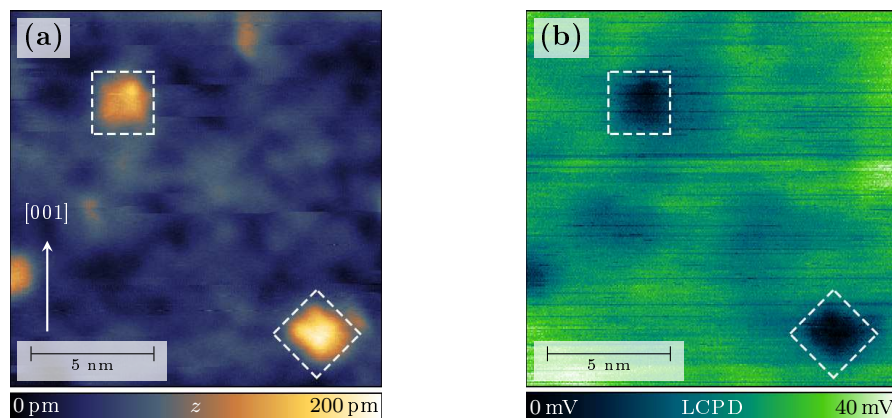
Figure 4.6.: FM-KPFM of CuTCPP on rutile TiO$_2$ (110). **(a)** Topography image and **(b)** corresponding slope corrected LCPD map of two differently bound CuTCPP molecules (PPP-NCL Pt, f_1=149.3 kHz, Δf_1=−115 Hz, A_1=3 nm, Q_1=20.4 k, V_{mod}=700 mV, f_{mod}=200 Hz).

4.2.4. DFT Calculations

The adsorption geometries inspired by AFM were used as input for DFT calculations in order to determine the exact adsorption site as well as the protonation state of the carboxylic acid anchors. For the latter it was taken into account that a carboxylic proton is either retained on the dye or transferred to a bridging oxygen nearby.[219] The simulations focused on the two symmetric configurations and the surface was considered to be free of defects for most of the calculations. Only for the square configuration it was accounted for the case of an oxygen vacancy below the central copper atom. This assumption is legitimated as follows. As noted previously, hydrogen adatoms were accumulating with time, meaning that the amount of hydrogen adatoms was supposed to be much lower during the evaporation than indicated by our images. Hence, during the evaporation, the majority of the defects were oxygen vacancies. However, both defects, oxygen vacancies that might react with the carboxylic acid and hydrogen adatoms, are supposed to lead to asymmetric adsorption geometries. Thus, for the study of symmetric geometries, it should be sufficient to consider the perfect rutile TiO$_2$ (110) surface for most of the cases.

The expected structures were relaxed by DFT calculations using the generalized gradient approximation (Sec. 3.4). Van der Waals forces were included using empirical pair potentials. The calculated heights of the molecule with respect to the plane through the unrelaxed bridging oxygen rows are given in Tab. 4.1. The copper atom, which reflects the center of the molecule, is about 70 pm higher in the cross geometries than in the squares. The average heights, calculated as the mean value of all the atoms of the porphyrin, differ by approximately 40 pm. In a first approximation, these height differences can be interpreted physically as consequence of the electrostatic interaction between the positively charged copper core of the porphyrin and the surface atom below, which is either a negative bridging oxygen or a positive titanium atom. The height difference between the two orientations is comparable to the one from AFM ($h_\diamond = 302 \pm 13$ pm and $h_\square = 250 \pm 21$ pm). It was thus assumed that the experimentally determined height difference was mainly caused by the real topography. This is further corroborated by the observation that the charging state of the two orientations was similar, as indicated by KPFM and DFT. The adsorption energies E_{ad} between the molecule and the substrate were calculated in order to determine the configurations that fit best with the experimental results. E_{ad} is defined by

$$E_{\mathrm{ad}} = E_{\mathrm{mol@sub}} - (E_{\mathrm{mol,free}} + E_{\mathrm{sub}}), \tag{4.1}$$

where $E_{\mathrm{mol,free}}$ and E_{sub} are the calculated energies for the isolated molecule and substrate slab, respectively. $E_{\mathrm{mol@sub}}$ is the energy of the combined molecule-titania system after adsorption. The three geometries shown in Fig. 4.7 have adsorption energies around -3.5 eV. They are supposed to be stable at room temperature. The other configurations have lower adsorption energies that are not likely to be stable under scanning conditions. The strongest binding is found for the fully protonated configurations. The preferred square configuration is on the pristine surface, and is centered on a bridging oxygen row (Fig. 4.7a). This geometry shows an attractive

Table 4.1.: Properties of different geometries from DFT calculations

configuration	height [pm]		$E_{\mathrm{ad}}{}^a$ [eV]		ΔQ_{mol} [q]	p_z [D]
	Cu	average				
square	251	255	-3.56	(-3.88)	-0.85	16.9
square on vacancy	261	257	-2.25		-0.59	14.7
cross	322	293	-3.65	(-3.04)	-0.70	26.3
cross partly deprot.	325	295	-3.36		-1.55	22.1
cross fully deprot.	324	299	+0.01		-2.85	16.2

^{a} Values in brackets denote the van der Waals contribution;

electrostatic interaction of the copper core and the polarized carboxylic protons with the bridging oxygen atoms. However, the overall charge distribution of the CuTCPP results in a net repulsive electrostatic force contribution. The entire attractive interaction is caused by van der Waals forces, whose amount is larger than the total adsorption energy E_{ad} and are thus able to compensate for the repulsive part. The cross configurations are centered on a five-fold coordinated titanium atom (see Figs. 4.7b,c). Their carboxylic acid anchors that are on the center titanium row can form covalent bonds to the surface titanium atoms below. The protonated cross shown in Fig. 4.7b is the most stable configuration. Deprotonation of the two presumably bound carboxylic groups does not enhance the binding strength (Fig. 4.7c). At the first glance this is contrary to the common assumption that carboxylic acids tend to deprotonate on titania.[46] Somehow, these reports consider small molecules where the carboxylic acid is actually found to bind preferentially in a bidentate mode. This mode might not be possible for large molecules because of strong van der Waals interaction.[185, 220] These forces promote flat adsorption geometries where the bidentate mode is sterically hindered. Furthermore, it was found by Bates et al. that deprotonation is less favored for monodentate binding modes because of lack of resonance stabilization.[219]

The calculated adsorption energies agree with the AFM results on the fact that both orientations should be present. The stability of the two orientations with respect to tip induced displacement can be explained by the nature of the molecule-surface interaction. The crosses can have covalent bonds and are therefore statistically less mobile than the squares that are mainly bound by van der Waals forces. The influence of the adsorption geometry on the electronic properties of the interface was assessed by calculating the interface dipole moment normal vector to the surface p_z and the charge transfer from the molecule to the surface ΔQ_{mol} (Tab. 4.1). The latter is given by the difference of the molecular charge of the free molecule, which includes charging due to possible deprotonation, and the adsorbed molecule. For all the considered geometries charge is transferred to the substrate upon adsorption. The interface has thus a dipole moment, which points away from the surface. This is consistent with the presented KPFM measurements.
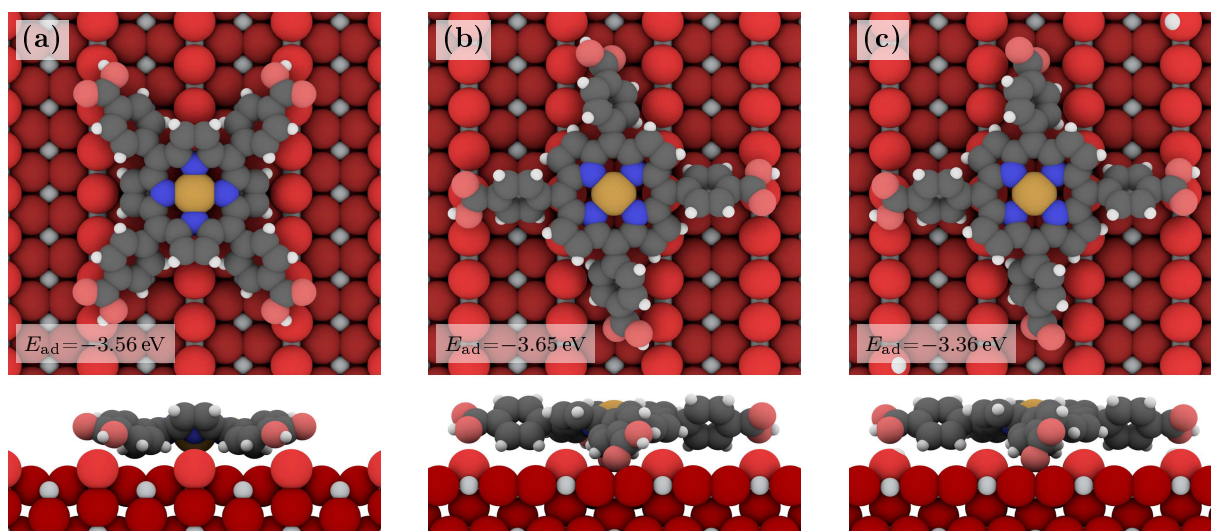
Figure 4.7.: Top and side views of the relaxed CuTCPP adsorption geometries from the DFT calculations that fit best with the nc-AFM images. **(a)** Square configuration, **(b)** fully protonated cross configuration and **(c)** partly deprotonated cross on pristine TiO$_2$. For the latter the released protons were put on bridging oxygen atoms (see top right and bottom left corners of the figure).

The calculated dipoles indicate that the cross configurations should have an even lower LCPD than the square configurations. Somehow, this difference was not detected in the KPFM images. These measurements were performed with a platinum coated silicon tip with a rather large tip apex, meaning the radius of tip curvature was larger than 15 nm, and an oscillation amplitude of 3 nm. Therefore, the experimental values were subject to considerable averaging by the tip shape but also by the oscillation amplitude.[116,221,222] This limited the sensibility for short-range electrostatic forces, and thus possibly prevented to resolve the expected LCPD difference between the two configurations. Nevertheless, FM-KPFM gives qualitative information about the surface dipole. It is expected that the resolution of FM-KPFM might be improved in future work by choosing sharper tips and smaller oscillation amplitudes.[116]

4.2.5. Conclusion

Individual adsorption geometries of CuTCPP on rutile TiO$_2$ (110) have been determined using room temperature nc-AFM operated at the second flexural resonance of the cantilever. The topography images revealed two configurations that were differently oriented with respect to the bridging oxygen rows. Further characterization of individual configurations was achieved by KPFM. The LCPD was decreased on the porphyrins and indicated that there was a charge transfer to the surface upon adsorption, which lead to an interfacial dipole moment. Atomic models of the adsorption geometries with different protonation states were inspired by the nc-AFM results and used as input for DFT calculations. Three out of five of the relaxed structures were in good

agreement with the experimental findings meaning their calculated properties, i.e. adsorption energy, height and dipole moment coincided. These experiments show that nc-AFM and KPFM are able to give highly accurate information about molecular adsorption, which is valuable for the application of such functionalized surfaces in applications like DSCs. For example the dipole moment pointing away from the surface might affect electron transfer of excited charge carriers over the interface. It is emphasized that these findings can be deduced from the experimental results alone. The study of individual molecular adsorption modes at room temperature is feasible by AFM and KPFM. This approach is promising to contribute to a deeper understanding of functionalized surfaces.

4.3. Anchoring of tr-ZnDCPP on Rutile TiO$_2$ (110)

The results from the measurements on CuTCPP suggested that the molecules undergo a rotation under annealing, which allows the covalent anchoring of two of the carboxyl groups to the surface. However, the previous DFT calculations indicated that the cross configuration with protonated anchors would also be stable. Inspired by these results, a combined SPM-PES experiment was conducted that focused on the investigation of this potential anchoring process. Since CuTCPP owns four carboxylic groups it is not an easy task to elucidate the role of the two remaining carboxyl groups on the adsorption mode. Therefore, tr-ZnDCPP was studied instead, which contains two carboxylic anchors located on opposite phenyl groups. In the protonated form, tr-ZnDCPP was supposed to adopt the same square configuration as CuTCPP and was expected to undergo a rotation if deprotonated.

The experiments were performed at the PEARL beamline of the Paul Scherrer Institute. Low temperature STM was used in order to investigate the adsorption configurations as well as their dependence on the sample temperature during evaporation or annealing. As indicated by previous KPFM measurements, the molecule might couple electronically to the surface. Thus their molecular orbitals can be affected by the binding or the adsorption geometry. XPS and VBS were applied to get more insight to the porphyrin-substrate coupling. These experiments further enabled to investigate surface reactions like the anchoring process or the possible removal of the metal core, which could also play a role for the chosen system.[223]

4.3.1. Immobilization of Porphyrins by Annealing

Preparatory examinations for the STM and PES study were made using nc-AFM. AFM measurements were directly made after deposition of tr-ZnDCPP to the freshly prepared rutile TiO$_2$ (110) surface held at room temperature. The topography images in Fig. 4.8a show many noise lines, which indicate weakly bound molecules that were displaced via interaction with the tip while scanning.[62, 215] Only few stable molecules were observed that appeared as bright dots with diameter of about 2 nm. They were mainly found on the terraces. Hardly any molecules adsorbed
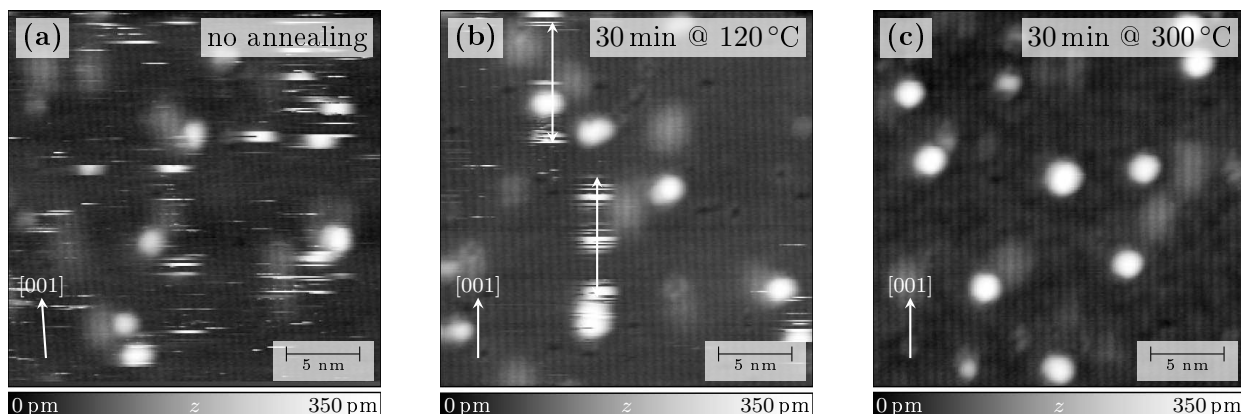
Figure 4.8.: Nc-AFM images of tr-ZnDCPP on rutile TiO$_2$ (110). **(a)** Directly after deposition to the sample held at room temperature. **(b)** After 30 min annealing at 120 °C and **(c)** further annealing for 30 min at 300 °C (PPP-NCL, f_1=156.7 kHz, A_1=10 nm, Δf_1=−4 Hz, Q_1=29.9 k).

on the step edges thus implying that the molecules had limited mobility and stayed close to their arrival sites. Hence it can be distinguished between two species of molecules one that was weakly bound and can be manipulated with the tip and the other that was stable and potentially anchored on the surface. The sample was then annealed to 120 °C for 30 min, in order to improve the scan stability. As shown in Fig. 4.8b the number of noise lines significantly decreased. From this image it can be seen that the tip induced displacements were preferentially along the [001] direction, as was also observed for CuTCPP before (Sec. 4.2.2). Further annealing to 300 °C for 30 min led to scans without noise lines meaning that all molecules were now strongly bound to the surface.

For comparison, nc-AFM topography images obtained for ZnTPP were generally fuzzy and there was no improvement of the scan condition upon annealing, meaning the annealing did not anchor the ZnTPP (see Sec. 4.4.2). In contrary, the formation of islands was observed for higher coverages, which indicates that the mobility of the molecules is increased. Thus it is evident that the diffusion barrier of tr-ZnDCPP is already increased by the carboxyl anchors. In fact, the initial adsorption configuration of tr-ZnDCPP after deposition is supposed to be stabilized by hydrogen bonds. Hence it becomes obvious that there has to be an even stronger type of molecule-surface interaction to facilitate the immobilization. Therefore, these AFM results support the hypothesis of covalent bond formation under annealing.

4.3.2. STM Investigation of Adsorption Modes

LT-STM was used to determine the adsorption modes before and after annealing. Deposition of tr-ZnDCPP to the sample held at low temperature (77 K) and subsequent transfer to the STM led to one single molecular orientation (Fig. 4.9a). The row structure of the surface was clearly resolved.
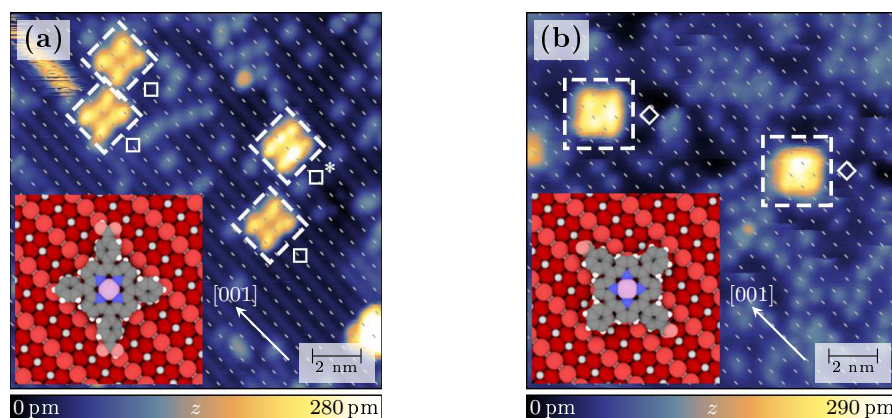
Figure 4.9.: Constant current STM images of tr-ZnDCPP on rutile TiO$_2$ (110). **(a)** After evaporation to the cold surface. The molecule denoted by □* indicates a porphyrin with brighter contrast, which is interacting with a subjacent defect (V_s=1.5 V, I_t=15 pA). **(b)** After annealing to 300 °C (V_s=2.0 V, I_t=10 pA). The image has an inverted STM contrast on TiO$_2$. Bridging oxygen rows are marked with dashed lines. The insets show the proposed models for the corresponding adsorption configuration.

Oxygen rows were imaged in dark and were partially decorated with hydrogen adatoms. The bright rows correspond to the titanium atoms. This is the generally expected imaging contrast for empty state imaging in STM ($V_s > 0$).[224] The center of the porphyrins was situated on the oxygen rows and the axis of the carboxyphenyl groups had a 45° angle with respect to these rows. This orientation allows for stabilization of the molecules by direct interaction, presumably hydrogen bonds, of the anchors with the bridging oxygen atoms. A proposed binding configuration is shown in the inset of Fig. 4.9a. In agreement with the AFM results, the STM scans sometimes revealed moving porphyrins along the [001] direction, implying that this particular adsorption mode was weakly bound. As is indicated in Fig. 4.9a, not all porphyrins showed the same contrast, which was most probably due to interaction with subjacent defects.[89,225]

An important change of molecular orientation was observed after heating the as deposited porphyrins to 300 °C for 30 min. The molecules remained on the terraces and were now all turned by 45° (Fig. 4.9b). The surface exhibited more hydrogen adsorbates after annealing. A part of the hydrogen atoms is supposed to originate from the deprotonation of the porphyrins while another part is known to come from the exposure to residual water in the preparation chamber during annealing. Despite the adsorbates, the molecules were still lying flat on the surface. Close inspection of Fig. 4.9b revealed that the STM imaging contrast on the sample was inverted. The hydrogen adsorbates were now on the bright rows. It is assumed that this contrast inversion is due to a tip change, which happened during in situ tip preparation on the surface. The assignment of the surface atoms is still unambiguous since the normal STM contrast was also observed on the same sample but with lower resolution on the molecules. A similar observation on bare rutile
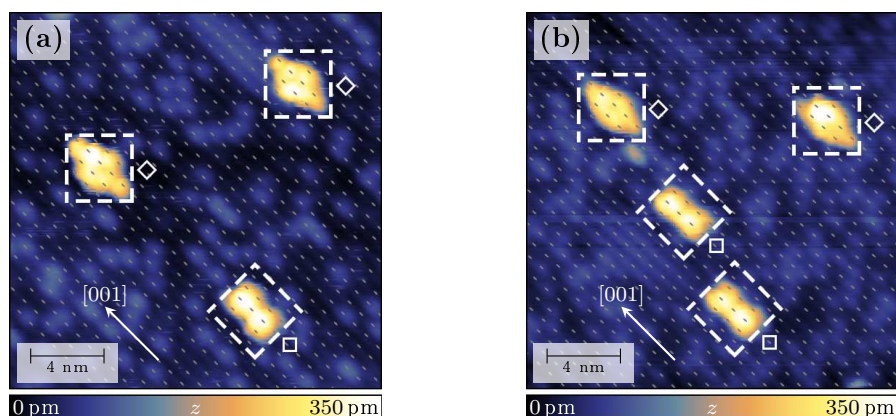
Figure 4.10.: Constant current STM images of ZnTPP on rutile TiO$_2$ (110). **(a)** After evaporation to the cold substrate (V_s=1.8 V, I_t=20 pA). **(b)** After 30 min annealing to 250 °C (V_s=1.8 V, I_t=10 pA). Bridging oxygen rows are marked with dashed lines.

(110) has been made for example by Diebold.[224] Considering the contrast inversion it was found that the center of the porphyrins was now shifted to a titanium row. In this configuration the carboxyl groups can easily anchor to five-fold titanium atoms. A suggestive model of the adsorption configuration is depicted in the inset of Fig. 4.9b. In order to justify the conclusions made for tr-ZnDCPP, the same LT-STM experiment was repeated for ZnTPP, which is exactly the same molecule as tr-ZnDCPP but without carboxylic anchors. After evaporation, the molecules were found in two distinct adsorption modes, which had the same orientation and binding sites as the ones described previously for tr-ZnDCPP (see Fig. 4.10a). The molecules looked slightly distorted along the [001] direction. Nevertheless, the two orientations could be clearly distinguished. The ratio of the two configurations was estimated from a set of 50 molecules and was approximately 1:1. Again an inverted STM contrast was observed on the substrate. Upon annealing to 250 °C the STM images still revealed these two orientations as shown in Fig. 4.10b. The temperature setpoint was chosen to be lower in this case because the evaporation temperature of ZnTPP is below 300 °C. The ratio of the two configurations was slightly changed to 4:3 in favor of the cross after annealing. However, this finding was most probably not linked to a conversion of the geometries but due to evaporation of the less interacting squares as will be justified later by the PES measurements. The STM results suggest that only tr-ZnDCPP rotates under annealing. This is a strong evidence that the carboxylic anchors are involved in the rotation and that they react with the surface.

4.3.3. XPS Investigation

In order to correlate the adsorption configuration with the molecule properties, PES measurements were conducted on the just deposited submonolayer (LC, for low coverage), the annealed
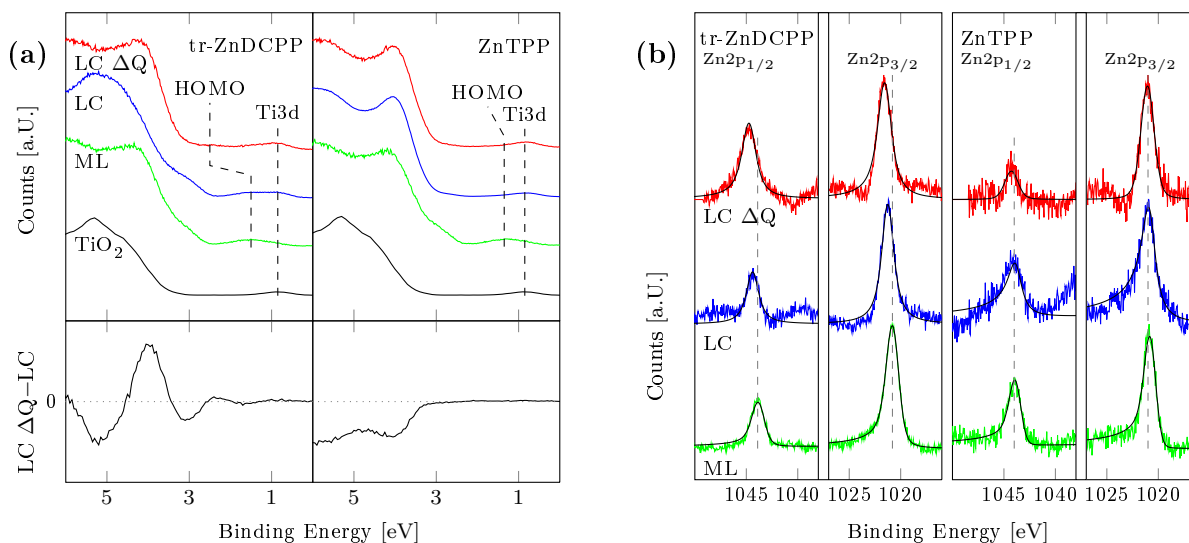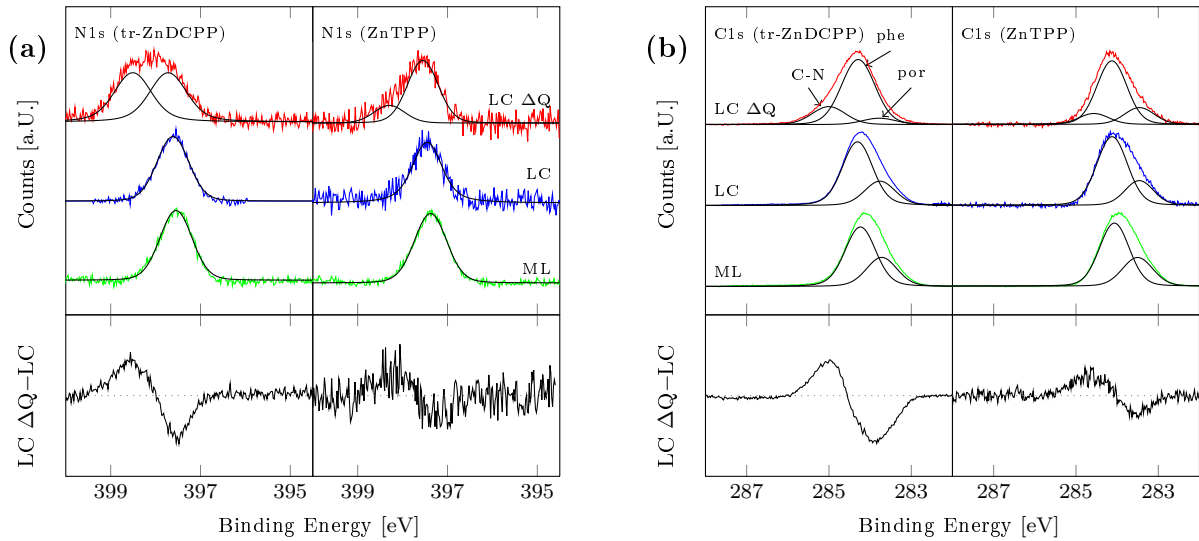
Figure 4.11.: VBS and XPS spectra of tr-ZnDCPP and ZnTPP on rutile TiO$_2$ (110) for submonolayer coverage after deposition (LC), after annealing (LC ΔQ) and multilayer (ML) coverage. **(a)** Valence band spectra obtained with a photon energy of $h\nu$=65 eV. **(b)** XPS of the Zn2p core level obtained with a photon energy of $h\nu$=1253 eV. The dashed lines indicate the position of the highest occupied molecular orbitals. The graphs at the bottom show the changes after annealing.

submonolayer (LC ΔQ) and on freshly deposited multilayers (ML). The multilayer measurements were performed to get the reference data of the porphyrins without surface interaction. Characterization of the bare substrate was performed too. These spectra are given in the appendix (see Sec. B). The spectra were fitted with Unifit using Voigt functions, which are a convolution of the natural line shape, given by a Lorentz profile, and the analyzer response function described by a Gaussian peak. The peak width of a certain core level was fixed to be the same for all the fits of a particular core level.

The valence band spectra are shown in Fig. 4.11a. Due to molecule induced work function shifts, they were aligned with respect to the known Ti3d defect state of the substrate, which is at 0.87 eV.[165, 181] The highest occupied molecular orbitals (HOMOs) are marked in the spectra and the extracted binding energies (BE) are given in Tab. 4.2. The HOMO is in particular important for the optical transitions in the molecule. Shifts of the HOMO are commonly linked to changes of the absorption wavelength. The HOMOs of the multilayer were at binding energies of 1.50 eV and 1.29 eV for tr-ZnDCPP and ZnTPP, respectively. In the LC spectra, these levels were hardly shifted and overlapped partially with the Ti3d defect state of the titania surface. The HOMO of tr-ZnDCPP shifted upon annealing as is indicated in the difference spectrum in Fig. 4.11a. The positive shift of the HOMO after annealing was attributed to positive charging of the molecule.[225] For ZnTPP, the HOMO intensity was rather low, making it hard to correctly identify the HOMO

Table 4.2.: PES binding energies of Zn2p and N1s levels as well as the highest occupied molecular orbitals.

		HOMO [eV]	Zn2p$_{1/2}$ [eV]	Zn2p$_{3/2}$ [eV]	N1s [eV]	
ZnDCPP	ML	1.50	1043.9	1020.8	397.5	-
	LC	1.51	1044.3	1021.2	397.6	-
	LC ΔQ	2.42	1044.8	1021.6	397.7	398.5
ZnTPP	ML	1.29	1044.0	1020.9	397.4	-
	LC	1.37	1044.1	1021.0	397.5	-
	LC ΔQ	1.41	1044.2	1021.0	397.5	398.3

position. However, the comparison of the complete valence band spectra as well as the difference spectrum in Fig. 4.11a suggested that there is no further shift after heating. The main change was a loss of ca. 20 % in signal intensity that was caused by re-evaporation of the porphyrins.

The BE of the Zn2p levels for the two porphyrins are given in Tab. 4.2 and the spectra are depicted in Fig. 4.11b. For both porphyrins the Zn2p peak of the low coverage was shifted to higher binding energies compared to the multilayer spectrum, as indicated by the dashed lines in Fig. 4.11b. This suggested partial charging due to coupling with the surface. For tr-ZnDCPP this effect amounted to 0.4 eV whereas it was 0.1 eV for ZnTPP. Since the Zn2p peak is expected to shift to lower binding energies by about 1.0 eV in case of demetalation, it was concluded that the molecules keep their metal cores.[223] The position of the tr-ZnDCPP Zn2p peak was further shifted by about 0.4 eV after annealing, which was attributed to additional charging of the core. This shift was not observed for ZnTPP.

Complementary information about the coupling of the porphyrin core with the substrate was gathered from the spectra of the N1s core level, which are depicted in Fig. 4.12a. The peaks of the N1s levels for the ML and LC coverage of the porphyrins were at the same position and were fitted with single peaks (see Tab. 4.2). The signal for the annealed porphyrins was split up in two components for both cases, resulting in a broadened or an asymmetric curve for tr-ZnDCPP and ZnTPP, respectively. The energy difference between these two peaks was 0.8 eV. The N1s spectrum of the annealed tr-ZnDCPP was fitted with two peaks of equal amplitude. Since there was one dominant adsorption configuration, the results suggested that the nitrogen atoms of tr-ZnDCPP were no longer indistinguishable after annealing. This could be an evidence for distortion of the porphyrin macrocycle, which might be due to stronger electrostatic interaction induced by the observed charging.

The tr-ZnDCPP spectrum gave evidence that the second peak in the ZnTPP N1s spectrum is related to the orientation of the molecules. However, the rotation alone does not suffice for explanation. From the STM experiments it was known that both orientations were already present for the just deposited ZnTPP. Nevertheless, the second N1s did not show up before annealing.

Figure 4.12.: XPS spectra of tr-ZnDCPP and ZnTPP on rutile TiO$_2$ (110) for submonolayer coverage after deposition (LC), after annealing (LC ΔQ) and multilayer (ML) coverage. **(a)** N1s spectra obtained with a photon energy of $h\nu$ =500 eV. **(b)** C1s spectra obtained with a photon energy of $h\nu$ =340 eV. The bottom graphs show the changes after annealing.

Since the ratio of the two modes did hardly change during annealing, it was concluded that the porphyrin has to be annealed and in the cross orientation in order to show a splitting of the N1s core level. Thus the correct orientation of the porphyrin core was a prerequisite for the increased interaction with the substrate, which was thermally activated. Since the two orientations differed in interaction strength, it was further concluded that the square mode was preferably re-evaporated during annealing, therefore explaining the altered ratio of the two configurations. The shapes of the C1s spectra were in good agreement with these observations. The spectra of the LC porphyrins show an asymmetry and were fitted with two peaks (see Fig. 4.12b). One for the phenyl (phe) contributions and one for the carbons of the delocalized porphyrin core (por).[226] After annealing there was another contribution at a BE of 285 eV, which was at the cost of the porphyrin core peak.[226] This peak corresponds to C-N bonds and appeared most probably due to the splitting of the N1s peak as described before.

4.3.4. Conclusion

The anchoring process of tr-ZnDCPP on rutile TiO$_2$ (110) was observed by means of low temperature STM. The formation of covalent bonds to the surface was induced by annealing of the evaporated porphyrins. The initially H-bond stabilized molecules were deprotonated and formed bonds to five-fold titanium atoms of the surface. This process was coupled to a rotation of the molecules. The interpretation of this experiment was corroborated by the study of ZnTPP, which was not able to form chemical bonds and showed no significant change upon annealing. Further

evidence for the immobilization of tr-ZnDCPP was given by nc-AFM at room temperature, where the stability against manipulation with the scanning tip was assessed. The coupling with the substrate was investigated using valence band spectroscopy and showed that charge transfer to the substrate was increased if the molecule was anchored by a carboxylic acid. XPS of the N1s core level further suggested that the structure of the macrocycle of annealed porphyrins in the cross configuration might be significantly deformed due to the increased interaction with the surface. It is further noted that the presented results are in good correspondence with results from KPFM and DFT on CuTCPP on rutile TiO_2 (110) presented in the previous section.

4.4. ZnCPPs on Rutile: Influence of the Carboxylic Anchor

Carboxylic anchors were shown to bind covalently on the rutile TiO_2 (110) surface, whereby the formation of the bond is a thermally activated process. Employing different porphyrins with different number and configuration of carboxylic anchoring groups is thus supposed to yield various adsorption geometries, which might differ in their properties. As a model system, 4 different ZnCPPs were studied in this work. The findings of this study will be discussed in the following and highlight the importance of the anchoring group for molecular immobilization. The section closes with high resolution nc-AFM experiments that aimed to identify the functional groups of adsorbed molecules.

The first study started with the investigation of ZnTCPP. The porphyrin was evaporated to the surface at T_s=25 °C and yielded noisy AFM topography images. The scan stability was significantly improved after annealing to only 150° for 30 min. Apparently a lower temperature
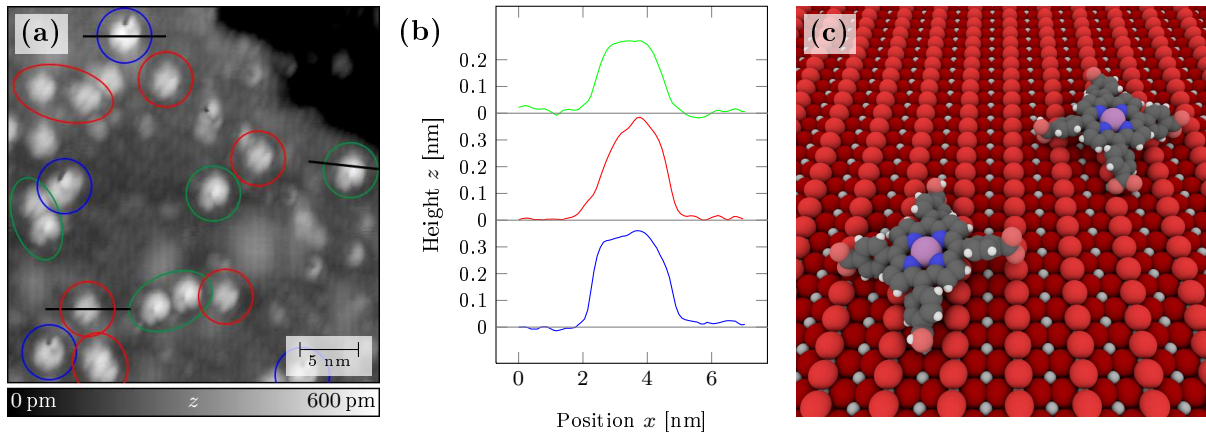
Figure 4.13.: ZnTCPP on rutile TiO_2 (110). **(a)** Nc-AFM topography after annealing to 150 °C. Different adsorption modes are marked with circles (SSS-NCL, f_1=151.3 kHz, A_1=10 nm, Δf_1=−7 Hz, Q_1=33.1 k). **(b)** Height profiles of the 3 modes identified in (a). **(c)** Proposed asymmetric binding modes resulting from anchoring to oxygen vacancies.

compared to tr-ZnDCPP is sufficient because the porphyrins owns 4 carboxylic groups and only one group has to be deprotonated to yield an immobilized molecule. A large scale nc-AFM topography of the annealed substrate is shown in Fig. 4.13a. At least three adsorption configurations were distinguished, which are marked with circles. Considering the height profiles depicted in Fig. 4.13b, it is probable that some of them are tilted. The well-known cross and square configurations were also identified. However, square configurations were hardly observable, indicating that at least one carboxylic acid was deprotonated for each molecule. Compared to the results of CuTCPP in Sec. 4.2, the surface showed more defects, the coverage was higher and the molecules were annealed in this experiment. Justified by the deprotonation of the anchors and the probable interaction with defects, it is thus plausible that several adsorption modes are observed. Two proposed modes that could result from binding of the anchor to an oxygen vacancy are shown in Fig. 4.13c.

Looking at porphyrins with different numbers of carboxylic anchors, such as ZnMCPP and cis-ZnDCPP, it was observed that they behaved similarly. The porphyrins tended to adopt orientations that were well aligned with the substrate. The interaction of the porphyrins with the rutile surface was rather strong meaning that the molecules were immobilized at room temperature. Still protonated molecules could however be moved by the scanning tip. The stability of the molecules with respect to tip induced movements might depend on the number of carboxyl groups since they are supposed to stabilize the square configuration by H-bonds to the bridging oxygen rows. For molecules that were annealed after deposition or evaporated to the hot substrate one can hardly find any moving molecules, which indicated that porphyrins are then covalently bound to the surface.

Even though most experiments were performed using low coverage ($\ll 1\,\mathrm{ML}$) the results have implications for the formation of self-assemblies. Due to the low mobility of the as deposited molecules they are not favored and also not observed for higher coverages. Mild annealing after deposition to the cold surface was not suitable to form self-assemblies because this enhances the reactivity of the anchors as well. But even if a temperature could be found up to which the mobility is increased without deprotonation, the defects of the surface would most probably hinder the formation of SAMs or at least limit them to smaller islands. Thus self-assemblies of porphyrins where the number of carboxylic anchors determines the structure of the SAM, like e.g. found on copper, where clusters of two or four molecules or rows and complete layers were found, could not be observed.[13, 19] Consequently, it has to be noted that if a functional group of the molecule is designed to yield a certain architecture of self-assemblies it is beneficial when this group does only hardly interact with the surface. Due to the strong interaction with the surface it is assumed that the structure of monolayers is templated by the substrate and would thus preferably lead to flat lying adsorption geometries. However, the study of high coverage films without annealing was beyond the scope of this work, since the scan conditions for such samples were generally quite unstable.
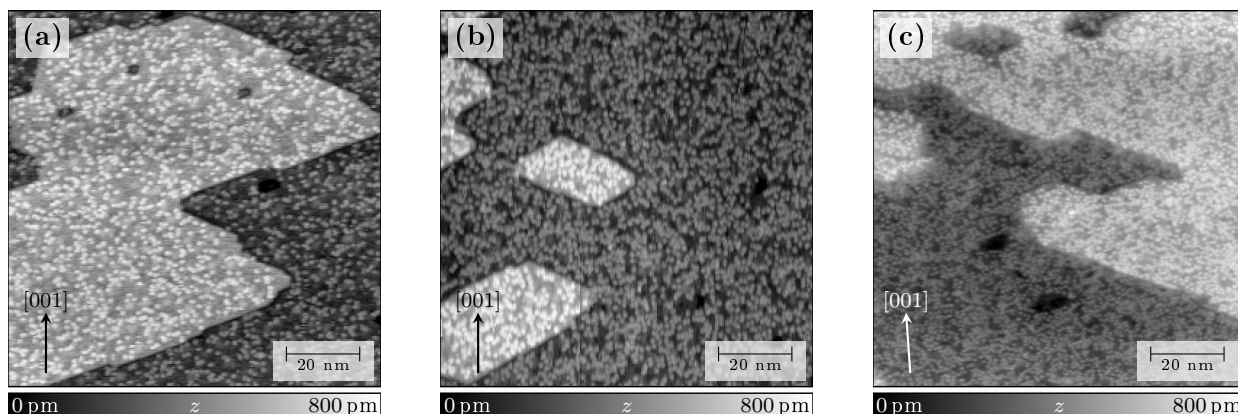
Figure 4.14.: Evaporation of ZnMCPP to the hot substrate (300 °C). Nc-AFM topography images were taken at room temperature after **(a)** 15 min, **(b)** 40 min and **(c)** 2 h of annealing. (PPP-NCH, f_1=327.9 kHz, A_1=5 nm, Q_1=37.4 k, Δf_1=−10 Hz for (a) and (b) and Δf_1=−30 Hz for (c))

4.4.1. Preparation of High Coverage Films

Another indication that the porphyrin interact strongly with the rutile TiO_2 (110) surface gets evident when one tries to form self-assembled monolayers with standing adsorption modes. They would be beneficial for the applications since the porphyrin core is less affected by the substrate then. A possible approach from Patthey et al. was to heat the substrate to the evaporation temperature of the molecule during deposition.[227] This is supposed to prevent the formation of multilayers and may further promote the lift off of the porphyrin core, thus allowing for standing configurations if the coverage is high enough. In the present work, this approach was tried for ZnMCPP, which has only one anchor group and may stand up even after chemical binding to the surface. The porphyrin was evaporated at 300 °C to the substrate having the same temperature. The images shown in Fig. 4.14 indicated disordered coverage of isolated porphyrins. From the scan stability it was concluded that the porphyrins were covalently bonded after cooling-down. The coverage was then increased stepwise. However this did not promote the formation of self-assemblies. Most probably the porphyrins were directly bonded after arrival to the surface. Furthermore, it is likely that the molecules did not get enough energy to lift the porphyrin core away from the surface to facilitate standing adsorption modes. Doing the evaporation before the annealing did not change the structure of the resulting layers too. In conclusion it has to be expected that the first layer of molecules will most likely adopt a flat adsorption geometry, while additional layers might yield standing configurations because the strong interaction with the substrate is no longer present.

81
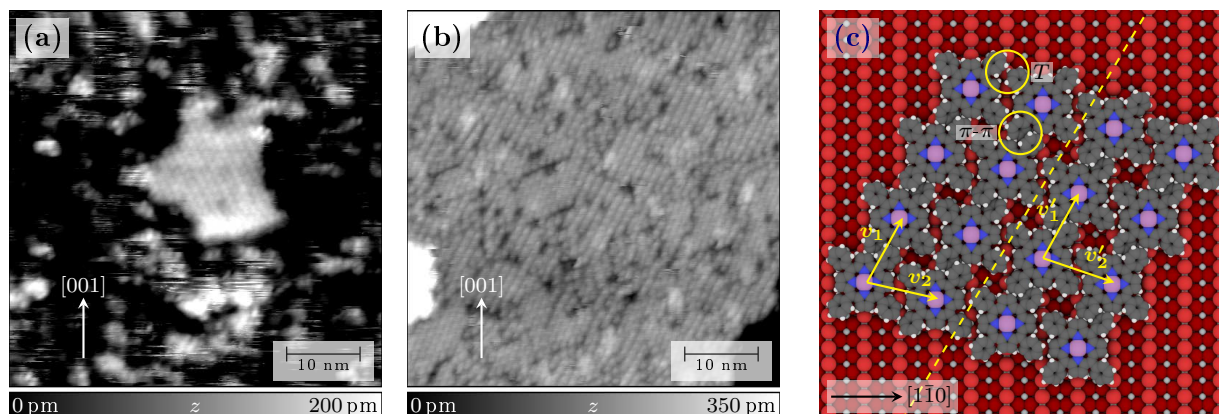
Figure 4.15.: ZnTPP on rutile TiO$_2$ (110). **(a)** Nc-AFM topography of a ZnTPP island after annealing to 120 °C (PPP-NCL, f_2=978.5 kHz, A_2=400 pm, Δf_2=−30 Hz, Q_2=13.5 k). The z-range was reduced to increase the contrast on the island. **(b)** Self-assembled monolayer of ZnTPP without annealing (same imaging parameters as in (a) except Δf_2=−105 Hz). **(c)** Suggested molecular model of the monolayer. The left part shows a close packing with an angle of 12° between v_2 and the [1$\bar{1}$0] direction. The molecular chains on the right are slightly shifted with respect to the [001] direction yielding an angle of 20°.

4.4.2. Molecular Islands of ZnTPP

The importance of the carboxylic anchor for the stabilization of the adsorption geometries gets even more apparent if one compares the results of the ZnCPPs with ZnTPP. Nc-AFM topography images of ZnTPP, which was evaporated to the sample at room temperature, were generally very noisy, indicating moving molecules. Stable high resolution imaging of isolated molecules was not achieved. Post-annealing of the samples at 120 °C for 30 min did hardly improve the imaging conditions but some regions exhibited small islands (Fig. 4.15a). Thus the higher mobility of ZnTPP allowed for self-assemblies also at lower coverages. The sample was further annealed overnight at 120 °C in order to promote the formation of larger islands. However, the size of the islands remained unchanged and the scans were still noisy outside the islands. A possible explanation for this observation could be the defect density of the surface, which might affected the mobility of the porphyrins and thus influenced the island formation. Maybe a certain size of defect free surface was even needed to start the growth of the islands. The molecules in the island were aligned within rows (see Fig. 4.15a). The lattice vectors of the resulting pattern have angles of about 25° and 80° with respect to the bridging oxygen rows. Scans on close to monolayer coverage samples allowed investigating the structure of these assemblies in more detail. As shown in Fig. 4.15b the main structure in the layer were chains that were oriented with an angle of 28° with respect to the [001] direction. The second lattice vector was not fixed. However, the predominant orientation enclosed an angle of 12° with the [1$\bar{1}$0] direction. The variation of the second lattice vector is explained by the fact that the molecular chains can be slightly shifted

along the [001] direction. A suggested model, showing two possible arrangements of the chains, is depicted in Fig. 4.15c. Both proposed structures are commensurate with the surface and are further stabilized by π-π and T-interactions of the phenyl rings as indicated in Fig. 4.15c.

4.4.3. Conclusion

In summary, ZnCPPs with various number of carboxylic group interact similar with the rutile TiO$_2$ (110) surface. They were immobilized after evaporation if they had at least one carboxylic group. Porphyrins that have been evaporated to the room temperature sample could be moved via interaction with the tip. Annealing of these surfaces resulted in more stable scan conditions because the molecules were covalently bonded. ZnTPP, which has no anchoring group, is presumably weakly bound to the terraces and is easily displaced while scanning. Annealing of a ZnTPP covered surface causes the growth of self-assembled layers but their size might be limited by the density of surface defects.

4.5. The Quest for High Molecular Resolution

So far, high resolution nc-AFM measurements were only made on highly symmetric porphyrins, i.e. with four carboxylic anchors. These measurements do not allow evaluating if functional groups such as the carboxyphenyl legs can be identified. Porphyrins with different substituents, i.e. cis-ZnDCPP and ZnMCPP were thus investigated in the following, in order to see if these functional groups can be visualized by nc-AFM. Bimodal and dual-pass AFM were applied to increase the sensitivity to short-range forces.
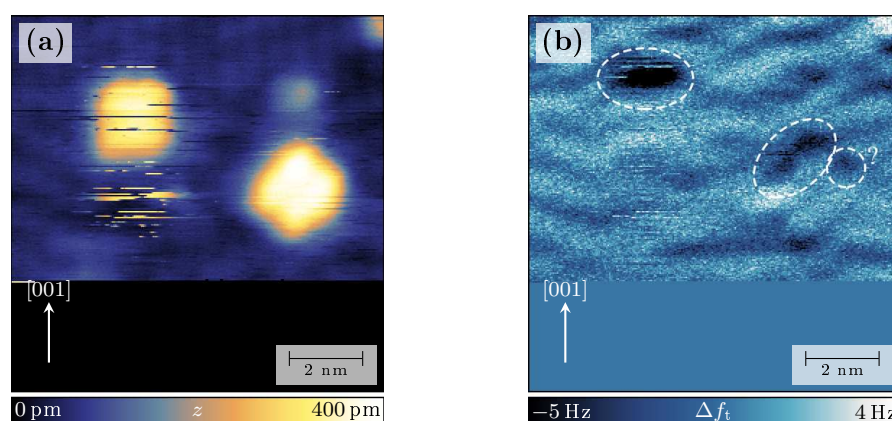
Figure 4.16.: High resolution bimodal nc-AFM of cis-ZnDCPP on rutile TiO$_2$ (110). **(a)** Topography image and **(b)** corresponding frequency shift of the first torsional resonance. The marked dips might be indicative for either phenyl or carboxyphenyl substituents. (SSS-NCL, f_2=944.1 kHz, A_2=400 pm, Δf_2=−15 Hz, Q_2=15.4 k, f_t=1.497 MHz, A_t=50 pm, Q_t=145.8 k)
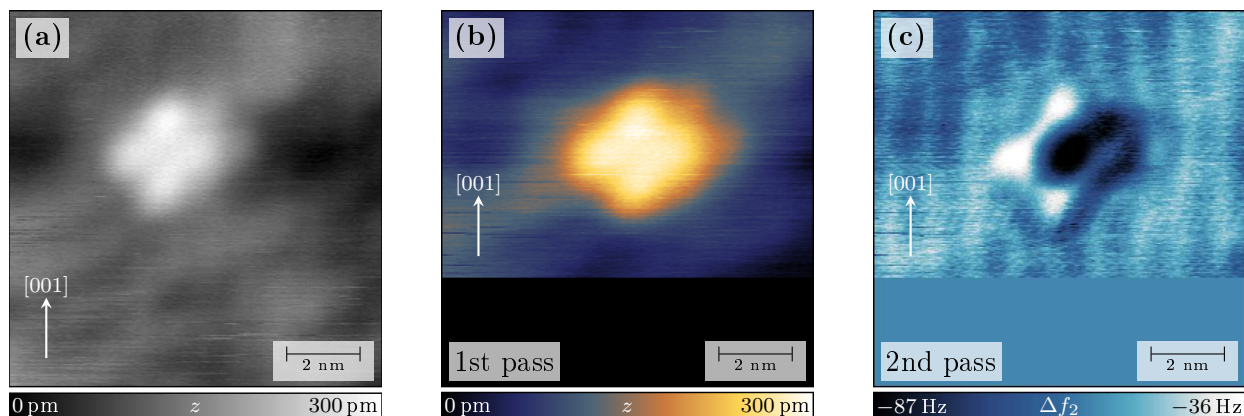
Figure 4.17.: High resolution dual-pass measurements of ZnMCPP on rutile TiO$_2$ (110). **(a)** Standard nc-AFM topography measured using the 2nd resonance (SSS-NCL, f_2=944.1 kHz, A_2=400 pm, Δf_2=-20 Hz, Q_2=15.6 k). **(b)** Topography of the first pass taken with Δf_2=-17 Hz and **(c)** corresponding frequency shift image taken with a z-offset of -300 pm.

Cis-ZnDCPP, which has two carboxyphenyl legs on the same side of the porphyrin macrocycle, was investigated first. Fig. 4.16a shows a topography image with two molecules right after deposition to the room temperature substrate. They adopted the well-known cross and square orientation. Somehow, there is hardly any asymmetry in the topography channel. Single mode AFM, was thus not able to resolve the different substituents. However, the additional use of the torsional resonance as presented in Fig. 4.16b revealed that one side of the molecule showed higher frequency shifts than the other. This could be indicative of either phenyl or carboxyphenyl substituents. However, the interpretation of torsional images is not straightforward. The molecule depicted on the right side of Fig. 4.16b further reveals another small dip. Since all the features are on the top side of the molecules one cannot exclude a tip artifact.

To further elucidate the question of the identification of the carboxyphenyl groups it is worthwhile to take a molecule that is even more asymmetric, like e.g. ZnMCPP. Evaporation to the hot substrate (300°) yielded cross shape molecules where the carboxyl groups were presumably anchored to the titanium rows. Instead of the bimodal AFM, a dual-pass method introduced by O. Custance an co-workers was used (Sec. 2.3.5).[39] In this method the topography of a line is recorded in the first pass and applied to the z-controller in the second pass, whereby an additional negative z-offset is applied. The image is then made by recording the frequency shift. The benefit of this measurement is that feedback problems such as the ones described in Appendix A can be prevented and the imaging can actually be done in the repulsive regime of the $\Delta f(z)$-curve. This measurement is similar to the constant height experiments usually performed at low temperatures. The first pass is done far from the surface so that a part of the information, that could still be achieved by approaching in the classical mode, e.g. the row structure of the substrate, is lost.

Fig. 4.17a shows a standard FM-AFM image of ZnMCPP on rutile TiO$_2$ (110) made by using the 2nd resonance of an SSS-NCL cantilever. Figs. 4.17b,c depict the results of dual-pass experiment made on the same molecule and the same cantilever. There is a clear dip in the frequency shift for one of the lobes, which can possibly be attributed to the carboxyphenyl part of the porphyrin. In order to verify this hypothesis and to get a deeper understanding of the imaging contrast it is suggested to use spectroscopic methods together with simulations. This was however beyond the scope of this work. Nevertheless, the experimental results emphasize the suitability of dual-pass nc-AFM not only for higher resolution but also for possible chemical identification of functional groups.

4.6. Conclusion

This chapter investigated the behavior of metallo-phenylporphyrins on the rutile TiO$_2$ (110) surface. It started with the preparatory examination of the bare substrate, where it was shown that defects can be identified with bimodal nc-AFM using the first torsional resonance. The obtained images were explained with a simple electrostatic model. MCPPs with different number of anchoring groups were studied afterwards. The MCPPs showed strong binding to the surface. Isolated molecules were imaged at room temperature and their adsorption configurations were determined by nc-AFM using the second resonance of the cantilever. In case of CuTCPP, two distinct configurations were found for which the electronic coupling to the surface was further investigated with FM-KPFM. LCPD maps indicated a surface dipole moment due to electron transfer from the molecule to the surface. This was further corroborated in DFT calculations, which were also in good agreement with the adsorption configurations determined by AFM. Generally it was found that MCPPs were immobilized due to the interaction of the carboxylic anchor with the surface. However, this interaction does not have to be covalent. It was found that already the formation of H-bonds between the carboxyl groups and the bridging oxygen atoms strengthened the binding. Therefore, porphyrins without anchoring groups could only be imaged in islands or monolayers, indicating that they were indeed more mobile. Single ZnTPP could only be imaged at low temperatures using LT-STM. The protonated porphyrins can be displaced on the surface by interaction with the tip. Thus scans of just deposited porphyrins were often noisy. However, the scan conditions were improved upon annealing giving evidence that the ZnCPPs can be covalently linked to the surface. This was further investigated using a combined STM and PES approach, where strong evidence was found that the carboxylic anchor deprotonates under annealing and binds to five-fold titanium atoms of the surface. Finally high resolution bimodal as well as dual-pass nc-AFM experiments were performed on selected porphyrins, which indicated that submolecular resolution with possible identification of functional groups might be feasible at room temperature.

5.

ZnCPPs on Anatase TiO$_2$ (101)

This chapter proceeds with the investigation of the known ZnCPPs on the application relevant anatase TiO$_2$ (101) surface. Nc-AFM measurements on the bare anatase substrate are presented in the beginning and are the basis for the following study, because there was much less reference information available than for rutile TiO$_2$ (110). High resolution nc-AFM is presented and two possible contrasts, which reveal different topographic information, are discussed. After this the focus is put on the interaction of ZnCPPs with the surface. The adsorption and diffusion behavior of ZnCPPs with different numbers of carboxylic anchors was investigated and the important influence of the carboxylic acid anchor for the immobilization on the surface is emphasized. Further the formation of covalent bonds to the surfaces was studied using samples where the ZnCPPs have been evaporated to the hot TiO$_2$ substrate. Isolated molecules of these samples were further imaged using high resolution dual-pass nc-AFM on the first and second resonance. These measurements allowed resolving the submolecular structure of ZnMCPP and were used to propose potential adsorption geometries. The chapter closes with bimodal dual-pass nc-AFM on tr-ZnDCPP wherein the torsional resonance was successfully used to resolve the surface and the molecule. The experimental results were compiled into atomic models of the adsorption configuration, which demonstrates the capability of dual-pass nc-AFM for high resolution characterization of single molecules at room-temperature.

5.1. The Anatase TiO$_2$ (101) Surface

Even though anatase is more important for the applications than rutile, which is due to its nanoscale stability, there are only few SPM studies with atomic resolution.[173,174,176,177,228,229] To the knowledge of the author, there are only two studies from the group of Custance et al., which obtained high resolution by AFM. However, in their case they used either a combined nc-AFM/STM approach or the dual-pass AFM measurement method.[39,178] This section attempts to characterize the pristine anatase TiO$_2$ surface on the atomic scale by using standard AFM. The results reveal different imaging contrasts and some of them have atomic resolution. Thus it is shown that atomic resolution on anatase TiO$_2$ is also feasible by standard nc-AFM.
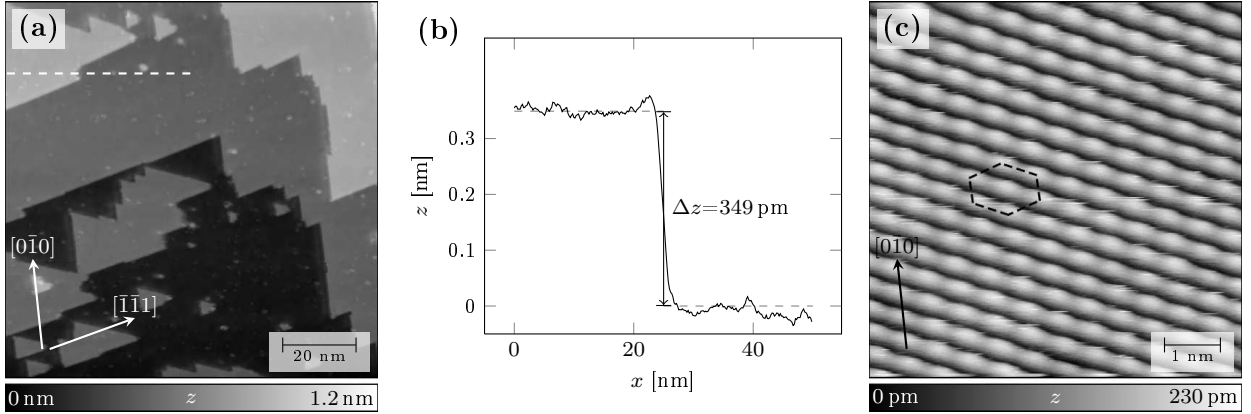
Figure 5.1.: Surface structure of the bulk terminated anatase TiO$_2$ (101) substrate. **(a)** Nc-AFM topography image of the bare substrate scanned with a silicon tip whose apex was most probably terminated with titania (PPP-NCH, f_1=321.7 kHz, A_1=5 nm, Δf_1=−15 Hz, Q_1=36.9 k). **(b)** Profile over the step edge as indicated with the dashed line in (a). **(c)** High resolution nc-AFM topography recorded with a functionalized tip (SSS-NCL, f_2=949.7 kHz, A_2=500 pm, Δf_2=−60 Hz, Q_2=13.3 k).

Natural anatase TiO$_2$ crystals exhibiting their (101) surface were prepared by repeated sputtering and annealing. The surface structure after sample preparation, such as the appearance of the step edges, depended strongly on the quality of the crystal, which is influenced by the amount of natural impurities and the reduction state. Surface preparation was most successful on highly reduced and homogeneous crystals with low impurity density. In these cases the step edges were nicely defined and the terrace size was up to 100 nm (see Fig. 5.1a). The terraces were terminated with step edges along the $\langle 010 \rangle$ and $\langle \bar{1}11 \rangle$ directions.[175] Their height was determined to be 349 ± 10 pm, as indicated in Fig. 5.1b and was in good agreement with the expected value from the bulk crystal structure of 352 pm.[157] Similar to the row structure on rutile TiO$_2$ (110), the anatase TiO$_2$ (101) exhibits a saw-tooth pattern along the [010] direction, that is terminated with two-fold oxygen atoms. High resolution of this surface structure was achieved on samples with adsorbates or defects, because they allowed for beneficial tip functionalization. The pick-up of adsorbates appeared randomly and while scanning. Fig. 5.1c depicts a high resolution scan recorded using the second resonance of a super sharp silicon tip after pick-up of an adsorbate. In this case the sample had a low coverage of tr-ZnDCPP and the tip possibly picked up one of them. The scan showed a characteristic hexagonal structure, which was attributed to the topmost two-fold oxygen atoms.[178] In accordance to literature, the distance between the rows was measured to be about 520 pm. The surface exhibited significantly less defects than rutile TiO$_2$ (110), as was already observed earlier and justified by the fact that oxygen vacancies in anatase occur preferably at subsurface sites.[176,230,231]
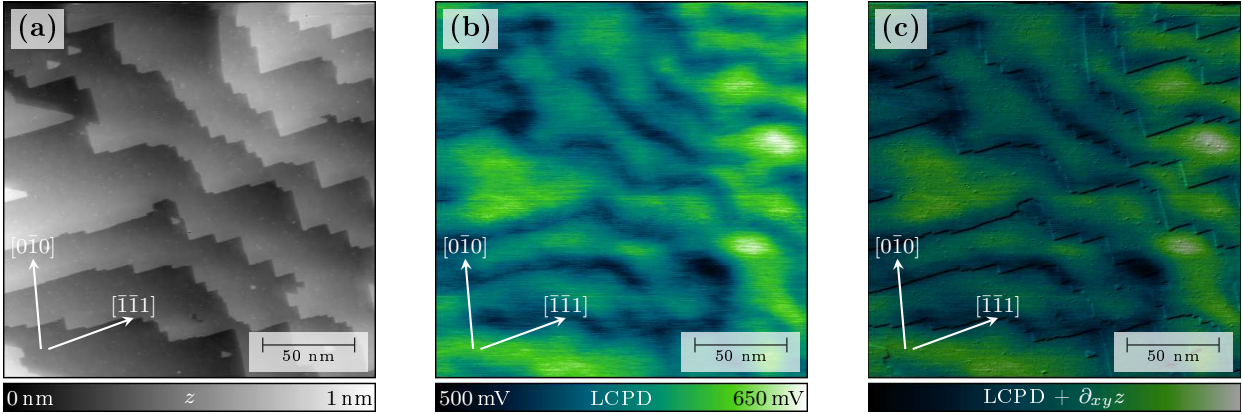
Figure 5.2.: KPFM of the bare anatase TiO$_2$ (101) surface. **(a)** Large scale topography image and **(b)** corresponding LCPD map (PPP-NCL Pt, f_1=169.4 kHz, A_1=10 nm, Δf_1=−20 Hz, Q_1=19.2 k, f_{mod}=1.0 kHz, V_{mod}=500 mV). **(c)** Differentiated topography overlaid with the LCPD map highlighting the lower work-function on the step edges.

Fig. 5.2 shows a large scale AFM topography and the corresponding contact potential difference map. The LCPD on the surface was in the range of 550–600 mV and step edges had a work function that was reduced by ca. 50–100 mV. As has been shown on other substrates, the work function depends on the exposed face.[232, 233] Since the (101) surface is the most stable termination of anatase, it has been found that its conduction band minimum is lower in energy than for the other faces.[234] Consequently, its work function is higher than for the microfacets at the step edges, explaining the experimental CPD contrast.

Similar to rutile, different high resolution imaging contrasts were observed on anatase (101) as well. Interestingly, in one case the topography contrast was also altered on the large scale as shown in Fig. 5.3a. Some of the step edges, such as the one marked in violet, appeared higher than the others. The tip oscillation also showed a clear position dependent dissipation signal (see Fig. 5.3b). Astonishingly, the tip change that led to this contrast was reversible. Switching between the normal contrast shown in Fig. 5.1a and the high resolution contrast was observed several times. Since the surface had a low amount of adsorbates it is obvious that the changes in topography and dissipation were caused by the pick-up of an adsorbate. An artifact originating from a slow z-controller feedback was excluded by comparing forward and backward scans. This assumption was further legitimated by results from Loppacher et al. where dissipation on step edges was observed after a tip crash and suggested to originate from an adsorbate that jumps back and forth when the tip enters the strong force field of the step edges.[237] The interaction at the step was presumably stronger, since the electrostatic forces were only compensated on the terraces. The discrimination of the two marked step edges along the same direction in Fig. 5.3a can then be explained by the asymmetry of the surface as described in Sec. 3.1.2. The local electrostatic field
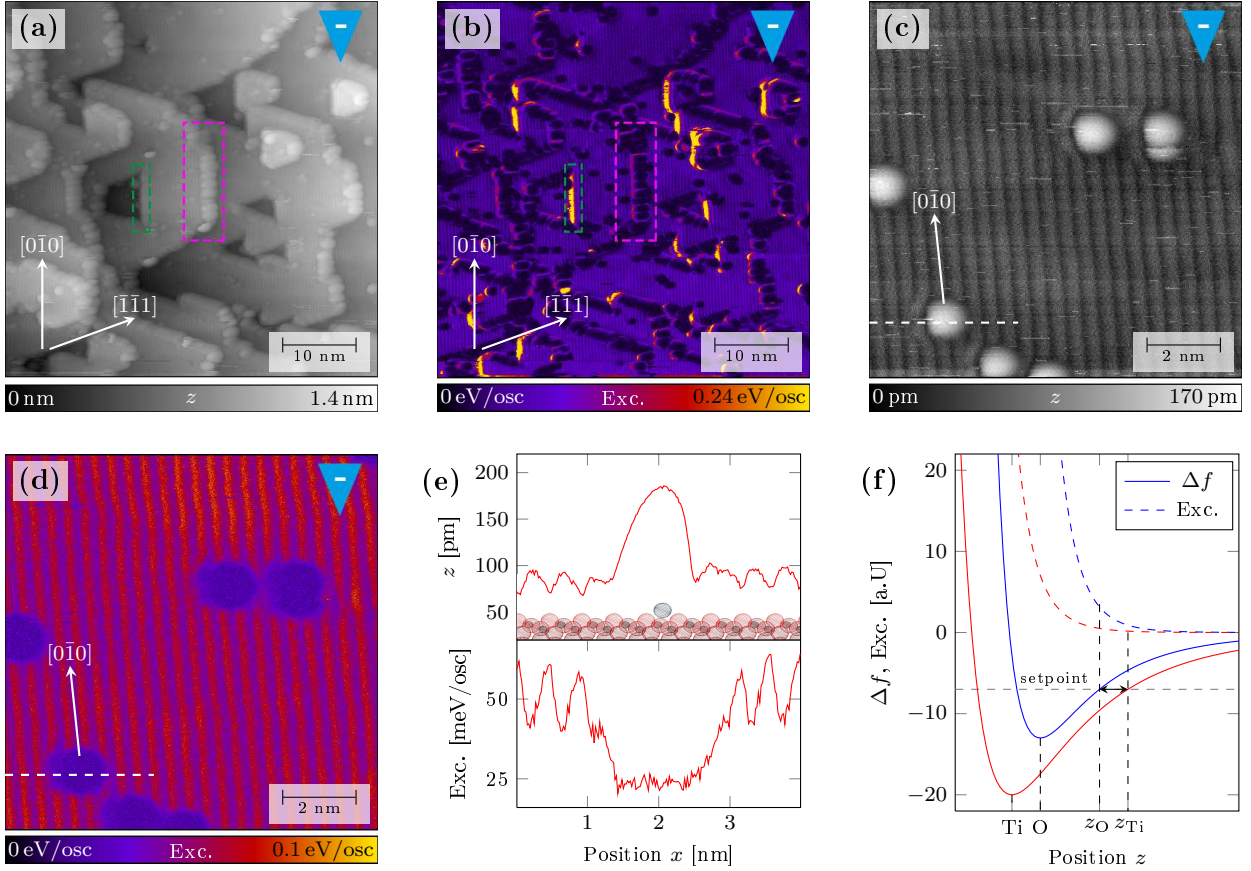
Figure 5.3.: High resolution nc-AFM contrast on anatase TiO$_2$ (101) obtained with a negatively polarized tip (PPP-NCH, f_1=324.5 kHz, A_1=5 nm, Q_1=37.4 k). **(a,b)** Large scale topography scan and corresponding dissipation map as calculated after [235, 236] (Δf_1=−25 Hz). **(c,d)** Small scale scans of the saw-tooth structure with the corresponding dissipation map. (Δf_1=−14 Hz). **(e)** Topography and excitation profiles over a defect as indicated in (c) and (d). **(f)** Qualitative explanation of the contrast formation by $\Delta f(z)$-curves.

and thus the strength of the dissipation on the individual edges might be affected by the different work function as well as the area of the exposed microfacets. Both were presumably larger on the steps marked in green.[180, 234]

Fig. 5.3c shows a high resolution image of the surface structure on the terraces. It reveals a stripe pattern along the [010] direction as well as some defects. The defects had a circular shape with a diameter of about 1 nm and were centered on bright rows in the topography image. Since surface vacancies are not that common on anatase it is obvious that the defects were in fact adsorbates from the chamber such as oxygen and water or from the sample like iron from the bulk of the crystal.[173, 228] The defect looked blown-up, which was probably due to the charging of the defect and possibly of the tip as well. The assignment of the rows to either oxygen or titanium atoms
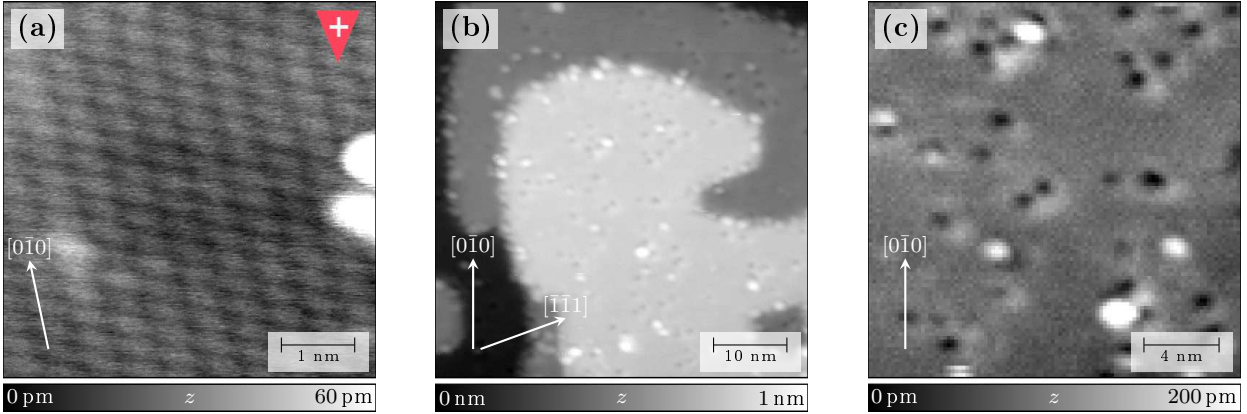
Figure 5.4.: Defects on anatase TiO$_2$ (101). **(a)** High resolution nc-AFM scan with a positively polarized tip apex. The feature on the left side indicates an atomic defect[178] (SSS-NCL: f_1=151.6 kHz, A_1=5 nm, Δf_1=−50 Hz, Q_1=32.7 k). **(b)** Large scale image of the surface after preparation (SSS-NCL: f_2=940.2 kHz, A_2=400 pm, Δf_2=−12 Hz, Q_2=17.1 k). **(c)** Zoom on the defects of the terrace shown in (b).

based on the topography was not straightforward, since the topography might have been affected by the presence of the local electric field. However, many of the possible adsorbates have been found to bind to five-fold titanium atoms, which are in a trough between the bridging oxygen rows.[228] Therefore, one can suggest that the topography contrast was inversed. This indicates that the attraction between tip and sample was stronger on the titanium atoms, which therefore caused the retraction of the tip. Model $\Delta f(z)$-curves for this case as well as proposed dissipation curves for the oxygen and titanium positions are illustrated in Fig. 5.3f. The dissipation is strongly distance dependent and is potentially higher on the oxygen atoms because the tip-sample distance is smaller there. This expectation was actually met by the experimental data shown in Fig. 5.3d. The dissipation contrast was reversed with respect to the measured topography as is illustrated in the profiles in Fig. 5.3e, which were taken over a defect and show the proposed assignment of the surface structure. Considering this experimental data, it is likely that the origin of the stronger attractive tip-sample interaction on the titanium atoms was caused by electrostatic forces, meaning the tip was presumably negatively polarized. Based on this interpretation one can further study the defect site. The defects were located on titanium rows and since they were blurred it can be assumed that they are positively charged as well. Possible candidates would thus be water or impurities from the bulk of the sample.

The image shown in Fig. 5.4a gives evidence that the contrast revealing the hexagonal structure of the surface could be caused by short-range electrostatic forces as well. The image was made with an oscillation amplitude of 5 nm and the corrugation on the hexagonal structure was only 10 pm. In contrast, Fig. 5.1c, which was made using the second resonance, had a corrugation of over 200 pm. The latter value was larger due to the smaller oscillation amplitude. But since it was

larger than the expected topography, it has to be affected by strongly site dependent tip-sample forces. Analogous to the previous argumentation, it can be proposed that this imaging contrast is due to a positively polarized tip. In this case, the measured topography agrees qualitatively with the expected one, which explains the absence of the dissipation signal in these images.

In summary, two high resolution contrasts that gave qualitatively different topography information were investigated and explained by the tip polarization. These contrasts might be suitable for the investigation of defects. As for example depicted in Figs. 5.4b,c, lower quality samples, or old and highly reduced crystals exhibited more defects. On these images one can at least distinguish two types of defects, one that appears as a dip and one that looks like an adsorbate. Most probably these defects interact with evaporated molecules. Scanning with these defects with different polarized tips might be a good tool to reveal their nature and understand their interaction with the molecular adsorbates in future studies.

5.2. ZnCPPs on Anatase TiO$_2$ (101)

The aim of this section is to examine the immobilization of ZnCPPs on the anatase TiO$_2$ (110) surface. First ZnCPPs with different number of carboxylic acids are studied and their influence on the binding strength and mobility is assessed. The reactivity of the substrate with respect to formation of covalent bonds to the adsorbates is discussed too.
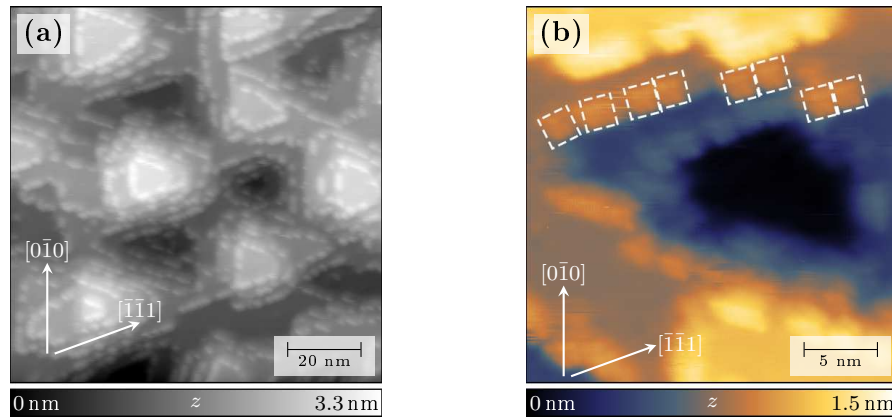
Figure 5.5.: ZnTCPP on anatase TiO$_2$ (101). **(a)** Large scale nc-AFM topography after deposition to the sample held at room temperature (SSS-NCL, f_1=151.4 kHz, A_1=6.5 nm, Δf_1=−9 Hz, Q_1=33.5 k). **(b)** High resolution image of the molecular arrangement on the step edges. The orientation of the ZnTCPPs on one step edge is marked with squares (SSS-NCL, f_2=994.2 kHz, A_2=400 pm, Δf_2=−19 Hz, Q_2=14.4 k).

5.2.1. ZnTCPP on Anatase TiO$_2$ (101)

Similar to the rutile TiO$_2$ (110) surface this study started with the investigation of ZnTCPP, a porphyrin with four carboxyphenyl substituents. In this part of the work the surface was reoxizided during the last preparation cycle. Hence, hardly any defects were present. The terrace size was rather small, which was primarily attributed to the quality of the crystal. Fig. 5.5 shows the surface after evaporation of ZnTCPP to the substrate held at room temperature. The porphyrins adsorbed exclusively on top of step edges, suggesting that they diffuse around till they reach a descending step. Compared to rutile (110), Fig. 5.5b shows a high resolution image of the molecules and how they aligned themselves with respect to the step edge. This behavior is different to the one observed for classical Ehrlich-Schwoebel barriers for which reflection and adsorption of the diffusing species is expected at descending and escalating steps, respectively.[92,93] This observation might be explained by the occurrence of binding sites at the steps that can only be accessed from the top.

5.2.2. Cis-ZnDCPP on Anatase TiO$_2$ (101)

Evaporation of cis-ZnDCPP for 10 min to the sample held at room temperature resulted in noisy topography scans, indicating a relatively high coverage of loosely bound or diffusing porphyrins (see Fig. 5.6a). The step edges were partially decorated and smaller clusters as well as single molecules were present on the terraces. The diffusion was presumably hindered compared to the ZnTCPP sample. This finding was primarily attributed to the defect density on the surface and not the different number of carboxylic acid substituents of the porphyrins. The crystal studied in
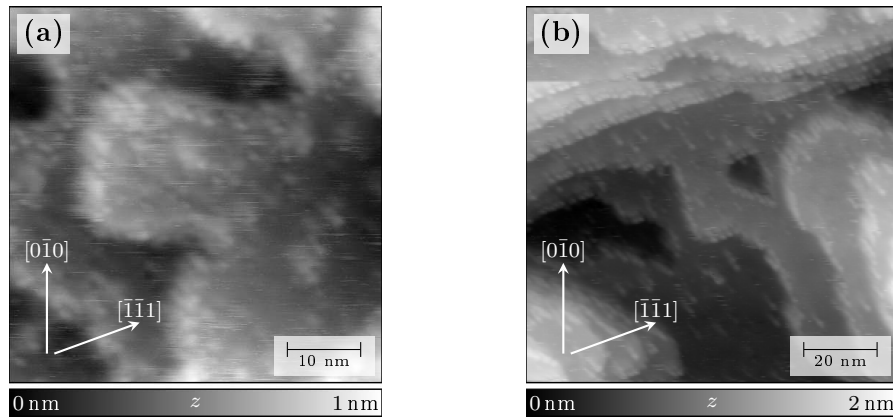
Figure 5.6.: Nc-AFM topography images of cis-ZnDCPP on anatase TiO$_2$ (101) taken with SSS-NCL cantilevers. **(a)** Noisy image just after evaporation, indicating moving porphyrins (f_2=944.2 kHz, A_2=400 pm, Δf_2=−11 Hz, Q_2=15.0 k). **(b)** Molecular arrangement on the step edges (f_1=151.4 kHz, A_1=10 nm, Δf_1=−5 Hz, Q_1=32.8 k).
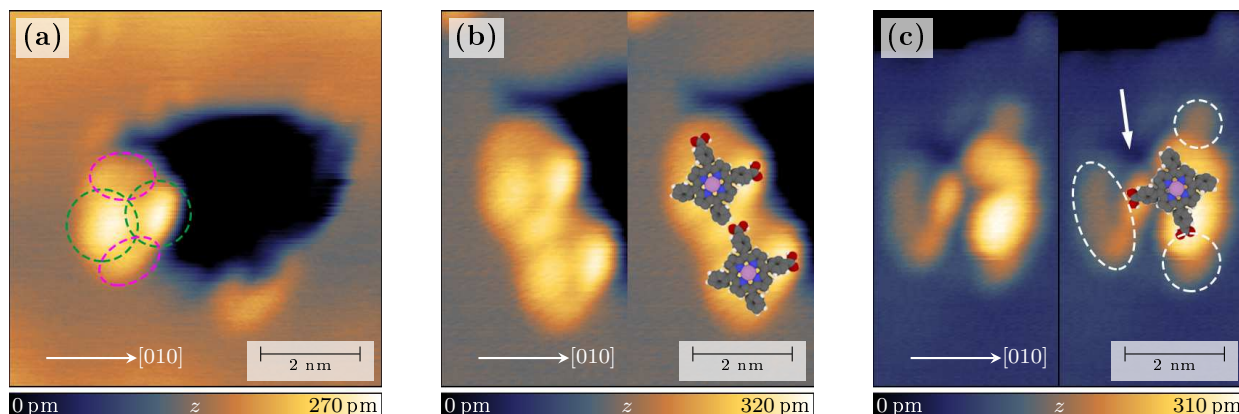
Figure 5.7.: High resolution nc-AFM images of cis-ZnDCPP on anatase TiO$_2$ (101) with suggested models of the adsorbed porphyrins (SSS-NCL, f_1=149.4 kHz, Q_1=33.7 k). **(a)** Single molecule adsorbed on a step edge (A_1=10 nm, Δf_1=−3.5 Hz). **(b)** Two stacked porphyrins on a step (A_1=10 nm, Δf_1=−4.5 Hz). **(c)** Isolated cis-ZnDCPP on the terrace that is probably stabilized by a defect (arrow) together with other small adsorbates (circles) (A_1=10 nm, Δf_1=−4.5 Hz).

this experiment had a low quality and showed more defects than the one used for the investigations on ZnTCPP (see Fig. 5.4b). After first scans, the sample was annealed for 30 min at 150 °C in order to allow the diffusion of weakly bound molecules and thus enable their binding to defects and steps. Fig. 5.6b shows the surface after annealing. The amount of streak lines was significantly decreased and a big part of the step was now covered with molecules. However, some porphyrins remained on the terraces due to binding to defects. High resolution on this sample was not achieved due to unstable scan conditions. It is further noted that the image Fig. 5.6b suffered from a double tip, thus some topographic features, especially at the step edges, were duplicated.

A crystal with lower defect density and low coverage of cis-ZnDCPP was investigated for improved analysis of single adsorption modes. Fig. 5.7a shows a single cis-ZnDCPP molecule at a step edge. The topography image indicates two bright lobes and two fainter protrusions, which are marked in green and violet, respectively. A part of the porphyrin jutted out beyond the step, presumably resulting in a slightly tilted molecular board. Fig. 5.7b depicts two molecules with the same adsorption configuration as the porphyrin in Fig. 5.7a. It also presents a suggested adsorption mode of the molecules. This configuration was found to be the preferred adsorption mode at step edges along the $\langle 11\bar{1}\rangle$-directions. Apart from the molecules at the edges, there were only few molecules adsorbed on the terraces. The shape of these molecules appeared bigger and could be divided into a molecular part and additional protrusions from surface defects as is indicated in Fig. 5.7c. Hence, it was suggested that molecules adsorbed on the terraces were presumably stabilized by defects.
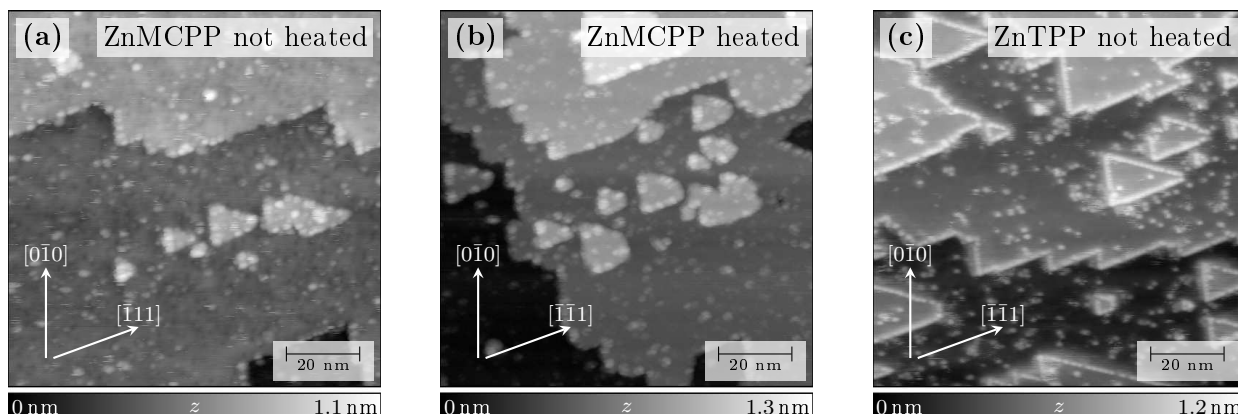
Figure 5.8.: Large scale nc-AFM topography images of ZnMCPP and ZnTPP on anatase (101). **(a)** ZnMCPP directly after deposition and **(b)** after annealing at 120 °C for 40 min (PPP-NCH, f_1=309.9 kHz, A_1=5 nm, Q_1=39.1 k, Δf_1=−15 Hz for (a), Δf_1=−17 Hz for (b)). **(c)** ZnTPP without annealing (PPP-NCH, f_1=321.7 kHz, A_1=5 nm, Δf_1=−13 Hz, Q_1=36.9 k).

5.2.3. Role of the Anchoring Group (ZnMCPP vs. ZnTPP)

The carboxylic acid can make a key difference for the molecular kinetics and processes on the surface as was already indicated by previous results on rutile (see Sec. 4.4). For a simple assessment of this effect, ZnMCPP was compared with ZnTPP. Low coverage deposition of ZnMCPP resulted in noisy nc-AFM scans as depicted in the topography image Fig. 5.8a. The streak lines were attributed to molecules that were not yet diffused to the step edge or loosely interacting with defects. The scan quality was enhanced after annealing for 40 min at 120 °C as indicated in Fig. 5.8b. More porphyrins were now found at the steps but some were also immobilized on the terraces. The noise lines were gone implying that porphyrins on the terraces exhibited a stronger binding after the annealing. In comparison, ZnTPP molecules covered the steps without annealing as shown in Fig. 5.8c, implying that they were more mobile and can diffuse without further thermal activation. Nevertheless, some ZnTPP were immobilized on the terraces, which was attributed to the interaction with defects as well. Large scale topography images revealed islands of flat lying ZnTPP with a typical size of 20–50 nm and a height of approximately 300 pm (see Fig. 5.9a). Since the islands were not necessarily connected to step edges, it was concluded that their growth started at defect sites. Most probably, the island formation can be attributed to the weak interaction of ZnTPP on anatase (110), which is a result of the absence of the carboxylic acid and enables diffusion. The growth of ZnMCPP islands was not observed and might only occur for high coverage, since the carboxylic anchor efficiently reduces the mobility of the porphyrin.
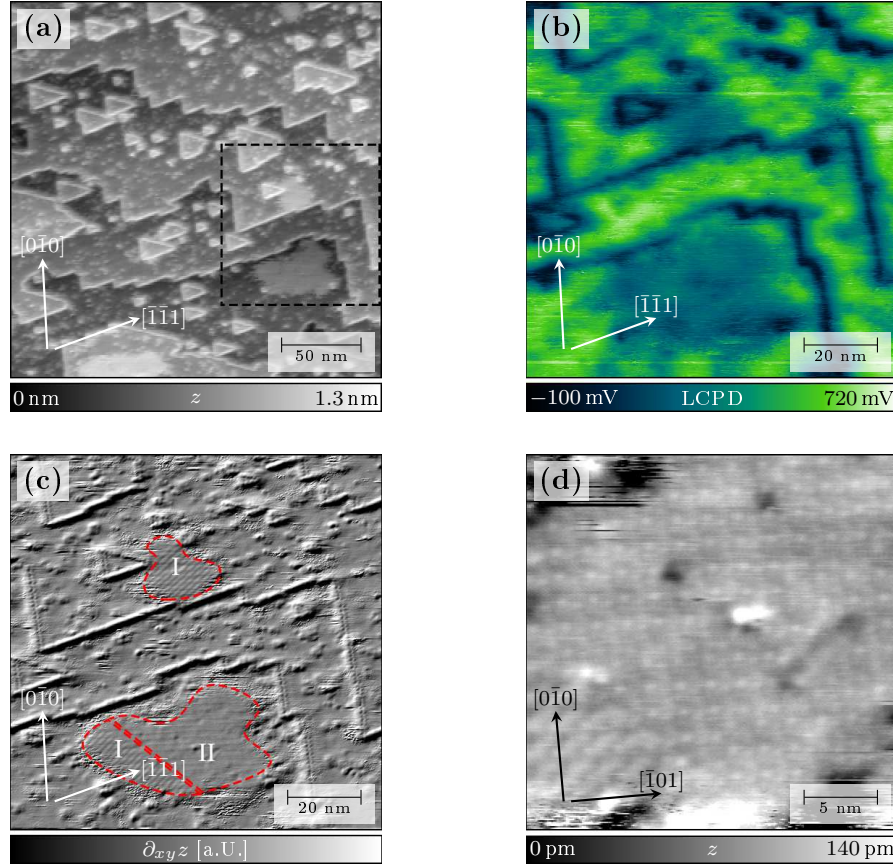
Figure 5.9.: Self-assemblies of ZnTPP on anatase TiO$_2$ (101) taken with a PPP-NCH cantilever (f_1=321.7 kHz, Q_1=37.3 k). **(a)** Large scale nc-AFM topography with islands (A_1=3 nm, Δf_1=−25 Hz). **(b)** Map of the local contact potential difference of the ZnTPP islands in the marked region in (a) as measured with FM-KPFM (A_1=3 nm, Δf_1=−25 Hz, f_{mod}=190 Hz, V_{mod}=500 mV). **(c)** Corresponding differentiated nc-AFM topography showing two structurally different self-assemblies, which are denoted with I and II. **(d)** High resolution AFM topography of the molecular structure on the lower islands (A_1=2 nm, Δf_1=−80 Hz).

5.2.4. Self-Assemblies of ZnTPP

For curiosity, further investigation of the islands by FM-KPFM was done. Fig. 5.9b shows the map of the local contact potential that corresponds to the marked area in Fig. 5.9a. The LCPD on the molecular islands is about 350–400 mV lower than on the bare substrate. The lowest LCPD is measured at the step edges decorated with molecules. As for rutile this could be indicative of a molecular surface dipole pointing away from the surface, originating from partial electron charge transfer from the molecule to the surface. This explanation might only be true for the islands and isolated molecules on the terraces. For molecules adsorbed at steps one has to consider that at least a part of the LCPD drop at step edges comes from the substrate as was revealed by KPFM of the

bare anatase TiO$_2$ (101) surface (see Fig. 5.2). The differentiated topography image of the region with two islands is depicted see Fig. 5.9c. Taking a closer look, one can distinguish two structural different self-assemblies marked with I and II. Their borders are indicated with red dashed lines. A high resolution nc-AFM topography image of the border region on the lower island is depicted in Fig. 5.9d. The island owned several defects. Thus it is probable that this island eventually evolved from the fusion of two smaller islands, whose growth started at individual defects. The island structure features bright dots with a periodicity of 2 nm along the [$\bar{1}$01] direction, which is about 4 times the periodicity of the underlying saw-tooth pattern. Hence, the self-assembly seemed commensurate with the substrate giving evidence that the island was templated by the substrate.

5.2.5. Covalent Anchoring of ZnMCPP

So far it was observed that the porphyrins preferentially sit on top of the step edges or, if present, interact with defects. Remembering the results from the rutile TiO$_2$ (110) surface, it would be interesting to know if the porphyrins can be immobilized on the terraces of anatase TiO$_2$ (101) as well. Hence ZnMCPP was evaporated to the substrate held at 300 °C, in order to facilitate the deprotonation and the binding of the carboxylic anchor directly after landing and therefore before diffusion to a nearby step edge. After the deposition the step edges were fully occupied as shown in Fig. 5.10a but the density of ZnMCPP on the terraces was also higher than the apparent density of surface defects. Thus the anchors did not immediately react with the surface and diffusion was still possible. Some porphyrins that remained on the terraces could still be
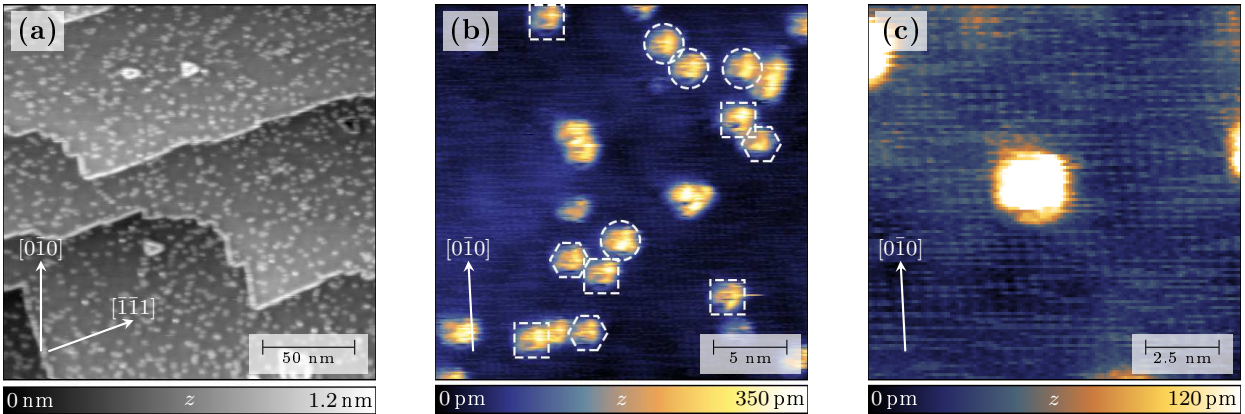
Figure 5.10.: High resolution nc-AFM topography images of ZnMCPP on anatase TiO$_2$ (101) (PPP-NCH, f_1=327.9 kHz, A_1=5 nm, Q_1=36.9 k). **(a)** Large scale nc-AFM topography of ZnMCPP evaporated to the 300 °C hot surface (Δf_1=−10 Hz). **(b)** High resolution AFM image, taken with a functionalized tip. Some of the porphyrins showed similar contrast and were marked with dashed forms (Δf_1=−25 Hz). **(c)** Zoom in with adjusted z-scale to highlight the saw-tooth structure of the substrate.
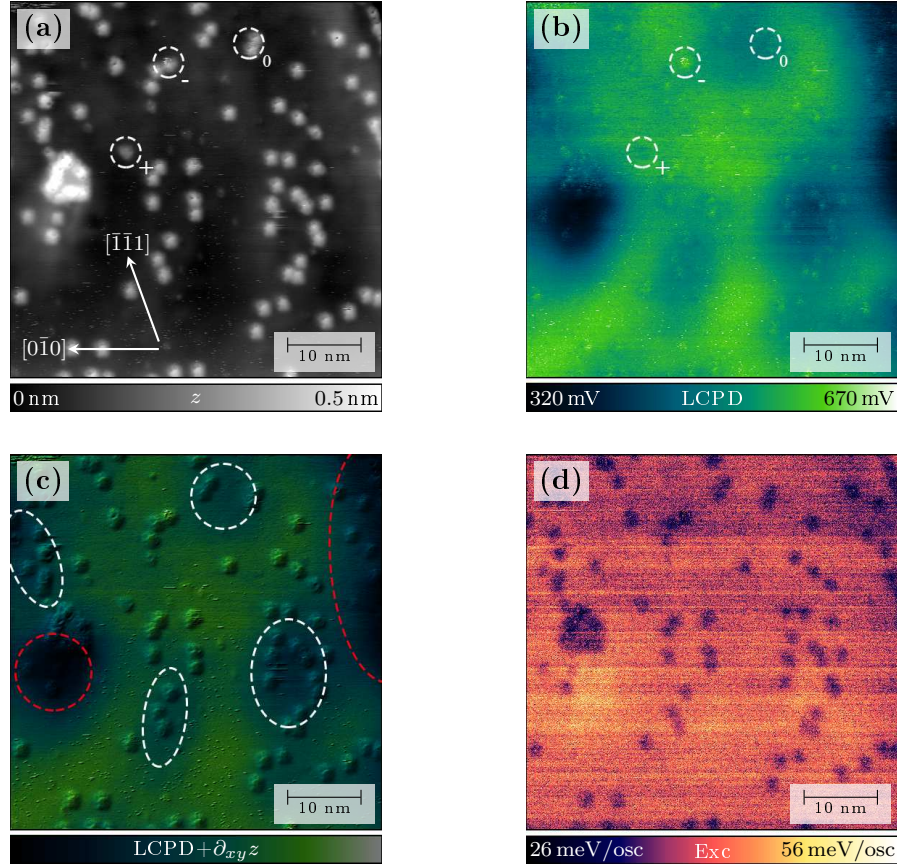
Figure 5.11.: KPFM of ZnMCPP on anatase TiO$_2$ (101). **(a)** Nc-AFM topography and **(b)** corresponding map of the LCPD. Some molecules with different LCPD are marked with dashed circles. The annotations indicate their suggested charging. **(c)** Differentiated topography overlaid with the LCPD map highlighting the influence of the molecules. White and red lines mark regions with lower LCPD due to molecules and step edges, respectively. **(d)** Dissipation per oscillation cycle as calculated after references [235, 236]. The dissipation on the substrate is higher than on the molecules. (PPP-NCH, f_1=327.9 kHz, A_1=5 nm, Δf_1=−25 Hz, Q_1=36.9 k, f_{mod}=180 Hz, V_{mod}=700 mV)

moved via interaction with the tip, indicating that only a small part of the porphyrins might have been immobilized. This finding was corroborated by the fact that huge clusters with several tens of nanometers height were observed. From this it was concluded that most of the molecules actually diffused to these clusters instead of binding to the surface. Possibly the formation of covalent bonds was hindered because of the inaccessibility of the surface titanium atoms, which are slightly buried between the oxygen atoms of the surface.

Pick-up of an adsorbate from the surface, most probably a ZnMCPP, resulted in additional contrast of the underlying substrate (see Figs. 5.10b,c). The contrast on the molecules revealed that the porphyrins adapted different adsorption geometries. Some of them were marked in

Fig. 5.10b. Unfortunately, higher resolution on the molecules, was not possible due to tip insta-bility. Figs. 5.11a,b show a large scale topography image and the corresponding LCPD map as measured by FM-KPFM. These results were also obtained with the functionalized tip. Most of the molecules showed a LCPD contrast that was some tens of mV higher or lower than the surface value as is indicated in Fig. 5.11b. Interestingly, some molecules were not visible in the LCPD map. This indicates that various adsorption configurations with different or even no interfacial charge transfer were present. In addition to the molecular features, the LCPD map showed re-gions with reduced CPD that could not clearly be correlated with the molecular coverage. This gets further apparent when looking at the differentiated topography that is overlaid with the LCPD map in Fig. 5.11c. Regions with a lower LCPD of about 430–500 mV are marked with white circles. These features might be explained by the presence of positively charged subsurface defects or charges as has been reported for rutile TiO$_2$ (110).[212] Other parts of the image that are marked in red showed LCPD values below 400 mV, which can be related to a reduction of the LCPD by the influence of nearby step edges (see Sec. 5.1). Interestingly, it has to be noted that the KPFM image was influenced by dissipation on the bare substrate but not on the molecules as shown in Fig. 5.11d. Every single porphyrin appeared as dip in the dissipation map. This cannot be described by well-known effects such as deformation of the adsorbate at the tip or the surface.[214,238–240] Nevertheless, it was assumed that the interpretation of the CPD contrast remains valid.

5.2.6. Conclusion

The investigation of ZnCPPs with different numbers of carboxylic acids showed that ZnCPPs do only weakly bind to the clean terraces of anatase TiO$_2$ (101). The evaporated molecules diffused to nearby step edges and it was suggested that they only bind to the terraces if defects are present. Covalent binding might be possible by annealing, but was less probable than on rutile TiO$_2$ (110). Even though the molecules were mobile at room temperature, the growth of molecular islands was only observed for ZnTPP, giving evidence that the carboxylic anchor limits the mobility even without covalent bonding. The electronic coupling of the island to the surface was investigated with KPFM and it got evident that the porphyrins might carry a positive partial charge. Interestingly, no covalent binding to the surface was needed for this coupling. Thus it might originated from a direct interaction of the porphyrin core with the substrate. For the annealed ZnMCPP it was observed that they can have positive, negative or no LCPD contrast. This is due to the fact that the porphyrins do not all have the same configuration. Some of them might be chemically bonded to the surface as well.
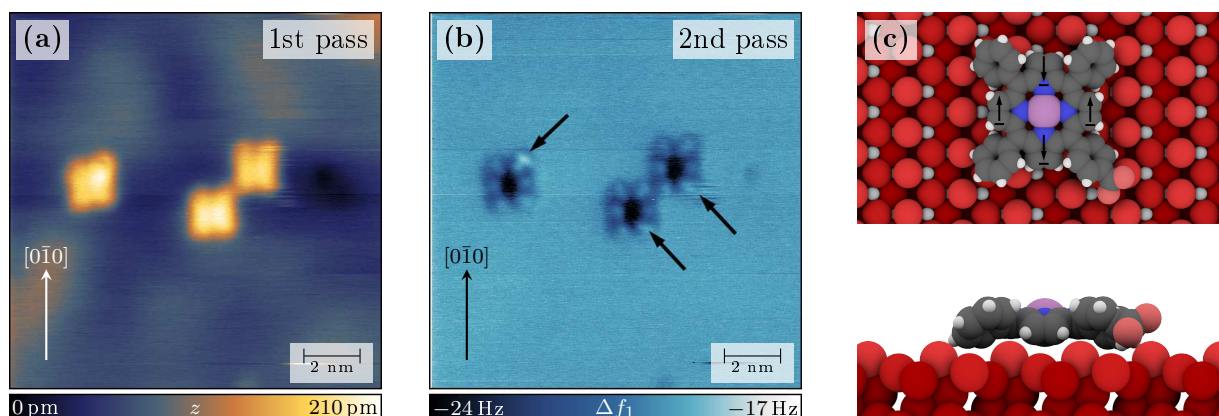
Figure 5.12.: Dual-pass nc-AFM of ZnMCPP on anatase TiO$_2$ (101) using the first resonance (PPP-NCH, f_1=327.9 kHz, A_1=5 nm, Q_1=36.9 k). **(a)** Nc-AFM topography taken during the 1st pass (Δf_1=−17 Hz). **(b)** Detuning image taken at a z-offset of −160 pm. **(c)** Sketch of the suggested adsorption configuration.

5.3. High Resolution Dual-Pass AFM of ZnCPPs

So far nc-AFM on covered anatase TiO$_2$ (101) allowed imaging of the substrate or the molecule structure. But the two contrasts in Sec. 5.1 or the one in Sec. 5.2.5 were not stable enough to yield high resolution on both. Thus it was not possible to determine adsorption sites with single mode nc-AFM. Hence, dual-pass (DP) nc-AFM experiments were done in order to elucidate the adsorption configuration of annealed ZnCPPs.[39] Different measurement settings such as various cantilevers, oscillation amplitudes and z-offsets were used. The measurements that were performed using first resonance DP-AFM will be discussed first. They will be followed by measurements performed on the second resonance, which was chosen to enhance the sensitivity to short-range forces by using smaller amplitudes. Finally, bimodal DP-AFM measurements that allowed resolving the atomic structure of the surface and the molecule will be presented.

The first DP-AFM measurements were done on ZnMCPP with a PPP-NCH cantilever oscillating on the 1st resonance at 5 nm oscillation amplitude. The topography obtained in the first pass is depicted in Fig. 5.12a and showed the ZnMCPP in a square shape orientation with four lobes that were attributed to the phenyl substituents. The frequency shift image recorded with a z-offset of −160 pm revealed additional structural features (see Fig. 5.12b). Each porphyrin displayed two times three lobes now, which were aligned along the [010] direction of the saw-tooth pattern. One of the lobes appeared slightly brighter and might correspond to the carboxylic anchor. The two lobes in the middle might be assigned to pyrrole rings that are bent away from the surface. The bending of the pyrrole rings has been shown to be coupled to the orientation of the phenyl legs.[31] Due to sterical reasons two pyrrole rings that face each other have to be bend towards the surface, whereas the others have to bend upwards.[31] Motivated by the DFT calculations of
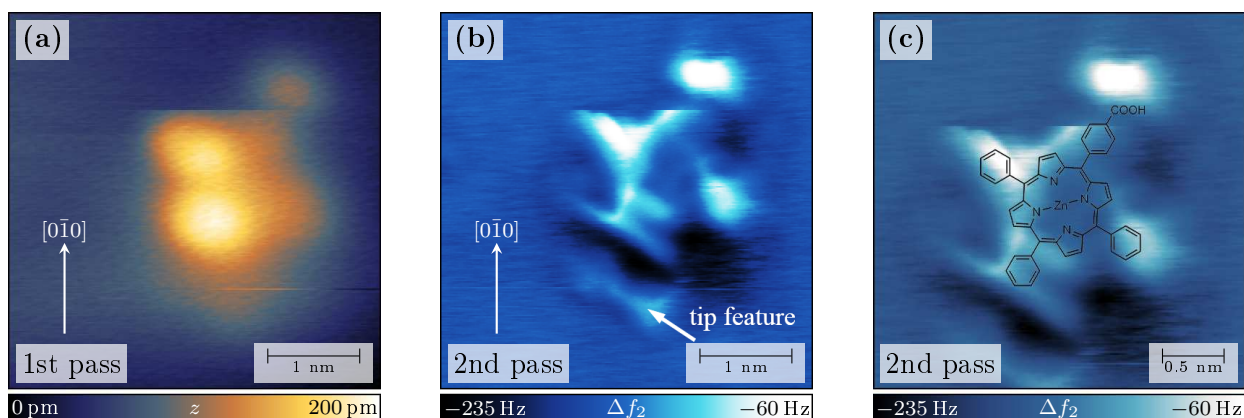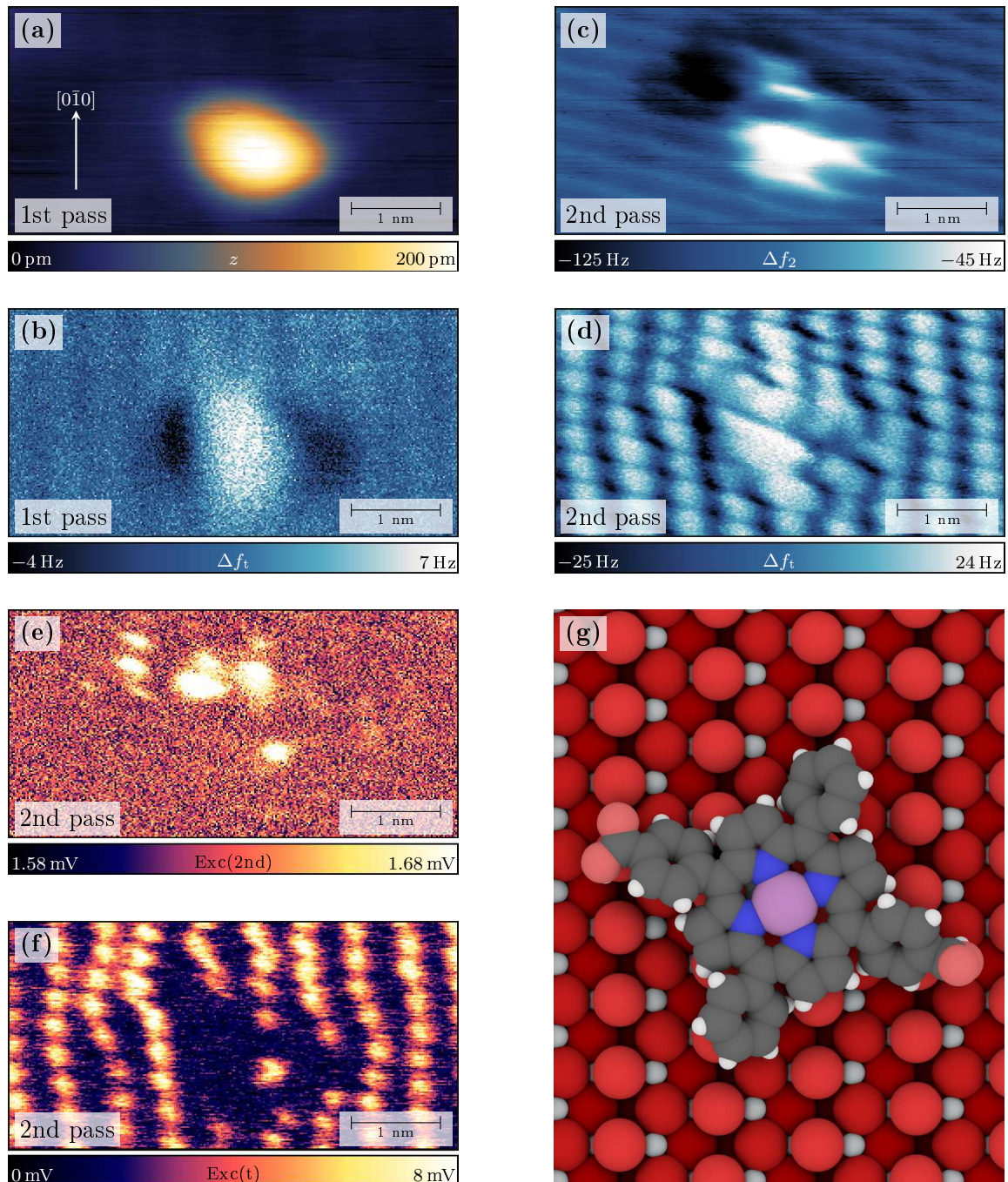
Figure 5.13.: Dual-pass nc-AFM of ZnMCPP on anatase TiO$_2$ (101) using the second resonance (PPP-NCL Pt, f_2=948.1 kHz, A_2=400 pm, Q_2=11.1 k). **(a)** Nc-AFM topography taken during the 1st pass (Δf_2=−60 Hz). **(b)** Detuning image taken at a z-offset of −400 pm during the 2nd pass. **(c)** Proposed orientation of the adsorbed porphyrin.

CuTCPP on rutile (110), it was assumed that the deformation of the porphyrin core was induced by the surface corrugation. An atomic model for the adsorption geometry was made based on these considerations and is shown in Fig. 5.12c. The central metal core is supposed to lie in between two rows of the two-fold oxygen atoms, allowing for good adaption of the whole molecule to the substrate with minor distortions of the porphyrin core.

Since the use of the second resonance was supposed to give an even higher resolution, like shown for ZnMCPP on rutile TiO$_2$ (110), it was applied in a subsequent experiment. A platinum cantilever was used as in the original publication of this technique.[39] The tip was prepared on the surface by bias pulsing, which lead to pick-up of sample material and sharpened the otherwise relatively blunt tip. The nc-AFM topography of ZnMCPP evaporated to the hot anatase surface is shown in Fig. 5.13a. The molecule appeared slightly tilted but the lobes of the porphyrin could still be identified. The second pass was made with an offset of −400 pm. The corresponding detuning image is depicted in Fig. 5.13b. The porphyrin core as well as features from the phenyl groups are visible. The macrocycle even reveals submolecular features that possibly originate from covalent bonds from the nitrogen atoms to the zinc core. Fig. 5.13c illustrates the suggested orientation of the molecule. The angle between the molecular axes along the phenyl groups and the substrate bridging oxygen atoms was about 30°. Scanning at closer distances was still stable but caused strong features from a double tip (see Fig. 5.13b). Despite the high molecular resolution it was not possible to resolve the substrate structure and therefore to determine the adsorption site.

A last experiment to finally image the molecule and the substrate structure simultaneously was done using bimodal DP-AFM measurements similar to the ones originally done by Moreno. In their experiment they used the first two normal resonances to resolve pentacene on anatase TiO$_2$

Figure 5.14.: Bimodal dual-pass nc-AFM of tr-ZnDCPP on anatase TiO$_2$ (101) using the second resonance (SSS-NCL, f_2=949.7 kHz, A_2=500 pm, Q_2=13.3 k, f_t=1.493 MHz, A_t=30 pm, Q_t=147.8 k). **(a,b)** Nc-AFM topography and torsional frequency shift measured during the 1st pass (Δf_2=−20 Hz). **(c,d)** Detuning images taken at a z-offset of −500 pm during the 2nd pass. **(e,f)** Dissipation images of the two channels obtained during the 2nd pass. **(g)** Suggested model for the adsorption configuration.

(101).[39] In our case the second normal resonance together with the torsional one were used to be more sensitive to the short-range forces. The results of the dual-pass bimodal nc-AFM experiment using tr-ZnDCPP, which was evaporated to the hot surface, are depicted in Fig. 5.14. The experiments were performed using a super sharp silicon cantilever. The topography as well and the frequency shift of the torsional resonance are given in Figs. 5.14a,b. The latter shows dips on the left side of the molecule that are similar to the ones observed for cis-ZnDCPP on rutile TiO_2 (110) (see Sec. 4.5). Interestingly, the observed dips for tr-ZnDCPP did not correlate with the structure of the molecule and it was assumed that they originate from an asymmetric e.g. tilted adsorption mode or from a tip asymmetry. The first pass already indicates a faint signal from the substrate surface, which was clearly resolved when performing the second pass with an offset of $-500\,pm$ as shown in Figs. 5.14c,d. The hexagonal structure of the surface was visible in both frequency shift channels. The bright features in Fig. 5.14c were assigned to the topmost oxygen atoms. This was justified by considering that the second pass was made in quasi static height and in the repulsive regime of the $\Delta f_2(z)$-curve, so that elevated sites showed a higher Δf_2. The torsional signal showed even a higher contrast on the substrate. This pattern was shifted with respect to the one of the Δf_2 map, indicating that bright dots originated from titanium atoms. Further atomic information was recorded in the excitation signal of the torsional channel (see Fig. 5.14f). The dissipation showed a hexagonal pattern, which corresponded to the one in the Δf_2 map and therefore to the oxygen atoms. Based on this interpretation it was possible to determine the adsorption site of the molecule and suggest a model of the adsorption configuration, which is depicted in Fig. 5.14g. Interestingly, the carboxylic acid on the right site is in a good position to bind to the titanium atom below.

In summary, high resolution imaging with submolecular resolution was achieved with the DP method. The orientation of the porphyrins could be resolved in each case, and was used to propose models for the molecular adsorption configurations. The information that was gained by the DP-AFM depended critically on the tip termination, the oscillation amplitude and the z-offset. Unfortunately, the tip preparation methods are not that reliable. Thus the tip had to be prepared by repeated attempts. Furthermore, it was observed that the tip should not only be sharp but also robust, so that it does not deform when scanning in the repulsive regime. Within the scope of the presented experiments, a platinum coated cantilever gave the best resolution on the molecule and is maybe even suitable to resolve the complete molecular structure at room temperature. However, reliable high resolution measurements comprising the substrate structure were also made with super sharp silicon tips. Using them in bimodal DP-AFM allowed the determination of the adsorption configuration as well as the adsorption site for tr-ZnDCPP on anatase TiO_2 (101).

5.4. Conclusion

The study of the bare anatase TiO$_2$ (101) surface underlines the difficulties in high resolution imaging of metal oxides. The atomic structure of the surface could only be resolved in a few cases, due to the low corrugation and the dominance of the surface oxygen atoms. Nevertheless, tip functionalization enabled two high resolution contrasts. Compared to the experiments on rutile (110), these two contrasts did not reveal the same structural information. But they were also attributed to the different polarity of the tip.

The study of ZnCPP on anatase (101) indicated that porphyrins with different numbers of anchoring groups behave similarly and that the interaction of the porphyrins with the substrate was weaker than for rutile TiO$_2$ (110). They had a relatively high mobility and were able to diffuse at room temperature. The diffusion resulted in preferable binding to step edges and the sticking to the edges was found to depend on the orientation of the steps. Porphyrins that stuck to the terraces were only obtained for the case of higher defect density. Based on these measurements it was concluded that most of the porphyrins are only weakly bond. Nevertheless, it was suggested that the carboxylic anchor increased the interaction with the surface. As an illustrating example, self-assemblies were only formed in the case of ZnTPP. The attempt to anchor the ZnCPPs on the surface by evaporation to the hot substrate indeed resulted in an increase of porphyrins on the terraces, which facilitated single molecule characterization. But unfortunately this method also yielded large molecular clusters, giving evidence that the molecules rather diffused to these clusters and did not like to bind to the surface. This means that controlled deposition of the molecules on anatase remains difficult at room temperature.

High resolution imaging was only possible for functionalized tips, which were inherently unstable at room temperature. Hence high resolution imaging of the molecule and the surface was hardly possible by single-pass nc-AFM. DP-AFM measurements were performed, in order to overcome this limitation. These measurements enabled to determine the orientation of the molecule and to resolve submolecular features but did hardly resolve the substrate. Fortunately, better resolution on the substrate could be achieved with bimodal DP-AFM. These results were successfully used to propose atomic models of the molecular adsorption mode of tr-ZnDCPP. It was thus demonstrated that nc-AFM can resolve the adsorption site and configuration of single molecules with high resolution and is thus of high value for the investigation of functionalized surfaces.

6.

Conclusion

This chapter summarizes the main findings of this thesis and gives an outlook on further experiments. It will start with the improvements made from the experimental point of view and will then go on with the gained scientific insights on the studied organic-inorganic interfaces. The relevance of the experimental results for the applications is critically discussed and possible experiments for deeper investigation of functionalized surfaces are proposed.

6.1. Advanced nc-AFM Methods

This work investigated the versatility of nc-AFM for high resolution imaging of surfaces and molecules at room temperature and under UHV conditions. It was explained how the atomic topography depends on the site specific interaction between the scanning tip and the surface. The tip termination, like e.g. its polarity, is crucial as has been observed for various substrates such as salts or also rutile TiO_2 (110).[112, 130] Different imaging contrasts were found in this work for rutile and also anatase. Two new distinct topography contrasts were resolved in the latter case that gave qualitatively different information. As for rutile, these contrasts could be explained by the polarity of the tip. These contrasts were only possible using functionalized tips. Even though, the tip changes occurred by chance, they offer an interesting way to investigate the substrate as well as properties of surface defect states.

The adsorption mode of single porphyrins on rutile TiO_2 (110) and anatase TiO_2 (101) was further investigated by nc-AFM using the second flexural resonance for topography mapping. The sensitivity to short-range forces was significantly increased and allowed increasing the minimum tip-sample distance. Therefore, the stability of the scans was improved and single adsorption configurations of CuTCPP could be characterized. The examination of the electronic coupling of these molecules was further possible by FM-KPFM. The proposed adsorption modes and their electronic interaction with the surface were in excellent agreement with density functional theory calculations, which underline the versatility of nc-AFM for the investigation of single molecules at room temperature.

Bimodal nc-AFM experiments that employed the first torsional resonance were used on the bare substrate as well as the molecules. It was found that bimodal nc-AFM can be successfully applied

to distinguish defects on the rutile TiO_2 (110). The assignment of the defect type could be made no matter the tip polarity. An achievement that was not possible with standard nc-AFM on the first resonance. The experimental results were verified by simple model calculations which might enable the identification of defects on other substrates as well. The torsional signal might even be useful for the determination of functional groups in molecules as was suggested by experiments on cis-ZnDCPP on rutile TiO_2 (110).

Dual-pass nc-AFM experiments were performed that allow scanning in the range of repulsive forces and thereby enabling an improved resolution limit of nc-AFM. Using this method, the submolecular structure of the porphyrins on anatase as well as rutile was imaged. The experimental results could be directly used to propose accurate models of the adsorption geometry of the molecules at room temperature. However, the substrate of anatase was not resolved in these measurements. Bimodal DP-AFM using the torsional resonance overcame this problem and revealed the adsorption orientation and site of tr-ZnDCPP on anatase TiO_2. Our results provide high resolution information that was not achieved so far at room temperature. Hence multi-pass AFM offers great possibilities for high resolution characterization of single molecules. The fact that the gathered information depends on the tip-sample distance could be further exploited in future experiments by implementing 3D spectroscopic measurements with multiple passes at different z-offsets. Further information could be gained by simultaneous KPFM.

6.2. Porphyrin Functionalized TiO_2

Comparing the rutile and anatase TiO_2 polymorphs, it gets evident that they interact differently with the adsorbed porphyrins. The main differences between them are their surface corrugation, the accessibility of the potential binding sites such as titanium atoms and the defect density on the surface. The periodicity of the surfaces differs by about 140 pm and the symmetry is reduced on anatase TiO_2 (101), resulting in a saw-tooth pattern along the [010] direction. The investigated porphyrins generally stuck to the rutile (110) surface. If carboxylic anchors were present, the adsorption configurations were presumably stabilized by H-bonds to bridging oxygen atoms of the surface. Thus the porphyrins were immobilized at room temperature, but could be manipulated via interaction with the scanning tip. The number of carboxylic anchors did have a minor effect on the adsorption. The porphyrins behave differently only if they carried no anchor group. In this case, the weaker interaction with the substrate enabled the formation of molecular islands after annealing. The determined flat adsorption geometries of the MCPPs were highly symmetric and adapted to the surface structure. This configuration caused electronic coupling to the surface, so that most of the studied porphyrins were slightly positively charged. The HOMO levels were shifted to lower energies, which probably changes their optical properties such as the adsorption bandwidth. These results are in agreement with literature on other porphyrins and phthalocyanines.[89,185] The as deposited porphyrins were not covalently linked upon adsorption. But it

was shown that this surface reaction can be induced by heating. This activates the carboxylic groups by deprotonation and enables their binding to five-fold titanium atoms of the surface. The adsorption behavior on anatase TiO_2 (101) was significantly different to the one on rutile (110). Evaporated porphyrins were mobile and diffused to nearby step edges. Only on defective surfaces, the porphyrins were found to possibly stay on the terraces. The difference in mobility is probably caused by the structure of the anatase surface. The ZnCPPs were designed to fit the periodicity of the rutile (110) surface. The periodicity of the anatase (101) surface is lower and thus it might be harder to accommodate the porphyrins. Furthermore, the (101) surface of anatase seemed to be less reactive, which is possibly correlated to the lower density of surface defects. Evaporation to the hot substrate revealed higher density of molecules on the terraces but in many cases they could still be moved by the tip. AFM and KPFM indicated various adsorption geometries and different coupling to the substrate. However, it remained unclear if the coupling to the surface depended alone on the molecular adsorption mode or if defects were involved as well. The annealing of the substrate even increased the mobility of the molecules, enabling their aggregation in large clusters. The covalent binding of the molecules to anatase could thus not be proven or even controlled.

The results from this study have implications for the application of porphyrins functionalized titania surfaces. It was directly confirmed on the molecular scale that the binding mode is crucial for the electronic and optical properties of the interface. All the observed adsorption modes were either flat or only tilted a little, thus enabling the direct interaction of the core with the substrate. This is generally not desired in the applications, where the molecular properties should be preserved upon adsorption. That this coupling is not beneficial was further demonstrated by applying the ZnCPPs in dye-sensitized solar cells, where the molecules are deposited by immersion in the sensitizer solution. The study is presented in appendix C and showed that molecules with only one carboxylic group were the most efficient, since they bind only at one side and are able to adsorb in an upright configuration, which is decoupled from the substrate. Somehow, upright adsorption modes could not be prepared in UHV, which complicates their investigation. Thus one has to think about solutions to prepare these adsorption modes as well. This and other questions will be addressed in the following outlook.

6.3. Outlook

The main goal of the investigation of functionalized surfaces is to get a deeper understanding of their working mechanism. So far only basic properties of the adsorbed molecules were investigated. Further studies involving light are needed in order to assess the performance of a single molecule in the application. Irradiation by laser light while measuring the LCPD would be suitable to address the optical activity as well as the absorption bandwidth of the molecule.[218] Simultaneous STM measurements could be further used to estimate the injection efficiency from

the tunneling current. These combined scanning probe experiments would allow characterizing and understanding their interaction with the surface in more detail.

Another issue for further investigation is the controlled preparation of active adsorption configurations with the goal to get the same modes as in the actual devices. The deposition of molecules by immersion into a liquid solution would be straightforward and has already been applied for smaller molecules.[241] This deposition method is also beneficial for larger molecules that are not stable enough for deposition by evaporation. Another solution to this problem is offered by electrospray deposition, which would still allow to studying low coverage samples and thus single molecules.[223, 229]

It is also necessary to investigate other crystallographic surfaces of titania, since devices are often based on nanoparticles. The reactivity and thus adsorption of the various edges might be critical for the device performance. The final step towards the complete understanding of the active interface in dye-sensitized solar cells would require to expand the measurements to liquid environments, which is however difficult because of the molecular motion involved.[242] Even though that the resolution in these investigations might not be as high as the one presented in this work, AFM as well as KPFM and STM are conceptually suitable to address all the above mentioned issues and it is assumed that the herein presented improvements of nc-AFM will significantly help thereby.

7.

Acknowledgments

First and foremost I thank Prof. Dr. Ernst Meyer for the possibility to do my PhD studies in his group. He always supported me in his uncomplicated way and gave me a lot of freedom concerning the planning of experiments and also responsibility for the teaching duties, which I highly appreciated. Secondly, I thank Dr. Thilo Glatzel and Dr. Antoine Hinaut for their experimental support and fruitful scientific discussions. Without their help I could never have done all the experiments. They further facilitated the external experiments at the Paul Scherrer Institute and were of great help for the preparation of this manuscript. I further thank my colleagues from the research group, especially Rémy Pawlak, Shigeki Kawai, Sara Freund and Tobias Meier for all their support and teamwork, the valuable discussions, and also for the great atmosphere in our office.

Furthermore I thank the following people that all contributed important parts to this dissertation. Dr. Carmen Perez Leon from Karlsruhe Institute of Technology (KIT) was of great help to adapt the preparation of the anatase single crystals in our system. The density functional theory calculations were made in the group of Prof. Dr. Stefan Goedecker and performed by Dr. Ali Sadeghi. Dr. Matthias Muntwiler, Dr. Jun Zhang and Patrick Ascher from the Paul Scherrer Institute gave essential support for the PES experiments at the PEARL beamline at the Swiss Light Source. The molecules for this work were provided by the group of Prof. Dr. Silvio Decurtins from University of Bern and his team, Dr. Shi-Xia Liu, Dr. Jesse Bergkamp and Luis Manuel Mateo. The experiments in this thesis were supported by the joint Swiss-Polish research programme and were done in collaboration with the research group of Prof. Dr. Marek Szymonski from the Jaggielonian University in Krakow. Namely I thank Dr. Bartosz Such, Łukasz Zając and Piotr Olszowski for the experimental support during the measurements at the Paul Scherrer Institute. Concerning the presented results on dye-sensitized solar cells, I am grateful to my project students, Chantelle Ekanem, David Marti, Gregor Haag and Raphael Pachlatko, who performed most of the experimental work. I am further indebted to my former colleague Dr. Gino Günzburger as well as Prof. Dr. Ed Constable and Prof. Dr. Cathrine Housecroft from the Chemistry Department and their group, especially Dr. Sebastian Fürer and Dr. Ewald Schönhofer, for the good collaboration in the field of DSCs. I further thank Michael Steinacher, Andreas Tonin and Roberto Maffiolini from the electronic workshop as well as Marco

Martina, Sascha Martin and the team of the mechanical workshop for all the technical support. Experimental physics is prone to many technical problems but you always had a fast solution at hand. I really enjoyed to work with all of you, and appreciate your valuable contributions to this present work.

Concerning the preparation of the manuscript, I am also obliged to Dr. Gino Günzburger, Miranda Oester and Madeline Diekmann for proofreading and layout advice. You provided me with valuable comments from the world outside the physics department and facilitated the better understandability of this work. Last but not least I thank my family and my best friend Michèle Jenne. Even though you often did not understand what I was doing, you always supported and encouraged me. Without your help this thesis would not have been possible.

Part III.

Appendix

A.

Remarks on Contrast Inversion

The tip has to sense the chemical forces in order to achieve high resolution on the molecules. As outlined in the theory chapter Sec. 2.3.2 the sensitivity is higher for small amplitudes. Therefore, it is hardly possible to reach high resolution with the common oscillation amplitudes applied on rutile, which are about $10\,\mathrm{nm}$. Approaching the tip into close proximity to the surface resulted often in partial inversion of the topography over the molecules. By exceeding a certain detuning frequency, the porphyrins started to show dips, which were presumably located on their carboxyphenyl groups. The explanation of this imaging artifact is the aim of this section.

There are two explanations for contrast inversion as explained by Rahe.[128] The first case can be explained by alteration of the $\Delta f(z)$ curve over the adsorbate as also outlined in the theory. If the Δf curve over the molecule and over the substrate have an intersection point in the attractive regime (positive slope), then the contrast can be inverted by approaching the tip. The frequency shift would stay constant when scanning over the molecule. In the second case the contrast inversion is due to slow feedback of the z-controller. In this case the frequency shift setpoint cannot be maintained while scanning over the molecules. Examination of topography and Δf profiles over the molecules, as depicted in Fig. A.1b, shows that the frequency shift of the cantilever changes. The shape of the profiles can be explained as follows. The slow feedback leads to a decrease of the Δf when the tip approaches the adsorbate. The tip can thus enter the repulsive regime if the frequency setpoint is close to the turning point of the $\Delta f(z)$ curve and or if the $\Delta f(z)$ is changed on the molecule. The controller will now still be trying to reach the setpoint, however, it will further approach the tip because the feedback of the z-controller is inverted in the repulsive regime. Therefore, the Δf will further increase. Eventually the tip flips back to the attractive regime when it leaves the molecule or if the tip sample interaction is changed. The actual detuning frequencies are now lower than the setpoint because the tip is still too close to the surface. Now the feedback loop is working correctly again and will retract the tip. A slight overshooting due to the slow feedback might be observed when reaching the frequency setpoint. The complete cycle for this inversion mechanism is illustrated in Fig. A.1d. This justification for the imaging contrast is further underlined by the fact that the profiles of the detuning are mirrored when changing the scan direction (Fig. A.1b). Even though more commonly observed for measurements on the first resonance with large amplitude, this effect can also occur on the second resonance (see Fig. A.1c).
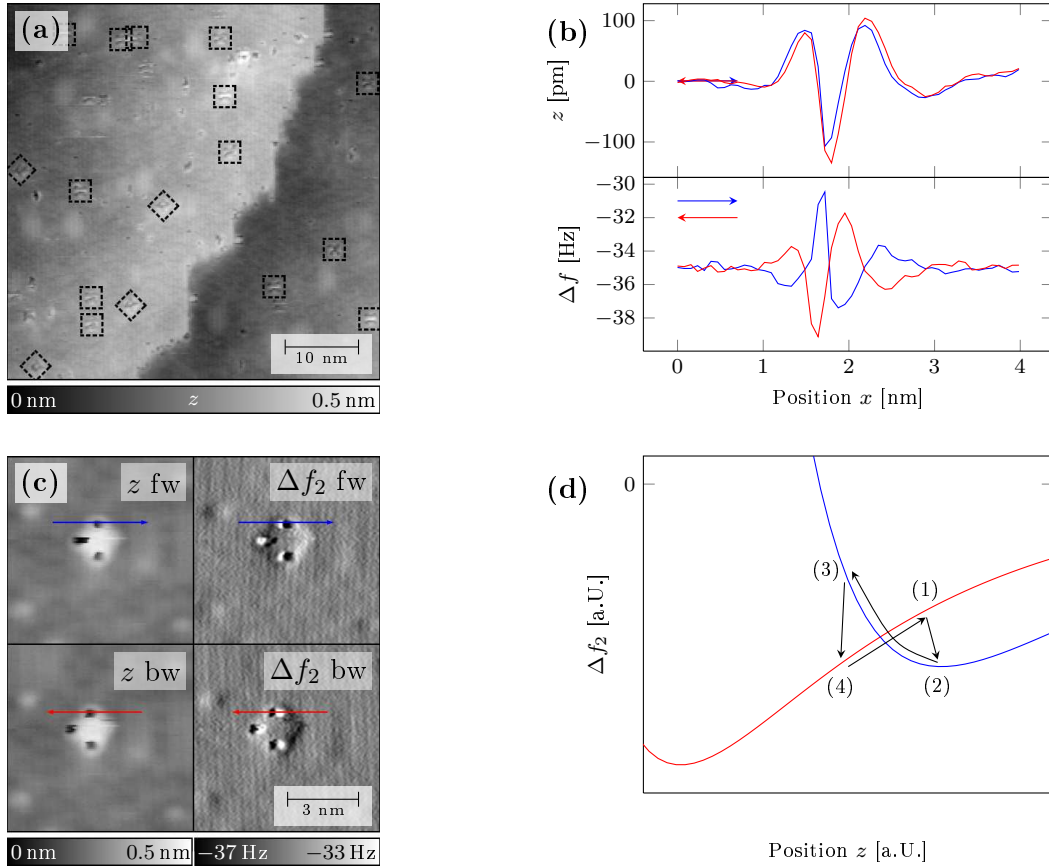
Figure A.1.: Contrast inversion for close contact imaging of CuTCPP on rutile TiO_2 (110). **(a)** Topography image (PPP-NCL, $f_1 = 154.9\,kHz$, $A_1 = 10\,nm$, $\Delta f_1 = -25\,Hz$, $Q_1 = 27.2\,k$. **(b)** Comparison of topography and detuning profiles taken in forward and backward scan direction over the upper lobe of the porphyrin as indicated in (c). **(c)** High resolution topography image of a single molecule using the second resonance ($f_2 = 971.1\,kHz$, $A_2 = 400\,pm$, $\Delta f_2 = -35\,Hz$, $Q_2 = 11.6\,k$). **(d)** Graphical explanation of the contrast inversion mechanism.

Despite the artifacts, these measurements can yield high resolution and stable scan conditions, that even allow deducing adsorption geometries (see Fig. A.1a). Nevertheless, the exact interpretation is sometimes complicated. For the case of the porphyrins, the artifacts occurred mostly on the phenyl lobes. However, they were not always present due to unknown reasons (see Fig. A.1c).

B.

XPS of the TiO$_2$ Substrates

The purity of the bare TiO$_2$ samples has been assessed with X-ray photoelectron spectroscopy as well as valence band spectroscopy. The experiments have been done at the PEARL beamline at the Swiss Light Source (Paul Scherrer Institute, Villigen CH).

B.1. Rutile TiO$_2$ (110)

The spectra of the synthetic rutile (110) sample are shown in Fig. B.1d. The spectrum in (a) is an overview. All peaks could be assigned to either XPS or Auger lines from oxygen or titanium. Therefore, no significant contamination is present on the surface. Fig. B.1b and Fig. B.1c show the XPS spectra of the Ti2p and O1s, respectively. The peaks of the Ti2p are at binding energies of 464.8 eV and 459.0 eV for the Ti2p$_{1/2}$ and Ti2p$_{3/2}$. The O1s is at 530.3 eV. These binding energies are in good agreement with literature.[243] The peak of Ti2p$_{3/2}$ has a shoulder that indicates a contribution from the Ti^{3+} state. The other peaks do not exhibit significant asymmetries or side peaks. Hence, the surface is relatively clean meaning the amount of contamination or surface defects is below the detection limit of this experiment. Fig. B.1d displays a valence band spectrum. The onset of the valence band is at a binding energy of about 3 eV. Besides the O2s peak found at 23 eV there is a features at 10.8 eV and about 1 eV. Both can be attributed to defects. The state in the band gap belongs to the Ti^{3+}, which occurs due to the formation of oxygen vacancies. The peak at 10.8 eV indicates hydrogen adatoms.[165, 244]

In summary, the XPS and VBS spectra reveal that the rutile crystal is highly reduced. The clear peak for the Ti^{3+} gap state indicates that there are many oxygen vacancies in the subsurface region and on the surface.
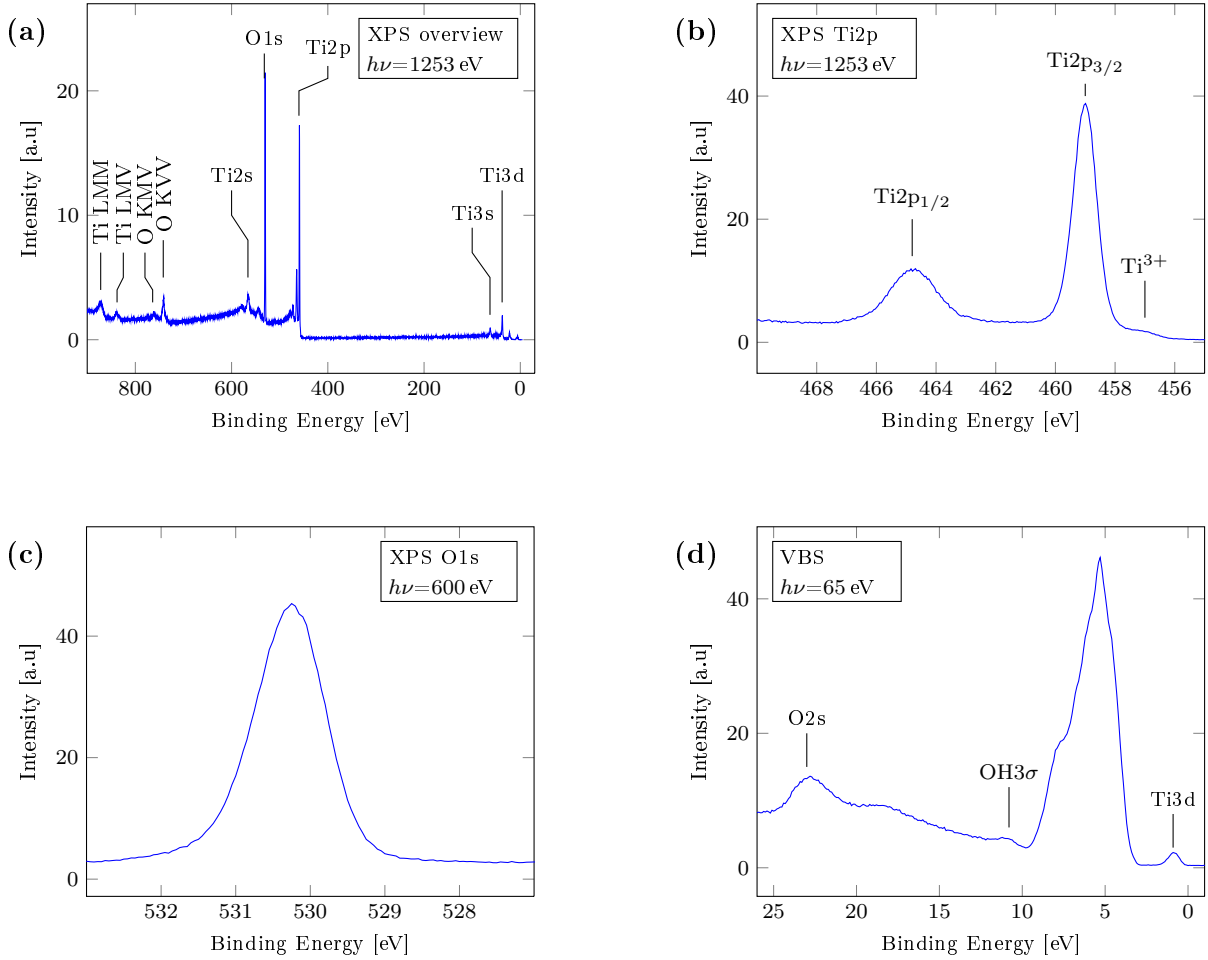
Figure B.1.: Photoemission spectroscopy of a synthetic rutile crystal exhibiting the (110) surface. **(a)** Overview spectrum of the surface after preparation by sputtering and annealing. **(b,c)** Close-up XPS spectra for the Ti2p and O1s levels. **(d)** Valence band spectroscopy indicating Ti^{3+} defects originating from oxygen vacancies as well as hydrogen adatoms (OH3σ).

B.2. Anatase TiO$_2$ (101)

The spectra of the natural anatase spectra are shown in Fig. B.2d. The overview spectra in Fig. B.2a does not show any significant contamination. All peaks could be attributed to oxygen or titanium atoms. Therefore, we can assume that the impurities remain in the bulk or subsurface region as for example studied by Setvin for the case of iron.[173] Fig. B.2b and Fig. B.2c display the Ti2p and O1s XPS spectra indicating binding energies of 464.5 eV, 458.7 eV and 529.5 eV for Ti2p$_{1/2}$, Ti2p$_{3/2}$ and O1s. The valence band spectrum is depicted in Fig. B.2d. The onset of the band at 2.8 eV and is slightly higher in energy than for rutile. A broad but faint feature is
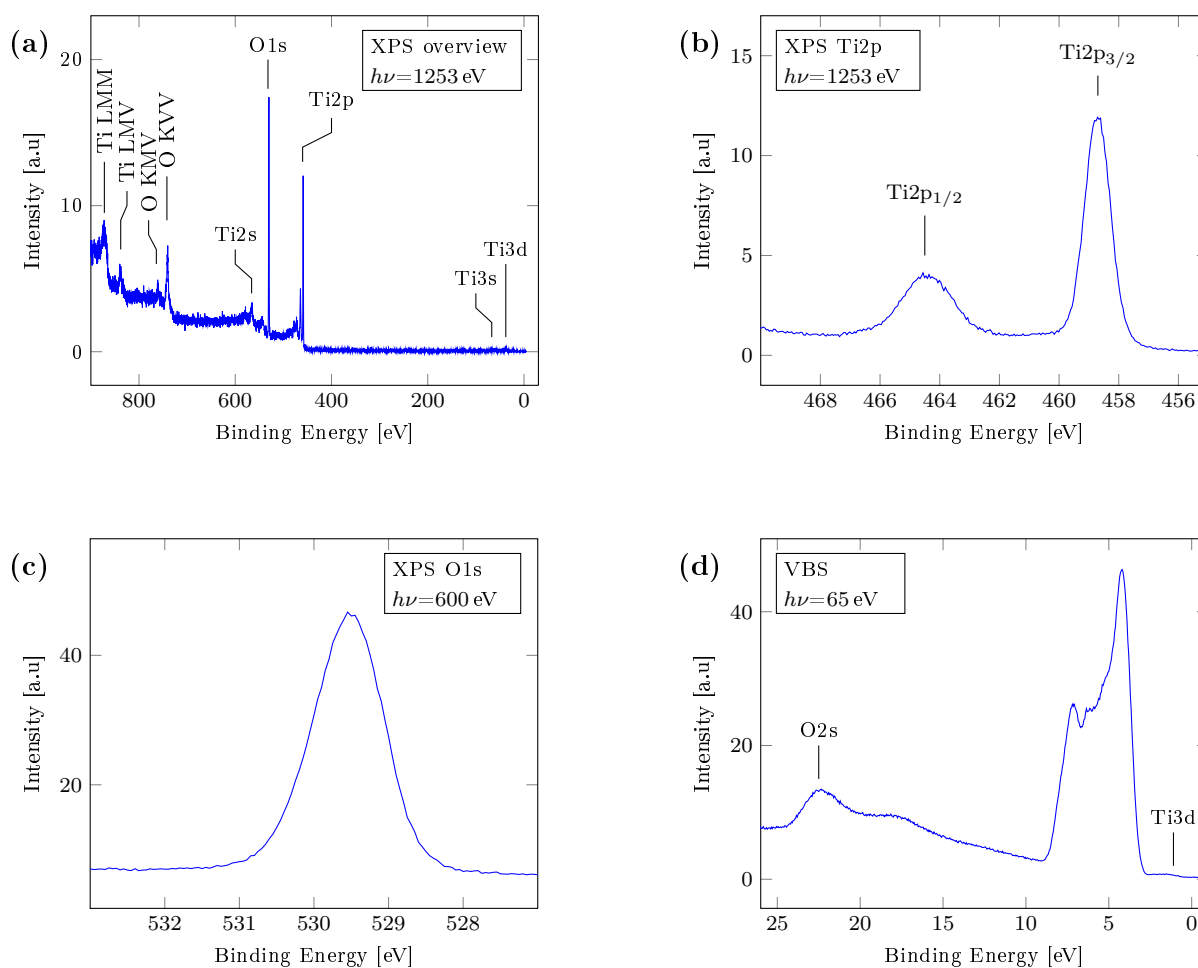
Figure B.2.: Photoemission spectroscopy of a natural anatase crystal exhibiting the (101) surface. **(a)** Overview spectrum of the surface after preparation by sputtering and annealing. **(b,c)** Close-up XPS spectrum for the Ti2p and O1s levels. **(d)** Valence band spectroscopy indicating Ti^{3+} defects originating from oxygen vacancies.

found in the gap region. Since the sample is highly reduced it might be attributed to Ti^{3+} as well. The signal is assumed to be from subsurface or bulk defects, because they are less stable on the surface.[176]

In conclusion the spectra are representative for anatase with clean surface but considerable subsurface and bulk reduction. Even though the crystal was a natural sample, there is no evidence for significant impurities, possibly implying that they remain in the bulk during sample preparation.

C.

Dye–Sensitized Solar Cells

The demand for remotely available, sustainable energy is constantly increasing. In this field, dye-sensitized solar cells (DSCs) that were invented in 1991 by Grätzel et al.,[18] are a cheap alternative to commercially available solar cells.[245] They can be fabricated in different colors and transparency and on flexible substrates,[246,247] thus extending the scope of application to, for example, windows or even clothes. In this appendix we applied the molecules from the UHV experiments in DSCs. The aim was to compare the results from scanning probe microscopy with the actual device performance and to evaluate if the conclusions from the main part of the thesis are transferable to DSCs.

The first part gives a short introduction to the working principle of DSCs. The second part reports characterization of DSCs made with the various zinc-carboxyphenylporphyrins. Experiments applying co-sensitization were done to elucidate the adsorption mode of the sensitizer. ZnMCPP, which was the most efficient dye in the DSCs from the first series, was further investigated using a simple mathematical model.

C.1. Theoretical Description

C.1.1. Working Principle

DSCs consist of different layers (Fig. C.1). The photoelectrode is made of a transparent substrate, e.g. glass, which is coated with a transparent conductive oxide (TCO) like fluorine doped tin oxide (FTO). A nanoporous titanium dioxide film with particle sizes of approximately $20\,\mathrm{nm}$ is deposited on top of it. Its surface is sensitized with a monolayer of dye molecules, which are bound to the titanium dioxide via anchoring groups. The interspace between the photoelectrode and the platinized counterelectrode is filled with an electrolyte. This electrolyte is often based on the I^-/I_3^- redox couple.[248,251]

When light impinges on the cell, electrons from the sensitizer are excited (see Eq. (1)) and injected into the conduction band (cb) of the titanium dioxide (see Eq. (2)). The oxidized dye is regenerated by the electrolyte (see Eq. (3)). Thereby $I_2^{-\cdot}$ develops, which disproportionates to I^-
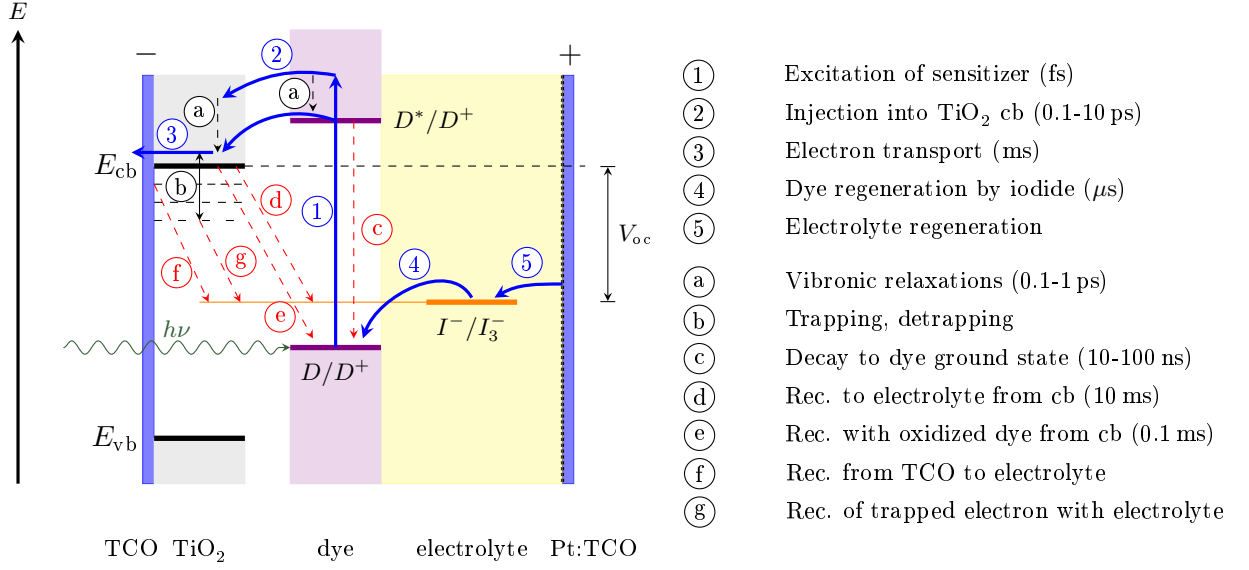
Figure C.1.: Schematic picture of a DSC. The desired electron transfer processes are indicated with blue arrows. Recombination pathways are shown as dashed red arrows. Typical times for the processes are given in the legend if available. The values were taken from [248–250].

and I_3^- (see Eq. (4)). The last-mentioned diffuses to the counterelectrode, where it is catalytically reduced to I^- by the platinum (see Eq. (5)).[252]

$$D + h\nu \rightarrow D^* \tag{1}$$

$$D^* \rightarrow D^+ + e^- (\text{TiO}_2) \tag{2}$$

$$D^+ + 2I^- \rightarrow D + I_2^{-\cdot} \tag{3}$$

$$2I_2^{-\cdot} \rightarrow I_3^- + I^- \tag{4}$$

$$I_3^- + 2e^- \rightarrow 3I^- \tag{5}$$

Electrons that have been injected to the titanium dioxide, are collected at the anode contact. The transport to the contact happens by multiple trapping and detrapping, since the mesoporous network exhibits a tail of trap states below the conduction band. Arrived at the front contact, the electrons flow through the outer circuit, where they perform work. After this they return to the cell at the counter electrode, whereby the current circuit is closed.

The desired electron transfer processes are impeded by recombination pathways as indicated in Fig. C.1. The balance of desired and undesired electron transfer processes determines the maximum current and voltage and thus the conversion efficiency η of a DSC. An upper limit is however given by the material parameter. For example the maximum open circuit voltage (V_{oc}) of the cell, which is the cell voltage under illumination when no current is flowing, is given by

the difference between the conduction band potential E_{cb} of the semiconductor and the redox potential $E_{\mathrm{F},0}$ of the electrolyte divided by the elementary charge q.

$$V_{\mathrm{oc,max}} = \frac{E_{\mathrm{cb}} - E_{\mathrm{F},0}}{q} \tag{C.1}$$

The theoretical limit of the current density J_{sc}, which is the current that is flowing when the cell is short-cut, is determined by the absorption coefficient $\alpha(\lambda)$ of the active layer and the illuminating photon flux $\phi(\lambda)$.

$$J_{\mathrm{sc,max}} = \int q\eta_{\mathrm{inj}}\alpha\mathrm{e}^{-(\alpha)x}\phi d\lambda \tag{C.2}$$

The actual values in the devices are lower, because they are also not only given by the properties of the single components but further influenced by the interaction between them.[253]

C.1.2. Recombination Processes

The key for high efficient DSCs is a high yield for the charge separation at the dye-semiconductor interface and a good charge transport. Both are limited by different recombination reactions (Fig. C.1). The first of them is the decay of the excited electron to the ground state, which might happen via vibronic relaxation and radiative decay or quenching of the excited dye by ions in the electrolyte.[253] Both processes are in the picosecond time range and thus ideally much slower than the electron injection into the conduction band.[250,252] After the electron has been injected into the conduction band, it can still recombine with the oxidized dye or, if the dye has already been regenerated, with electrolyte ions. It is unclear if this latter process happens only via the conduction band or if also trapped electrons could recombine. Because the electrolyte penetrates into the mesoporous $\mathrm{TiO_2}$ film this kind of recombination is also possible when the electron has traveled a certain distance in the semiconductor. The last possibility for recombination is at the FTO-electrolyte interface. This can strongly influence the conversion efficiency but can be blocked or reduced by deposition of a thin and compact titania covering layer.[254]

C.1.3. Charge Transport

The electronic structure of the mesoporous film exhibits intraband trap states that are caused by surface states, grain boundaries between particles and bulk defects. The electron transport in the titania is therefore no longer described by a pure diffusion model but by the multiple trapping (MT) model.[249] In this model charge transfer happens by multiple hopping between conduction band and trap states. The energy for the release to the conduction band is provided by thermal excitation or light absorption. Thus the electron collection efficiency, which is the probability that an injected electron reaches the photoanode, is still high.
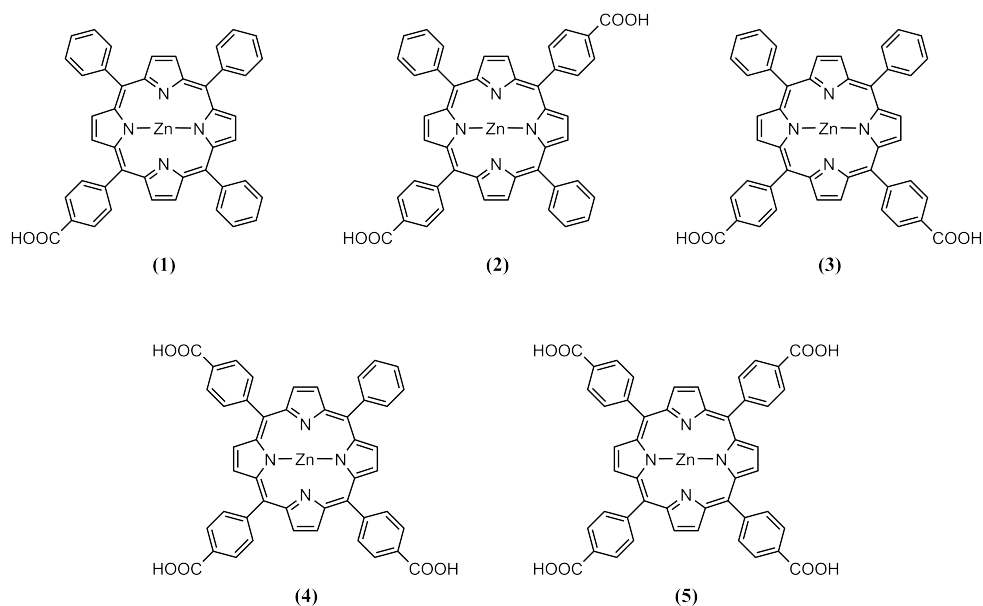
Figure C.2.: Stuctures of the Zn-carboxyphenylporphyrins used in this work.

C.2. Zn-carboxyphenylporphyrins as Sensitizers

The structures of the used Zn-carboxyphenylporphyrins are shown in Fig. C.2. In the first part of the experiments we tried to find and characterize the most efficient sensitizers out of these five. To further enhance the performance we systematically applied chenodeoxycholic acid (see Fig. C.3a) as co-adsorbate. This is supposed to minimize the interaction between single dye molecules and should improve the injection efficiency of the sensitizer as was e.g. shown for carotenoic acids.[255,256] In the second part we use additional methods such as external quantum efficiency, open circuit voltage decay and charge extraction measurements to get a detailed description of the cell and their material parameters. The results of these experiments were then used in a mathematical model to simulate current-voltage (IV) curves and compare them with the experimental ones.

C.3. Methods

C.3.1. Cell Assembly

If not otherwise noted, the DSCs were made out of materials supplied by Solaronix SA. The schematic setup for the DSC is shown in Fig. C.3b. Glass slides with fluorine doped tin oxide coating and with pre-deposited transparent, mesoporous titania layers (Solaronix electrodes, Art. 74111) with dimensions $6\,\text{mm} \times 6\,\text{mm} \times 10\,\mu\text{m}$ were heated to $500\,^{\circ}\text{C}$ for $15\,\text{min}$. After cooling-down, they were immersed in THF (Sigma Aldrich, reagent grade) based sensitizer solutions
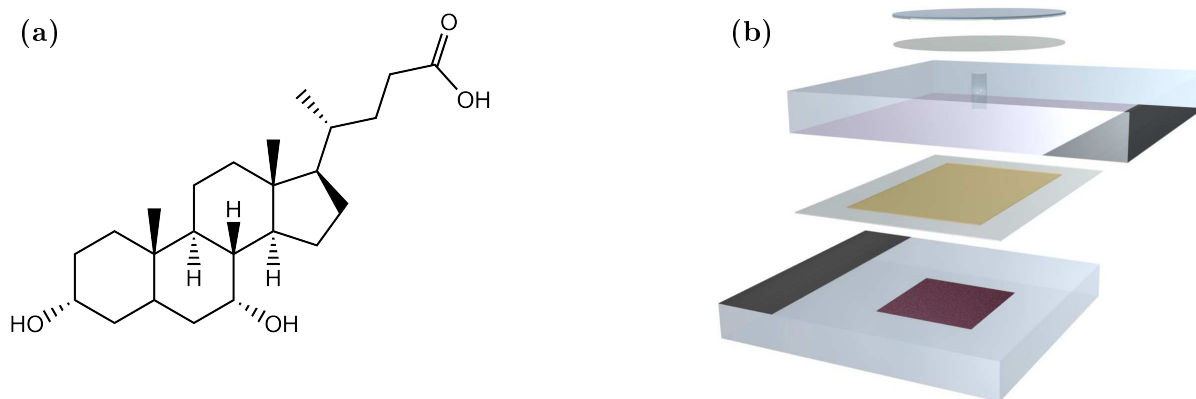
Figure C.3.: (a) Molecular structure of the chenodeoxycholic acid (cheno), which was used as co-sensitizer. **(b)** Schematic view of the DSC design used in our work. From bottom to top: photoanode with sensitized TiO$_2$ layer, surlyn sealing gasket with electrolyte, counterelectrode with hole for filling of the electrolyte, surlyn sealing and cover glass.

overnight. The various sensitizers are shown in Fig. C.2 and were gratefully received from the research group of Prof. Silvio Decurtins from University of Bern. In some cases chenodeoxycholic acid was used as co-sensitizer (Sigma Aldrich). For all the solutions, the total concentration of sensitizer and co-sensitizer was 0.5 mM. After sensitization the layers were rinsed with THF and dried under nitrogen flux. Counter electrodes with pre-deposited platinum catalyst (Solaronix electrode, Art. 74201), were activated by heating to 400 °C for 15 min. The photoanode and the counter electrode were glued together using surlyn sealing gaskets (Meltonix 1170-60). For this the stack of electrodes with the sealing gasket in between was heated through the counter electrode by applying a special soldering iron with 250 °C for 30 s. The electrolyte was inserted by vacuum back filling through a pre-drilled hole in the counter electrode. This hole was subsequently sealed with surlyn and a cover glass. For the first investigation of the influence of the co-adsorbate we used a home made electrolyte containing 0.1 M LiI, 50 mM I$_2$, 0.5 M 1-methylbenzimidazole and 0.6 M 1-butyl-3-methylimidazolium iodide in methoxypropionitrile. For the simulations, the DSC were filled with a commercial electrolyte (Iodolyte Z-50). The contact pads on each electrode were coated with high purity silver paint (Acheson Silver, DAG 1415) to improve the contact resistance.

C.3.2. IV-Characterization

Current-voltage (IV) curves were measured under standard AM1.5G light of a sun simulator (Sun 2000 Sun Simulator, ABET Technologies, AAB classification after ASTM E 927 standard) in combination with a home built IV curve tracer. During the measurement the cells were masked using a black cover with an aperture diameter of 5.5 mm.

C.3.3. External Quantum Efficiency

The external quantum efficiency is defined by the ratio of incoming photons to the number of collected electrons and given by

$$\eta_{\text{EQE}}(\lambda) = \frac{J_{\text{sc}}}{q\phi(\lambda)}. \tag{C.3}$$

It can be measured by shining monochromatic light to the cell while measuring the short circuit current. For the case of DSCs, the external quantum efficiency depends strongly on the light intensity. Therefore, it was measured using modulated monochromatic light in combination with a LED bias light simulating 1 sun illumination. The measurements were performed with a Spe-Quest quantum efficiency setup from Rera Systems, which was equipped with a 100 W halogen lamp, a $\lambda 300$ grating monochromator from Lot Oriel and a SR830 lock-in amplifier from Stanford Research. This setup was also used for the absorption measurements.

The transmission of single components as well as dummy cells was measured using the procedure from.[257]

C.3.4. Electrochemical Impedance Spectroscopy

For further investigation of the additive influence we applied electrochemical impedance spectroscopy (EIS). The experiments were performed with a DSSC Modulab Setup from Solartron. The recorded spectra were fitted using a standard transmission line model from literature.[258] The corresponding equivalent circuit is displayed in Fig. C.4. The impedance for this circuit is

$$Z = R_{\text{s}} + \left(\frac{1}{Z_{\text{TL}}} + \frac{1}{Z_{\text{BL}}} \right)^{-1} + Z_{\text{d}} + Z_{\text{Pt}}. \tag{C.4}$$

Z_{TL} is the impedance of the transmission line derived by[258]

$$Z_{\text{TL}} = \left(\frac{R_{\text{t}} R_{\text{r}}}{1 + (i\omega)^{\alpha} R_{\text{r}} C_{\mu}} \right)^{1/2} \coth \left(\frac{R_{\text{t}}}{R_{\text{r}}} \left(1 + (i\omega)^{\alpha} R_{\text{r}} C_{\mu} \right) \right)^{1/2}, \tag{C.5}$$
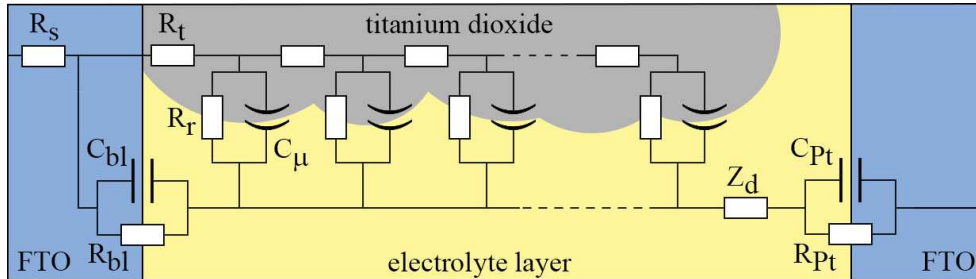
Figure C.4.: Equivalent circuit used for fitting of the impedance spectroscopy data. The titania electrolyte interface is modeled using a transmission line. The electrolyte FTO interfaces and the diffusion in the electrolyte are described by RC elements and a Warburg impedance element Z_{d}, respectively.

where R_s, R_r and R_t denote the serial, recombination and charge transfer resistance, respectively. C_μ is the chemical capacitance of the active layer and α is the exponent used for the constant phase elements. Z_d is the Warburg diffusion impedance[259,260]

$$Z_\text{d} = R_\text{d} \frac{\tanh \sqrt{(i\omega/\omega_\text{d})}}{\sqrt{(i\omega/\omega_\text{d})}}, \tag{C.6}$$

which describes the diffusion in the electrolyte, where R_d is the diffusion resistance of ions and ω_d is the characteristic frequency of the diffusion. The counter electrode and the interface between the anode and the electrolyte are described by simple RC elements with impedance Z_Pt and Z_BL, respectively.

C.3.5. Simulation using Matlab

Simple Mathematical Model

The previously described processes can be used to build up a mathematical model of DSCs. A complete description would contain the rate equations for all the different charge carriers in the cell, i.e. electrons in the titania, dye molecules and electrolyte ions, thus giving a set of coupled differential equations.[261] Here we only consider the most fundamental part, which are the electrons in the conduction band of the titania. The model equation that also accounts for an exponential tail of trap states below the conduction band is given by[261]

$$(1-\vartheta)\frac{\partial n_\text{cb}}{\partial t}\left(1 + m\beta \frac{N_\text{t}}{N_\text{cb}^{m\beta}} n_\text{cb}^{m\beta-1}\right) = \frac{1-\vartheta}{\omega^2}\gamma D_0 \frac{\partial^2 n_\text{cb}}{\partial x^2} + \int T_\text{FTO}\eta_\text{inj}\alpha_\text{s}e^{-(\alpha_\text{s}+\alpha_\text{r})x}\phi d\lambda - \frac{n_\text{cb} - n_\text{cb,0}}{\tau_0}. \tag{C.7}$$

This model only considers recombination of electrons in the conduction band to the electrolyte and assumes that this process is of first order. Furthermore, it is based on the quasi-static approximation, that assumes that hopping between the conduction band and the trap states is fast compared to other processes.[261,262] To apply this model we have to determine the parameters. The transmission of the FTO cover glass T_FTO as well as the absorption coefficients from the dye and the mixed electrolyte-titania phase, α_s and α_r, can be easily determined by transmission measurements of single components and dummy cells.[257] From quantum efficiency measurements one can deduce η_inj and the diffusion length L. L is directly related to the recombination lifetime τ_0 and the diffusion coefficient D_0 of electrons in the conduction band. The tailing parameter β of the trap states is defined by the trap state distribution given by

$$g(E_\text{F}) = \frac{N_\text{t}\beta}{k_\text{B}T}e^{\beta\frac{E-E_\text{cb}}{k_\text{B}T}}, \tag{C.8}$$

where N_t is the total density of trap states and E_F the Fermi energy level in the TiO$_2$. The parameter β can be determined from charge extraction measurements.[263] The non-ideality factor

m describes the deviation of the density of electrons in the conduction band n_{cb} from normal Boltzmann statistics.

$$n_{\mathrm{cb}}(E_{\mathrm{F}}) = N_{\mathrm{cb}} e^{\frac{E_{\mathrm{F}} - E_{\mathrm{cb}}}{m k_{\mathrm{B}} T}} \qquad (C.9)$$

Here N_{cb} is the density of states in the conduction band. The cell voltage is the difference between the redox energy level of the electrolyte $E_{\mathrm{F},0}$ and the Fermi level in the titania $E_{\mathrm{F,n}}$ divided by the elementary charge q

$$V = \frac{E_{\mathrm{F,n}} - E_{\mathrm{F,redox}}}{q}. \qquad (C.10)$$

Together with Eq. (C.9) we can express the cell voltage in terms of carrier densities.

$$V = \frac{m k_{\mathrm{B}} T}{q} \ln\left(\frac{n_{\mathrm{cb}}}{n_{\mathrm{cb},0}}\right) \qquad (C.11)$$

From this it follows that m can be determined by measuring the dependence of the open circuit voltage under different light intensities I and using

$$\frac{dV_{\mathrm{oc}}}{d\ln I} = \frac{m k_{\mathrm{B}} T}{q}. \qquad (C.12)$$

Estimation of the Diffusion Length and Injection Efficiency

The approach for the determination of the diffusion length and injection efficiency is based on the common diffusion equation for conduction band electrons under steady state conditions, which follows directly from the model in Eq. (C.7).[257, 264]

$$\frac{1-\vartheta}{\omega^2} \gamma D_0 \frac{\partial^2 n_{\mathrm{cb}}}{\partial x^2} + T_{\mathrm{FTO}} \eta_{\mathrm{inj}} \alpha_{\mathrm{s}} e^{-(\alpha_{\mathrm{s}} + \alpha_{\mathrm{r}})x} \phi - \frac{n_{\mathrm{cb}} - n_{\mathrm{cb},0}}{\tau_0} = 0 \qquad (C.13)$$

The porosity ϑ, the tortuosity ω and the constrictivity γ are material characteristics that account for the structure of the titania layer. We note that they are not explicitly needed. We can simply define a reduced diffusion constant $D_0^* = \frac{1-\vartheta}{\omega^2} \gamma D_0$, which can be used directly for the simulations later on. This model strictly assumes that η_{inj} and D_0^* are constants. In reality D_0^* and η_{inj} might depend on the Fermi level and the absorption wavelength, respectively. Eq. (C.13) can be solved analytically using the following approximate boundary conditions.[257]

$$n_{\mathrm{cb}}(0) = n_{\mathrm{cb},0} \qquad\qquad \frac{\partial}{\partial x} n_{\mathrm{cb}}(d) = 0$$

Here it is assumed that the electron transfer to the substrate is fast enough to keep the excess of electrons close to the dark equilibrium value.[264] An assumption that is sufficiently met for measurements done at short-circuit conditions. From the solution we readily calculate the EQE using Eq. (C.3) together with Fick's first law.

$$\eta_{\mathrm{EQE}} = \frac{D_0^*}{\phi} \frac{dn_{\mathrm{cb}}(0)}{dx} \qquad (C.14)$$

The values for α_s and α_r can be determined experimentally. If we substitute the diffusion length $L = \sqrt{(D_0^* \tau_0)}$, we receive η_{EQE} as a function of injection efficiency and diffusion length.[257]

$$\eta_{\mathrm{EQE}}(L, \eta_{\mathrm{inj}}) = \frac{T_{\mathrm{FTO}} L \eta_{\mathrm{inj}} \alpha_s \mathrm{e}^{-\alpha_{\mathrm{tot}}d} \left((L\alpha_{\mathrm{tot}} - 1) \mathrm{e}^{\left(\alpha_{\mathrm{tot}} + \frac{2}{L}\right)d} + (L\alpha_{\mathrm{tot}} + 1) \mathrm{e}^{\alpha_{\mathrm{tot}}d} - 2L\alpha_{\mathrm{tot}} \mathrm{e}^{\frac{d}{L}} \right)}{(\mathrm{e}^{\frac{2d}{L}} + 1) \left(L^2 \alpha_{\mathrm{tot}}^2 - 1 \right)}$$

(C.15)

where $\alpha_{\mathrm{tot}} = \alpha_s + \alpha_r$. A fit to this equation allows retrieving the injection efficiency and the diffusion length as fit parameters.

Estimation of Remaining Parameters

For the simulation of IV curves there is still one missing parameter, which is the electron lifetime τ_0. This parameter can be obtained by fitting the open circuit voltage decay to Eq. (C.16) from Peter et al. that has the from[265, 266]

$$V_{\mathrm{oc}} = -\frac{mk_{\mathrm{B}}T}{q(1 - m\beta)} \ln (c_1 + c_2 t)$$

(C.16)

$$c_1 = \exp\left\{ \frac{(m\beta - 1)qV_{\mathrm{oc}}(0)}{mk_{\mathrm{B}}T} \right\}$$

(C.17)

$$c_2 = \tau_0^{-1} (1 - m\beta) \frac{N_{\mathrm{cb}}}{N_{\mathrm{t}} m\beta} \left(\frac{n_{\mathrm{cb},0}}{N_{\mathrm{cb}}} \right)^{1 - m\beta}$$

(C.18)

For this we assumed that the conduction band is $0.85\,\mathrm{V}$ above the redox energy level of the electrolyte. Using Eq. (C.11), we can directly give $N_{\mathrm{cb}}/n_{\mathrm{cb},0}$. With this guess we additionally calculated the total trap state density N_{t}, thus the number of fitting constants in Eq. (C.16) was minimized to two, namely τ_0 and N_{cb}.

Simulation of IV-Curves

For the simulation of IV-curves we used the steady state form of Eq. (C.7)

$$0 = \frac{1 - \vartheta}{\omega^2} \gamma D_0 \frac{\partial^2 n_{\mathrm{cb}}}{\partial x^2} + \int T_{\mathrm{FTO}} \eta_{\mathrm{inj}} \alpha_s \mathrm{e}^{-(\alpha_s + \alpha_r)x} \phi d\lambda - \frac{n_{\mathrm{cb}} - n_{\mathrm{cb},0}}{\tau_0}$$

(C.19)

and solved it on the desired interval of voltages using the ode45 solver function from matlab. For each voltage we used the mixed boundary condition

$$n_{\mathrm{cb}}(x = 0) = n_{\mathrm{cb},0} \mathrm{e}^{\frac{qV_{oc}}{mk_{\mathrm{B}}T}}, \qquad\qquad \frac{d}{dx} n_{\mathrm{cb}}(x = d) = 0.$$

Since the solver can only handle boundary conditions of the type $n_{\mathrm{cb}}(x) = a$ and $n'_{\mathrm{cb}}(x) = b$ we applied a shooting method on the solver which uses an estimated initial $n'_{\mathrm{cb}}(0)$ to calculate the corresponding $n'_{\mathrm{cb}}(d)$. The estimate is iteratively changed till the calculated $n'_{\mathrm{cb}}(d)$ fits with the desired boundary conditions. In this case the solver outputs the correct solution for our boundary value problem due to the uniqueness of the solution of this differential equation.

C.4. Results and Discussion

C.4.1. IV-Characterization

Tab. C.1 shows the IV-characteristics of the DSCs without any additive. Cells that use ZnCPPs with more than one carboxylic group have lower efficiency than ZnMCPP. Due to the number of carboxylic anchors the other dyes can have more binding modes, that also support flat adsorption geometries that are more coupled to the substrate and maybe not that efficient (or even inactive). One could further argue that those modes need more space thus less dye can be bound. This would be consistent with the lower short-circuit current densities and open circuit voltages of the cells.

In order to avoid $\pi - \pi$ interaction of the porphyrins we optimized the ZnMCPP cell using chenodeoxycholic acid as co-sensitizer. The IV-characteristics of the DSCs made with different ratios of additive to dye concentration are depicted in Tab. C.2. We observed that the efficiency increases up to a certain additive-dye ratio. The peak efficiency was obtained for the cells with 40 % additive. η was improved by 11 %. Thus by decreasing the dye loading with co-adsorption the single molecules get more efficient, implying that the interaction between them was indeed lowering the cell efficiency. If the amount of additive is further increased (more than 60 %) the cell shows low efficiency because of too low dye coverage. Application of the additive to the other ZnCPPs did not boost their performance. The parameters from IV-measurements are gathered

Table C.1.: IV-characterization of DSCs sensitized with different ZnCPPs (without additive)

Dye	V_{oc} [mV]	J_{sc} [$\frac{\mathrm{mA}}{\mathrm{cm}^2}$]	FF [%]	η [%]
ZnMCPP (**1**)	545.1 ± 3.5	2.04 ± 0.19	68.7 ± 0.8	0.76 ± 0.07
cis-ZnDCPP (**2**)	473.8 ± 13.6	0.96 ± 0.17	59.9 ± 2.8	0.27 ± 0.07
tr-ZnDCPP (**3**)	440.3 ± 17.3	0.51 ± 0.02	49.1 ± 6.5	0.11 ± 0.02
ZnTrCPP (**4**)	487.1 ± 7.3	1.45 ± 0.11	61.8 ± 3.9	0.44 ± 0.07
ZnTCPP (**5**)	454.1 ± 3.5	0.76 ± 0.07	55.7 ± 3.1	0.19 ± 0.02

Table C.2.: IV-characterization of DSCs sensitized with ZnMCPP and different amounts of cheno.

Dye [mM]	Cheno [mM]	V_{oc} [mV]	J_{sc} [$\frac{\mathrm{mA}}{\mathrm{cm}^2}$]	FF [%]	η [%]
0.5	0	545.1 ± 3.5	2.04 ± 0.19	68.7 ± 0.8	0.76 ± 0.07
0.4	0.1	550.8 ± 7.1	2.04 ± 0.14	68.7 ± 1.7	0.78 ± 0.07
0.3	0.2	550.0 ± 4.2	2.20 ± 0.16	69.9 ± 0.6	0.85 ± 0.07
0.2	0.3	540.8 ± 10.4	1.81 ± 0.30	67.8 ± 3.8	0.67 ± 0.16
0.1	0.4	510.2 ± 7.7	1.06 ± 0.14	63.2 ± 3.8	0.35 ± 0.07

Table C.3.: IV-characterization of DSCs sensitized with 0.3 mM of different ZnCPPs and 0.2 mM cheno.

Dye	V_{oc} [mV]	J_{sc} [$\frac{mA}{cm^2}$]	FF [%]	η [%]
ZnMCPP (**1**)	550.0 ± 4.2	2.20 ± 0.16	69.9 ± 0.6	0.85 ± 0.07
cis-ZnDCPP (**2**)	391.2 ± 38.5	0.37 ± 0.09	37.7 ± 2.5	0.06 ± 0.02
tr-ZnDCPP (**3**)	407.7 ± 42.2	0.36 ± 0.22	40.9 ± 9.6	0.08 ± 0.07
ZnTrCPP (**4**)	480.1 ± 8.8	1.02 ± 0.12	60.1 ± 3.0	0.30 ± 0.05
ZnTCPP (**5**)	449.6 ± 7.4	0.59 ± 0.09	51.9 ± 4.1	0.14 ± 0.03

in Tab. C.3. This is presumably due to the case that there is hardly any stacking because of flat adsorption geometries. Hence we conclude that the co-adsorption only decreased the dye loading but did not change the injection properties of the sensitizer molecules.

C.4.2. Electrochemical Impedance Spectroscopy

Spectra were recorded for five different light intensities in order to evaluate the variation of the fit parameters versus the cell potential. Three DSCs were assembled and measured for each configuration. Fig. C.5a shows a typical impedance spectra and the corresponding fit to the complete transmission line model (see Fig. C.4). The most important fit parameter is the recombination resistance R_r, which is given in Fig. C.5b. The main conclusion from this graph is that R_r increases with the addition of the co-adsorbate, meaning injected electrons recombine less. Thus the open circuit voltage could also be increased by about 30 mV for the case of the optimized DSC with 40 % chenodeoxycholic acid. It has to be noted that this increase mainly comes from
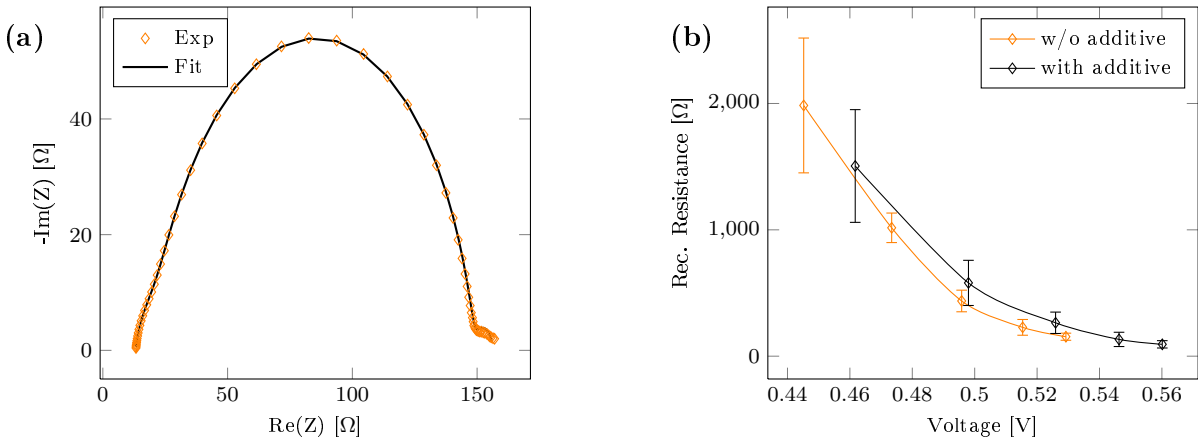
Figure C.5.: (a) Typical EIS spectra of a ZnMCPP sensitized solar cell. **(b)** Dependence of the recombination resistance on the cell potential for a ZnMCPP cell without and with cheno as co-adsorbate (dye:cheno=3:2).

the improved recombination and injection kinetics, since the conduction band was hardly shifted by the addition of chenodeoxycholic acid, as was found when plotting the chemical capacitance vs. the cell potential (not shown).

C.4.3. Simulation of DSCs with Matlab

Optical Characterization

The optical absorption spectra of the different DSC components are shown in Fig. C.6a. The titania as well as the electrolyte only show absorption for short wavelengths, i.e. below 450 nm. The porphyrin shows its main absorption at 430 nm with two smaller side bands at approximately 565 nm and 610 nm. We note that in order to get the correct spectra for the sensitizer it is essential to measure it on the titania together with the electrolyte. For accurate absorption values one has to use thin films with thicknesses $d < 1\,\mu m$. Otherwise, saturation effects are likely to occur.

Quantum Efficiency

The experimental EQE as well as the fit to Eq. (C.15) are depicted in Fig. C.6b. Fitting of the whole experimental curve was not possible with the applied model. Fit to different regions of the spectra imply that η_{inj} increases for shorter wavelength. For the simulation we used only the fit that matched with the long wavelength region. The physical origin of this observation could be that highly excited electrons from the sensitizer are directly injected to the conduction band without thermalizing to the LUMO thus using an additional injection channel.

Charge Extraction

Charge extraction measurements were done in order to determine the tailing parameter β of the trap state distribution described in Eq. (C.8). The fit to the experimental results, which was done in the low voltage region to avoid contribution of charge carriers from the conduction band, is shown in Fig. C.6c. We note that the received β=0.175 is lower than common literature values by about a factor of two.[261, 266, 267] Since our cells did not employ a blocking layer at the FTO front contact our β might have been underestimated, then in this case not all the charge carriers from the traps are collected.

Illumination Dependence of Open Circuit Voltage

The non-ideality factor m was determined by a linear fit of V_{oc} vs. illumination intensity curves. The slope of the fit is related to m by Eq. (C.12). As can be seen from Fig. C.6d the slope of the experimental curve is not constant. For medium light intensities the fit gave m=4.12 ± 0.31 For the high intensities we got m=1.85. We note that the first value is quite large compared to literature values of around 1-1.5, which is most probably due to recombination via the FTO at the

(a)

(b)

(c)

(d)
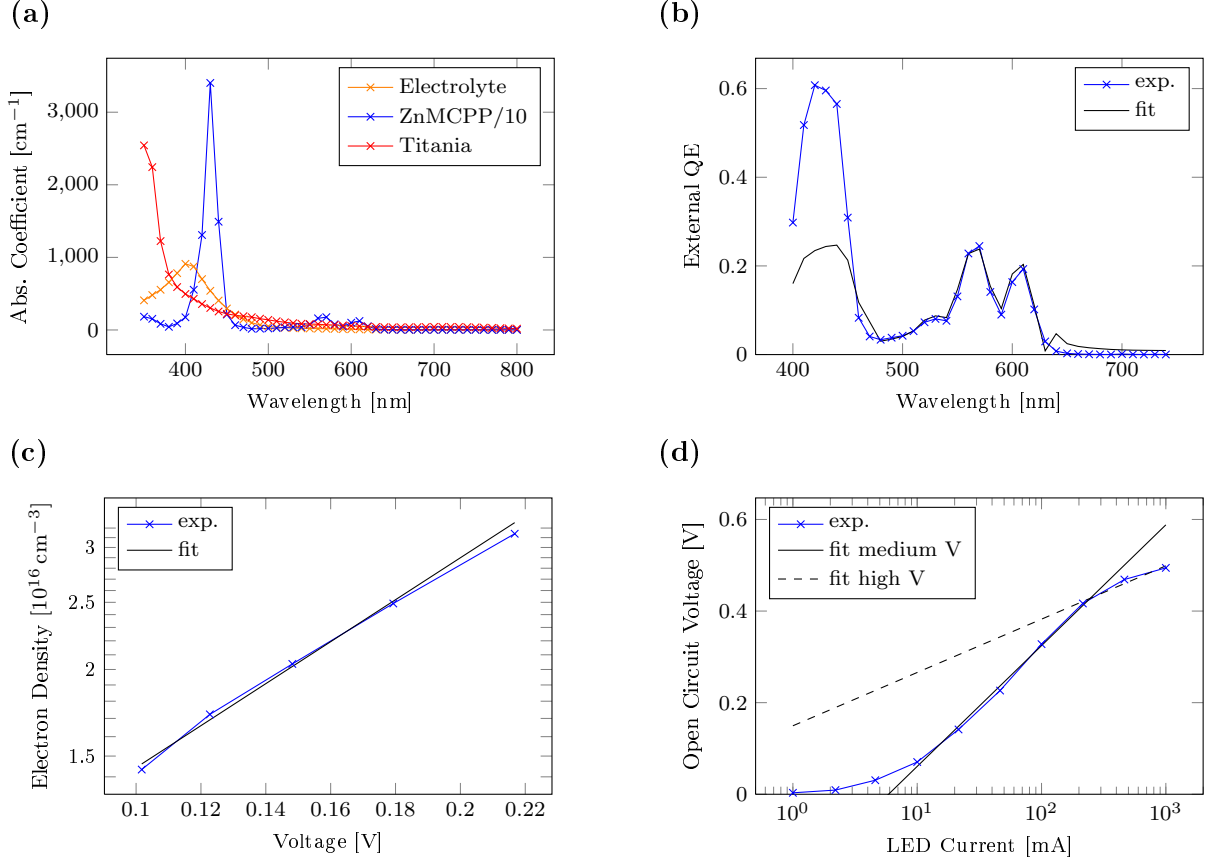
Figure C.6.: **(a)** Absorption coefficients of the different components. **(b)** Fit of the experimental EQE to Eq. (C.15). The fit results apply only for a limited fitting interval of 450–650 nm. **(c)** Extracted charge carrier density of traps states and corresponding fit for the determination of the tailing parameter β. **(d)** Illumination dependence of the open circuit voltage.

anode contact as observed by Peter an co-workers.[268] Since the influence of this recombination is small at higher voltages we used m=1.85 for the input of the simulations. For more detailed studies one should consider to prevent the recombination at the photoanode contact by depositing compact TiO_2 blocking layers on the FTO.

Open Circuit Voltage Decay

The electron lifetime τ_0 was determined from the open circuit voltage decay by using Eq. (C.16). For this fit we used a total trap density of $2.7 \times 10^{18}\,cm^{-3}$. The density of conduction band states and the electron lifetime were calculated to N_{cb}=$2.17 \times 10^{18}\,cm^{-3}$ and τ=$1.56 \times 10^{-4}\,s$, respectively. Compared to the value of N_{cb}=$7.26 \times 10^{17}\,cm^{-3}$, which was calculated from the
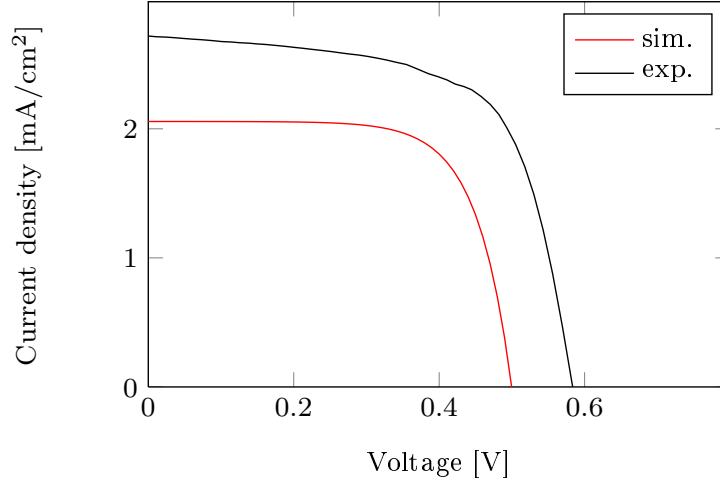
Figure C.7.: Comparison of an experimental and a simulated IV-curve for a ZnMCPP sensitized DSC.

literature value of the averaged effective mass of $m_{\mathrm{e}}^*/m_{\mathrm{e}}$=0.0948,[168] our value is too high. This could mean that our guess for $E_{\mathrm{cb}} - E_{\mathrm{F,redox}}$=0.85 V was slightly too high. Nevertheless, we found that modifying this assumption did hardly influence the outcome of the simulated IV-curve.

Simulation

The experimental and simulated IV-curves are shown in Fig. C.7. We observe that the experimental current density and open circuit voltage are higher than the simulated ones. The difference in current might be due to the fact that the injection efficiency for the high energy photons was underestimated. This could also partly explain the difference in V_{oc}. Additionally we found that the V_{oc} strongly depends on m. As shown in Fig. C.6d the non-ideality factor m is not constant. We only used the value that applies for high cell potentials. One could argue that an effective, meaning average, m should be used instead. This would increase the V_{oc} and lead to a better match between experiment and simulation.

Somehow, it is clear that an effective m would not lead to a better description of the DSC. To further improve the simulations we have to reconsider the assumptions of the model. For the recombination order of electrons to the electrolyte we took $b = 1$. This is just the simplest way to describe the recombination. In reality, the chemistry and kinetics of the recombination are more intricate and could be modeled with $b \neq 1$. The b can be determined from the effective electron lifetime τ_n, which can be calculated from open circuit voltage decay measurements. The lifetime is defined by[269]

$$\frac{1}{\tau_n} = -\frac{1}{n}\frac{dn}{dt}.$$

Together with Eq. (C.11) we obtain

$$\tau_n = \frac{mk_BT}{q}\left(\frac{dV_{oc}}{dt}\right)^{-1}. \tag{C.20}$$

In order to determine the reaction order we remember the general model for the recombination given by[269]

$$\frac{dn_{cb}}{dt} \cong -kn_{cb}^b,$$

where k is the reaction rate constant. Using Eq. (C.20), the effective electron lifetime becomes

$$\tau_n = \frac{1}{kn_{cb}^{b-1}}.$$

Combining this with Eq. (C.11) yields

$$b = 1 - \frac{mk_BT}{q}\frac{d\ln\tau_n}{dV_{oc}}. \tag{C.21}$$

If we consider b in our model it can be shown that Eq. (C.12) is modified to

$$\frac{dV_{oc}}{d\ln I} = \frac{m}{b}\frac{k_BT}{q}, \tag{C.22}$$

and thus m can no longer be determined directly from the illumination dependence of the open circuit voltage. Nevertheless, m can be calculated by combining Eq. (C.22) and Eq. (C.21). The received m can be used to get b.

For more accurate calculations one would have to consider that b and k depend on the potential.[269] The physical origin comes from the possibility of changing recombination pathways with respect to cell potential.[268]

C.5. Summary

From the investigation of the zinc-carboxyphenylporphyrins in DSCs, we found that the best conversion efficiency is achieved for ZnMCPP. From the experiments with chenodeoxycholic acid as co-adsorbate we concluded that this dye most probably adopted a standing adsorption configuration that minimized the coupling of the substrate with the sensitizer and that allows a higher coverage. The insights from the simulation elucidate the general cell setup. We found that the non-ideality factor m is not constant as assumed by the model. This was generally interpreted as a high recombination at the photo anode contact, which should be prevented in future experiments by deposition of a compact blocking layer on the FTO.[268] This presumably allows getting more accurate results from the other experimental methods that could then be analyzed using the expanded model with non-linear recombination. Another drawback of the model is the assumption of constant η_{inj} for the evaluation of the quantum efficiency spectra. The fit results imply that

there are at least two injection channels. However, this finding cannot be implemented easily into the model since more information about the electronic structure at the interface is necessary. Overall the simulation helped to get a more detailed understanding of the ZnMCPP sensitized cell. The examination might be time consuming. Nevertheless, this combined experimental and mathematical approach is beneficial. Even though the model might not apply to the experimental facts in the beginning it facilitated a more complete and systematic analysis of the DSCs and their working principles.

Bibliography

[1] R. P. Feynman, There is plenty of room at the bottom, Talk to the APS in Pasadena, 1959.

[2] G. Binnig, H. Rohrer, C. Gerber, E. Weibel, Surface Studies by Scanning Tunneling Microscopy, *Phys. Rev. Lett.* **49**, 57-61 (1982), doi:10.1103/PhysRevLett.49.57.

[3] G. Binnig, C. F. Quate, C. Gerber, Atomic Force Microscope, *Phys. Rev. Lett.* **56**, 930-933 (1986), doi:10.1103/PhysRevLett.56.930.

[4] J. A. Stroscio D. M. Eigler, Atomic and Molecular Manipulation with the Scanning Tunneling Microscope, *Science* **254**, 1319-1326 (1991), doi:10.1126/science.254.5036.1319.

[5] O. Custance, R. Perez, S. Morita, Atomic Force Microscopy as a Tool for Atom Manipulation, *Nat. Nano.* **4**, 803-810 (2009), doi:10.1038/nnano.2009.347.

[6] R. Pawlak, S. Fremy, S. Kawai, T. Glatzel, H. Fang, et al., Directed Rotations of Single Porphyrin Molecules Controlled by Localized Force Spectroscopy, *ACS Nano* **6**, 6318-6324 (2012), doi:10.1021/nn301774d.

[7] S. Kawai, A. S. Foster, F. F. Canova, H. Onodera, S.-I. Kitamura, et al., Atom Manipulation on an Insulating Surface at Room Temperature, *Nat. Commun.* **5**, 4403(1-7) (2014), doi:10.1038/ncomms5403.

[8] G. Whitesides, J. Mathias, C. Seto, Molecular Self-Assembly and Nanochemistry: A Chemical Strategy for the Synthesis of Nanostructures, *Science* **254**, 1312-1319 (1991), doi:10.1126/science.1962191.

[9] J. V. Barth, J. Weckesser, C. Cai, P. Günter, L. Bürgi, et al., Building Supramolecular Nanostructures at Surfaces by Hydrogen Bonding, *Angew. Chem., Int. Ed.* **39**, 1230-1234 (2000), doi:10.1002/(SICI)1521-3773(20000403)39:7<1230::AID-ANIE1230>3.0.CO;2-I.

[10] T. Yokoyama, S. Yokoyama, T. Kamikado, Y. Okuno, S. Mashiko, Selective Assembly on a Surface of Supramolecular Aggregates with Controlled Size and Shape, *Nature* **413**, 619-621 (2001), doi:10.1038/35098059.

[11] J. A. Theobald, N. S. Oxtoby, M. A. Phillips, N. R. Champness, P. H. Beton, Controlling Molecular Deposition and Layer Structure with Supramolecular Surface Assemblies, *Nature* **424**, 1029-1031 (2003), doi:10.1038/nature01915.

[12] S. Stepanow, M. Lingenfelder, A. Dmitriev, H. Spillmann, E. Delvigne, et al., Steering Molecular Organization and Host-Guest Interactions Using Two-Dimensional Nanoporous Coordination Systems, *Nat. Mater.* **3**, 229-233 (2004), doi:10.1038/nmat1088.

[13] J. V. Barth, Molecular Architectonic on Metal Surfaces, *Annu. Rev. Phys. Chem.* **58**, 375-407 (2007), doi:10.1146/annurev.physchem.56.092503.141259.

[14] A. Kühnle, Self-Assembly of Organic Molecules at Metal Surfaces, *Curr. Opin. Colloid Interface Sci.* **14**, 157-168 (2009), doi:10.1016/j.cocis.2008.01.001.

[15] J. S. Lindsey, Self-Assembly in Synthetic Routes to Molecular Devices. Biological Principles and Chemical Perspectives: A Review, *New J. Chem.* **15**, 153-180 (1991), .

[16] K. E. Drexler, Molecular Nanomachines: Physical Principles and Implementation Strategies, *Annu. Rev. Biophys. Biomol. Struct.* **23**, 377-405 (1994), doi:10.1146/annurev.bb.23.060194.002113.

[17] G. Ozin, I. Manners, S. Fournier-Bidoz, A. Arsenault, Dream Nanomachines, *Adv. Mater.* **17**, 3011-3018 (2005), doi:10.1002/adma.200501767.

[18] B. O'Regan M. Grätzel, A Low-Cost, High-Efficiency Solar-Cell Based on Dye-Sensitized Colloidal TiO_2 Films, *Nature* **353**, 737-740 (1991), doi:10.1038/353737a0.

[19] M. Jurow, A. E. Schuckman, J. D. Batteas, C. M. Drain, Porphyrins as Molecular Electronic Components of Functional Devices, *Coord. Chem. Rev.* **254**, 2297-2310 (2010), doi:10.1016/j.ccr.2010.05.014.

[20] R. Zhang, A. A. Elzatahry, S. S. Al-Deyab, D. Zhao, Mesoporous Titania: From Synthesis to Application, *Nano Today* **7**, 344-366 (2012), doi:10.1016/j.nantod.2012.06.012.

[21] G. Huyang, J. Canning, M. L. Åslund, M. Naqshbandi, B. Gibson, et al., Porphyrin-Doped Solgel-Lined Structured Optical Fibers for Local and Remote Sensing, *Opt. Lett.* **36**, 1975-1977 (2011), doi:10.1364/OL.36.001975.

[22] M. K. Nazeeruddin, D. Di Censo, R. Humphry-Baker, M. Grätzel, Highly Selective and Reversible Optical, Colorimetric, and Electrochemical Detection of Mercury(II) by Amphiphilic Ruthenium Complexes Anchored onto Mesoporous Oxide Films, *Adv. Funct. Mater.* **16**, 189-194 (2006), doi:10.1002/adfm.200500309.

[23] B. Borca, V. Schendel, R. Pétuya, I. Pentegov, T. Michnowicz, et al., Bipolar Conductance Switching of Single Anthradithiophene Molecules, *ACS Nano* **9**, 12506-12512 (2015), doi:10.1021/acsnano.5b06000.

[24] M. J. Comstock, N. Levy, A. Kirakosian, J. Cho, F. Lauterwasser, et al., Reversible Photomechanical Switching of Individual Engineered Molecules at a Metallic Surface, *Phys. Rev. Lett.* **99**, 038301(1-4) (2007), doi:10.1103/PhysRevLett.99.038301.

[25] V. Schendel, B. Borca, I. Pentegov, T. Michnowicz, U. Kraft, et al., Remotely Controlled Isomer Selective Molecular Switching, *Nano Lett.* **16**, 93-97 (2016), doi:10.1021/acs.nanolett.5b02974.

[26] A. Yella, H.-W. Lee, H. N. Tsao, C. Yi, A. K. Chandiran, et al., Porphyrin-Sensitized Solar Cells with Cobalt (II/III) Based Redox Electrolyte Exceed 12 Percent Efficiency, *Science* **334**, 629-634 (2011), doi:10.1126/science.1209688.

[27] F. De Angelis, S. Fantacci, A. Selloni, M. Grätzel, M. K. Nazeeruddin, Influence of the Sensitizer Adsorption Mode on the Open-Circuit Potential of Dye-Sensitized Solar Cells, *Nano Lett.* **7**, 3189-3195 (2007), doi:10.1021/nl071835b.

[28] R. Ambre, K.-B. Chen, C.-F. Yao, L. Luo, E. W.-G. Diau, et al., Effects of Porphyrinic meso-Substituents on the Photovoltaic Performance of Dye-Sensitized Solar Cells: Number and Position of p-Carboxyphenyl and Thienyl Groups on Zinc Porphyrins, *J. Phys. Chem. C* **116**, 11907-11916 (2012), doi:10.1021/jp302145x.

[29] R. B. Ambre, G.-F. Chang, C.-H. Hung, Three p-Carboxyphenyl Groups Possessing Zinc Porphyrins: Efficient, Stable, and Cost-Effective Sensitizers for Dye-Sensitized Solar Cells, *Chem. Commun.* **50**, 725-727 (2014), doi:10.1039/C3CC47985D.

[30] J. Rochford, D. Chu, A. Hagfeldt, E. Galoppini, Tetrachelate Porphyrin Chromophores for Metal Oxide Semiconductor Sensitization: Effect of the Spacer Length and Anchoring Group Position, *J. Am. Chem. Soc.* **129**, 4655-4665 (2007), doi:10.1021/ja068218u.

[31] W. Auwärter, D. Écija, F. Klappenberger, J. V. Barth, Porphyrins at Interfaces, *Nat. Chem.* **7**, 105-120 (2015), doi:10.1038/nchem.2159.

[32] F. Rosei, M. Schunack, Y. Naitoh, P. Jiang, A. G. Gourdon, et al., Properties of Large Organic Molecules on Metal Surfaces, *Prog. Surf. Sci.* **71**, 95-146 (2003), doi:10.1016/S0079-6816(03)00004-2.

[33] C. J. Villagomez, T. Zambelli, S. Gauthier, A. Gourdon, S. Stojkovic, et al., {STM} Images of a Large Organic Molecule Adsorbed on a Bare Metal Substrate or on a thin Insulating Layer: Visualization of {HOMO} and {LUMO}, *Surf. Sci.* **603**, 1526-1532 (2009), doi:10.1016/j.susc.2008.10.057.

[34] L. Gross, F. Mohn, N. Moll, P. Liljeroth, G. Meyer, The Chemical Structure of a Molecule Resolved by Atomic Force Microscopy, *Science* **325**, 1110-1114 (2009), doi:10.1126/science.1176210.

[35] L. Gross, Recent Advances in Submolecular Resolution with Scanning Probe Microscopy, *Nat. Chem.* **3**, 273-278 (2011), doi:10.1038/nchem.1008.

[36] S. Kawai, A. Sadeghi, X. Feng, P. Lifen, R. Pawlak, et al., Obtaining Detailed Structural Information about Supramolecular Systems on Surfaces by Combining High-Resolution Force Microscopy with ab Initio Calculations, *ACS Nano* **7**, 9098-9105 (2013), doi:10.1021/nn403672m.

[37] S. Kawai, A. Sadeghi, F. Xu, L. Peng, A. Orita, et al., Extended Halogen Bonding between Fully Fluorinated Aromatic Molecules, *ACS Nano* **9**, 2574-2583 (2015), doi:10.1021/nn505876n.

[38] B. Schuler, G. Meyer, D. P. na, O. C. Mullins, L. Gross, Unraveling the Molecular Structures of Asphaltenes by Atomic Force Microscopy, *J. Am. Chem. Soc.* **137**, 9870-9876 (2015), doi:10.1021/jacs.5b04056.

[39] C. Moreno, O. Stetsovych, T. K. Shimizu, O. Custance, Imaging Three-Dimensional Surface Objects with Submolecular Resolution by Atomic Force Microscopy, *Nano Lett.* **15**, 2257-2262 (2015), doi:10.1021/nl504182w.

[40] K. Iwata, S. Yamazaki, P. Mutombo, P. Hapala, M. Ondracek, et al., Chemical Structure Imaging of a Single Molecule by Atomic Force Microscopy at Room Temperature, *Nat. Commun.* **6**, 7766(1-7) (2015), doi:10.1038/ncomms8766.

[41] M. Schunack, L. Petersen, A. Kühnle, E. Lægsgaard, I. Stensgaard, et al., Anchoring of Organic Molecules to a Metal Surface: HtBDC on Cu(110), *Phys. Rev. Lett.* **86**, 456-459 (2001), doi:10.1103/PhysRevLett.86.456.

[42] S. Fortuna, P. Gargiani, M. G. Betti, C. Mariani, A. Calzolari, et al., Molecule-Driven Substrate Reconstruction in the Two-Dimensional Self-Organization of Fe-Phthalocyanines on Au(110), *J. Phys. Chem. C* **116**, 6251-6258 (2012), doi:10.1021/jp211036m.

[43] A. Höfer, K. Duncker, M. Kiel, S. Wedekind, W. Widdra, Adsorption of α-Sexithiophene on Au(001): Molecule-Induced Partial Lifting of the Substrate Reconstruction, *Phys. Rev. B* **83**, 075414(1-7) (2011), doi:10.1103/PhysRevB.83.075414.

[44] T. Trevethan, B. Such, T. Glatzel, S. Kawai, A. L. Shluger, et al., Organic Molecules Reconstruct Nanostructures on Ionic Surfaces, *Small* **7**, 1264-1270 (2011), doi:10.1002/smll.201001910.

[45] M. A. Filler S. F. Bent, The Surface as Molecular Reagent: Organic Chemistry at the Semiconductor Interface, *Prog. Surf. Sci.* **73**, 1-56 (2003), doi:10.1016/S0079-6816(03)00035-2.

[46] C. L. Pang, R. Lindsay, G. Thornton, Chemical Reactions on Rutile TiO$_2$(110), *Chem. Soc. Rev.* **37**, 2328-2353 (2008), doi:10.1039/B719085A.

[47] S. P. Pujari, L. Scheres, A. T. M. Marcelis, H. Zuilhof, Covalent Surface Modification of Oxide Surfaces, *Angew. Chem., Int. Ed.* **53**, 6322-6356 (2014), doi:10.1002/anie.201306709.

[48] L. Zhang J. M. Cole, Anchoring Groups for Dye-Sensitized Solar Cells, *ACS Appl. Mater. Interfaces* **7**, 3427-3455 (2015), doi:10.1021/am507334m.

[49] T. Toledano, R. Garrick, O. Sinai, T. Bendikov, A.-E. Haj-Yahia, et al., Effect of Binding Group on Hybridization Across the Silicon/Aromatic-Monolayer Interface, *J. Electron Spectrosc. Relat. Phenom.* **204, Part A**, 149-158 (2015), doi:10.1016/j.elspec.2015.05.019.

[50] G. Nesher, H. Shpaisman, D. Cahen, Effect of Chemical Bond Type on Electron Transport in GaAs-Chemical Bond-Alkyl/Hg Junctions, *J. Am. Chem. Soc.* **129**, 734-735 (2007), doi:10.1021/ja065399r.

[51] E. Leary, A. La Rosa, M. T. Gonzalez, G. Rubio-Bollinger, N. Agrait, et al., Incorporating Single Molecules into Electrical Circuits. The Role of the Chemical Anchoring Group, *Chem. Soc. Rev.* **44**, 920-942 (2015), doi:10.1039/C4CS00264D.

[52] Y. Xue, X. Li, H. Li, W. Zhang, Quantifying Thiol-Gold Interactions Towards the Efficient Strength Control, *Nat. Commun.* **5**, 4348(1-9) (2014), doi:10.1038/ncomms5348.

[53] T. A. Su, M. Neupane, M. L. Steigerwald, L. Venkataraman, C. Nuckolls, Chemical Principles of Single-Molecule Electronics, *Nat. Rev. Mater.* **1**, 1-15 (2016), doi:10.1038/natrevmats.2016.2.

[54] E. Galoppini, Linkers for Anchoring Sensitizers to Semiconductor Nanoparticles, *Coord. Chem. Rev.* **248**, 1283 - 1297 (2004), doi:10.1016/j.ccr.2004.03.016.

[55] W. Liu, A. Tkatchenko, M. Scheffler, Modeling Adsorption and Reactions of Organic Molecules at Metal Surfaces, *Acc. Chem. Res.* **47**, 3369-3377 (2014), doi:10.1021/ar500118y.

[56] N. Atodiresei, V. Caciuc, P. Lazić, S. Blügel, Chemical Versus van der Waals Interaction: The Role of the Heteroatom in the Flat Absorption of Aromatic Molecules C_6H_6, C_5NH_5 and $C_4N_2H_4$ on the Cu(110) Surface, *Phys. Rev. Lett.* **102**, 136809(1-4) (2009), doi:10.1103/PhysRevLett.102.136809.

[57] M. Kittelmann, P. Rahe, A. Gourdon, A. Kühnle, Direct Visualization of Molecule Deprotonation on an Insulating Surface, *ACS Nano* **6**, 7406-7411 (2012), doi:10.1021/nn3025942.

[58] T. Xu, S. Mohr, M. Amende, M. Laurin, T. Döpper, et al., Benzoic Acid and Phthalic Acid on Atomically Well-Defined MgO(100) Thin Films: Adsorption, Interface Reaction, and Thin Film Growth, *J. Phys. Chem. C* **119**, 26968-26979 (2015), doi:10.1021/acs.jpcc.5b07591.

[59] P. Rahe, M. Kittelmann, J. L. Neff, M. Nimmrich, M. Reichling, et al., Tuning Molecular Self-Assembly on Bulk Insulator Surfaces by Anchoring of the Organic Building Blocks, *Adv. Mater.* **25**, 3948-3956 (2013), doi:10.1002/adma.201300604.

[60] C. M. Hauke, R. Bechstein, M. Kittelmann, C. Storz, A. F. M. Kilbinger, et al., Controlling Molecular Self-Assembly on an Insulating Surface by Rationally Designing an Efficient Anchor Functionality That Maintains Structural Flexibility, *ACS Nano* **7**, 5491-5498 (2013), doi:10.1021/nn401589u.

[61] S. Maier, L.-A. Fendt, L. Zimmerli, T. Glatzel, O. Pfeiffer, et al., Nanoscale Engineering of Molecular Porphyrin Wires on Insulating Surfaces, *Small* **4**, 1115-1118 (2008), doi:10.1002/smll.200701259.

[62] B. Such, T. Trevethan, T. Glatzel, S. Kawai, L. Zimmerli, et al., Functionalized Truxenes: Adsorption and Diffusion of Single Molecules on the KBr(001) Surface, *ACS Nano* **4**, 3429-3439 (2010), doi:10.1021/nn100424g.

[63] A. Hinaut, A. Pujol, F. Chaumeton, D. Martrou, A. Gourdon, et al., An NC-AFM and KPFM Study of the Adsorption of a Triphenylene Derivative on KBr(001), *Beilstein J. Nanotechnol.* **3**, 221-229 (2012), doi:10.3762/bjnano.3.25.

[64] M. Watkins, T. Trevethan, M. L. Sushko, A. L. Shluger, Designing Molecular Architecture to Control Diffusion and Adsorption on Insulating Surfaces, *J. Phys. Chem. C* **112**, 4226-4231 (2008), doi:10.1021/jp077680d.

[65] I. H. Campbell, S. Rubin, T. A. Zawodzinski, J. D. Kress, R. L. Martin, et al., Controlling Schottky Energy Barriers in Organic Electronic Devices Using Self-Assembled Monolayers, *Phys. Rev. B* **54**, R14321-R14324 (1996), doi:10.1103/PhysRevB.54.R14321.

[66] W. Moench, *Semiconductor Surfaces and Interfaces, 3rd ed*, Springer-Verlag, Berlin Germany, 2001, doi:10.1007/978-3-662-04459-9.

[67] S. Bastide, R. Butruille, D. Cahen, A. Dutta, J. L. A. Shanzer , et al., Controlling the Work Function of GaAs by Chemisorption of Benzoic Acid Derivatives, *J. Phys. Chem. B* **101**, 2678-2684 (1997), doi:10.1021/jp9626935.

[68] Y. Kuzumoto M. Kitamura, Work Function of Gold Surfaces Modified Using Substituted Benzenethiols: Reaction Time Dependence and Thermal Stability, *Appl. Phys. Express* **7**, 035701(1-4) (2014), doi:10.7567/APEX.7.035701.

[69] A. Natan, Y. Zidon, Y. Shapira, L. Kronik, Cooperative Effects and Dipole Formation at Semiconductor and Self-Assembled-Monolayer Interfaces, *Phys. Rev. B* **73**, 193310(1-4) (2006), doi:10.1103/PhysRevB.73.193310.

[70] N. Gozlan, U. Tisch, H. Haick, Tailoring the Work Function of Gold Surface by Controlling Coverage and Disorder of Polar Molecular Monolayers, *J. Phys. Chem. C* **112**, 12988-12992 (2008), doi:10.1021/jp803124j.

[71] H. Ishii, K. Sugiyama, E. Ito, K. Seki, Energy Level Alignment and Interfacial Electronic Structures at Organic/Metal and Organic/Organic Interfaces, *Adv. Mater.* **11**, 605-625 (1999), doi:10.1002/(SICI)1521-4095(199906)11:8<605::AID-ADMA605>3.0.CO;2-Q.

[72] H. Peisert, M. Knupfer, T. Schwieger, G. G. Fuentes, D. Olligs, et al., Fluorination of Copper Phthalocyanines: Electronic Structure and Interface Properties, *J. Appl. Phys.* **93**, 9683-9692 (2003), doi:10.1063/1.1577223.

[73] S.-B. Lei, K. Deng, D.-L. Y. Q.-D. Zeng, C. Wang, Charge-Transfer Effect at the Interface of Phthalocyanine Electrode Contact Studied by Scanning Tunneling Spectroscopy, *J. Phys. Chem. B* **110**, 1256-1260 (2006), doi:10.1021/jp0535036.

[74] L. Ramoino, M. von Arx, S. Schintke, A. Baratoff, H.-J. Güntherodt, et al., Layer-Selective Epitaxial Self-Assembly of Porphyrins on Ultrathin Insulators, *Chem. Phys. Lett.* **417**, 22-27 (2006), doi:10.1016/j.cplett.2005.10.006.

[75] T.-K. Lee J. L. Birman, Molecule Adsorbed on Plane Metal Surface: Coupled System Eigenstates, *Phys. Rev. B* **22**, 5953-5960 (1980), doi:10.1103/PhysRevB.22.5953.

[76] J. Repp, G. Meyer, S. M. Stojković, A. Gourdon, C. Joachim, Molecules on Insulating Films: Scanning-Tunneling Microscopy Imaging of Individual Molecular Orbitals, *Phys. Rev. Lett.* **94**, 026803(1-4) (2005), doi:10.1103/PhysRevLett.94.026803.

[77] F. Bussolotti R. Friedlein, Hybridization and Charge Transfer at the Anthracene/Cu(110) Interface: Comparison to Pentacene, *Phys. Rev. B* **81**, 115457(1-7) (2010), doi:10.1103/PhysRevB.81.115457.

[78] J. Ziroff, F. Forster, A. Schöll, P. Puschnig, F. Reinert, Hybridization of Organic Molecular Orbitals with Substrate States at Interfaces: PTCDA on Silver, *Phys. Rev. Lett.* **104**, 233004(1-4) (2010), doi:10.1103/PhysRevLett.104.233004.

[79] S. Ahmadi, M. N. Shariati, S. Yu, M. Göthelid, Molecular Layers of ZnPc and FePc on Au(111) Surface: Charge Transfer and Chemical Interaction, *J. Chem. Phys.* **137**, 084705(1-7) (2012), doi:10.1063/1.4746119.

[80] L. C. Giancarlo G. W. Flynn, Scanning Tunneling and Atomic Force Microscopy Probes of Self-Assembled, Physisorbed Monolayers: Peeking at the Peaks, *Annu. Rev. Phys. Chem.* **49**, 297-336 (1998), doi:10.1146/annurev.physchem.49.1.297.

[81] K. L. Syres, A. G. Thomas, W. R. Flavell, B. F. Spencer, F. Bondino, et al., Adsorbate-Induced Modification of Surface Electronic Structure: Pyrocatechol Adsorption on the Anatase TiO$_2$ (101) and Rutile TiO$_2$ (110) Surfaces, *J. Phys. Chem. C* **116**, 23515-23525 (2012), doi:10.1021/jp308614k.

[82] P. S. Bagus, V. Staemmler, C. Wöll, Exchangelike Effects for Closed-Shell Adsorbates: Interface Dipole and Work Function, *Phys. Rev. Lett.* **89**, 096104(1-4) (2002), doi:10.1103/PhysRevLett.89.096104.

[83] O. H. Pakarinen, J. M. Mativetsky, A. Gulans, M. J. Puska, A. S. Foster, et al., Role of van der Waals Forces in the Adsorption and Diffusion of Organic Molecules on an Insulating Surface, *Phys. Rev. B* **80**, 085401(1-5) (2009), doi:10.1103/PhysRevB.80.085401.

[84] R. Bennewitz, S. Schär, V. Barwich, O. Pfeiffer, E. Meyer, et al., Atomic-Resolution Images of Radiation Damage in KBr, *Surf. Sci.* **474**, L197-L202 (2001), doi:10.1016/S0039-6028(00)01053-0.

[85] L. Nony, E. Gnecco, A. Baratoff, A. Alkauskas, R. Bennewitz, et al., Observation of Individual Molecules Trapped on a Nanostructured Insulator, *Nano Lett.* **4**, 2185-2189 (2004), doi:10.1021/nl048693v.

[86] O. Pfeiffer, E. Gnecco, L. Zimmerli, S. Maier, E. Meyer, et al., Force Microscopy on Insulators: Imaging of Organic Molecules, *J. Phys.: Conf. Ser.* **19**, 166-174 (2005), doi:10.1088/1742-6596/19/1/027.

[87] J. K. Gimzewski, C. Joachim, R. R. Schlittler, V. Langlais, H. Tang, et al., Rotation of a Single Molecule within a Supramolecular Bearing, *Science* **281**, 531-533 (1998), doi:10.1126/science.281.5376.531.

[88] T. Ala-Nissila, R. Ferrando, S. C. Ying, Collective and Single Particle Diffusion on Surfaces, *Adv. Phys.* **51**, 949-1078 (2002), doi:10.1080/00018730110107902.

[89] M. Lackinger, M. S. Janson, W. Ho, Localized Interaction of Single Porphyrin Molecules with Oxygen Vacancies on TiO$_2$(110), *J. Chem. Phys.* **137**, 234707(1-7) (2012), doi:10.1063/1.4771904.

[90] R. Jöhr, A. Hinaut, R. Pawlak, A. Sadeghi, S. Saha, et al., Characterization of Individual Molecular Adsorption Geometries by Atomic Force Microscopy: Cu-TCPP on Rutile TiO$_2$ (110), *J. Chem. Phys.* **143**, 094202(1-7) (2015), doi:10.1063/1.4929608.

[91] T. Glatzel, L. Zimmerli, S. Koch, S. Kawai, E. Meyer, Molecular Assemblies Grown between Metallic Contacts on Insulating Surfaces, *Appl. Phys. Lett.* **94**, 063303(1-3) (2009), doi:10.1063/1.3080614.

[92] R. L. Schwoebel E. J. Shipsey, Step Motion on Crystal Surfaces, *J. Appl. Phys.* **37**, 3682-3686 (1966), doi:10.1063/1.1707904.

[93] G. Ehrlich F. G. Hudda, Atomic View of Surface Self-Diffusion: Tungsten on Tungsten, *J. Chem. Phys.* **44**, 1039-1049 (1966), doi:10.1063/1.1726787.

[94] M. Itoh T. Ohno, Absence of a Step-Edge Barrier on a Polar Semiconductor Surface with Reconstruction, *Phys. Rev. B* **62**, 1889-1896 (2000), doi:10.1103/PhysRevB.62.1889.

[95] M. Battaglia, A. Buckingham, J. Williams, The Electric Quadrupole Moments of Benzene and Hexafluorobenzene, *Chem. Phys. Lett.* **78**, 421-423 (1981),
doi:10.1016/0009-2614(81)85228-1.

[96] M. O. Sinnokrot, E. F. Valeev, C. D. Sherrill, Estimates of the Ab Initio Limit for π-π Interactions: The Benzene Dimer, *J. Am. Chem. Soc.* **124**, 10887-10893 (2002), doi:10.1021/ja025896h.

[97] S. Freund, A. Hinaut, R. Pawlak, S.-X. Liu, S. Decurtins, et al., Morphology Change of C60 Islands on Organic Crystals Observed by Atomic Force Microscopy, *ACS Nano* **10**, 5782-5788 (2016), doi:10.1021/acsnano.5b07971.

[98] G. Binnig H. Rohrer, Scanning Tunneling Microscopy, *Surf. Sci.* **126**, 236-244 (1983), doi:10.1016/0039-6028(83)90716-1.

[99] J. M. R. Weaver D. W. Abraham, High Resolution Atomic Force Microscopy Potentiometry, *J. Vac. Sci. Technol., B* **9**, 1559-1561 (1991), doi:10.1116/1.585423.

[100] M. Nonnenmacher, M. P. O'Boyle, H. K. Wickramasinghe, Kelvin Probe Force Microscopy, *Appl. Phys. Lett.* **58**, 2921-2923 (1991), doi:10.1063/1.105227.

[101] G. Binnig, H. Rohrer, C. Gerber, E. Weibel, 7×7 Reconstruction on Si(111) Resolved in Real Space, *Phys. Rev. Lett.* **50**, 120-123 (1983), doi:10.1103/physrevlett.50.120.

[102] V. M. Hallmark, S. Chiang, J. F. Rabolt, J. D. Swalen, R. J. Wilson, Observation of Atomic Corrugation on Au(111) by Scanning Tunneling Microscopy, *Phys. Rev. Lett.* **59**, 2879-2882 (1987), doi:10.1103/PhysRevLett.59.2879.

[103] F. Giessibl, Atomic Resolution of the Silicon(111)-(7×7) Surface by Atomic Force Microscopy, *Science* **267**, 68-71 (1995), doi:10.1126/science.267.5194.68.

[104] S.-I. Kitamura M. Iwatsuki, High-Resolution Imaging of Contact Potential Difference with Ultrahigh Vacuum Noncontact Atomic Force Microscope, *Appl. Phys. Lett.* **72**, 3154-3156 (1998), doi:10.1063/1.121577.

[105] G. H. Enevoldsen, T. Glatzel, M. C. Christensen, J. V. Lauritsen, F. Besenbacher, Atomic Scale Kelvin Probe Force Microscopy Studies of the Surface Potential Variations on the TiO$_2$ (110) Surface, *Phys. Rev. Lett.* **100**, 236104(1-4) (2008), doi:10.1103/PhysRevLett.100.236104.

[106] S. Morita, R. Wiesendanger, E. Meyer, editors, *Noncontact Atomic Force Microscopy*, Vol. 1, Springer, 2002, doi:10.1007/978-3-642-56019-4.

[107] S. Morita, F. J. Giessibl, R. Wiesendanger, editors, *Noncontact Atomic Force Microscopy*, Vol. 2, Springer, 2009, doi:10.1007/978-3-642-01495-6.

[108] S. Morita, F. J. Giessibl, E. Meyer, R. Wiesendanger, editors, *Noncontact Atomic Force Microscopy*, Vol. 3, Springer, 2015, doi:10.1007/978-3-319-15588-3.

[109] Y. Sugimoto, P. Pou, M. Abe, P. Jelinek, R. Pérez, et al., Chemical Identification of Individual Surface Atoms by Atomic Force Microscopy, *Nature* **446**, 64-67 (2007), doi:10.1038/nature05530.

[110] R. Pérez, M. C. Payne, I. Štich, K. Terakura, Role of Covalent Tip-Surface Interactions in Noncontact Atomic Force Microscopy on Reactive Surfaces, *Phys. Rev. Lett.* **78**, 678-681 (1997), doi:10.1103/PhysRevLett.78.678.

[111] F. Bocquet, L. Nony, C. Loppacher, T. Glatzel, Analytical Approach to the Local Contact Potential Difference on (001) Ionic Surfaces: Implications for Kelvin Probe Force Microscopy, *Phys. Rev. B* **78**, 035410(1-13) (2008), doi:10.1103/PhysRevB.78.035410.

[112] F. J. Giessibl, Theory for an Electrostatic Imaging Mechanism Allowing Atomic Resolution of Ionic Crystals by Atomic Force Microscopy, *Phys. Rev. B* **45**, 13815-13818 (1992), doi:10.1103/PhysRevB.45.13815.

[113] H. Hamaker, The London-van der Waals Attraction between Spherical Particles, *Physica* **4**, 1058-1072 (1937), doi:10.1016/S0031-8914(37)80203-7.

[114] J. Israelachvili, *Intermolecular and Surface Forces*, Academic Press, London, 1992, doi:10.1016/B978-0-12-375182-9.10025-9.

[115] S. Sadewasser, *Kelvin Probe Force Microscopy*, chapter Experimental Technique and Working Modes, pages 7–24, Springer, 2012, doi:10.1007/978-3-642-22566-6_2.

144

[116] A. Sadeghi, A. Baratoff, S. A. Ghasemi, S. Goedecker, T. Glatzel, et al., Multiscale Approach for Simulations of Kelvin Probe Force Microscopy with Atomic Resolution, *Phys. Rev. B* **86**, 075407(1-20) (2012), doi:10.1103/PhysRevB.86.075407.

[117] S. Hudlet, M. Saint Jean, C. Guthmann, J. Berger, Evaluation of the Capacitive Force between an Atomic Force Microscopy Tip and a Metallic Surface, *Eur. Phys. J. B* **2**, 5-10 (1998), doi:10.1007/s100510050219.

[118] M. Guggisberg, M. Bammerlin, C. Loppacher, O. Pfeiffer, A. Abdurixit, et al., Separation of Interactions by Noncontact Force Microscopy, *Phys. Rev. B* **61**, 11151-11155 (2000), doi:10.1103/PhysRevB.61.11151.

[119] F. J. Giessibl, Advances in Atomic Force Microscopy, *Rev. Mod. Phys.* **75**, 949-983 (2003), doi:10.1103/RevModPhys.75.949.

[120] C. Chen, *Introduction to Scanning Tunneling Microscopy*, Oxford University Press, New York, 1993, doi:10.1093/acprof:oso/9780199211500.001.0001.

[121] F. Ohnesorge G. Binnig, True Atomic Resolution by Atomic Force Microscopy Through Repulsive and Attractive Forces, *Science* **260**, 1451-1456 (1993), doi:10.1126/science.260.5113.1451.

[122] T. Schimmel, T. Koch, J. Küppers, M. Lux-Steiner, True Atomic Resolution Under Ambient Conditions Obtained by Atomic Force Microscopy In the Contact Mode, *Appl. Phys. A* **68**, 399-402 (1999), doi:10.1007/s003390050912.

[123] Y. Martin, C. C. Williams, H. K. Wickramasinghe, Atomic Force Microscope-Force Mapping and Profiling on a Sub 100 ÅScale, *J. Appl. Phys.* **61**, 4723-4729 (1987), doi:10.1063/1.338807.

[124] T. R. Albrecht, P. Grütter, D. Horne, D. Rugar, Frequency Modulation Detection Using High-Q Cantilevers for Enhanced Force Microscope Sensitivity, *J. Appl. Phys.* **69**, 668-673 (1991), doi:10.1063/1.347347.

[125] F. J. Giessibl, Forces and Frequency Shifts in Atomic-Resolution Dynamic-Force Microscopy, *Phys. Rev. B* **56**, 16010-16015 (1997), doi:10.1103/PhysRevB.56.16010.

[126] F. J. Giessibl, A Direct Method to Calculate Tip-Sample Forces from Frequency Shifts in Frequency-Modulation Atomic Force Microscopy, *Appl. Phys. Lett.* **78**, 123-125 (2001), doi:10.1063/1.1335546.

[127] S. Sadewasser M. C. Lux-Steiner, Correct Height Measurement in Noncontact Atomic Force Microscopy, *Phys. Rev. Lett.* **91**, 266101(1-4) (2003), doi:10.1103/PhysRevLett.91.266101.

[128] P. Rahe, R. Bechstein, J. Schütte, F. Ostendorf, A. Kühnle, Repulsive Interaction and Contrast Inversion in Noncontact Atomic Force Microscopy Imaging of Adsorbates, *Phys. Rev. B* **77**, 195410(1-6) (2008), doi:10.1103/PhysRevB.77.195410.

[129] J. V. Lauritsen, A. S. Foster, G. H. Olesen, M. C. Christensen, A. Kühnle, et al., Chemical Identification of Point Defects and Adsorbates on a Metal Oxide Surface by Atomic Force Microscopy, *Nanotechnology* **17**, 3436-3441 (2006), doi:10.1088/0957-4484/17/14/015.

[130] R. Bechstein, C. González, J. Schütte, P. Jelínek, R. Pérez, et al., 'All-inclusive' Imaging of the Rutile TiO$_2$ (110) Surface Using NC-AFM, *Nanotechnology* **20**, 505703(1-7) (2009), doi:10.1088/0957-4484/20/50/505703.

[131] S. Kawai, T. Glatzel, S. Koch, B. Such, A. Baratoff, et al., Systematic Achievement of Improved Atomic-Scale Contrast via Bimodal Dynamic Force Microscopy, *Phys. Rev. Lett.* **103**, 220801(1-4) (2009), doi:10.1103/PhysRevLett.103.220801.

[132] S. Kawai, T. Glatzel, S. Koch, B. Such, A. Baratoff, et al., Ultrasensitive Detection of Lateral Atomic-Scale Interactions on Graphite (0001) via Bimodal Dynamic Force Measurements, *Phys. Rev. B* **81**, 085420(1-7) (2010), doi:10.1103/PhysRevB.81.085420.

[133] S. Kawai, S.-I. Kitamura, D. Kobayashi, S. Meguro, H. Kawakatsu, An Ultrasmall Amplitude Operation of Dynamic Force Microscopy with Second Flexural Mode, *Appl. Phys. Lett.* **86**, 193107(1-3) (2005), doi:10.1063/1.1923200.

[134] N. F. Martinez, S. Patil, J. R. Lozano, R. Garcia, Enhanced Compositional Sensitivity in Atomic Force Microscopy by the Excitation of the First Two Flexural Modes, *Appl. Phys. Lett.* **89**, 153115(1-3) (2006), doi:10.1063/1.2360894.

[135] O. Pfeiffer, R. Bennewitz, A. Baratoff, E. Meyer, P. Grütter, Lateral-Force Measurements in Dynamic Force Microscopy, *Phys. Rev. B* **65**, 161403(1-4) (2002), doi:10.1103/PhysRevB.65.161403.

[136] J. R. Lozano R. Garcia, Theory of Multifrequency Atomic Force Microscopy, *Phys. Rev. Lett.* **100**, 076102(1-4) (2008), doi:10.1103/PhysRevLett.100.076102.

[137] A. Kikukawa, S. Hosaka, R. Imura, Vacuum Compatible High-Sensitive Kelvin Probe Force Microscopy, *Rev. Sci. Instrum.* **67**, 1463-1467 (1996), doi:10.1063/1.1146874.

[138] C. Sommerhalter, T. W. Matthes, T. Glatzel, A. Jäger-Waldau, M. C. Lux-Steiner, High-Sensitivity Quantitative Kelvin Probe Microscopy by Noncontact Ultra-High-Vacuum Atomic Force Microscopy, *Appl. Phys. Lett.* **75**, 286-288 (1999), doi:10.1063/1.124357.

[139] T. Kunstmann, A. Schlarb, M. Fendrich, D. Paulkowski, T. Wagner, et al., Combined Normal and Torsional Mode in Frequency-Modulation Atomic Force Microscopy for Lateral Dissipation Measurement, *Appl. Phys. Lett.* **88**, 153112(1-3) (2006), doi:10.1063/1.2194367.

[140] S. Kawai, F. F. Canova, T. Glatzel, T. Hynninen, E. Meyer, et al., Measuring Electric Field Induced Subpicometer Displacement of Step Edge Ions, *Phys. Rev. Lett.* **109**, 146101(1-5) (2012), doi:10.1103/PhysRevLett.109.146101.

[141] L. Kelvin, Contact Electricity of Metals, *Philos. Mag.* **46**, 82-120 (1898), doi:10.1080/14786449808621172.

[142] A. Kikukawa, S. Hosaka, R. Imura, Silicon PN Junction Imaging and Characterizations Using Sensitivity Enhanced Kelvin Probe Force Microscopy, *Appl. Phys. Lett.* **66**, 3510-3512 (1995), doi:10.1063/1.113780.

[143] U. Zerweck, C. Loppacher, T. Otto, S. Grafström, L. M. Eng, Accuracy and Resolution Limits of Kelvin Probe Force Microscopy, *Phys. Rev. B* **71**, 125424(1-9) (2005), doi:10.1103/PhysRevB.71.125424.

[144] T. Glatzel, S. Sadewasser, M. Lux-Steiner, Amplitude or Frequency Modulation-Detection in Kelvin Probe Force Microscopy, *Appl. Surf. Sci.* **210**, 84 -89 (2003), doi:10.1016/S0169-4332(02)01484-8.

[145] C. N. Berglund W. E. Spicer, Photoemission Studies of Copper and Silver: Theory, *Phys. Rev.* **136**, A1030-A1044 (1964), doi:10.1103/PhysRev.136.A1030.

[146] S. Suga A. Sekiyama, *Photoelectron Spectroscopy: Bulk and Surface Electronic Structures*, chapter Theoretical Background, pages 7–31, Springer Berlin Heidelberg, Berlin, Heidelberg, 2014, doi:10.1007/978-3-642-37530-9_2.

[147] V. Y. Young G. B. Hoflund, Photoelectron Spectroscopy (XPS and UPS), Auger Electron Spectroscopy (AES), and Ion Scattering Spectroscopy (ISS), in *Handbook of Surface and Interface Analysis*, pages 19–64, CRC Press, 2009, doi:10.1201/9781420007800-c3.

[148] S. Hofmann, *Auger- and X-Ray Photoelectron Spectroscopy in Materials Science: A User-Oriented Guide*, chapter Optimizing Measured Signal Intensity: Emission Angle, Incidence Angle and Surface Roughness, pages 205–257, Springer Berlin Heidelberg, Berlin, Heidelberg, 2013, doi:10.1007/978-3-642-27381-0_5.

[149] K. Siegbahn, *ESCA; Atomic, Molecular and Solid State Structure Studied by Means of Electron Spectroscopy*, Uppsala : Almqvist & Wiksells, 1967.

[150] K. Siegbahn, Electron Spectroscopy for Chemical Analysis (E.S.C.A.), *Philos. Trans. R. Soc., A* **268**, 33-57 (1970).

[151] N. H. Vu, H. V. Le, T. M. Cao, V. V. Pham, H. M. Le, et al., Anatase-Rutile Phase Transformation of Titanium Dioxide Bulk Material: A DFT + U Approach, *J. Phys.: Condens. Matter* **24**, 405501(1-10) (2012), doi:10.1088/0953-8984/24/40/405501.

[152] N. Satoh, T. Nakashima, K. Yamamoto, Metastability of Anatase: Size Dependent and Irreversible Anatase-Rutile Phase Transition in Atomic-Level Precise Titania, *Sci. Rep.* **3**, 1959(1-6) (2013), doi:10.1038/srep01959.

[153] D. A. Hanaor C. C. Sorrell, Review of the Anatase to Rutile Phase Transformation, *J. Mater. Sci.* **46**, 855-874 (2011), doi:10.1007/s10853-010-5113-0.

[154] H. Zhang J. F. Banfield, Thermodynamic Analysis of Phase Stability of Nanocrystalline Titania, *J. Mater. Chem.* **8**, 2073-2076 (1998), doi:10.1039/A802619J.

[155] H. Lu, W. Zhang, Q. Jiang, Phase Stability of Nanoanatase, *Adv. Eng. Mater.* **5**, 787-788 (2003), doi:10.1002/adem.200300359.

[156] L. Kavan, M. Grätzel, S. Gilbert, C. Klemenz, H. Scheel, Electrochemical and Photoelectrochemical Investigation of Single-Crystal Anatase, *J. Am. Chem. Soc.* **118**, 6716-6723 (1996), doi:10.1021/ja954172l.

[157] C. J. Howard, T. M. Sabine, F. Dickson, Structural and Thermal Parameters for Rutile and Anatase, *Acta Crystallogr., Sect. B* **47**, 462-468 (1991), doi:10.1107/S010876819100335X.

[158] M. Ramamoorthy, D. Vanderbilt, R. D. King-Smith, First-Principles Calculations of the Energetics of Stoichiometric TiO_2 Surfaces, *Phys. Rev. B* **49**, 16721-16727 (1994), doi:10.1103/PhysRevB.49.16721.

[159] U. Diebold, The Surface Science of Titanium Dioxide, *Surf. Sci. Rep.* **48**, 53-229 (2003), doi:10.1016/S0167-5729(02)00100-0.

[160] G. Charlton, P. B. Howes, C. L. Nicklin, P. Steadman, J. S. G. Taylor, et al., Relaxation of TiO_2(110)-(1×1) Using Surface X-Ray Diffraction, *Phys. Rev. Lett.* **78**, 495-498 (1997), doi:10.1103/PhysRevLett.78.495.

[161] S. Pétigny, H. Mostéfa-Sba, B. Domenichini, E. Lesniewska, A. Steinbrunn, et al., Superficial Defects Induced by Argon and Oxygen Bombardments on (110) TiO_2 Surfaces, *Surf. Sci.* **410**, 250-257 (1998), doi:10.1016/S0039-6028(98)00297-0.

[162] M. Li, W. Hebenstreit, U. Diebold, A. M. Tyryshkin, M. K. Bowman, et al., The Influence of the Bulk Reduction State on the Surface Structure and Morphology of Rutile TiO2(110) Single Crystals, *J. Phys. Chem. B* **104**, 4944-4950 (2000), doi:10.1021/jp9943272.

[163] K. Hameeuw, G. Cantele, D. Ninno, F. Trani, G. Iadonisi, Influence of Surface and Subsurface Defects on the Behavior of the Rutile TiO$_2$(110) Surface, *Phys. Status Solidi A* **203**, 2219-2222 (2006), doi:10.1002/pssa.200566015.

[164] O. Bikondoa, C. L. Pang, R. Ithnin, C. A. Muryn, H. Onishi, et al., Direct Visualization of Defect-Mediated Dissociation of Water on TiO$_2$(110), *Nat. Mater.* **5**, 189-192 (2006), doi:10.1038/nmat1592.

[165] S. Wendt, P. T. Sprunger, E. Lira, G. K. H. Madsen, Z. Li, et al., The Role of Interstitial Sites in the Ti3d Defect State in the Band Gap of Titania, *Science* **320**, 1755-1759 (2008), doi:10.1126/science.1159846.

[166] C. M. Yim, C. L. Pang, G. Thornton, Oxygen Vacancy Origin of the Surface Band-Gap State of TiO$_2$(110), *Phys. Rev. Lett.* **104**, 036806(1-4) (2010), doi:10.1103/PhysRevLett.104.036806.

[167] D. O. Scanlon, C. W. Dunnill, J. Buckeridge, S. A. Shevlin, A. J. Logsdail, et al., Band Alignment of Rutile and Anatase TiO$_2$, *Nat. Mater.* **12**, 798-801 (2013), doi:10.1038/nmat3697.

[168] J. Zhang, P. Zhou, J. Liu, J. Yu, New Understanding of the Difference of Photocatalytic Activity among Anatase, Rutile and Brookite TiO$_2$, *Phys. Chem. Chem. Phys.* **16**, 20382-20386 (2014), doi:10.1039/C4CP02201G.

[169] M. Lazzeri, A. Vittadini, A. Selloni, Structure and Energetics of Stoichiometric TiO$_2$ Anatase Surfaces, *Phys. Rev. B* **63**, 155409(1-9) (2001), doi:10.1103/PhysRevB.63.155409.

[170] N.-G. Park, J. van de Lagemaat, A. J. Frank, Comparison of Dye-Sensitized Rutile- and Anatase-Based TiO$_2$ Solar Cells, *J. Phys. Chem. B* **104**, 8989-8994 (2000), doi:10.1021/jp994365l.

[171] T. Luttrell, S. Halpegamage, J. Tao, A. Kramer, E. Sutter, et al., Why is Anatase a Better Photocatalyst than Rutile? - Model Studies on Epitaxial TiO$_2$ Films, *Sci. Rep.* **4**, 4043(1-8) (2014), doi:10.1038/srep0404.

[172] D. D. Mulmi, T. Sekiya, N. Kamiya, S. Kurita, Y. Murakami, et al., Optical and Electric Properties of Nb-Doped Anatase TiO$_2$ Single Crystal, *J. Phys. Chem. Solids* **65**, 1181-1185 (2004), doi:10.1016/j.jpcs.2003.12.009.

[173] M. Setvín, B. Daniel, V. Mansfeldova, L. Kavan, P. Scheiber, et al., Surface Preparation of TiO$_2$ Anatase (101): Pitfalls and How to Avoid Them, *Surf. Sci.* **626**, 61-67 (2014), doi:10.1016/j.susc.2014.04.001.

[174] O. Dulub U. Diebold, Preparation of a Pristine TiO$_2$ Anatase (101) Surface by Cleaving, *J. Phys.: Condens. Matter* **22**, 084014(1-4) (2010), doi:10.1088/0953-8984/22/8/084014.

[175] W. Hebenstreit, N. Ruzycki, G. S. Herman, Y. Gao, U. Diebold, Scanning Tunneling Microscopy Investigation of the TiO_2 Anatase (101) Surface, *Phys. Rev. B* **62**, R16334-R16336 (2000), doi:10.1103/PhysRevB.62.R16334.

[176] Y. He, O. Dulub, H. Cheng, A. Selloni, U. Diebold, Evidence for the Predominance of Subsurface Defects on Reduced Anatase TiO_2(101), *Phys. Rev. Lett.* **102**, 106105(1-4) (2009), doi:10.1103/PhysRevLett.102.106105.

[177] C. Dette, M. A. Pérez-Osorio, C. S. Kley, P. Punke, C. E. Patrick, et al., TiO_2 Anatase with a Bandgap in the Visible Region, *Nano Lett.* **14**, 6533-6538 (2014), doi:10.1021/nl503131s.

[178] O. Stetsovych, M. Todorovic, T. K. Shimizu, C. Moreno, J. W. Ryan, et al., Atomic Species Identification at the (101) Anatase Surface by Simultaneous Scanning Tunnelling and Atomic Force Microscopy, *Nat. Commun.* **6**, 7265(1-9) (2015), doi:10.1038/ncomms8265.

[179] A. Vittadini, A. Selloni, F. P. Rotzinger, M. Grätzel, Structure and Energetics of Water Adsorbed at TiO_2 Anatase 101 and 001 Surfaces, *Phys. Rev. Lett.* **81**, 2954-2957 (1998), doi:10.1103/PhysRevLett.81.2954.

[180] X.-Q. Gong, A. Selloni, M. Batzill, U. Diebold, Steps on Anatase TiO_2(101), *Nat. Mater.* **5**, 665-670 (2006), doi:10.1038/nmat1695.

[181] A. G. Thomas, W. R. Flavell, A. K. Mallick, A. R. Kumarasinghe, D. Tsoutsou, et al., Comparison of the Electronic Structure of Anatase and Rutile TiO_2 Single-Crystal Surfaces using Resonant Photoemission and X-Ray Absorption Spectroscopy, *Phys. Rev. B* **75**, 035105(1-12) (2007), doi:10.1103/PhysRevB.75.035105.

[182] A. A. Ismail D. W. Bahnemann, Metal-Free Porphyrin-Sensitized Mesoporous Titania Films for Visible-Light Indoor Air Oxidation, *ChemSusChem* **3**, 1057-1062 (2010), doi:10.1002/cssc.201000158.

[183] J. Niu, B. Yao, Y. Chen, C. Peng, X. Yu, et al., Enhanced Photocatalytic Activity of Nitrogen Doped TiO_2 Photocatalysts Sensitized by Metallo Co, Ni-Porphyrins, *Appl. Surf. Sci.* **271**, 39-44 (2013), doi:10.1016/j.apsusc.2012.12.175.

[184] H. Imahori, S. Kang, H. Hayashi, M. Haruta, H. Kurata, et al., Photoinduced Charge Carrier Dynamics of Zn-Porphyrin-TiO_2 Electrodes: The Key Role of Charge Recombination for Solar Cell Performance, *J. Phys. Chem. A* **115**, 3679-3690 (2011), doi:10.1021/jp103747t.

[185] S. Godlewski M. Szymonski, Adsorption and Self-Assembly of Large Polycyclic Molecules on the Surfaces of TiO_2 Single Crystals, *Int. J. Mol. Sci.* **14**, 2946-2966 (2013), doi:10.3390/ijms14022946.

[186] L. Howald, E. Meyer, R. Lüthi, H. Haefke, R. Overney, et al., Multifunctional Probe Microscope for Facile Operation in Ultrahigh Vacuum, *Appl. Phys. Lett.* **63**, 117-119 (1993), doi:10.1063/1.109732.

[187] L. Zimmerli, *Assemblies of Organic Molecules on Insulating Surfaces Investigated by nc-AFM*, PhD thesis, University of Basel, 2007, doi:10.5451/unibas-004464655.

[188] S. Maier, *Contact Dynamics from the Atomic Scale to Nanostructured Surfaces*, PhD thesis, University of Basel, 2006, doi:10.5451/unibas-004165902.

[189] S. Koch, *Investigation of Hexagonal 2D Super Structures by Dynamic Force Spectroscopy*, PhD thesis, University of Basel, 2012, doi:10.5451/unibas-005976956.

[190] P. Steiner, *Modulation of Contact Resonance Frequency in Friction Force Microscopy on the Atomic Scale*, PhD thesis, University of Basel, 2011, doi:10.5451/unibas-005584754.

[191] S. Wendt, J. Matthiesen, R. Schaub, E. K. Vestergaard, E. Lægsgaard, et al., Formation and Splitting of Paired Hydroxyl Groups on Reduced $TiO_2(110)$, *Phys. Rev. Lett.* **96**, 066107(1-4) (2006), doi:10.1103/PhysRevLett.96.066107.

[192] Z. Zhang, O. Bondarchuk, B. D. Kay, J. M. White, Z. Dohnálek, Imaging Water Dissociation on $TiO_2(110)$: Evidence for Inequivalent Geminate OH Groups, *J. Phys. Chem. B* **110**, 21840-21845 (2006), doi:10.1021/jp063619h.

[193] C. L. Pang, A. Sasahara, H. Onishi, Q. Chen, G. Thornton, Noncontact Atomic Force Microscopy Imaging of Water Dissociation Products on $TiO_2(110)$, *Phys. Rev. B* **74**, 073411(1-4) (2006), doi:10.1103/PhysRevB.74.073411.

[194] C. L. Pang, S. A. Haycock, H. Raza, P. W. Murray, G. Thornton, et al., Added Row Model of $TiO_2(110)$ 1×2, *Phys. Rev. B* **58**, 1586-1589 (1998), doi:10.1103/PhysRevB.58.1586.

[195] M. Li, W. Hebenstreit, L. Gross, U. Diebold, M. Henderson, et al., Oxygen-Induced Restructuring of the $TiO_2(110)$ Surface: A Comprehensive Study, *Surf. Sci.* **437**, 173-190 (1999), doi:10.1016/S0039-6028(99)00720-7.

[196] G. H. Enevoldsen, H. P. Pinto, A. S. Foster, M. C. R. Jensen, A. Kühnle, et al., Detailed Scanning Probe Microscopy Tip Models Determined from Simultaneous Atom-Resolved AFM and STM Studies of the TiO_2 (110) Surface, *Phys. Rev. B* **78**, 045416(1-19) (2008), doi:10.1103/PhysRevB.78.045416.

[197] SPECS Zurich GmbH, Nanonis application note: Automated amplitude calibration in non-contact afm mode, pdf.

[198] A. Szabo N. S. Ostlund, *Modern Quantum Chemistry: Introduction to Advanced Electronic Structure Theory*, Dover Publications: New York, 1996.

[199] T. D. Crawford H. F. Schaefer, *An Introduction to Coupled Cluster Theory for Computational Chemists*, pages 33–136, John Wiley & Sons, Inc., 2007, doi:10.1002/9780470125915.ch2.

[200] J. Klimeš A. Michaelides, Perspective: Advances and Challenges in Treating van der Waals Dispersion Forces in Density Functional Theory, *J. Chem. Phys.* **137**, 120901(1-12) (2012), doi:10.1063/1.4754130.

[201] M. Mura, A. Gulans, T. Thonhauser, L. Kantorovich, Role of van der Waals Interaction in Forming Molecule-Metal Junctions: Flat Organic Molecules on the Au(111) Surface, *Phys. Chem. Chem. Phys.* **12**, 4759-4767 (2010), doi:10.1039/B920121A.

[202] M. L. Sushko, A. Y. Gal, A. L. Shluger, Interaction of Organic Molecules with the TiO_2 (110) Surface: Ab Inito Calculations and Classical Force Fields, *J. Phys. Chem. B* **110**, 4853-4862 (2006), doi:10.1021/jp055486q.

[203] T. Trevethan A. L. Shluger, Modeling the Diffusive Motion of Large Organic Molecules on Insulating Surfaces, *J. Phys. Chem. C* **112**, 19577-19583 (2008), doi:10.1021/jp806355m.

[204] L. Genovese, A. Neelov, S. Goedecker, T. Deutsch, S. A. Ghasemi, et al., Daubechies Wavelets as a Basis Set for Density Functional Pseudopotential Calculations, *J. Chem. Phys* **129**, 014109(1-14) (2008), doi:10.1063/1.2949547.

[205] J. P. Perdew, J. A. Chevary, S. H. Vosko, K. A. Jackson, M. R. Pederson, et al., Atoms, Molecules, Solids, and Surfaces: Applications of the Generalized Gradient Approximation for Exchange and Correlation, *Phys. Rev. B* **46**, 6671-6687 (1992), doi:10.1103/PhysRevB.46.6671.

[206] C. Hartwigsen, S. Goedecker, J. Hutter, Relativistic Separable Dual-Space Gaussian Pseudopotentials from H to Rn, *Phys. Rev. B* **58**, 3641-3662 (1998), doi:10.1103/PhysRevB.58.3641.

[207] A. Willand, Y. O. Kvashnin, L. Genovese, A. Vazquez Mayagoitia, A. K. Deb, et al., Norm-Conserving Pseudopotentials with Chemical Accuracy Compared to All-Electron Calculations, *J. Chem. Phys* **138**, 104109(1-11) (2013), doi:10.1063/1.4793260.

[208] S. Grimme, Semiempirical GGA-Type Density Functional Constructed with a Long-Range Dispersion Correction, *J. Comput. Chem.* **27**, 1787-1799 (2006), doi:10.1002/jcc.20495.

[209] L. Genovese, T. Deutsch, S. Goedecker, Efficient and Accurate Three-Dimensional Poisson Solver for Surface Problems, *J. Chem. Phys* **127**, 054704(1-6) (2007), doi:10.1063/1.2754685.

[210] R. F. Bader, *Atoms in Molecules*, Wiley Online Library, 1990, doi:10.1002/0470845015.caa012.

[211] G. Henkelman, A. Arnaldsson, H. Jónsson, A Fast and Robust Algorithm for Bader Decomposition of Charge Density, *Comput. Mater. Sci.* **36**, 354-360 (2006), doi:10.1016/j.commatsci.2005.04.010.

[212] J. Onoda, C. L. Pang, A. Yurtsever, Y. Sugimoto, Subsurface Charge Repulsion of Adsorbed H-Adatoms on $TiO_2(110)$, *J. Phys. Chem. C* **118**, 13674-13679 (2014), doi:10.1021/jp503402w.

[213] S. Wendt, R. Schaub, J. Matthiesen, E. Vestergaard, E. Wahlström, et al., Oxygen Vacancies on $TiO_2(110)$ and their Interaction with H_2O and O_2: A Combined High-Resolution STM and DFT Study, *Surf. Sci.* **598**, 226-245 (2005), doi:10.1016/j.susc.2005.08.041.

[214] A. Yurtsever, Y. Sugimoto, M. Abe, S. Morita, NC-AFM Imaging of the TiO_2 (110)-(1×1) Surface at Low Temperature, *Nanotechnology* **21**, 165702(1-7) (2010), doi:10.1088/0957-4484/21/16/165702.

[215] M. Watkins, T. Trevethan, A. L. Shluger, L. N. Kantorovich, Dynamical Processes at Oxide Surfaces Studied with the Virtual Atomic Force Microscope, *Phys. Rev. B* **76**, 245421(1-7) (2007), doi:10.1103/PhysRevB.76.245421.

[216] A. Sasahara, H. Uetsuka, H. Onishi, Local Work Function of a Rutile $TiO_2(110)$-$(1x1)$ Surface Observed by Kelvin Probe Force Microscopy, *Surf. Sci.* **529**, L245-L250 (2003), doi:10.1016/S0039-6028(03)00031-1.

[217] A. Sasahara, C. L. Pang, H. Onishi, Local Work Function of Pt Clusters Vacuum-Deposited on a TiO_2 Surface, *J. Phys. Chem. B* **110**, 17584-17588 (2006), doi:10.1021/jp063665h.

[218] M. Ikeda, N. Koide, L. Han, A. Sasahara, H. Onishi, Work Function on Dye-Adsorbed TiO_2 Surfaces Measured by Using a Kelvin Probe Force Microscope, *J. Phys. Chem. C* **112**, 6961-6967 (2008), doi:10.1021/jp077065+.

[219] S. Bates, G. Kresse, M. Gillan, The Adsorption and Dissociation of ROH Molecules on $TiO_2(110)$, *Surf. Sci.* **409**, 336-349 (1998), doi:10.1016/S0039-6028(98)00278-7.

[220] A. Greuling, P. Rahe, M. Kaczmarski, A. Kühnle, M. Rohlfing, Combined NC-AFM and DFT Study of the Adsorption Geometry of Trimesic Acid on Rutile TiO_2 (110), *J. Phys.: Condens. Matter* **22**, 345008(1-10) (2010), doi:10.1088/0953-8984/22/34/345008.

[221] S. Sadewasser, C. Leendertz, F. Streicher, M. C. Lux-Steiner, The Influence of Surface Topography on Kelvin Probe Force Microscopy, *Nanotechnology* **20**, 505503(1-10) (2009), doi:10.1088/0957-4484/20/50/505503.

[222] R. Baier, C. Leendertz, M. C. Lux-Steiner, S. Sadewasser, Toward Quantitative Kelvin Probe Force Microscopy of Nanoscale Potential Distributions, *Phys. Rev. B* **85**, 165436(1-6) (2012), doi:10.1103/PhysRevB.85.165436.

[223] A. Rienzo, L. C. Mayor, G. Magnano, C. J. Satterley, E. Ataman, et al., X-ray Absorption and Photoemission Spectroscopy of Zinc Protoporphyrin Adsorbed on Rutile TiO_2(110) Prepared by in Situ Electrospray Deposition, *J. Chem. Phys.* **132**, 084703(1-6) (2010), doi:10.1063/1.3336747.

[224] U. Diebold, J. Lehman, T. Mahmoud, M. Kuhn, G. Leonardelli, et al., Intrinsic Defects on a TiO_2(110) (1×1) Surface and their Reaction with Oxygen: A Scanning Tunneling Microscopy Study, *Surf. Sci.* **411**, 137-153 (1998), doi:10.1016/S0039-6028(98)00356-2.

[225] R. Pawlak, A. Sadeghi, R. Jöhr, A. Hinaut, T. Meier, et al., Hydroxyl-Induced Partial Charge States of Single Porphyrins on Titania Rutile, *J. Phys. Chem. C* **121**, 3607-3614 (2017), doi:10.1021/acs.jpcc.6b11873.

[226] C. Castellarin-Cudia, P. Borghetti, G. Di Santo, M. Fanetti, R. Larciprete, et al., Substrate Influence for the Zn-Tetraphenyl-Porphyrin Adsorption Geometry and the Interface-Induced Electron Transfer, *ChemPhysChem* **11**, 2248-2255 (2010), doi:10.1002/cphc.201000017.

[227] L. Patthey, H. Rensmo, P. Persson, K. Westermark, L. Vayssieres, et al., Adsorption of Bi-Isonicotinic Acid on Rutile TiO_2(110), *J. Chem. Phys.* **110**, 5913-5918 (1999), doi:10.1063/1.478491.

[228] M. Setvin, B. Daniel, U. Aschauer, W. Hou, Y.-F. Li, et al., Identification of Adsorbed Molecules via STM Tip Manipulation: CO, H_2O, and O_2 on TiO_2 Anatase (101), *Phys. Chem. Chem. Phys.* **16**, 21524-21530 (2014), doi:10.1039/C4CP03212H.

[229] C. S. Kley, C. Dette, G. Rinke, C. E. Patrick, J. Cechal, et al., Atomic-Scale Observation of Multiconformational Binding and Energy Level Alignment of Ruthenium-Based Photosensitizers on TiO_2 Anatase, *Nano Lett.* **14**, 563-569 (2014), doi:10.1021/nl403717d.

[230] H. Cheng A. Selloni, Energetics and Diffusion of Intrinsic Surface and Subsurface Defects on Anatase TiO_2(101), *J. Chem. Phys.* **131**, 054703(1-10) (2009), doi:10.1063/1.3194301.

[231] P. Scheiber, M. Fidler, O. Dulub, M. Schmid, U. Diebold, et al., (Sub)Surface Mobility of Oxygen Vacancies at the TiO_2 Anatase (101) Surface, *Phys. Rev. Lett.* **109**, 136103(1-5) (2012), doi:10.1103/PhysRevLett.109.136103.

[232] S. Sadewasser, T. Glatzel, M. Rusu, A. Jäger-Waldau, M. C. Lux-Steiner, High-Resolution Work Function Imaging of Single Grains of Semiconductor Surfaces, *Applied Physics Letters* **80**, 2979-2981 (2002), doi:10.1063/1.1471375.

[233] A. Imanishi, . Etsushi Tsuji, Y. Nakato, Dependence of the Work Function of TiO$_2$ (Rutile) on Crystal Faces, Studied by a Scanning Auger Microprobe, *J. Phys. Chem. C* **111**, 2128-2132 (2007), doi:10.1021/jp0668403.

[234] N. Martsinovich A. Troisi, How TiO$_2$ Crystallographic Surfaces Influence Charge Injection Rates from a Chemisorbed Dye Sensitiser, *Phys. Chem. Chem. Phys.* **14**, 13392-13401 (2012), doi:10.1039/C2CP42055D.

[235] B. Anczykowski, B. Gotsmann, H. Fuchs, J. Cleveland, V. Elings, How to Measure Energy Dissipation in Dynamic Mode Atomic Force Microscopy, *Appl. Surf. Sci.* **140**, 376-382 (1999), doi:10.1016/S0169-4332(98)00558-3.

[236] S. Kawai, T. Glatzel, B. Such, S. Koch, A. Baratoff, et al., Energy Dissipation in Dynamic Force Microscopy on KBr(001) Correlated with Atomic-Scale Adhesion Phenomena, *Phys. Rev. B* **86**, 245419(1-10) (2012), doi:10.1103/PhysRevB.86.245419.

[237] C. Loppacher, R. Bennewitz, O. Pfeiffer, M. Guggisberg, M. Bammerlin, et al., Experimental Aspects of Dissipation Force Microscopy, *Phys. Rev. B* **62**, 13674-13679 (2000), doi:10.1103/PhysRevB.62.13674.

[238] M. Klocke D. E. Wolf, Dissipation Signals due to Lateral Tip Oscillations in FM-AFM, *Beilstein J. Nanotechnol.* **5**, 2048-2057 (2014), doi:10.3762/bjnano.5.213.

[239] M. Lange, D. van Vörden, R. Möller, A Measurement of the Hysteresis Loop in Force-Spectroscopy Curves Using a Tuning-Fork Atomic Force Microscope, *Beilstein J. Nanotechnol.* **3**, 207-212 (2012), doi:10.3762/bjnano.3.23.

[240] N. Oyabu, P. Pou, Y. Sugimoto, P. Jelinek, M. Abe, et al., Single Atomic Contact Adhesion and Dissipation in Dynamic Force Microscopy, *Phys. Rev. Lett.* **96**, 106101(1-4) (2006), doi:10.1002/adfm.200500309.

[241] D. C. Grinter, T. Woolcot, C.-L. Pang, G. Thornton, Ordered Carboxylates on TiO$_2$(110) Formed at Aqueous Interfaces, *J. Phys. Chem. Lett.* **5**, 4265-4269 (2014), doi:10.1021/jz502249j.

[242] K. Voïtchovsky, N. Ashari-Astani, I. Tavernelli, N. Tétreault, U. Rothlisberger, et al., In Situ Mapping of the Molecular Arrangement of Amphiphilic Dye Molecules at the TiO$_2$ Surface of Dye-Sensitized Solar Cells, *ACS Appl. Mater. Interfaces* **7**, 10834-10842 (2015), doi:10.1021/acsami.5b01638.

[243] U. Diebold T. E. Madey, TiO$_2$ by XPS, *Surf. Sci. Spectra* **4**, 227-231 (1996), doi:10.1116/1.1247794.

[244] R. L. Kurtz, R. Stock-Bauer, T. E. Msdey, E. Román, J. L. D. Segovia, Synchrotron Radiation Studies of H$_2$O Adsorption on TiO$_2$(110), *Surf. Sci.* **218**, 178-200 (1989), doi:10.1016/0039-6028(89)90626-2.

[245] R. McConnell, Assessment of the Dye-Sensitized Solar Cell, *Renewable Sustainable Energy Rev.* **6**, 271-293 (2002), doi:10.1016/S1364-0321(01)00012-0.

[246] H. C. Weerasinghe, F. Huang, Y.-B. Cheng, Fabrication of Flexible Dye Sensitized Solar Cells on Plastic Substrates, *Nano Energy* **2**, 174-189 (2013), doi:10.1016/j.nanoen.2012.10.004.

[247] S. Sheehan, P. Surolia, O. Byrne, S. Garner, P. Cimo, et al., Flexible Glass Substrate Based Dye Sensitized Solar Cells, *Sol. Energy Mater. Sol. Cells* **132**, 237-244 (2015), doi:10.1016/j.solmat.2014.09.001.

[248] A. Hagfeldt, G. Boschloo, L. Sun, L. Kloo, H. Pettersson, Dye-Sensitized Solar Cells, *Chem. Rev.* **110**, 6595-6663 (2010), doi:10.1021/cr900356p.

[249] J. Bisquert, D. Cahen, G. Hodes, S. Rühle, A. Zaban, Physical Chemical Principles of Photovoltaic Conversion with Nanoparticulate, Mesoporous Dye-Sensitized Solar Cells, *J. Phys. Chem. B* **108**, 8106-8118 (2004), doi:10.1021/jp0359283.

[250] J.-E. Moser, *Dye-Sensitized Solar Cells*, chapter Dynamics of Interfacial and Surface Electron Transfer Processes, pages 403–406, EPFL Press, 2010.

[251] K.Kalyanasundaram, editor, *Dye-Sensitized Solar Cells*, EPFL Press, 2010.

[252] G. Boschloo A. Hagfeldt, Characteristics of the Iodide/Triiodide Redox Mediator in Dye-Sensitized Solar Cells, *Acc. Chem. Res.* **42**, 1819-1826 (2009), doi:10.1021/ar900138m.

[253] B. C. O'Regan J. R. Durrant, Kinetic and Energetic Paradigms for Dye-Sensitized Solar Cells: Moving from the Ideal to the Real, *Acc. Chem. Res.* **42**, 1799-1808 (2009), doi:10.1021/ar900145z.

[254] P. J. Cameron L. M. Peter, Characterization of Titanium Dioxide Blocking Layers in Dye-Sensitized Nanocrystalline Solar Cells, *J. Phys. Chem. B* **107**, 14394-14400 (2003), doi:10.1021/jp030790+.

[255] X.-F. Wang, R. Fujii, S. Ito, Y. Koyama, Y. Yamano, et al., Dye-Sensitized Solar Cells Using Retinoic Acid and Carotenoic Acids: Dependence of Performance on the Conjugation Length and the Dye Concentration, *Chem. Phys. Lett.* **416**, 1-6 (2005), doi:10.1016/j.cplett.2005.09.020.

[256] S. Rangan, S. Coh, R. A. Bartynski, K. P. Chitre, E. Galoppini, et al., Energy Alignment, Molecular Packing, and Electronic Pathways: Zinc(II) Tetraphenylporphyrin Derivatives Adsorbed on TiO_2(110) and ZnO(1120) Surfaces, *J. Phys. Chem. C* **116**, 23921-23930 (2012), doi:10.1021/jp307454y.

[257] P. R. F. Barnes, A. Y. Anderson, S. E. Koops, J. R. Durrant, B. C. O'Regan, Electron Injection Efficiency and Diffusion Length in Dye-Sensitized Solar Cells Derived from Incident Photon Conversion Efficiency Measurements, *J. Phys. Chem. C* **113**, 1126-1136 (2009), doi:10.1021/jp809046j.

[258] J. Bisquert, G. Garcia-Belmonte, F. Fabregat-Santiago, N. S. Ferriols, P. Bogdanoff, et al., Doubling Exponent Models for the Analysis of Porous Film Electrodes by Impedance. Relaxation of TiO_2 Nanoporous in Aqueous Solution, *J. Phys. Chem. B* **104**, 2287-2298 (2000), doi:10.1021/jp993148h.

[259] A. Hauch A. Georg, Diffusion in the Electrolyte and Charge-Transfer Reaction at the Platinum Electrode in Dye-Sensitized Solar Cells, *Electrochim. Acta* **46**, 3457-3466 (2001), doi:10.1016/S0013-4686(01)00540-0.

[260] F. Fabregat-Santiago, G. Garcia-Belmonte, I. Mora-Sero, J. Bisquert, Characterization of Nanostructured Hybrid and Organic Solar Cells by Impedance Spectroscopy, *Phys. Chem. Chem. Phys.* **13**, 9083-9118 (2011), doi:10.1039/C0CP02249G.

[261] P. R. F. Barnes, A. Y. Anderson, J. R. Durrant, B. C. O'Regan, Simulation and Measurement of Complete Dye Sensitised Solar Cells: Including the Influence of Trapping, Electrolyte, Oxidised Dyes and Light Intensity on Steady State and Transient Device Behaviour, *Phys. Chem. Chem. Phys.* **13**, 5798-5816 (2011), doi:10.1039/C0CP01554G.

[262] J. Bisquert V. S. Vikhrenko, Interpretation of the Time Constants Measured by Kinetic Techniques in Nanostructured Semiconductor Electrodes and Dye-Sensitized Solar Cells, *J. Phys. Chem. B* **108**, 2313-2322 (2004), doi:10.1021/jp035395y.

[263] N. Duffy, L. Peter, R. Rajapakse, K. Wijayantha, A Novel Charge Extraction Method for the Study of Electron Transport and Interfacial Transfer in Dye Sensitised Nanocrystalline Solar Cells, *Electrochem. Commun.* **2**, 658-662 (2000), doi:10.1016/S1388-2481(00)00097-7.

[264] J. Halme, G. Boschloo, A. Hagfeldt, P. Lund, Spectral Characteristics of Light Harvesting, Electron Injection, and Steady-State Charge Collection in Pressed TiO_2 Dye Solar Cells, *J. Phys. Chem. C* **112**, 5623-5637 (2008), doi:10.1021/jp711245f.

[265] A. B. Walker, L. M. Peter, K. Lobato, P. J. Cameron, Analysis of Photovoltage Decay Transients in Dye-Sensitized Solar CellsÂ , *J. Phys. Chem. B* **110**, 25504-25507 (2006), doi:10.1021/jp064860z.

[266] J. R. Jennings, A. Ghicov, L. M. Peter, P. Schmuki, A. B. Walker, Dye-Sensitized Solar Cells Based on Oriented TiO_2 Nanotube Arrays: Transport, Trapping, and Transfer of Electrons, *J. Am. Chem. Soc.* **130**, 13364-13372 (2008), doi:10.1021/ja804852z.

[267] K. Fredin, J. Nissfolk, G. Boschloo, A. Hagfeldt, The Influence of Cations on Charge Accumulation in Dye-Sensitized Solar Cells, *J. Electroanal. Chem.* **609**, 55-60 (2007), doi:10.1016/j.jelechem.2007.05.013.

[268] L. M. Peter, Characterization and Modeling of Dye-Sensitized Solar Cells, *J. Phys. Chem. C* **111**, 6601-6612 (2007), doi:10.1021/jp069058b.

[269] A. Zaban, M. Greenshtein, J. Bisquert, Determination of the Electron Lifetime in Nanocrystalline Dye Solar Cells by Open-Circuit Voltage Decay Measurements, *ChemPhysChem* **4**, 859-864 (2003), doi:10.1002/cphc.200200615.

List of Figures

List of Tables

Abbreviations

AFM	Atomic force microscopy
AM	Amplitude modulation
CPD	Contact potential difference
CuTCPP	Copper(II) 5,10,15,20-tetra(4-carboxyphenyl)porphyrin
DFT	Density functional theory
DP	Dual-pass
DSC	Dye-sensitized solar cell
EIS	Electrochemical impedance spectroscopy
EQE	External quantum efficiency
FM	Frequency modulation
FTO	Fluorine doped tin oxide
HOMO	Highest occupied molecular orbital
IV	Current-voltage
KPFM	Kelvin probe force microscopy
LCPD	Local contact potential difference
LUMO	Lowest unoccupied molecular orbital
MCPP	Metallo-carboxyphenylporphyrin
nc	non-contact
PES	Photoelectron spectroscopy
PLL	Phase locked loop
SPM	Scanning probe microscopy
STM	Scanning tunneling microscopy
UHV	Ultra-high vacuum
VBS	Valence band spectroscopy
vdW	Van der Waals
XPS	X-ray photoelectron spectroscopy
ZnCPP	Zinc(II)-(4-carboxyphenyl)porphyrin
cis-ZnDCPP	Zinc(II) 5,10-di(4-carboxyphenyl)-15,20-diphenylporphyrin
tr-ZnDCPP	Zinc(II) 5,15-di(4-carboxyphenyl)-10,20-diphenylporphyrin
ZnMCPP	Zinc(II) 5-(4-carboxyphenyl)-10,15,20-triphenylporphyrin
ZnTCPP	Zinc(II) 5,10,15,20-tetra(4-carboxyphenyl)porphyrin

A	Oscillation amplitude
Δf	Frequency shift
E_ad	Adsorption energy
E_b	Binding energy (XPS Spectroscopy)
E_cb	Conduction band energy
E_F	Fermi energy
χ	Electronegativity
η	Conversion efficiency
E_vac	Vacuum energy
f	Oscillation frequency
F_el	Electrostatic force
FF	Fill factor
F_ts	Tip-sample force
I_t	Tunneling current
J_sc	Short circuit current
μ_m	Chemical potential
ω	Angular frequency of the oscillation
Q	Quality factor of the oscillation
q	Elementary charge
V_g	Gap voltage
V_oc	Open circuit voltage
V_s	Sample voltage

List of Publications

Papers

1.) R. Jöhr, A. Hinaut, R. Pawlak, A. Sadeghi, S. Saha, S. Goedecker, B. Such, M. Szymonski, E. Meyer and Th. Glatzel, *Characterization of Individual Molecular Adsorption Geometries by Atomic Force Microscopy: Cu-TCPP on Rutile TiO$_2$ (110)*, **The Journal of Chemical Physics 143**, 094202, (2015), doi:10.1063/1.4929608

2.) R. Jöhr, L. Zajac, G. Günzburger, H. Hug, B. Such, M. Szymonski, E. Meyer and Th. Glatzel, *Impact of Photocatalysis on Carotenoic Acid Dye-Sensitized Solar Cells*, **Hybrid Materials (De Gruyter Journal) 2**, 17-24, (2015), doi:10.1515/hyma-2015-0003

3.) R. Jöhr, A. Hinaut, R. Pawlak, L. Zajac, P. Olszowski, B. Such, Th. Glatzel, J. Zhang, M. Muntwiler, J. Bergkamp, S.-X. Liu, S. Decurtins, M. Szymonski and E. Meyer, *Thermally Induced Anchoring of a Zinc-Carboxyphenylporphyrin on Rutile TiO$_2$ (110)*
(Manuscript submitted)

4.) R. Pawlak, A. Sadeghi, R. Jöhr, A. Hinaut, T. Meier, L. Zajac, P. Olszowski, S. Kawai, B. Such, Th. Glatzel, M. Szymonski, and E. Meyer, *Hydroxyl-Induced Partial Charge States of Single Porphyrins on Titania Rutile*, **The Journal of Physical Chemistry C 121**, 6, 3607-3614, (2017), doi:10.1021/acs.jpcc.6b11873

5.) A. Henning, G. Günzburger, R. Jöhr, Yossi Rosenwaks, Biljana Bozic-Weber, Catherine E. Housecroft, Edwin C. Constable, E. Meyer and Th. Glatzel, *Kelvin Probe Force Microscopy of Nanocrystalline TiO$_2$ Photoelectrodes*, **Beilstein Journal of Nanotechnology 4**, 418-428, (2013), doi:10.3762/bjnano.4.49

6.) P. Olszowski, L. Zajac, S. Godlewski, B. Such, R. Jöhr, Th. Glatzel, E. Meyer, M. Szymonski, *Role of a Carboxyl Group in the Adsorption of Zn Porphyrins on TiO$_2$(011)-(2 × 1) Surface*, **The Journal of Physical Chemistry C 119**, 37, 21561-21566, (2015), doi:10.1021/acs.jpcc.5b07002

7.) L. Zajac, P. Olszowski, S. Godlewski, B. Such, R. Jöhr, R. Pawlak, A. Hinaut, Th. Glatzel, E. Meyer, M. Szymonski, *Ordered Heteromolecular Overlayers Formed by Metal Phthalocyanines and Porphyrines on Rutile Titanium Dioxide Surface Studied at Room Temperature*, **The Journal of Chemical Physics 143**, 224702, (2015), doi:10.1063/1.4936658

8.) J. S. Prauzner-Bechcicki, L. Zajac, P. Olszowski, S. Godlewski, R. Jöhr, A. Hinaut, Th. Glatzel, B. Such, E. Meyer, M. Szymonski, *Scanning Probe Microscopy Studies on the Adsorption of Selected Molecular Dyes on Titania*, **Beilstein Journal of Nanotechnology 7**, 1642-1653, (2016), doi:10.3762/bjnano.7.156

9.) L. Zajac, P. Olszowski, S. Godlewski, L. Bodek, B. Such, R. Jöhr, R. Pawlak, A. Hinaut, Th. Glatzel, E. Meyer, M. Szymonski, *Self-Assembling of Zn Porphyrins on a (110) Face of Rutile TiO_2 - The Anchoring Role of Carboxyl Groups*, **Applied Surface Science 379**, 277-281, (2016), doi:10.1016/j.apsusc.2016.04.069

10.) P. Olszowski, L. Zajac, S. Godlewski, B. Such, R. Pawlak, A. Hinaut, R. Jöhr, Th. Glatzel, E. Meyer, M. Szymonski, *Ordering of Zn-centered porphyrin and phthalocyanine on $TiO_2(011)$: STM studies*, **Beilstein Journal of Nanotechnology 8**, 99-107, (2017), doi:10.3762/bjnano.8.11

Presentations

1. Interaction of Metallo-Carboxyphenyl Porphyrins with Rutile and Anatase TiO_2, R. Jöhr, A. Hinaut, R. Pawlak, L. Zajac, B. Such, M. Muntwiler, Th. Glatzel, S. Decurtins, M. Szymonski and E. Meyer, EMN Meeting on Titanium Oxides, 27-03-2016, Honolulu, (USA), invited.

2. Interaction of Metallo-Carboxyphenyl Porphyrins with Rutile and Anatase TiO_2, R. Jöhr, A.Hinaut, R. Pawlak, A. Sadeghi, L. Zajac, B. Such, S. Goedecker, M. Szymonski, Th. Glatzel and E. Meyer, 8th International Workshop on Nanoscale Pattern Formation at Surfaces, 14-07-2015, Krakow, (Poland).

3. Interaction of Metalloporphyrins with Rutile (110) and Anatase (101) TiO_2, R. Jöhr, A. Hinaut, R. Pawlak, A. Sadeghi, S. Goedecker, E. Meyer and Th. Glatzel, MolCHsurf X 2015, 08-06-2015, Bern, (Switzerland).

4. Investigation of Adsorption Geometries of Single Cu-TCPP on Rutile TiO_2 (110), R. Jöhr, A. Hinaut, R. Pawlak, E. Meyer and Th. Glatzel, E-MRS Fall Meeting, 16-09-2014, Warsaw, (Poland).

Posters

1. Adsorption Geometries of Single Cu-TCPP Molecules on Rutile TiO$_2$ (110), R. Jöhr, A. Hinaut, R. Pawlak, A. Sadeghi, S. Goedecker, S. Decurtins, T. Glatzel and E. Meyer, 18th International Conference on non-contact Atomic Force Microscopy, 10-09-2015, Cassis, (France).

2. Influence of Carboxyl Groups on the Porphyrin Morphology, L. Zajac, P. Olszowski, R. Jöhr, Th. Glatzel, E. Meyer, B. Such and M. Szymonski, 8th International Workshop on Nanoscale Pattern Formation at Surfaces, 14-07-2015, Krakow, (Poland).

3. Investigation of Interfacial Processes in Dye-Sensitized Solar Cells by Means of Electrochemical Impedance Spectroscopy, R. Jöhr, J. Nussbaum, S. Freund, E. Meyer and Th. Glatzel, 6th International Conference on Hybrid and Organic Photovoltaics 2014, 12-05-2014, Lausanne, (Switzerland).

Curriculum Vitae

Name: Res Jöhr
Date of Birth: 25. July 1986
Place of Birth: Bern

Education

2012-2016	PhD student in experimental physics
	(Research group of Prof. E. Meyer, University of Basel)
2010-2012	M.Sc. in Nanosciences (Major in Physics)
	(University of Basel)
2007-2010	B.Sc. in Nanosciences
	(University of Basel)
2005-2007	Military service
	(Officer and specialist for NBC defense, SVF leadership I certificate)
2002-2005	Matura (Major in Biology and Chemistry)
	(Gymnasium Schadau, Thun)
1992-2002	Primary and Secondary School
	(Steffisburg)

Teaching

2012-2016	Teaching assistant for:
	- Lectures in Physics of Semiconductors and Photovoltaics
	- Experimental support of project students
2009-2012	Undergraduate teaching assistant for:
	- Lectures in Mathematical Methods (Part I-III)
	- Introduction lectures to Physics (Part I & II)